Scanning Tunneling Microscopy of Ni and Fe Nanocrystals on $SrTiO_3$



Aatif Rasheed

Linacre College

A thesis submitted for the degree of

MSc by Research in Materials

Michaelmas Term 2019

Abstract

The equilibrium crystal shapes (ECS) of Ni and Fe were investigated on three different terminations of $SrTiO_3$ {(001), (110), and (111)}. Firstly, to investigate surface reconstructions, $SrTiO_3$ substrates were subjected to various thermal cycles. $SrTiO_3$ is capable of producing a multitude of surface reconstructions such as (2 × 1), (2 × 2), (√5 × √5) R26.6°, and c(4 × 2) on (001) termination; (4 × 1) on (110) termination; and (4 × 4) and (6 × 6) on (111) termination. On $SrTiO_3$ (001) sample, Ni grew itself in the form of a truncated pyramidal shape with (001) as the top facet, four (110) side facets and one (001) base facet. This shape of Ni nanocrystals was also observed on a $SrTiO_3$ (001) sample that was subjected to sputtering followed by annealing at 920 ºC for 1 h. On $SrTiO_3$ (110) sample, Ni grew itself in the form of truncated huts with (110) as the top facet, two (111) side facets, two (001) side facets, and one (110) base facet. On $SrTiO_3$ (111) sample, Ni grew in two forms: icosahedron and truncated octahedron. Point, edge and face orientations of icosahedrons were observed. The icosahedron had (111) facets while truncated octahedron had (111) top facet, three (111) side facets, three (001) side facets, and one (111) base facet. On $SrTiO_3$ (001) sample, Fe grew itself in the form of truncated pyramid shape with (001) as the top facet, four (110) side facets, and one (001) base facet. On another $SrTiO_3$ (001) substrate, Fe grew in the form of truncated square-shaped and truncated rectangular-shaped nanocrystals. A surface texture was also observed and was found sensitive to tip bias. On $SrTiO_3$ (110) sample, Fe grew itself in the form of truncated huts with (110) as the top facet, two (111) side facets, two (001) side facets, and one (110) base facet. On $SrTiO_3$ (111) sample, Fe grew in two forms: truncated octahedron and truncated hut. Wulffman simulations of the nanocrystals were generated and adhesion energies were calculated.

Preface

The work reported in this thesis is original work that was carried out by the author, unless indicated otherwise, from October 2016 to September 2019, under the supervision of Professor Martin Castell, in the Department of Materials at the University of Oxford. Some of the work contained in this thesis has been presented at scientific conferences whose detail is provided as below:

Poster presentations:

1. Atif Rasheed and Martin R. Castell. Growth of Truncated Pyramidal Ni Nanocrystals on a $SrTiO_3$ (001) Support. ISSC-22 Interdisciplinary Surface Science Conference, University of Swansea, Village Hotel, Swansea, United Kingdom, April 15th - 18th 2019.

2. Atif Rasheed and Martin R. Castell. Growth of Icosahedral and Truncated Octahedral Ni Nanocrystals on a $SrTiO_3$ (111) Support. Surface Science Day, University of Birmingham, United Kingdom, December 17th 2018.

3. Atif Rasheed and Martin R. Castell. Influence of Surface Defects on the Nucleation and Growth of Ag Nanocrystals on $SrTiO_3$ (001). nanoScience @ Surfaces Summer School 2018, Cambridge University, United Kingdom, July 30th – August 2nd 2018.

Acknowledgments

First and foremost, I would like to thank my supervisor, Professor Martin Castell, who brought me into the microscopic world to investigate the structures down to the nanometer scale. I also want to express my appreciation for his patience on spending many hours on meetings with me and discussing the work. He always encouraged me to explore the insight of the research and motivate me to solve the problem from different aspects. I am also thankful to Martin for suggesting me to attend several international scientific conferences. This allowed me to share my research ideas with other researchers around the world and spark inspirations on my research projects.

Working with a group of people during my stay at Oxford is an invaluable experience for me. I would like to thank my colleagues in the research group, Shuqiu Wang (Sue), Xiao Hu, Peiyu Chen, and Yakun Gu for training me on using UHV-STM, teaching me how to make tips, and advice on making images better using the SmartAlign software. Other colleagues during my time in the STM group have been a pleasure to work with: Fubiao Gu, Yuhan Zhu, Krishnan Murugappan and Ben Armitage, and thanks for their peer support. I appreciate our engineer Chris Spencer for the technical assistance and solutions for any difficult situation that happened to me while I was using STM.

I would like to thank the administrative and technical support staffs from our department: the kind support from Marion Beckett and Adrian Taylor from Department Graduate Office, and Paul Warren, Chris Akinola and Robert Saunders from Department IT Services for saving my PC.

Great thanks to my College, Linacre College, which provided a great social and comfortable living environment and provided me financial support for summer school at Cambridge University. I would also like to thank Oxford – Sir Anwar Pervez Graduate Research Scholarship without which joining Oxford was not possible.

Contents

1 Introduction: 1

1.1 Background 2

1.2 Thesis plan 5

2 Experimental Techniques 6

2.1 Introduction 7

2.2 Scanning tunneling microscopy (STM) 7

2.3 Methods and procedure 8

2.3.1 Sample preparation 8

2.3.2 Sputtering 10

2.3.3 Tip making 11

2.3.4 UHV-STM 14

2.3.5 STM system baking 17

2.3.6 Metal deposition 18

2.4 Summary 19

3 Literature survey 20

3.1 Overview 21

3.2 Growth modes 23

3.2.1 Frank-van der Merwe (FM) layer-by-layer growth mode 23

3.2.2 Volmer-Weber (VW) island growth mode 23

3.2.3 Stranski-Krastanov (SK) layer-plus-island growth mode 23

3.3 Wetting: 24

3.4 Interface 25

3.5 How to create nanoparticles 31

3.6 Epitaxy: supported nanocrystals 31

3.6.1 Commensurate-incommensurate epitaxy: 32

3.6.2 Coincidence epitaxy: 35

3.6.3 Substrates 36

3.6.4 Morphology: 39

3.7 How does the nanoscale influence metallurgical behavior? 42

3.8 Core-shell nanoparticles 44

3.9 Summary 46

3.10 Conclusions 49

4 $SrTiO_3$ 50

4.1 Background 51
4.1.1 Overview 51
4.1.2 Experimental details 52
4.2 Results 54
4.2.1 $SrTiO_3$ (001) 54
4.2.2 $SrTiO_3$ (110) 69
4.2.3 $SrTiO_3$ (111) 69
4.3 Conclusions 70
5 Ni Nanocrystals 71
5.1 Background 72
5.1.1 Overview 72
5.1.2 Experimental details 73
5.2 Results 73
5.2.1 Ni on $SrTiO_3$ (001)-(2 × 1) 73
5.2.2 Ni on $SrTiO_3$ (001)-Nanolines 79
5.2.3 Ni on $SrTiO_3$ (110) 84
5.2.4 Ni on $SrTiO_3$ (111) 95
5.3 Conclusions 100
6 Fe Nanocrystals 102
6.1 Background 103
6.2 Experimental details 103
6.3 Results and discussion 103
6.3.1 Fe on $SrTiO_3$ (001) 103
6.4 Wulffman simulations for iron oxide 111
6.5 Chamfered rectangular nanocrystals 113
6.6 Chamfered square nanocrystals 117
6.7 Co-existence of the two shapes 121
6.8 Bias-dependence 126
6.9 Fe on $SrTiO_3$ (110) 130
6.9.1 Fe on $SrTiO_3$(111) 137
6.10 Conclusions 140
7 Conclusions and Future work 142
7.1 Conclusions 143
7.1.1 $SrTiO_3$ 143
7.1.2 Ni on $SrTiO_3$ 143
7.1.3 Fe on $SrTiO_3$ 143

7.2 Future work 144
8 References: 146

Chapter 1:

Introduction

1.1 Background

One of the objectives of contemporary research in electronics is to fabricate high-performance electronic devices at low cost. To achieve this goal, both precursors and processing techniques must be economical. As businesses can only thrive when they are lucrative, only those processing techniques are used that can give maximum profit to the business owners. A great variety of diverse electronic products is ubiquitous around us that indicates that industry has already tailored the processing techniques to at least an extent where those techniques make the businesses profitable. Those low-cost processing techniques can only produce low-cost, high-performance electronic devices when the precursors are also low-cost. In electronics, high-performance usually means superior (i) electronic, (ii) thermal, (iii) (non-) magnetic, and (iv) mechanical properties coming at a low cost.

To achieve the above-stated properties in one material is still a challenge. For example, Pt and Au are high-performance electronic materials [1,2]. However, they are expensive. Similarly, certain rare-earth metals based compounds have superior magnetic properties [3–5]. Nonetheless, they lack in other aforementioned properties. One of the traditional materials which can be high-performance as well as low-cost is Fe [6]. Nevertheless, Fe is magnetic at room temperature and certain electronic applications require the materials to be non-magnetic [7,8]. But what if we can make iron non-magnetic at room temperature by controlling its crystal structure? Sadly, no article is yet available, to the best of author's knowledge, in which the crystal structure of Fe has been modified at nanoscale based on the processing parameters. The variation in the electronic, thermal, magnetic, and mechanical properties of Fe nanocrystals with modified crystal structure is also not available. Therefore, the objective of the current study is to investigate whether austenite

can be stabilized in the form of nanocrystals at room temperature. Also, can a correlation between crystal structure and magnetic properties be established?

Under normal conditions, pure Fe crystallizes as body-centered cubic (bcc) [9]. When heated, Fe retains its bcc structure until 910 °C after which it converts to face-centered cubic (fcc) structure called austenite or gamma (γ) iron. The γ-Fe is stable until about 1395 °C after which it again converts to expanded bcc structure called as delta (δ) iron. The δ-Fe remains stable until about 1535 °C after which Fe melts. As properties of bulk structure depend on crystal structure, getting a specific phase of Fe becomes crucial for specific applications. For example, α-Fe is magnetic while γ-Fe is non-magnetic. Therefore, α-Fe is preferred when magnetic properties are desired, and γ-Fe is required for non-magnetic properties. Although γ-Fe can be easily used for non-magnetic applications, the problem is that it is a high-temperature phase and thermodynamically unstable at room temperature. Therefore, the first challenge is to stabilize γ-phase at room temperature. Fortunately, it can be stabilized under a given set of conditions. The austenite can be stabilized by three ways: (i) by adding austenite stabilizers, (ii) by optimizing processing parameters, and (iii) by controlling size and shape of nanocrystals. Once austenite stabilized iron is successfully produced, the next objective will be to tailor its morphology and magnetic properties by controlling the surface of the substrate.

The surface of the substrate is very crucial as the topography and morphology of nanocrystals will be dictated by the interplay among substrate surface energy, the surface energy of produced nanocrystals and interfacial energy [10]. If interfacial energy is higher than the sum of surface energies of the substrate and nanocrystals, needle- or rod-like nanocrystals will be produced to reduce the interfacial area and to keep the system at lowest possible energy state [11]. Similarly, if interfacial energy is lower than the sum of surface energies of the substrate and nanocrystals, dome-shaped islands will be observed

will large base and minimum height possible [12]. The surface areas of needles, rods, domes, and islands will be different and hence so will their electronic and magnetic properties. Therefore, the surface of a substrate is very critical in achieving the desired morphology and electronic and magnetic properties of grown nanocrystals. In a substrate surface, there are two main defining features: (i) termination, and (ii) reconstruction.

The termination is the plane in which the substrate is grown [10]. As growth mechanism can be different at grain boundaries, a single crystal substrate is preferred. As every embryo formed in a liquid requires to be converted into a nucleus to be stable, atoms attach to the embryo and then to the nucleus. If solidification continues, mostly a polycrystalline material is achieved with defects such as vacancies, interstitial and substitutional foreign atoms, dislocations, stacking faults, and grain boundaries. As all of those defects may adversely affect the growth of nanocrystals, the substrate must be as much free from these defects as possible. Luckily, it is possible to avoid these defects if processing parameters are meticulously controlled. Czochralski's, float zone, and Bridgman-Stockbarger methods are three most commonly used methods to produce single crystals of sufficiently large size that can easily be used to act as substrates for the growth of nanocrystals. The desired termination may be produced by controlling the processing parameters. Once a specific termination is achieved, the next objective will be to get specific reconstruction on the surface of the substrate.

Unlike bulk atoms, surface atoms do not have a neighbor above them with whom they can make bonds. Therefore, surface thermodynamics is different from the bulk thermodynamics. The surface atoms do not position themselves in the same way as done by bulk atoms. Accordingly, the surface structure is different from that of the bulk structure at the atomic scale. This different surface structure is called a reconstruction [10]. As topography and morphology of nanocrystals are dependent on the surface energy of

substrate and different surface reconstructions have different surface energy values, surface reconstruction is an important factor to grow nanocrystals for electronic and magnetic applications. Therefore, attempt is made in the current work to stabilize the austenite at nanoscale by employing different austenite stabilizers, controlling morphology of nanocrystals, and controlling the processing parameters (mainly thermal cycle). To compare Fe nanocrystals with a fcc structure, Ni nanocrystals were grown and studied in detail. The next section describes the structure of the thesis.

1.2 Thesis plan

Separate chapters have been made for each system investigated. The next chapters (chapter 2) is about experimental techniques in which tools, techniques, and methods used to grow and characterize nanocrystals are briefly explained In chapter 3 is about the literature review in which fundamental aspects and key concepts related to the field are described. In chapter 4, various reconstructions produced on $SrTiO_3$ (001) are shown and discussed. Ni and Fe nanocrystals are reported in chapters 5 and 6, respectively. In chapter 7, main conclusions of the current work are highlighted and possible future work is suggested. At the end, references cited in the current work are listed.

Chapter 2:

Experimental Techniques

2.1 Introduction

The surfaces could easily be understood at bulk scale based on basic features such as color, hardness, and coefficient of friction. However, plummeting down to the nanoscale, the characterization of surfaces was only possible with the advent of powerful surface characterization techniques such as scanning tunneling microscopy (STM), low-energy electron diffraction (LEED), X-ray induced photoelectron spectroscopy (XPS), magnetic force microscopy (MFM), and X-ray diffraction (XRD). In 1981, Gerd Binnig and Heinrich Rohrer invented STM and studied structures of conductive surfaces at atomic resolution [13,14]. The impact of STM in the field of surface science was so much conspicuous that they were awarded Nobel Prize in Physics just after five years of their invention.

To carry out the proposed project, multiple tools and techniques were used whose detail is provided in the sections below.

2.2 Scanning tunneling microscopy (STM)

STM can provide images with atomic scale resolution and can also be used as a pick-and-drop facility for individual atoms. Eigler and Schweizer wrote “IBM” using 35 xenon atoms where each letter was 5 nm high [15]. The working principle of STM is based on electron tunneling which was first demonstrated by Giaever in his experiments during the early 1960s [16]. The electron tunneling in vacuum was demonstrated by Young et al. during the 1970s [17]. In the field emission regime, Young combined electron tunneling and three-dimensional scanning and developed “topographiner” [18]. In the 1980s, Binnig and Rohrer developed scanning tunneling microscope and captured the images of surface atoms [19]. In modern STMs available, the number of parameters that can be controlled is increasing that led to the development of various spectroscopic methods such as variable

and fixed tip-sample distance current-voltage spectroscopy, voltage-dependent imaging and current image spectroscopy.

The tunneling current increases by an order of magnitude if a tip is brought 1 Å closer to the current position. The tunneling current decreases in a similar way. Therefore, to achieve stable tunneling, the separation between the tip and the surface in STM must be minimal and almost immaculate damping out of vibrations. In three dimensions, the position of the tip is precisely controlled by highly sensitive piezoelectric drivers. The tunneling current $I(x)$ with respect to the radius of curvature of the tip R is $I(x) \propto exp\left(-2\kappa x/_R\right)$ where x is a lateral position relative to the center of tip and κ is typically ~ 1 Å. In general, a tip with a radius of curvature equal to 100 nm can produce an image with a resolution of 5 nm.

2.3 Methods and procedure

2.3.1 Sample preparation

Single crystal epi-polished $SrTiO_3$ substrates with 0.5 wt% Nb doping provided by PI-KEM Ltd., UK were used in this work. The sample size was 7.0 × 2.0 × 0.5 mm. A pure stoichiometric $SrTiO_3$ sample is a good insulator with a band gap of about 3.2 eV at room temperature. Slightly doping with an electron donor Nb changes $SrTiO_3$ from insulator to n-type semiconductor. Modification of the sample conductivity enables the surface preparation and experimental analysis by STM. Samples are ultrasonically cleaned in acetone and methanol separately for fifteen minutes, dried with an air duster and then mounted on the sample holder. The heating sample holder was used in this experiment as shown in Figure 2-1 while the mounting procedure is shown in Figure 2-2. The sample is placed on the two molybdenum posts and screwed in carefully using two tantalum clips to secure the sample in place. The resistance of the sample is desired to be less than 3Ω. The mounted sample is then put into the specimen exchange chamber (base pressure of 10^{-5} Pa)

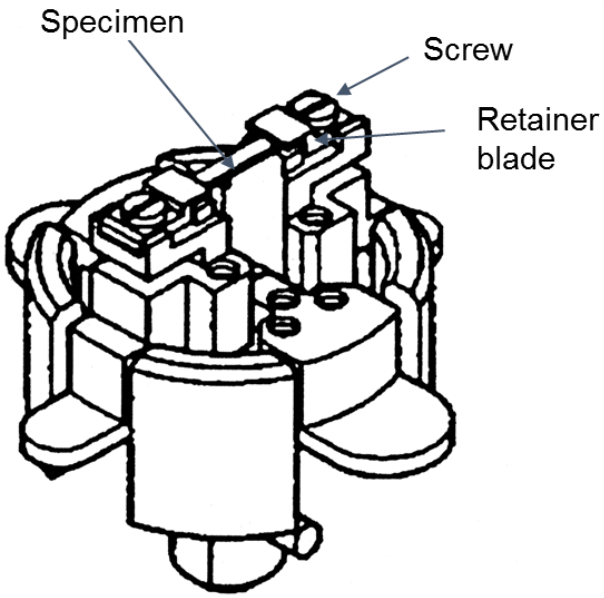


Figure 2-1: Sample heating holder [20]**.**

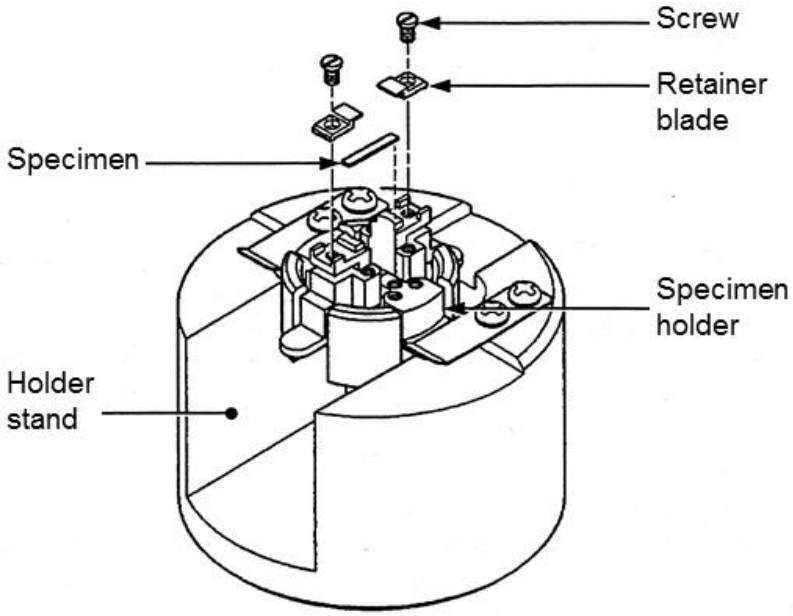


Figure 2-2: Mounting the sample on the heating sample holder [20]**.**

and transferred into the treatment chamber (base pressure of 10^{-8} Pa).

The direct heating method is used to prepare the sample surface. As shown in Figure 2-3, the electric terminals for direct heating are located at the top and bottom of the specimen stage block. The external power supply connects these two terminals to provide the voltage

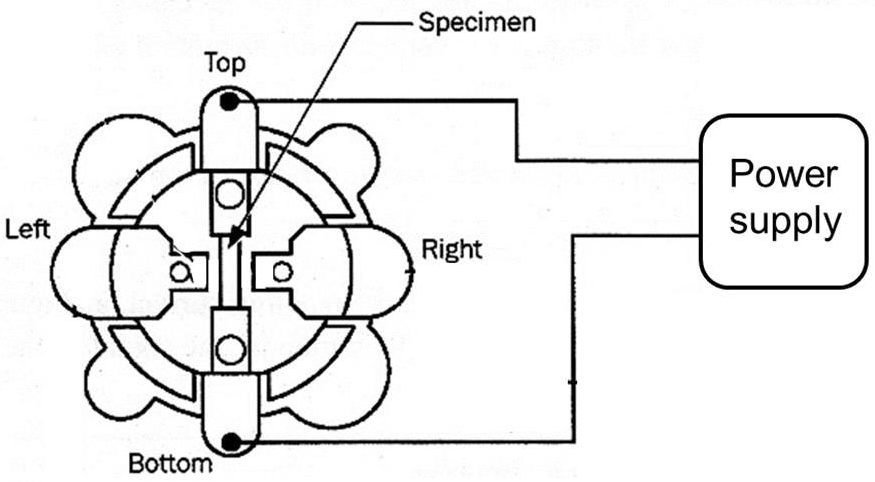


Figure 2-3: Heating connection for direct heating method [20]**.**

bias. A direct current is produced that passes through the sample and heats it. The sample is degassed and annealed (in UHV or O_2) to prepare different reconstructed surfaces. The temperature of the sample is measured by the disappearing filament optical pyrometer from HeatWave Labs, Inc. The pyrometer can measure temperatures ≥ 800 °C.

2.3.2 Sputtering

In STM, sputtering is mainly carried out to clean the surface and to remove deposited nanocrystals. This cleaning is carried out to reuse the sample. The sputtering takes place by bombarding the surface with high energy ions. In this work, Ar gas was used to produce plasma. An EX03 Ion gun system is installed onto the treatment chamber for sputtering purposes. This system can generate ions with 300 eV to 3 keV energy with a current of 10 μA to 20 μA, respectively. The ion gun is composed of gas line cover and lens column. Inert Ar gas is introduced into the source region of the ion gun through a gas pipe. The pressure value determines the quantity of Ar atoms in the source region, i.e., ionization region. The sputtering process is described in Figure 2-4. There are two filaments installed in the ion gun. During sputtering, one of the filaments is heated up to the temperature where the electrons are emitted. The emitted electrons are accelerated and travel through

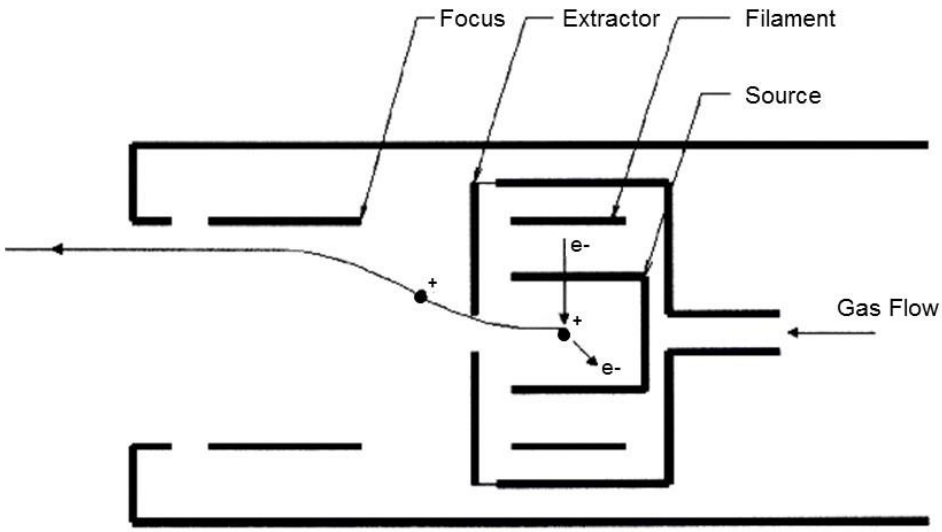


Figure 2-4: Schematic diagram of the EX03 ion gun [21]**.**

the cage of the source region to the region where they are occupied by inert Ar gas. The flow of electrons is the indication of the emission current.

The collision between the electrons and Ar atoms causes the ionization of Ar species that results in the generation of positively charged Ar ions (Ar^+). The high positive potential is applied to the ion gun which allows Ar^+ ions to accelerate through the aperture in the extractor lens and travel to the sample. Several lenses are installed in the lens column to focus and shape the Ar^+ ion beam. The beam current, as an indication of the quantity of Ar^+ ions striking to the target sample, can be controlled by the pressure and the emission current [53]. Ar^+ ions bombarded at the sample surface can remove contaminations and create the surface defects. The non-stoichiometric sample surface after sputtering is favorable for surface reconstructions and formation of new structures during the annealing process.

2.3.3 Tip making

A tungsten (W) tip was used that was prepared by electrochemical etching of a tungsten wire (diameter 0.3mm) in a 2 mol/L NaOH solution. A piece of W wire (~10 mm) was ultrasonic cleaned in acetone and methanol for ten minutes and then dried with an air

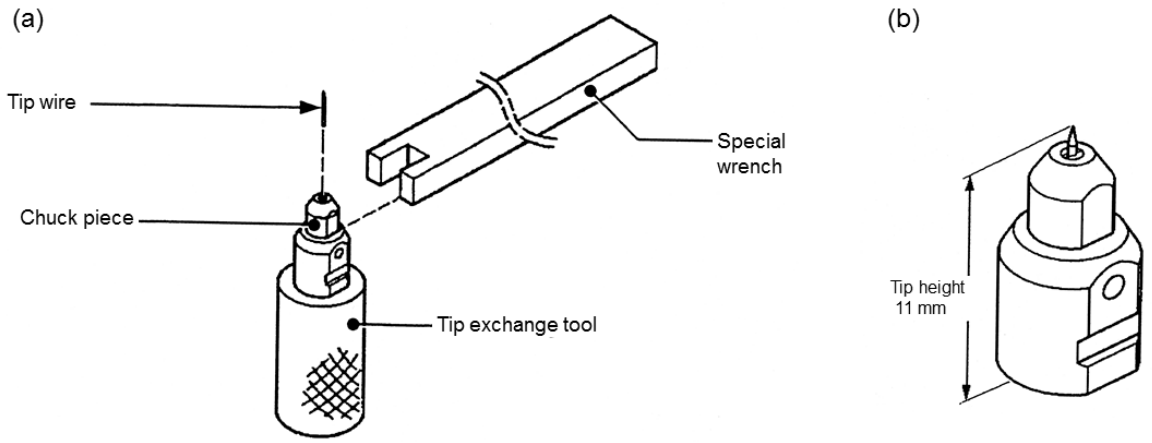


Figure 2-5: (a) Tip wire mounting in the tip holder. (b) JEOL tip holder showing the suitable tip height [20]**.**

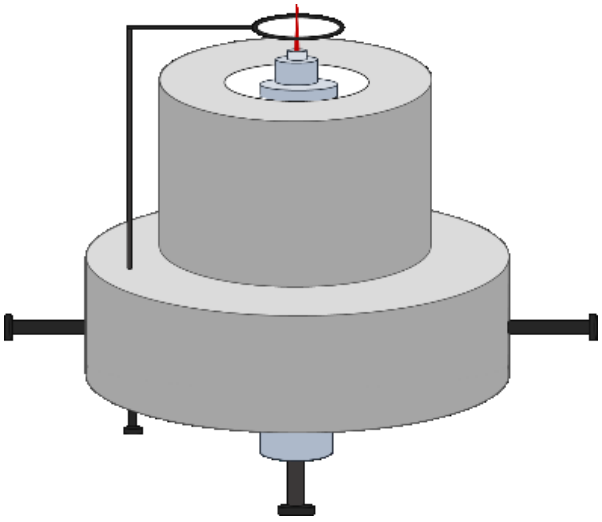


Figure 2-6: Schematic diagram of the special tip port for tip making. The W tip is in red [22]**.**

duster. Then the W wire was inserted into a JEOL tip holder (Figure 2-5(a)). It was fastened by a special wrench to secure the tip in place and leave the suitable tip height (11 mm) (Figure 2-5(b)). The tip holder was loaded into a special tip port (Figure 2-6) and put through the center of the Pt wire loop. The rest of the W wire is cut off with 4 mm left between the Pt loop and the end of the W wire. The Pt loop is connected to the cathode, and the tip holder is connected to the anode. The electrical power is supplied by the specially designed power supply. The Pt loop is placed very close to the liquid level of NaOH solution to form the NaOH solution meniscus and close the electrical circuit.

During the electrochemical etching process, the W tip which is connected to the tip holder acts as the anode, and Pt loop acts as the cathode. The etching occurs at the air-electrolyte interface where the meniscus of the NaOH solution forms. The chemical reactions are described as follows:

$$\text{Anode reaction: } W + 8OH^- \rightarrow WO_4^{2-} + 4H_2O + 6e^- \quad \textbf{2-1}$$

$$\text{Cathode reaction: } 6H^+ + 6e^- \rightarrow 3H_2 \quad \textbf{2-2}$$

$$\text{Total reaction: } W + 2H_2O + 2OH^- = WO_4^{2-} + 3H_2 \quad \textbf{2-3}$$

During etching, the anode material of the W wire is constantly consumed. It becomes thinner at the etching interface (Figure 2-7). Once it becomes thin enough, the bottom part of the tip of the solution drops off and leaves a sharp fracture surface at the etching interface [54].

The power supply for the tip making apparatus is sensitive to the change of the resistance

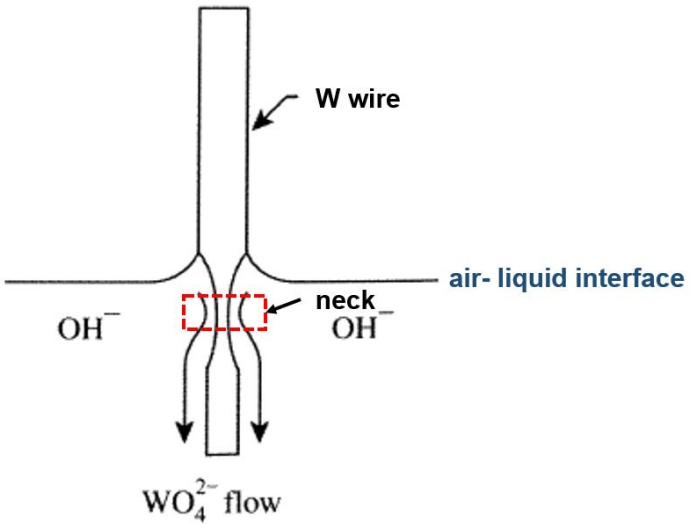


Figure 2-7: Schematic diagram showing the electrochemical etching process of the W wire in the 2 mol/L NaOH electrolyte solution. The neck marked becomes thinner during etching (marked by red dash rectangle) [23]**.**

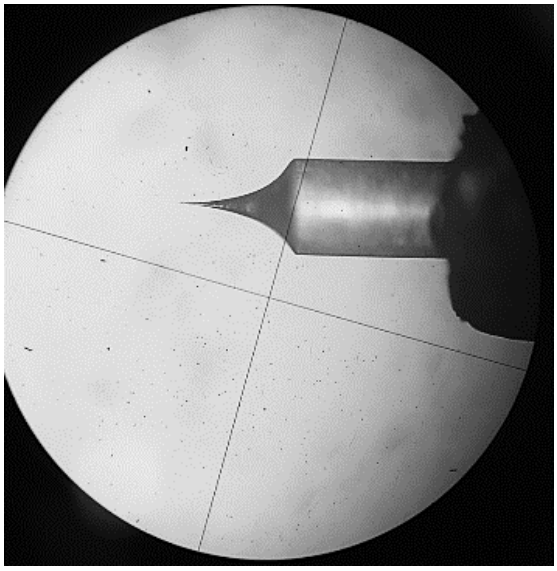


Figure 2-8: Example of a sharp W tip prepared by electrochemical etching in the 2 mol/L NaOH solution. The tip is inspected under an optical microscope [22]**.**

and automatically shuts down once the electrical circuit breaks to stop further etching. The tip is then rinsed with acetone and methanol to remove the excess NaOH, dried with an air duster and inspected under an optical microscope. An example of the fresh, sharp tip prepared by the electrochemical etching method is shown in Figure 2-8. Because the OH^- is consumed during each reaction, NaOH solution should regularly be changed to obtain the proper etching speed.

2.3.4 UHV-STM

The surfaces were imaged using the STM model JSTM-4500s as shown in Figure 2-9. The STM comprised of three chambers: Imaging chamber, a treatment chamber, and an exchange chamber. The chambers are being partitioned by two gate valves. The tip and samples are inserted into and taken out of STM using exchange chamber. The chamber needs to be exposed to air to transport a sample/tip in or out of STM. To create vacuum in the chamber, the chamber is equipped with a turbo molecular pump (TMP) which can lower the pressure up to 10^{-6} Pa. The tip/sample is transferred to the treatment chamber where the sample is processed (degassing, sputtering, annealing) if required. The sample is

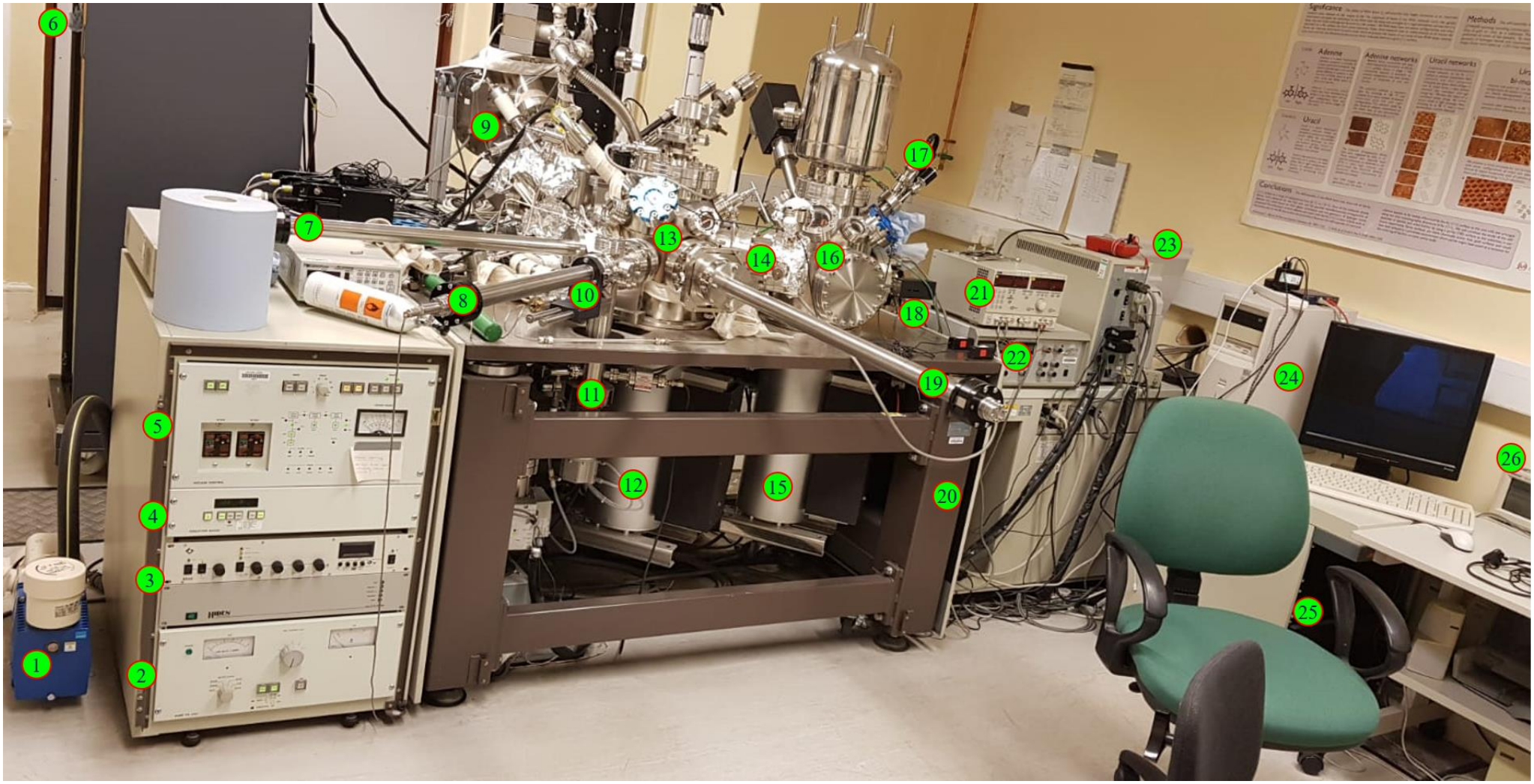


Figure 2-9: Photo of custom-built ultra-high vacuum scanning tunneling microscope (UHV-STM), Model JEOL JSTM-4500s system designed by Japanese Electron Optics Laboratories (JEOL) [22]**.**

1. Turbo-molecular pump (TMP) with capacity of 240 L/s.
2. Pump PS unit
3. Sputtering control unit
4. Pressure gage unit
5. Valve control unit
6. Control unit for e-beam evaporator
7. Transfer arm connecting Treatment and Imaging chambers
8. Transfer arm connecting Specimen exchange chamber and Treatment chamber
9. SEM unit
10. Specimen exchange chamber connected with TMP that can reduce pressure up to $\leq 10^{-5}$ Pa.
11. TMP connection
12. Ion pump for Treatment chamber with capacity of 200 L/s.
13. Treatment chamber connected with ion pump and Ti-sublimation pump that can reduce pressure up to $\leq 10^{-8}$ Pa.
14. LEED screen
15. Ion pump for Imaging chamber with capacity of 200 L/s.
16. Imaging chamber connected with ion pump and Ti-sublimation pump that can reduce pressure up to $\leq 10^{-8}$ Pa.
17. Oxford Applied Research mini e-beam evaporator ENG4. The e-beam evaporator has four grooves where four metals rods can be inserted. At the tip of each rod, a tungsten filament is fitted at ground potential.
18. Tip and coarse specimen movement motors. Automatic Z-direction approach mechanism. X-Y specimen movement: X = ±2 mm, Y = ±2 mm.
19. Transfer arm connecting Treatment chamber with SEM chamber
20. Gimbal piston suspension type air suspension vibration insulation table.
21. Power supply to heat the sample
22. LEED control unit
23. SEM computer
24. STM computer
25. STM control unit
26. Oscilloscope

then transferred to the imaging chamber to be imaged. Both treatment and imaging chambers have a pressure of 10^{-8} Pa created with the help of ion pumps and titanium sublimation pumps (TSP). The imaging chamber is also equipped with an electron beam evaporator that can accommodate up to four rods. The rods are evaporated by heating in a controlled way. Once the evaporation rate is controlled, the shutter is opened, and vapors are condensed on the substrate to form nanocrystals.

2.3.5 STM system baking

Sample surface treatments (e.g., degassing, annealing and evaporation) may introduce contamination to both STM and treatment chambers. To maintain the UHV condition, it is necessary to carry out a "baking" operation. Before starting the baking operation, the ion pumps are switched off, but the Turbo-molecular Pump (TMP) is left running. The glass observation windows must be covered by aluminum foil to avoid cracking due to the dramatic change of the thermal gradient. All the electronics attached to the STM chamber should be removed to avoid any damage caused by extensive heat. Other attached components, such as the sputtering gun and the e-beam gun, are removed. The magnets on the transferring arms are removed to avoid any demagnetization under high temperature. Because baking is carried out at a temperature of around 150 °C, every inflammable or heat sensitive materials should be kept away from the chambers. The ribbon heater is wrapped around the transferring arms, treatment and STM chambers to heat up the components.

Baking can work for either the treatment chamber or both (treatment and imaging) chambers. Only the turbo-molecular pump (TMP) attached to the specimen exchange chamber is running during the baking process. During baking, hydrocarbons and moisture are removed from the chamber walls and pumped out by the TMP. Baking usually takes at least two days. The titanium sublimation pumps (TSPs) are degassed when turning off the

baking operation. The pressure in each chamber is usually in the 10^{-5} Pa range when turning off the baking. The chambers are then self-cooled to the room temperature when the baking heater is switched off. A UHV condition in the 10^{-8} Pa range will be reached in 8-12 hours after baking is finished.

It is necessary to vent the entire system when fixing existing apparatus or to install a new apparatus onto the microscope. The chambers are vented by introducing N_2 gas through specimen exchange chamber to the main chambers. Every component is sealed with copper gaskets. Copper gaskets are replaced by a fresh one every time the components are reassembled.

2.3.6 Metal deposition

The e-beam evaporator (Model EGCO4) was used in this project (Figure 2-10). The evaporator is attached to the imaging chamber and operated in the UHV environment [24]. The deposition rate can be controlled from less than 0.1 Å/min to over 50 Å/min [24]. Metal deposition is achieved through electron beam induced thermal evaporation of materials. A high voltage is applied to the target rod which generates a voltage gradient

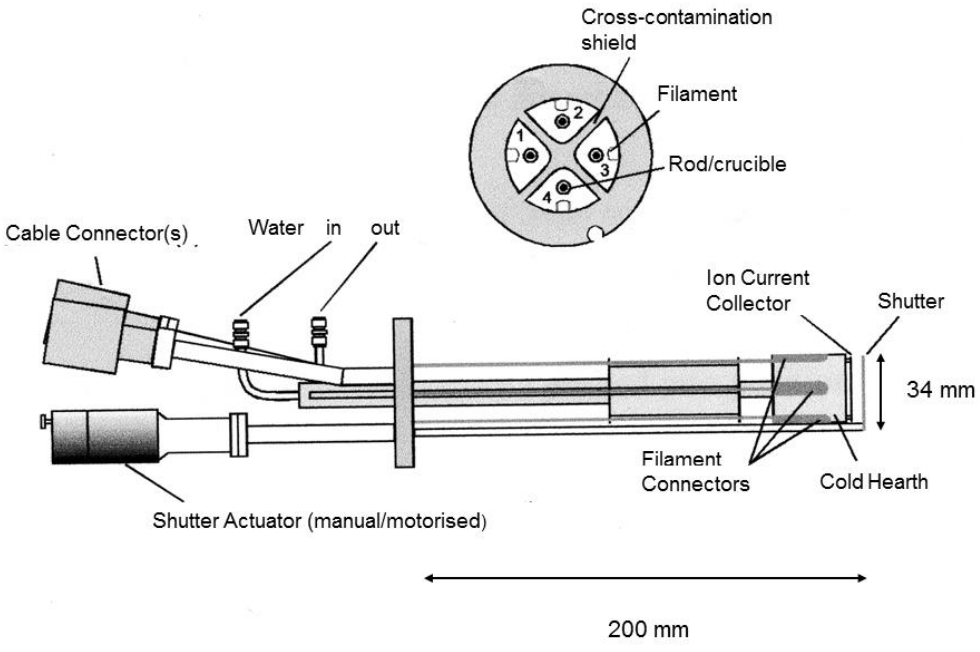


Figure 2-10: Schematic picture of EGCO4 e-beam evaporator [24]**.**

between the filament and the rod. The electrons are emitted from the filament by increasing the filament temperature by adjusting the current. The emitted electron is at earth potential and accelerated towards the tip of the target rod. The target metal rod gets bombarded with the electron emitted from the W filament. The emission current can reach up to 100 mA with power reaching up to 200 W [24]. This is a sufficiently high power to evaporate some high melting point metals such as tungsten. Only the target rod is required to heat up to the evaporation temperature. The rods in other pockets are protected from melting by running chilled water to keep the rods at ambient temperature.

To start the evaporation process, the value of EHT is adjusted to 2 kV. This is the voltage applied to the target metal rod to create the voltage gradient between the rod and the filament. The targeted metal rod with its pocket number is selected. Then, the filament current is gradually increased until the desired flux is achieved. The shutter is opened, and deposition is continued for a desired amount of time. Deposition can be carried out on either warm or room temperature substrates. After deposition, the shutter is closed immediately. Filament current and EHT are carefully reduced to zero by following the procedure in the reverse order described above. Post-annealing may be carried out directly after deposition for the crystallization of the nanocrystals.

2.4 Summary

In this chapter, a few techniques related to surface characterizations were introduced. The key equipment in this project is custom built UHV-STM that will be used to grow nanocrystals and to image surfaces and nanocrystals. To grow nanocrystals, high purity metal rods are inserted into e-beam evaporator (Model EGC04) which operates in the UHV environment. Metal deposition is achieved through electron beam induced thermal evaporation of materials. The evaporated material deposits on a substrate and system is post-annealed to achieve nanocrystals.

Chapter 3:

Literature Review

3.1 Overview

In this review, some key concepts related to the project have been introduced. As the growth of nanocrystals is one of the milestones of the current project, some of the common methods used to produce nanocrystals are reported. Those methods can broadly be divided into two types: (1) colloidal methods [25] and (2) epitaxial methods [26]. In colloidal methods, the reaction between two or more precursors, suspended in a fluid, takes place yielding nanocrystals or nanoparticles. In the case of epitaxial methods, precursors are evaporated which then deposit on a substrate. The morphology and properties of nanocrystals depend on various factors in which one of the important factors is epitaxy. In this project, supported nanocrystals are produced on $SrTiO_3$ (STO) as substrate, and therefore epitaxial methods are discussed in detail. The nanocrystals grow on a substrate in three different modes: (1) Frank-van der Merwe (FM), (2) Volmer-Weber (VW), and (3) Stranski-Krastanov (SK) growth modes. Based on the sequence and shape of the growing material, the three modes are also called (1) layer-by-layer, (2) island, and (3) layer-plus-island growth modes, respectively. The preferred growth mode in the current project is VW growth mode. To get an epitaxial relationship, the substrate surface plays a crucial role and hence should be meticulously prepared. Unlike bulk atoms, as surface atoms do not have neighbors above them to make bonds with, the surface structure is significantly different from the bulk. The surface structure is either termed as relaxation or reconstruction. As grain boundaries and defects can influence the growth of nanocrystals, usually a single crystal, free of defects, is preferred as a substrate. The termination is relevant to grow nanocrystals as certain reconstructions can only be produced on a specific termination. The reconstructions are named using two main methods: (1) Park-Madden matrix notation, and (2) Wood's notation. The junction of nanocrystals and substrate has unique features and hence requires in-depth study. There can be lattice mismatch that can

produce either strain or misfit dislocations. In addition, the nanocrystals and substrate can either react chemically, or composition may be differed at the interface because of diffusion. Therefore, a separate phase may exist at the interface with unique properties that are different from both the nanocrystals and the substrate.

When a single element is deposited on a substrate, the system may be simple and easy to study. However, when alloying is desired at the nanoscale (nano-alloying), the system may get complex as solvent and solute elements may settle in various configurations of which four possibilities are schematically shown in Figure 3-1. The first possibility is that the two elements are completely immiscible and form two separate islands (Figure 3-1 (a)). In this case, nano-alloying is not feasible under the given set of conditions. If the two elements are not miscible, but their surface energies are significantly different, then one element of low surface energy may cover the other element with high surface energy to reduce the overall surface energy. If Figure 3-1 (b) or (c) is obtained, then a new field may be open to

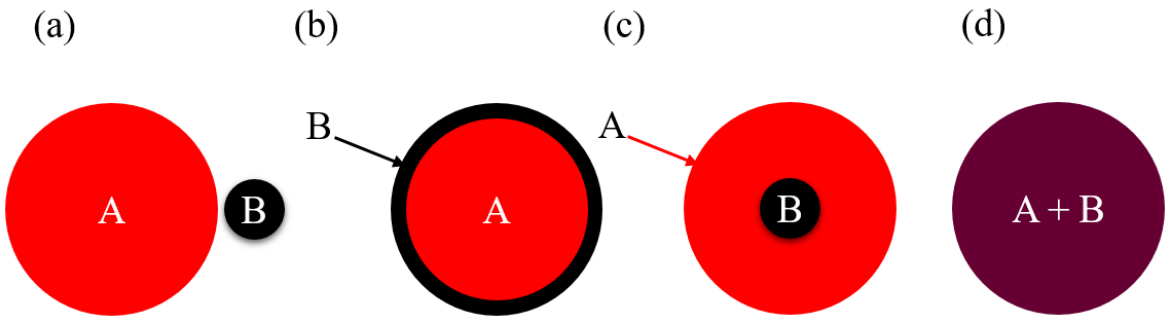


Figure 3-1: Four possible configurations of nano-alloying. (a) Solvent and solute are completely immiscible forming two separate nano-islands. (b) If solvent's surface energy is significantly higher than that of solute, then Solvent element (A) settles first and gets covered by solute element (B). (c) If solute's surface energy is significantly higher than that of solvent, then solute element (B) settles first and gets covered by solvent element (A). In both cases, solvent and solute are not miscible at nanoscale even though they might show miscibility at macroscale. (d) The solvent and solute elements are completely miscible forming a nanoalloy (A + B).

explore, i.e., core-shell nanoparticles (CSNs). If two elements are completely miscible, then they would form a nanoalloy. If Figure 3-1 (d) is obtained, the nanoalloy may be studied for its desired features. The other possibility is a partial miscibility. Because of large surface-to-volume ratio, the influence of nanoscale on the metallurgical behavior may not be predicted based on macroscale data, and therefore in-depth analysis of nano-alloying and nanostructures is essentially required.

3.2 Growth modes

3.2.1 Frank-van der Merwe (FM) layer-by-layer growth mode

It takes place when Eq. 3-1 is satisfied where γ_{fv}, γ_{sv}, and γ_{fs} are the surface or interface free energies of the film-vapor, substrate-vapor and film-substrate interface, respectively [27,28]. The clusters of epitaxial layer bond more strongly to the substrate than to each other and grow in a two-dimensional manner. It results in the formation of a smooth, planar surface layer.

$$\gamma_{sv} > \gamma_{fv} + \gamma_{fs} \qquad \textbf{3-1}$$

3.2.2 Volmer-Weber (VW) island growth mode

It prevails when Eq. 3-2 is satisfied [29]. The deposited atoms have a stronger bonding force with each other than with the substrate. Clusters nucleate in a three-dimensional manner and ‘ball up’ at the surface.

$$\gamma_{sv} < \gamma_{fv} + \gamma_{fs} \qquad \textbf{3-2}$$

3.2.3 Stranski-Krastanov (SK) layer-plus-island growth mode

It is a modification of the FV growth mode [30]. During the epitaxial growth process, the energy balance changes as a result of in-situ developed strain. At the first stage of initial nucleation, a sufficient number of atoms condense on the substrate and wet the substrate surface. Due to factors including the lattice mismatch between growing layer and

substrate, strain energy is produced. As the growth of the film continues, the strain energy would increase until the generation of misfit dislocations to relieve the lattice strain. If strain energy is too high to be compensated by misfit dislocations, island formation will become more energetically favorable than layer growth [31]. The growth modes are schematically shown in Figure 3-2.

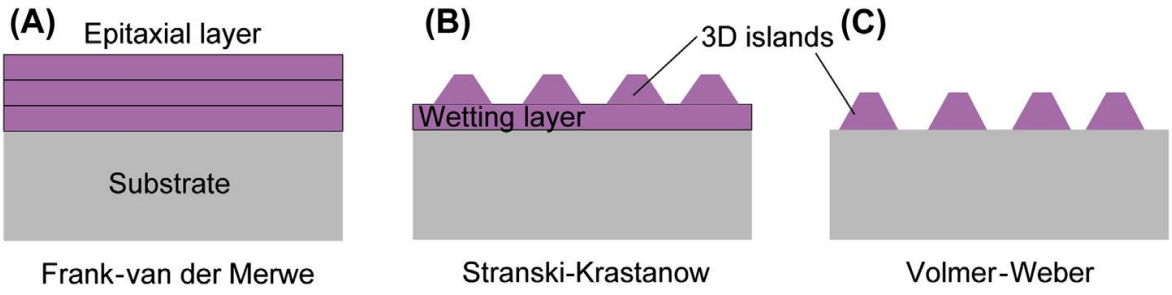


Figure 3-2: Illustration of growth modes in heteroepitaxy. (A) Frank-van der Merwe, (B) Stranski-Krastanov, and (C) Volmer-Weber modes [32]**.**

3.3 Wetting:

When a liquid drop L is placed on a solid surface S, the interfacial energies come into play to determine the shape of the liquid drop as shown in Figure 3-3. To keep the system at the

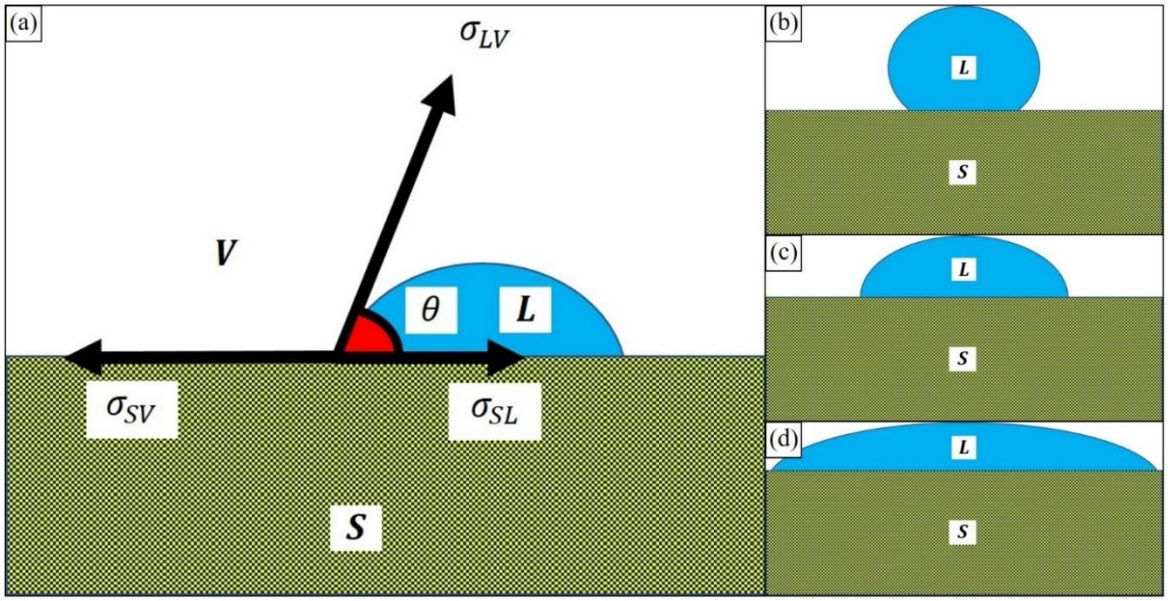


Figure 3-3: (a) A liquid drop L on a solid substrate S with contact angle θ in the presence of a vapor V. (b) Non-wetting. (c) Partial wetting. (d) Full wetting.

lowest possible energy state, the system will either try to reduce the interface between liquid drop and solid surface or will try to increase it. If the system tries to keep the interface at the lowest possible limit, it is called non-wetting. If the system tries to increase the interface as wide as possible, it is called full wetting. And the intermediate case is called partial wetting. The wetting is defined in terms of angle θ using Young-Dupré equation (3-3 and 3-4). Full wetting takes place when $\sigma_{SV} \geq \sigma_{\mathrm{LV}} + \sigma_{\mathrm{SL}}$.

$$\sigma_{SV} = \sigma_{\mathrm{LV}} \cos\theta + \sigma_{\mathrm{SL}} \quad \textbf{3-3}$$

$$\cos\theta = \frac{\sigma_{SV} - \sigma_{SL}}{\sigma_{LV}} \quad \textbf{3-4}$$

Winterbottom developed a mathematical model to predict the shapes of the particles at the interface based on surface tension and surface energy [33]. He defined γ^* as the general surface tension for the particle where γ^* is equal to γ_{PV} for particle-vapor interface and $(\gamma_{SP} - \gamma_{SV})$ for particle-substrate interface orientation. In this case, the equilibrium shape of a particle in contact with a substrate will be identical to an equilibrium free particle with surface tension γ^*. By using Gibbs-Wulff construction, the four possible substrate-particle configurations are shown in Figure 3-4. As interface is a pertinent factor in wetting, it has been discussed in detail in the following section.

3.4 Interface

The atomic structure where substrate and nanocrystals meet, i.e., interface, is different from the bulk and significantly influences the growth mechanism, morphology and

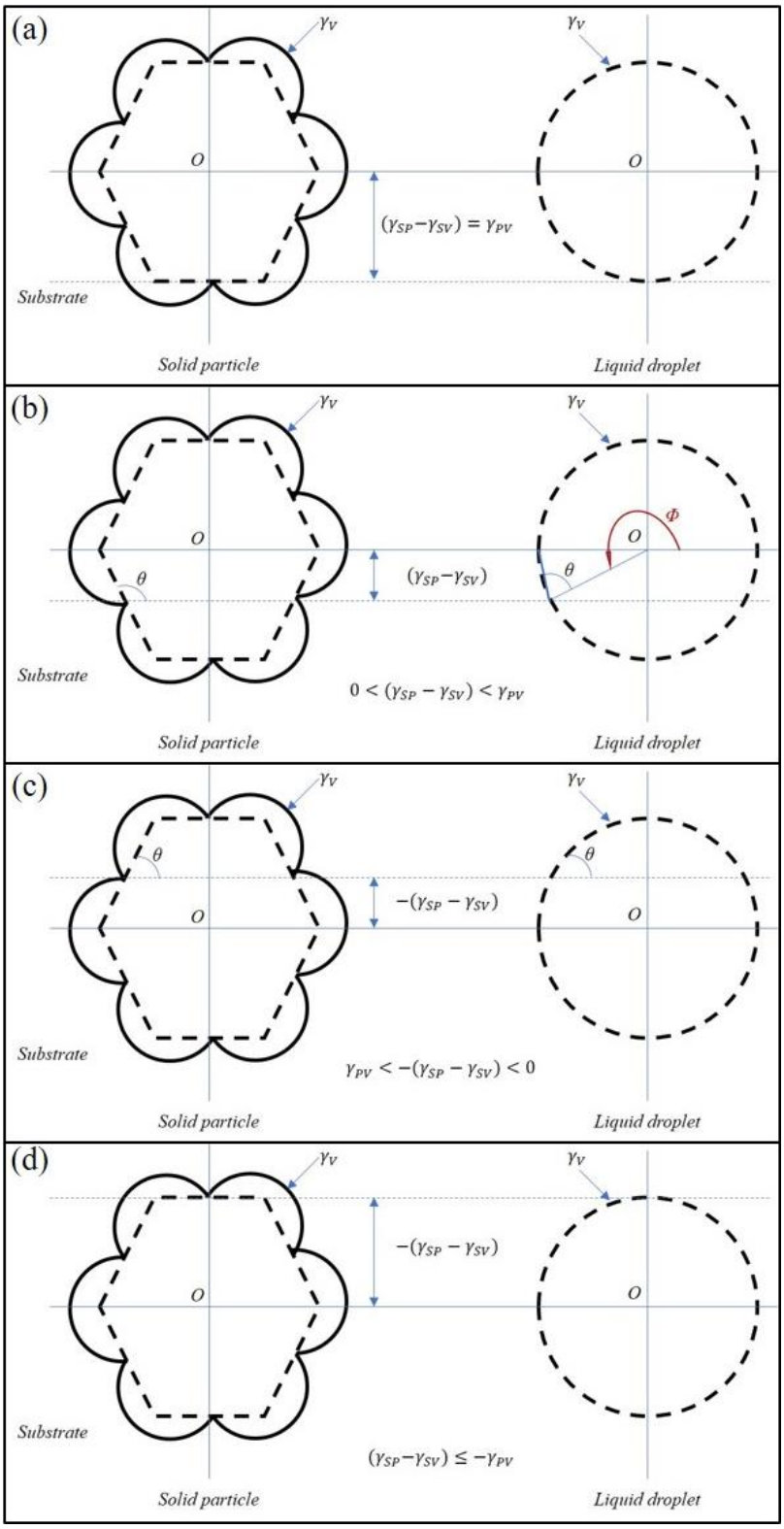


Figure 3-4: γ^* plot and corresponding equilibrium shapes for the two-dimensional liquid and solid system. (a) Non-wetting occurs when $(\gamma_{SP} - \gamma_{SV}) \geq \gamma_{PV}$. (b) Partial wetting-I occurs when $\gamma_{PV} > (\gamma_{SP} - \gamma_{SV}) > 0$. (c) Partial wetting-II occurs when $-\gamma_{PV} < (\gamma_{SP} - \gamma_{SV}) \leq 0$. (d) Complete wetting occurs when $(\gamma_{SP} - \gamma_{SV}) \leq -\gamma_{PV}$. Adapted from [33]**.**

physical and mechanical properties of nanocrystals [34,35]. Reconstruction phenomenon at the interface between complex oxides produces novel magnetic, metallic, and superconducting two-dimensional phases [36]. Novel quantum states, such as ferromagnetism [37–41], superconductivity [42–44], and their coexistence [45–47], are also present at the interface of heterojunctions [48]. $LaAlO_3$/STO recorded substantial rearrangement of oxygen octahedra in the interfacial region as well as in the vicinity [49]. The heterostructures of transition metal oxides are of great interest due to the interface magnetic and electronic states [50]. The oxide interfaces show propitious electronic behavior not shown by bulk compounds [51]. The crystallography at the interface is different from both the substrate and the deposited materials. Some of the interfacial crystallography patterns reported are listed in Table 3-1. The lattice mismatch, lattice strain, and alleviation of lattice strain by misfit dislocations are important phenomena to investigate while studying interface at the nanoscale. The lattice mismatch values of nanocrystals on STO are shown in Table 3.2. Up to a certain value, the lattice mismatch is compensated by strain after which the mismatch is compensated by misfit dislocations. The atomic distances may or may not change at the interface when the phase transformation takes place. For example, the atomic distance at the interface of fcc Co and hcp Co was found unaltered [52].

When two dissimilar materials are combined, the atomic bonding at the interface undergoes a distortion to accommodate the chemical and physical discrepancies [35]. Such distortions will also contribute to the interfacial properties [35]. For instance, the change of crystal symmetry can be accommodated near the interface, which can lead to the change of electronic properties of the materials and induce a ferroelectric-like dipole from the paraelectric phases [53]. The lattice is distorted by creating a dipole to screen the uncompensated ferroelectric charge [54,55] and polar discontinuity [56] at the interface

Table 3-1: Interfacial crystallography between nanocrystals and STO substrate.

Sr.	Nanocrystal element	Interfacial crystallography	Ref.
1	Mn_3O_4(101) nanoplatelets with step-like growth	In-plane: $[2\bar{3}\bar{1}]Mn_3O_4$ II [100]STO, Out-of-plane: $[\bar{1}01]Mn_3O_4$ II $[\bar{1}11]$STO	[57]
2	Mn_3O_4(112) nanowires	In-plane: $[2\bar{3}\bar{1}]Mn_3O_4$ II [100]STO, Out-of-plane: $[\bar{1}01]Mn_3O_4$ II $[\bar{1}11]$STO	[57]
3	TiO_2(001)	(001)TiO_2 II (001)STO, [100]TiO_2 II [100]STO	[58]
4	Pt	[001]Pt II [001]STO, [010]Pt II [010]STO	[1]
5	Pd nanowires (NW)	(110)Pd II (110)STO, <110>Pd II <110>STO	[59]
6	Pd nanowires (NW)	<110>Pd II <110>STO	[59]
7	Cu	(001)Cu II (001)STO, [100]Cu II [100]STO	[60]
8	Au	(001)Au II (001)STO, [110]Au II [100]STO and (111)Au II (001)STO, [110]Au II [100]STO	[2]
9	Cu	(100)metal II (100)STO : [010]metal II [010]STO	[61]
10	Pd	(011)Pd II (001)STO, [110]Pd II [100]STO	[62]
11	Pd	(111)Pd II (001)STO, [111]Pd II [110]STO	[62]
12	Pd	(001)Pd II (001)STO, [100]Pd II [100]STO	[62]
13	Co	(001)Co II (001)STO, [100]Co II [100]STO	[63]
14	Fe	(001)Fe II (001)STO, [100]Fe II [100]STO	[6]
15	TiO_2(001)	(001)film II (001)sub, [100]film II [100]sub	[64]

with inherent ferroelectric materials. Moreover, the driving force for the inter-diffusion at the interface can be varied depending on the degree of the polar discontinuity, resulting in the intrinsic disorder at the interface [65–67]. STO has been used as a lattice mismatched substrate for the growth of high-temperature superconductors [68,69]. The band gap of

Table 3-2: Lattice mismatch of nanocrystals with STO.

Sr.	Nanocrystal element	Lattice mismatch (%)	Ref.
1	NbO_2	c-axis=-7.85%, b-axis=-1.3%	[70,71]
2	Mn_3O_4 (101) nanoplatelets with step-like growth	58 in-plane, 35 out-of-plane	[57]
3	Mn_3O_4 (112) nanowires	58 in-plane, 35 out-of-plane	[57]
4	NiO	7.00	[72]
5	WO_3	-2.43	[11]
6	Fe_3O_4	7.50	[73]
7	Ni	9.86	[74]
8	TiO_2 (001)	3.10	[58]
9	Manganite $La_{2/3}Sr_{1/3}MnO_3$ (LSMO)	0.74	[75]
10	Ag	4.61	[76]
11	Pt	0.49	[1]
12	Pt	0.38	[77]
13	Pt	0.12	[78]
14	Pd nanowires (NW)	0.28	[59]
15	Cu	-7.43	[60]
16	Pt	1.92	[79]
17	Pt	1.92	[80]
18	Au	4.43	[61]
19	Ag	4.61	[61]
20	Pt	1.92	[61]
21	Cu	-7.43	[61]
22	Au	4.43	[2]
23	Pd	-0.38	[62]
24	Co	-35.98	[63]
25	Co	fcc = 9.2, bcc = 27.8	[63]
26	Fe	-26.50	[6]

27	Fe	-7.81	[6]
28	Ag	4.61	[81]
29	Au	4.43	[82]
30	Co-doped TiO_2	0.12	[64]
31	TiO_2 (001)	3.10	[64]

$LaAlO_3$ is 5.6 eV while that of STO is 3.2 eV. Due to the lattice mismatch at the interface between these two materials, transfer of electrons takes place through the interface at a rate of one electron per two unit cells of the system [83].

The lattice parameters of nanocrystals may change depending on the epitaxial relationship. For example, Pt nanocrystals were grown on STO by Feng et al. [1] and Son et al. [79]. The lattice parameters of Pt were reported to be 3.924 Å and 3.938 Å, respectively. It is due to strain arising from the epitaxial relationship. If lattice parameter is changing with a thickness of the nanocrystal, then it would mean that the epitaxial relationship is dwindling with the incorporation of misfit dislocations. The lattice parameters can be determined by using moiré patterns. Based on the moiré pattern, the calculated lattice parameters can be used to calculate the elastic strains in nanocrystals [52]. TEM is the most commonly used technique to observe moiré patterns.

The epitaxial relationship starts degrading when the lattice mismatch increases beyond a certain value depending on the system and conditions involved. For example, in general, when the lattice mismatch is 0.1%, the epitaxial relationship is still established. But it will not be the case if lattice mismatch value soars to 5%. It is because the atoms are displaced from the minima of energy parabola to compensate for the mismatch. As their displacement increases the system energy exponentially, a compensation of 5% mismatch by the displacement of atoms is not energetically feasible. Therefore, a high value of lattice mismatch can only be compensated by the relatively low energy misfit dislocations.

However, in some cases, high lattice mismatches can still be compensated by the displacement of the atoms. For example, in the case of superlattice structures, the epitaxial relationship was still retained when lattice mismatch was as high as 14% in fcc Au and hcp Co system [84–86].

3.5 How to create nanoparticles

The specific surface area of nanoparticles is significantly high because of which the contribution of surface energy toward overall energy of the nanoparticles is enormous. To lower the overall energy, the nanoparticles are eager to react instantly. Sometimes, the reactions may lead to some propitious results. However, in most cases, the results may be undesired. Oxidation is one example of those undesired reactions in many cases. To avoid undesired reactions, the nanoparticles are surrounded by the inert environment. The inert environment can either be a specific fluid or absence of any fluids (vacuum). In the case of fluidic methods, nanoparticles are suspended in the desired fluid such as a sol-gel method. In vacuum-based methods, elements are evaporated and deposited on a substrate in a vacuum chamber. Therefore, the methods to produce nanoparticles can broadly be divided into two types: (1) colloidal methods that produce suspensions, and (2) epitaxial methods that produce supported nanocrystals. The third category of nanoparticles production is solid state processes such as ball milling. A brief introduction of colloidal methods is provided below.

3.6 Epitaxy: supported nanocrystals

Epitaxy is the phenomenon referred to as the deposition of a crystalline material (called epitaxial layer or epitaxial film) over another crystalline material (called substrate). If both materials are the same, it is called homoepitaxy and heteroepitaxy if otherwise. When a material is deposited on a crystalline substrate, atoms of deposited material align themselves with respect to the atoms of the substrate. The relationship at the interface of

Table 3-3: Epitaxy modes between nanocrystals and STO.

Sr.	Authors	Year	Nanocrystal element	Epitaxy mode	Ref.
1	Sun et al.	2013	Ni	Cube-on-cube	[74]
2	Enterkin et al.	2011	Pt	Cube-on-cube	[77]
3	Silly and Castell	2006	Au	Commensurate epitaxy	[2]
4	Silly and Castell	2005	Pd	Coincidence	[62]
5	Silly and Castell	2005	Pd	Coincidence	[62]
6	Silly and Castell	2005	Pd	Cube-on-cube commensurate epitaxy	[62]

epitaxial layer and substrate is called epitaxial relationship. Many oxide heteroepitaxial devices confront the need to manage different possible interface atomic configurations, which can have important effects on the electronic structure at the most electrically sensitive regions of the device. For example, in (001)-oriented manganite tunnel junctions or cuprate Josephson junctions, a perovskite, such as STO, is typically used as an insulating barrier [87]. In particular, STO single crystalline substrate has been widely used to realize low-dimensional oxide structures, such as ultrathin films [88] and nanowires [89], with properties that are radically different from those of their bulk hosts [90]. The epitaxial relationships of nanocrystals grown on STO are listed in Table 3-3. The cube-on-cube and coincidence are most commonly observed epitaxies. Various epitaxy types are described below.

3.6.1 Commensurate-incommensurate epitaxy:

In case of commensurate epitaxy, the lattice points of the film coincide with all symmetry equivalent substrate lattice points as shown in Figure 3-5.

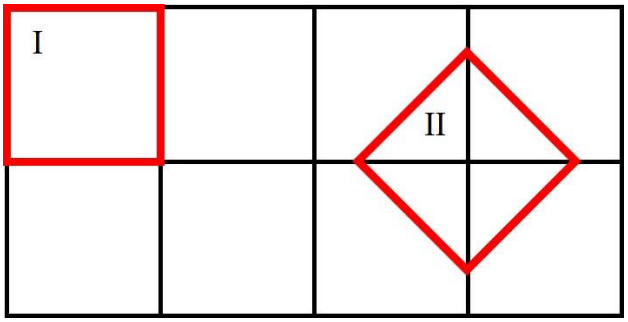


Figure 3-5: Schematic of commensurate epitaxy. (I) All lattice points are coinciding with that of the substrate. (II) None of the lattice points of film coincide with the lattice points of the substrate. However, all lattice points of the film are on the lines formed by joining the lattice points of the substrate.

In contrary, in case of incommensurate epitaxy, even though the thin film can be grown in the form of a single crystal, a correlation cannot be established between lattice points of film and substrate. For example, when Cu is grown on Si, silicides of various morphologies are observed one of which is shown in Figure 3-6.

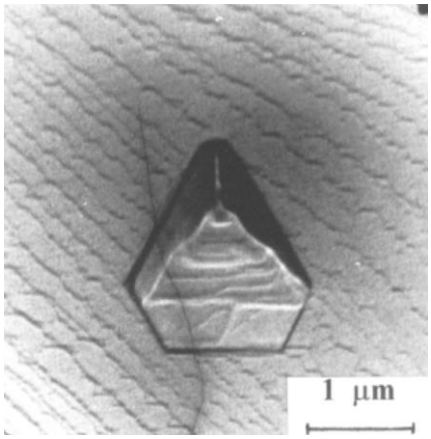


Figure 3-6: Low energy electron microscopy (LEEM) image of Cu silicide crystal grown by Cu deposition onto Si (111) at elevated temperature. The image was taken at an electron energy of 4 eV [91]**.**

The two-dimensional silicide which precedes the growth of three-dimensional silicide crystal has an incommensurate structure and causes step [92].

agglomeration and step faceting [92]. The thickness of the film can trigger a transformation from commensurate to incommensurate epitaxy. This transformation can be observed in Ag when grown on Pt (111) as shown in Figure 3-7.

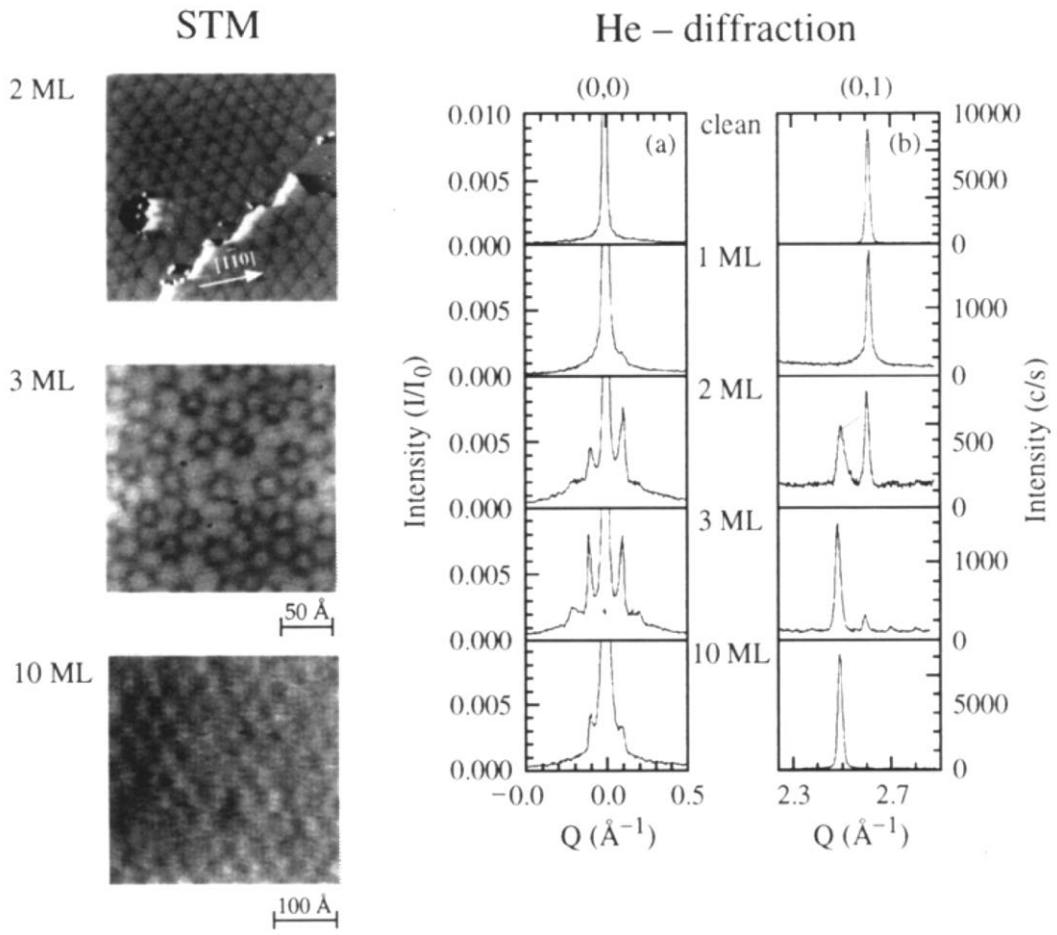


Figure 3-7: Transition from a domain wall phase to a weakly modulated incommensurate phase with increasing layer thickness of Ag films on Pt (111): STM images and He-diffraction pattern (λ = 1.02 Å) [92]**.**

When the film thickness is small, there exists commensurate epitaxy. As the film thickness increases to 10 ML coverage, commensurate epitaxy is lost and is not only visible in the STM images but also in the He-diffraction pattern.

The transition from the pseudomorphic monolayer through a series of domain wall structures with more or less localized strain relieved to a weakly modulated morié phase with increasing film thickness can be understood qualitatively based on Frank- van der

Merwe growth mode. The elastic strain energy increases proportionally with the film thickness. For the monolayer, the elastic energy is smaller than the energy to relax the film, and the adlayer adopts a pseudomorphic structure. As the thickness and associated strain energy increase, the film relaxes gradually to its natural bulk structure. Initially, this is achieved through the introduction of hcp-fcc stacking faults, where the strain is locally relieved. At close-packed interfaces, the introduction of these defects is energetically favorable. However, the domain wall structures still contain substantial residual in-plane elastic distortions. By the gradual transition from the anisotropic striped or trigonal structures to hexagonal networks with larger domain wall widths, the residual in-plane strain is progressively lowered. Finally, the relaxation is completely isotropic with no in-plane strain resulting in weakly modulated incommensurate structure (moiré) with the bulk lattice constant of the film.

3.6.2 Coincidence epitaxy:

In coincidence epitaxy, the lattice points of the film coincide with the lattice points of the substrate. However, it is not true for all lattice points. The two cases of coincidence epitaxy are shown in Figure 3-8.

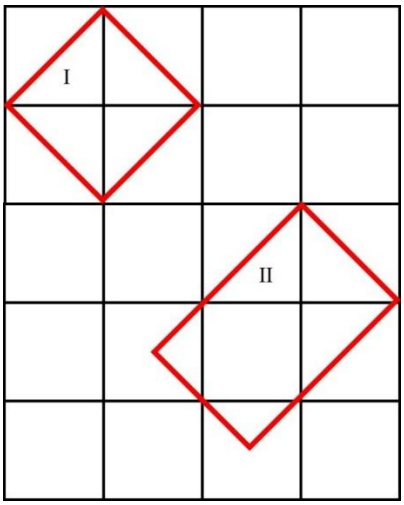


Figure 3-8: Schematic of coincidence epitaxy. (I) All lattice points of the film lie on the lattice points of the substrate. (II) Only some lattice points of film coincide with the lattice points of the substrate.

In case I, the lattice points of substrate coincide with that of film. However, every lattice point of the substrate is not overlapped by that of film. The lattice points of the film follow the lines made by joining the lattice points of the substrate. In case II, some lattice points of the film follow those lines while other lattice points do not coincide with the lattice points/lines of the substrate. As epitaxy is between substrate and nanocrystals, the fundamental aspects of substrates need to be investigated in order to understand the epitaxial relationships.

3.6.3 Substrates

The termination is the plane in which the substrate is grown [10]. As growth mechanism can be different at grain boundaries, a single crystal substrate is preferred. As every embryo formed in a liquid requires to be converted into a nucleus to be stable, atoms attach to the embryo and then to the nucleus. If solidification continues, mostly a polycrystalline material is achieved with defects such as vacancies, interstitial and substitutional foreign atoms, dislocations, stacking faults, and grain boundaries. As all of those defects may adversely affect the growth of nanocrystals, the substrate must be as much free from these defects as possible. Luckily, it is possible to avoid these defects if processing parameters are meticulously controlled. Czochralski's, float zone, and Bridgman-Stockbarger methods are three most commonly used methods to produce single crystals of sufficiently large size that can easily be used as substrates for the growth of nanocrystals. The desired termination may be produced by cutting the crystal at a specific angle. Once a specific termination is achieved, the next objective will be to get a relaxation or a reconstruction on the surface of the substrate.

Relaxation is a subtle rearrangement in the position of entire layers of atoms relative to the bulk positions, either normal or lateral. For most metals, the normal relaxation results in a reduced interlayer spacing between the first and second atomic layers. Neither the

periodicity nor the symmetry parallel to the surface becomes different in this case. Reconstruction, however, changes the periodicity of the surface structure, which involves both the two-dimensional structure of the surface layers and the position of the entire layer. It could result in either a conservative atom number in a layer or having a different number than in bulk materials [93,94].

Unlike bulk atoms, surface atoms do not have a neighbor above them with whom they can make bonds. Therefore, surface thermodynamics is different from the bulk thermodynamics. The surface atoms do not position themselves in the same way as done by bulk atoms. Accordingly, the surface structure is different from that of the bulk structure at the atomic scale. This different surface structure is called a reconstruction [10]. As topography and morphology of nanocrystals are dependent on the surface energy of substrate and different surface reconstructions have different surface energy values, surface reconstruction is an important factor to grow nanocrystals of desired electronic and magnetic properties. The reconstruction is commonly defined using two main methods: (1) Park-Madden matrix notation and (2) Wood's notation.

3.6.3.1 Park-Madden matrix notation

Define a, b as the basic translation vectors of the two-dimensional structure in bulk as shown in vector diagram Figure 3-9.

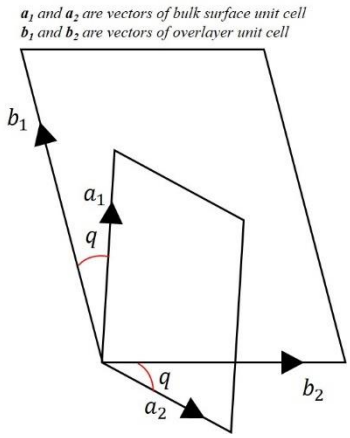


Figure 3-9: Vector diagram of surface and bulk atoms [95]**.**

For the reconstructed plane the basic translation vectors, a_r and b_r are [95]:

$$a_r = G_{11}a + G_{12}b$$
$$b_r = G_{21}a + G_{22}b \qquad \textbf{3-5}$$

The matrix defined by G_{11}, G_{12}, G_{21} and G_{22} reflects the relationship between the bulk termination and the reconstructed surface:

$$\begin{pmatrix} G_{11} & G_{12} \\ G_{21} & G_{22} \end{pmatrix} \qquad \textbf{3-6}$$

What needs to be clarified is that this matrix only describes the individual layer's structure. It is not relative to the relaxation of the surface layer.

3.6.3.2 Wood's notation

Wood's notation is comparatively more commonly used to describe the surface reconstruction. The vector diagram is shown in Figure 3-10.

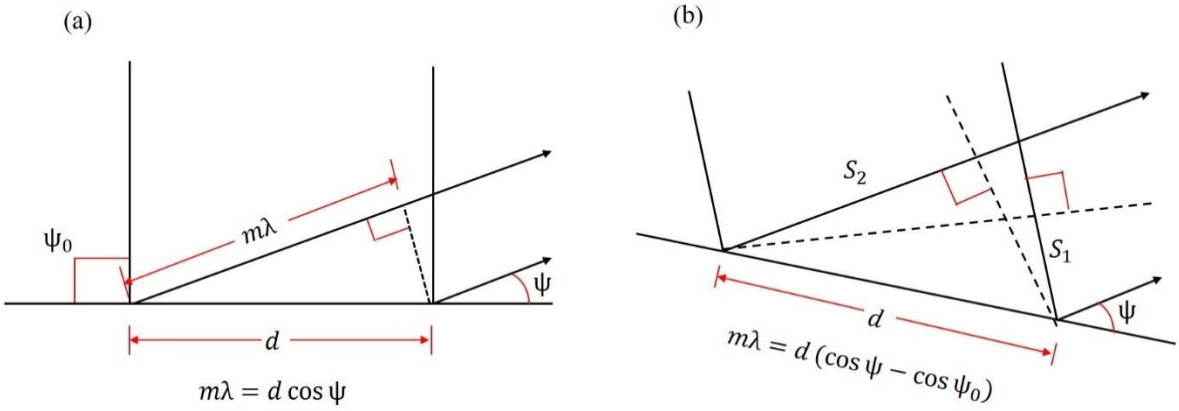


Figure 3-10: Schematic diagram of diffraction from surface rows: (a) normal incidence, (b) general case [96]**.**

The matrix above is reduced into a more compact notation [96]:

$$X(hkl) - u(m \times n)R\varphi \qquad \textbf{3-7}$$

Where X is the material; (*hkl*) is given by Miller indices to explain the reconstruction plane; u can be either p (primitive) or c (centered) depending on the type of unit cell; m and n describe the change of interatomic spacing in directions a and b respectively; ψ is the

rotation angle of the reconstructed plane. Usually, if the unit cell is primitive, u will be left out. For a reconstructed surface with no rotation referring to the original plane, Rψ will be omitted as well.

3.6.4 Morphology:

The substrate and epitaxial relationships strongly influence the morphology of nanocrystals, and a plethora of morphologies can be produced by controlling the processing parameters. Some of the common shapes of nanoparticles include tube [97–100], rod [101–108], wire [109–116], disk [117], octahedron [118,119], hexagon [120–123], prism [124,125] and cube [126–131]. Various morphologies of Au nanocrystals are shown in Figure 3-11.

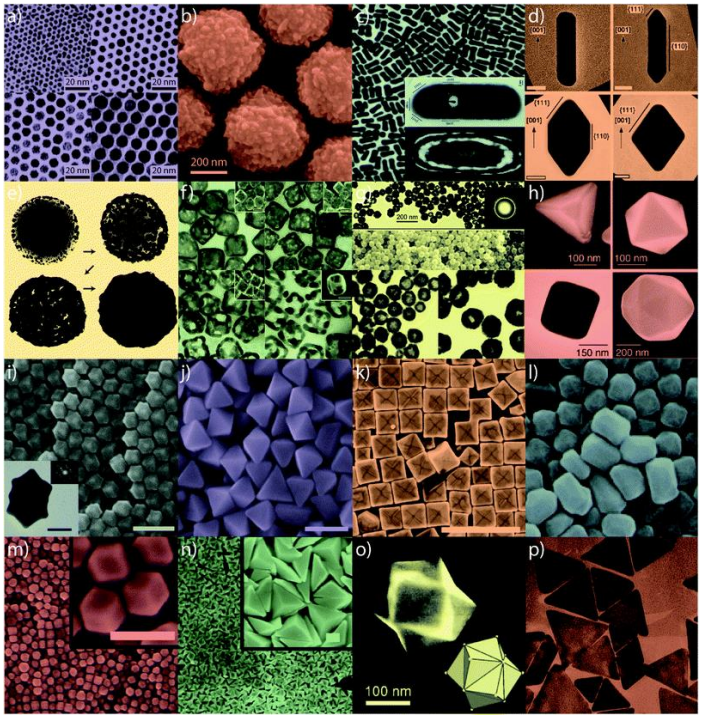


Figure 3-11: Various morphologies of Au nanoparticles: (a) Small nanospheres [132]**. (b) Large nanospheres** [133]**. (c) Nanorods** [134,135]**. (d) Sharpened nanorods** [136]**. (e) Nanoshells** [137]**. (f) Nanocages/frames** [138]**. (g) Hollow nanospheres** [139]**. (h) Tetrahedra/octahedra/cubes/icosahedra** [140]**. (i) Rhombic dodecahedra** [141]**. (j) Octahedra** [141]**. (k) Concave nanocubes** [142]**. (ℓ) Tetrahexahedra** [143]**. (m) Rhombic dodecahedra** [144]**. (n) Obtuse triangular bipyramids** [144]**. (o) Trisoctahedra** [145]**. (p) Nanoprisms** [146]**.**

It was reported that the catalytic activity of Au nanocrystals supported on oxide substrates was dependent on their size when they were used to oxidize CO through heterogenous catalysis [147–149]. Because of surface anisotropy effect, the coercivity of magnetic nanocrystals depends on their shape [150]. Similarly, melting point [151], optical properties [152], electrical properties [153,154], and catalytic selectivity [155–157] are also shape-dependent. It was further observed that plasmon resonance and sensitivity to surface-enhanced Raman scattering of silver and gold particles also depend on their morphology [158].

The nanocrystals of different shapes were achieved on STO whose detail is provided in Table 3-4. In general, the shapes of nanocrystals can be divided into four main types: (1) truncated, (2) dome-like, (3) needle-like, and (4) irregular. When Ni nanocrystals are grown on STO (001)-c(4×2) substrate, they adopt the shape of the truncated pyramid [74]. The epitaxial relationship is cube-on-cube epitaxy as shown by Co [63], Pd [62], Cu [60], Pt [159], and Ir [160]. A dome-like shape was observed in the case of very fine self-organized nanoclusters in the $SrIn_{0.1}Ti_{0.9}O_3$ (SITO) films deposited on STO substrate by laser molecular-beam epitaxy [12,161]. Moulik et al. [11] reported that needle-like nanocrystals of WO_3 were produced on STO substrate grown by using pulsed laser deposition (PLD). WO_3, an n-type indirect wide band gap semiconductor, is an extensively studied material due to its appreciable applications in smart-windows, mirrors, optical

Table 3-4: Morphologies of nanocrystals grown on STO.

Sr.	Authors	Year	Nanocrystal element	Nanocrystal morphology	Ref.
1	Cheng et al.	2014	NiO	Rectangular and square-based pyramid (hut-shaped)	[72]
2	Moulik et al.	2014	WO_3	Needle-like	[11]
3	Takahashi et al.	2014	Fe_3O_4	Pyramid	[73]
4	Sun et al.	2013	Ni	Truncated pyramid	[74]
5	Oropeza et al.	2013	TiO_2 (001)	Square-shaped islands	[58]
6	Cheung et al.	2013	NiO	Rectangular-based pyramid	[165]
7	Zhang et al.	2011	Ag	Icosahedral	[76]
8	Yoo et al.	2010	Pd nanowires (NW)	Isosceles triangle	[59]
9	Yoo et al.	2010	Pd nanowires (NW)	Elongated square pyramid	[59]
10	Silly and Castell	2009	Cu	Icosahedra in the point orientation	[60]
11	Silly and Castell	2009	Cu	Truncated pyramid shape with truncated edges	[60]
12	Cheng et al.	2009	InP	Island	[166]
13	Silly and Castell	2006	Au	Flat	[2]
14	Silly and Castell	2005	Pd	Hut	[62]
15	Silly and Castell	2005	Pd	Hexagonal disk	[62]
16	Silly and Castell	2005	Pd	Truncated pyramid	[62]
17	Silly and Castell	2005	Co	Square	[63]
18	Silly and Castell	2005	Co	Truncated pyramid	[63]
19	Silly and Castell	2005	Fe	Truncated pyramid	[6]
20	Silly and Castell	2005	Ag	Face with flat triangular top	[81]
21	Silly and Castell	2005	Ag	Edge with a ridge separating two triangular facets	[81]
22	Silly and Castell	2005	Ag	Point pyramidal with five side facets	[81]
23	Silly and Castell	2005	Ag	Truncated triangle top surface	[81]

Table 3-4 continued.					
24	Zhang et al.	2004	$SrIn_{0.1}Ti_{0.9}O_3$(SITO)	Dome	[12]
25	Szafraniak et al.	2004	$PbZr_{0.52}Ti_{0.48}O_3$ (PZT)	Irregular shape	[149]
26	Lyubinetsky et al.	2003	Cu_2O	Square/rectangular clusters with flat tops	[167]

shutters, and display devices. It has well-established electrochromic [162] and photochromic [163] effects in visible and infrared wavelengths with high coloration efficiency [164]. The crystal structure of WO_3 is monoclinic at room temperature [168–170]. The lattice constants of WO_3 is 3.81 Å. The WO_3 film was oriented in [100] direction. They further reported that needle-like nanocrystals of WO_3 recorded markedly increased photocurrent (50%) even in light off condition at room temperature, at a wavelength of 360 nm, and at 0.1 V bias voltage [11]. The nanocrystals can be of irregular shapes observed in case of lead zirconate (PZT) nanocrystals on Nb-doped STO (001) substrate [149].

3.7 How does the nanoscale influence metallurgical behavior?

Working at the nanoscale is not akin to working at the macroscale. Because of high surface-to-volume ratio, the surface energy value of material at the nanoscale is manifolds greater than the same amount of the same material at the macroscale. This gigantic contribution of surface energy gives nanoparticles certain powers that macroparticles do not own. For example, the same Al which seems ordinary metal at macroscale becomes explosive when ground down to 10 µm size particles. Similarly, Au, which melts at 1083 °C in bulk form, may be liquified at about 500 °C when in the form of 2 nm size nanoparticles as shown in Figure 3-12 [171]. The optical properties are also size-dependent and Au nanoparticles exhibit different colors based on light scattering as shown

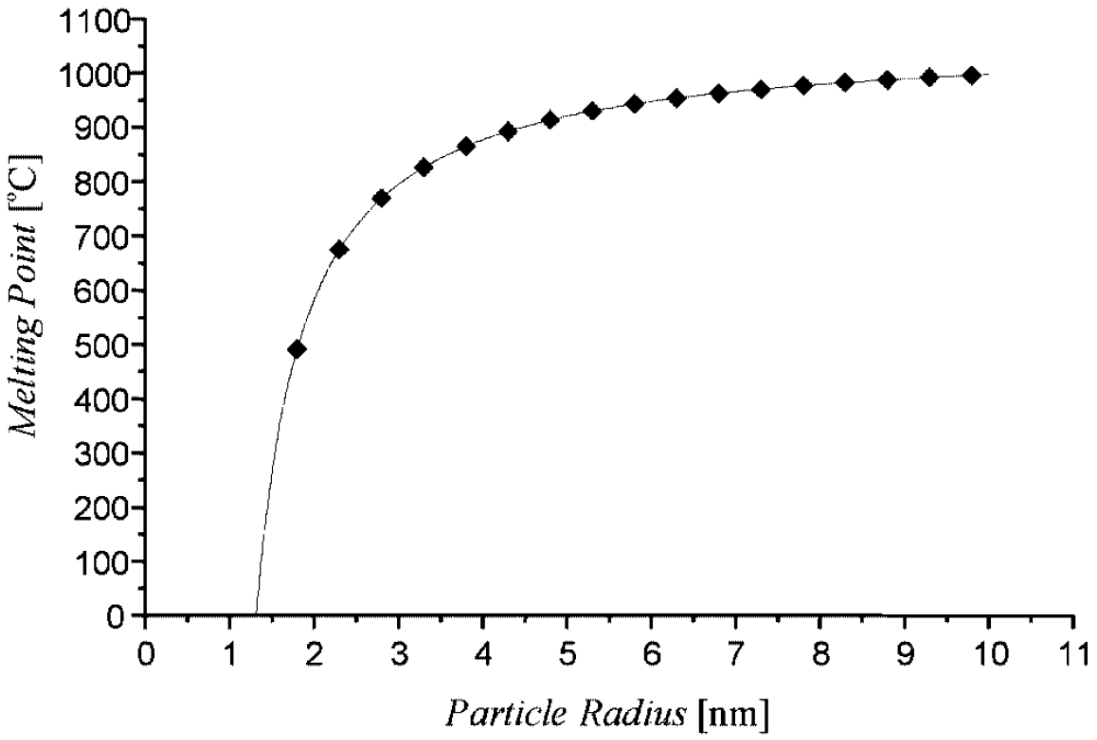


Figure 3-12: Variation in melting point with particle size of Au nanoparticles [171]**.**

in Figure 3-13. The magnetic properties such as permanent magnetization, magnetic saturation, and blocking temperature are also size-dependent [172].

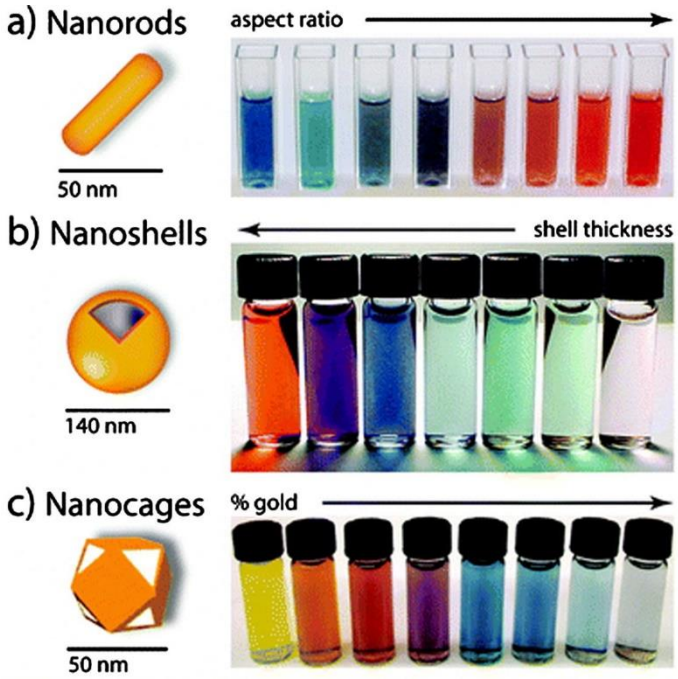


Figure 3-13: Variation in light scattering with size, shape, and concentration of Au nanoparticles: (a) Au nanoparticles [173]**. (b) Nanoshells** [174]**. (c) Nanocages** [175]**.**

One of the features in which nanoparticles differ from macroparticles is reactivity. Au is inert in its bulk form, however, its nanoparticles act as a catalyst and show high catalytic efficiency. For instance, when one dimension of Au thin film becomes less than the thickness of three atoms, it shows marked enhancement in the catalytic activity [176–180]. Because of the high surface-to-volume ratio, the reactivity of nanoparticles surpasses by many orders of magnitude that of macroparticles. Therefore, while working at the nanoscale, it is ensured that nanoparticles do not undergo undesired reactions such as oxidation. The nanoscale does not only change the reactivity, but it may also change the crystal structure of nanocrystals that may produce phases of unique properties (Table 3-5). For example, it has been reported that Co showed body-centered tetragonal (bct), bcc, hcp, fcc, twinned fcc, and coexistence of two structures based on the growth conditions [84–86].

3.8 Core-shell nanoparticles

It was observed in the 1980s that unique properties could be achieved by combining two or more ingredients such as colloidal semiconductor hybrid nanoparticles [181–183]. In the 1990s, research started in a specialized field of hybrid nanoparticles, i.e., concentric multilayer semiconductor nanoparticles. The field is now generally called core-shell nanoparticles (CSNs) [184–186]. CSNs have come into research limelight because of the versatility and tailorability of their scientific properties that make them suitable for many applications ranging from catalysis to biology [187]. In catalysis, surfaces are of main interest as they are mainly involved in reactions. Instead of using nanoparticles fully made of expensive materials, such as precious metals, using CSNs in which core is made of an

Table 3-5: Crystal structures of nanocrystals grown on STO.

Sr.	Authors	Year	Nanocrystal element	Crystal structure	Ref.
1	Hadamek et al.	2016	NbO_2	Tetragonal	[70,71]
2	Sun et al.	2013	Ni	fcc	[74]
3	Zhang et al.	2011	Ag	fcc	[76]
4	Feng et al.	2011	Pt	fcc	[1]
5	Enterkin et al.	2011	Pt	fcc	[77]
6	Komanicky et al.	2010	Pt	fcc	[78]
7	Yoo et al.	2010	Pd nanowires (NW)	fcc	[59]
8	Yoo et al.	2010	Pd nanowires (NW)	fcc	[59]
9	Silly and Castell	2009	Cu	fcc	[60]
10	Son et al.	2009	Pt	fcc	[79]
11	Christensen et al.	2009	Pt	fcc	[80]
12	Francis and Salvador	2006	Au	fcc	[61]
13	Francis and Salvador	2006	Ag	fcc	[61]
14	Francis and Salvador	2006	Pt	fcc	[61]
15	Francis and Salvador	2006	Cu	fcc	[61]
16	Silly and Castell	2006	Au	fcc	[2]
17	Silly and Castell	2005	Pd	fcc	[62]
18	Silly and Castell	2005	Co	fcc	[63]
19	Silly and Castell	2005	Co	fcc, bcc	[63]
20	Silly and Castell	2005	Fe	bcc	[6]
21	Silly and Castell	2005	Ag	fcc	[81]
22	Wang et al.	2004	Au	fcc	[82]

economical material, such as Fe, would reduce the cost of the whole process. In addition, the desired properties can be obtained and tailored easily by making CSNs. The different types of CSNs are schematically shown in Figure 3-14. In general, there are four main types of CSNs: (1) organic/organic, (2) inorganic/inorganic, (3) organic/inorganic, and (4)

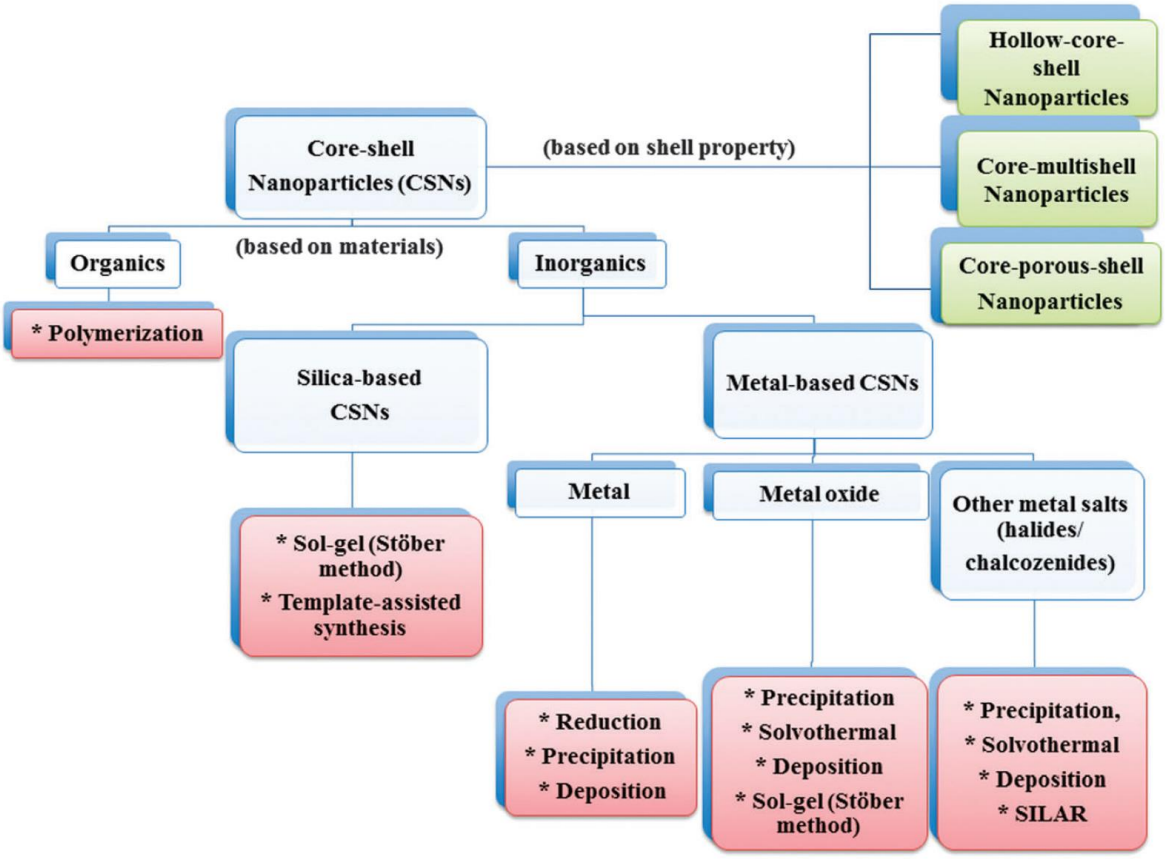


Figure 3-14: Different types of CSNs [187].

inorganic/organic. As shell material is mostly involved in reactions, the selectivity of shell material is dependent on the application.

3.9 Summary

Some basic aspects of surface science and growth of nanocrystals and nanoparticles have been introduced. The significance of surface-related phenomena and interactions of nanocrystals with surfaces were highlighted. Some of the important points discussed are listed below;

1. The nanocrystals and nanoparticles can be produced using multiple ways that can be divided into two categories: (1) colloidal methods and (2) epitaxial methods.
2. In colloidal methods, two or more precursors are suspended in a suitable fluid. The precursors react with each other forming nanoparticles.

3. In epitaxial methods, the material of which nanocrystals are to be produced is evaporated.

   The vapors then condense on the desired substrate forming nanocrystals. The surface energies, interfacial interactions, and epitaxial relationships play a crucial role in defining the morphology of grown nanocrystals.
4. There are three main modes in which nanocrystals grow on a substrate: (1) Frank-van der Merwe (FM) or layer-by-layer growth mode, (2) Volmer-Weber (VW) or island growth mode, and (3) Stranski-Krastanov (SK) or layer-plus-island growth mode.
5. The interfacial interactions and epitaxial relationships strongly depend on the surface condition of the substrate. Therefore, special attention is required while preparing the surface of a substrate. Usually a single crystal substrate is used to grow nanocrystals.
6. There are two important aspects of a single crystal substrate: (1) termination and (2) reconstruction. In a single crystal, all atoms are arranged in one type of plane, and that plane is called termination. As surface atoms are not fully surrounded by other atoms, their arrangement is different from that in bulk. That specific arrangement of surface atoms is called reconstruction. The reconstructions are named using two main methods: (1) Park-Madden matrix notation, and (2) Wood's notation.
7. Epitaxy is related to the deposition of a crystalline material (called epitaxial layer or epitaxial film) over another crystalline material (called substrate). If both epitaxial layer and substrate are of the same material, the epitaxy is called homoepitaxy. If both materials are different, it is called heteroepitaxy. During deposition, atoms of deposited material align themselves with respect to the atoms

of the substrate. The relationship at the interface of epitaxial layer and substrate is called epitaxial relationship.

8. The epitaxy strongly influences the morphology of nanocrystals, and different morphologies exhibit different physical and chemical properties. For example, it was reported that the catalytic activity of Au nanocrystals supported on oxide substrates was dependent on their size when they were used to oxidize CO through heterogeneous catalysis [147–149].
9. At the interface, the atomic arrangement is different from the bulk. The properties near the interface start changing due to the different atomic arrangement. A separate phase may also exist at the interface with unique properties. Reconstruction phenomenon at the interface between complex oxides produces novel metallic, magnetic, and superconducting two-dimensional phases [36]. Novel quantum states, such as ferromagnetism [37–41], superconductivity [42–44], and their coexistence [45–47], are also present at the interface of heterojunctions [48]. The lattice mismatch, lattice strain, and compensation of lattice strain by misfit dislocations are important aspects to investigate while studying interface at the nanoscale.
10. Different materials have different lattice constants. In the case of heteroepitaxy, the atoms of deposited material align themselves along the same plane as that of the substrate. As the lattice constants of deposited material and the substrate are different, there is a lattice mismatch at the interface. To compensate for the lattice mismatch, the atomic planes of the deposited material have either to expand or contract. This expansion or contraction produces lattice strain in the whole film. If lattice strain exceeds certain value depending on the system, lattice strain is compensated by misfit dislocations.

11. One of the features in which nanoparticles differ from macroparticles is reactivity. Au is inert in its bulk form, however, when ground down to nanometer size, it acts as a catalyst and shows high catalytic efficiency. For instance, when one dimension of Au thin film becomes less than the thickness of three atoms, it shows marked enhancement in the catalytic activity [176–180].
12. One important field related to the nanoparticles is core-shell nanoparticles (CSNs) as they can offer diverse properties and applications. In CSNs, a material is encapsulated by another material. The inner material is called ‘core,’ and the outer material is called ‘shell.’ In general, there are four types of CSNs: (1) organic/organic, (2) inorganic/inorganic, (3) organic/inorganic, and (4) inorganic/organic.

3.10 Conclusions

From the review of the literature, it can be concluded that the research in the field of nanocrystals grown on different substrates has only been conducted using single elements (metals and semiconductors) or nanocrystals of existing compounds. One important aspect in which the current research has yet not extended is to try to create phases that are not generally available at room temperature at bulk scale. One way of studying this aspect is to investigate the influence of nano-alloying on the phase transformation. As there is no sufficient data on nano-alloying in the field of nanocrystals grown on various substrates and considering the fact that the behavior of materials at the nanoscale is disparate from that at bulk scale, a deeper understanding of nano-alloying on the behavior of materials at the nanoscale will be a important contribution in the field of materials science.

Chapter 4:

$SrTiO_3$

4.1 Background

4.1.1 Overview

$SrTiO_3$ has cubic perovskite structure with a lattice parameter of 0.3905 nm. In the unit cell (Figure 4-1), the center of the cube is occupied by Sr that has 2+ charge.

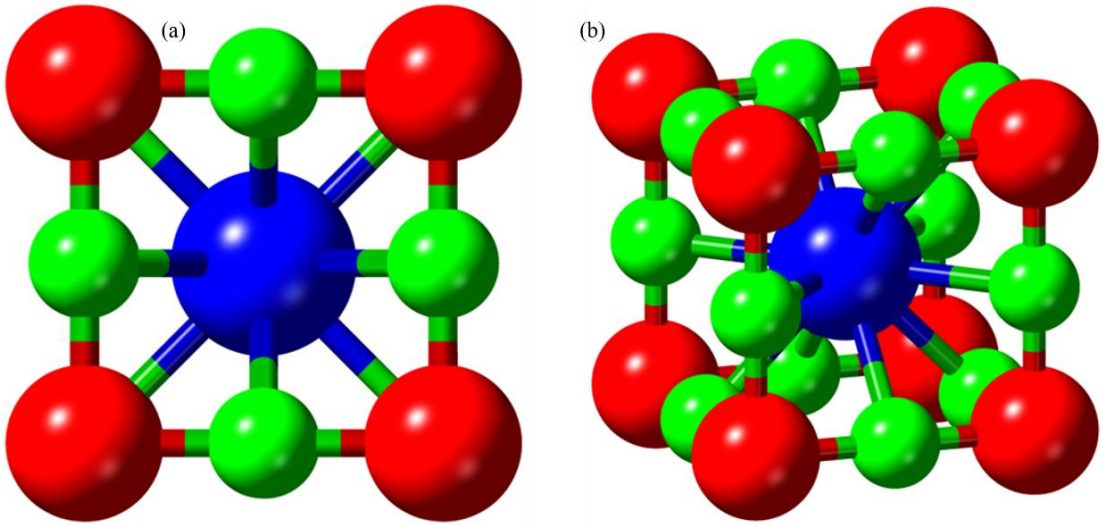


Figure 4-1: (a) 2D and (b) 3D views of $SrTiO_3$ unit cell.

At the cube corners sits Ti with 4+ charge. Oxygen settles at the centers of cube edges taking a charge of 2- thereby making the unit cell electrically neutral. In its stoichiometric form $SrTiO_3$ has band gap of 3.2 eV and is non-conductive [188–191]. When doped with La^{3+} or Y^{3+} on a Sr site, or Nb^{5+} on a Ti site, insulating $SrTiO_3$ can be converted into n-type extrinsic semiconductor. When insulating $SrTiO_3$ is annealed in UHV, oxygen vacancies are generated making it n-type semiconductor. p-type behavior can be produced through substitutional doping with Sc^{3+} on a Ti site [192]. The vacuum anneals do not conserve material on the $SrTiO_3$ surface and Auger electron spectroscopy proved that these nanostructures are TiO_2 rich [193].

$SrTiO_3$ has been widely used for the growth of high T_c superconducting thin films [194], to act as a crystalline gate dielectric in silicon-based devices [195,196] and a buffer material for the growth of GaAs on Si [197]. Another reason for the widespread use of $SrTiO_3$ is self- assembly of nanostructures on its surface. Because of their unique properties, self-

assembled nanostructures are a potential candidate for novel electronic devices such as quantum dot lasers and single electron transistors [198,199]. Castell showed for the first time self-assembly of nanostructures on $SrTiO_3$ (001)-c(4 × 2) [200]. Several different variants have since been reported [201,202].

When $SrTiO_3$ is subjected to various thermal cycles under different environments, various surface reconstructions are observed with different periodicities. Some of the periodicities are close to those of many metals. When those metals are deposited on the $SrTiO_3$ and the system is optimally post-annealed, deposited metals take nice geometric forms such as icosahedron, truncated pyramid, hut, truncated hut and truncated octahedron. These forms are equilibrium crystal shapes (ECS) of those metals under a given set of conditions. One of the reasons that nanocrystals of metals take geometric shape is epitaxy at the nanocrystal-substrate interface. Most of the metals are cubic and $SrTiO_3$ is also cube and can generate cube-on-cube epitaxy. It makes $SrTiO_3$ a suitable candidate to be used as a substrate for the growth and investigation of ECS of various metals.

In this work, $SrTiO_3$ was used as substrate to investigate ECS of Ni and Fe nanocrystals. As the surface structure of the substrate can significantly influence the epitaxial relationships with the deposited metals which in turn control the ECS of nanocrystals, it was important to investigate the surface structures of $SrTiO_3$ under different set of conditions. Hence, this chapter is dedicated to $SrTiO_3$ surface reconstructions and self-assembled nanostructures.

4.1.2 Experimental details

0.5 wt% Nb-doped $SrTiO_3$ samples were purchased from PI-KEM. Three different terminations were studied; (001), (110) and (111). Various thermal cycles applied to the samples, after which the results obtained are shown and discussed in this chapter, are listed in Tables 4-1-4.

Table 4-1: Experimental steps for unsputtered $SrTiO_3$ (001).

Sr.	Temp. (°C)	Time	Comments
1	800	30 min	A pair of screw dislocations were observed on the surface.
2	850	30 min	Irregular terraces were observed.
3	900	30 min	Straight terraces were observed.
4	1200	15 min	Terraces consisting of two different domains with domain boundaries.

Table 4-2: Experimental steps for sputtered $SrTiO_3$ (001).

Sr.	Temp. (°C)	Time	Comments
1	900	30 min	Irregular terraces were observed covered in nanolines. Atom/vacancy hopping was also observed while imaging at room temperature.
2	980	30 min	Terraces were observed covered in nanolines.
3	900	30 min	Terraces were observed covered in nanolines.
4	900	1 h	Terraces were observed covered in nanolines.
5	960	30 min	Waffle structure was observed.
6	980	15 min	Nanolines and nanodots started to disappear from the surface.
7	1100	10 min	Dendritic terraces were observed

Table 4-3: Experimental steps for sputtered $SrTiO_3$ (110).

Sr.	Temp. (°C)	Time	Reconstructions	Comments
1	900	1 h	(4 × 1)	Terraces were observed with right-angle steps.

Table 4-4: Experimental steps for sputtered $SrTiO_3$ (111).

Sr.	Temp. (°C)	Time	Reconstructions	Comments
1	900	1 h	(4 × 4) – (6 × 6)	Terraces were observed with two different domains.

4.2 Results

4.2.1 $SrTiO_3$ (001)

4.2.1.1 Screw dislocations

When $SrTiO_3$ (001) was annealed at 800 °C for 30 min, a pair of screw dislocations emerged onto the surface as shown in Figure 4-2 (a). The 3D view of the step produced as a result is shown in Figure 4-2 (b). The step height is ~ 0.4 nm that corresponds to height

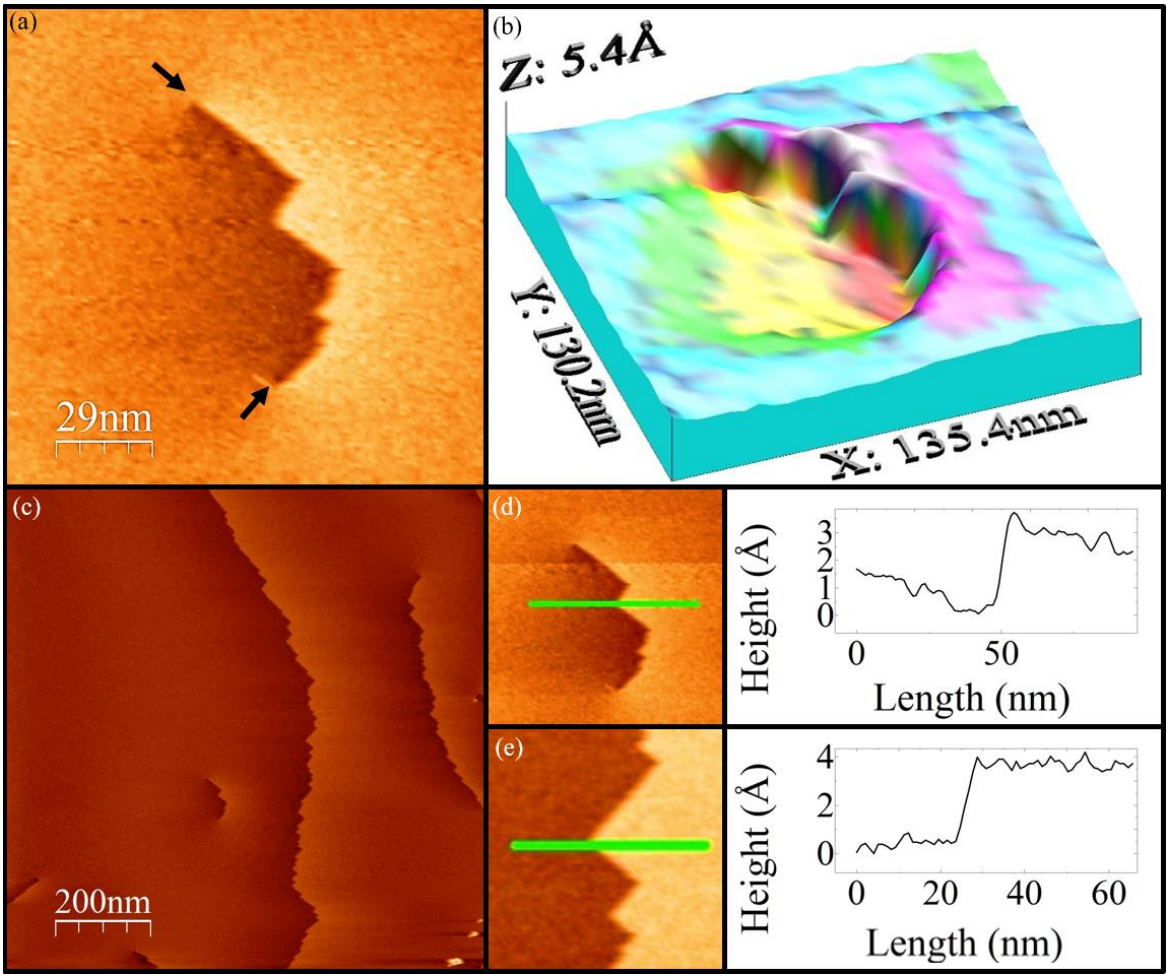


Figure 4-2: (a) $SrTiO_3$ (001); V_s = 1.0 V, I_t = 0.2 nA. The sample was annealed at 800 °C for 30 min. Arrows show a pair of screw dislocations being emerged on the surface. (b) 3D view of the screw dislocations. The step created by the screw dislocations is corrugated. The screw dislocations combined forming terraces on the surface as shown in (c); V_s = 1.0 V, I_t = 0.2 nA. (d) The screw dislocations produced a step with height 0.4 ± 0.027 nm. (e) The terrace height is also 0.4 ± 0.020 nm.

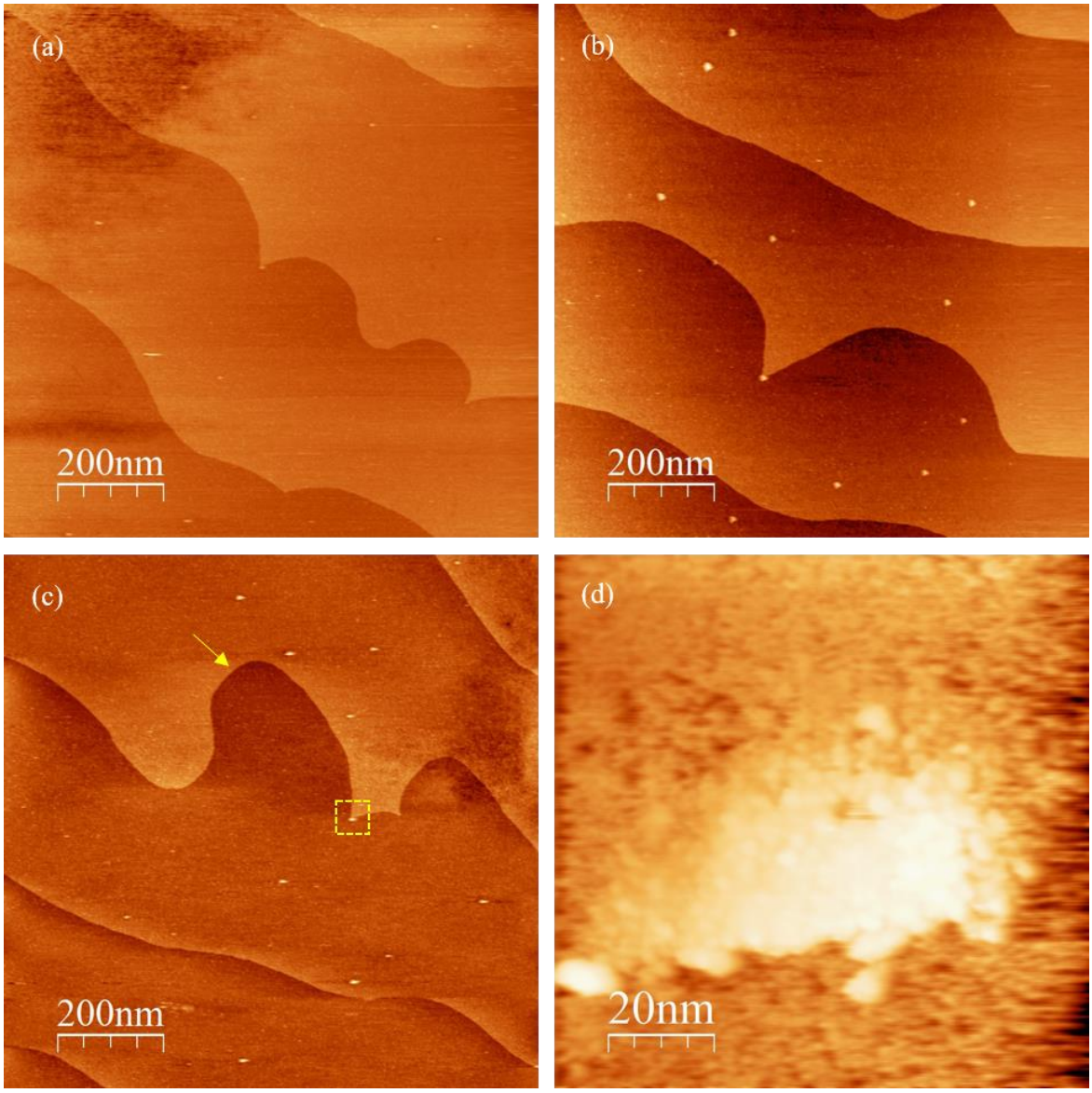


Figure 4-3: (a-d) $SrTiO_3$ (001); V_s = 2.0 V, I_t = 0.2 nA. The sample was annealed at 850 °C for 30 min. The terraces are not straight that can be because of thermal gradient and clusters of atoms.

of one unit cell of $SrTiO_3$ (001). The step height produced by the pair of screw dislocations (Figure 4-2 (d)) and terrace height (Figure 4-2 (e)) are the same (~ 0.4 nm). When the sample was heated at 830 °C for 30 min, the surface got covered by irregular terraces as shown in Figure 4-3 (a-c). The irregularity can be caused by impurities and notches at the surface. A magnified image of Figure 4-3 (c) is shown in Figure 4-3 (d) where some dirt/impurity can be observed. This cluster could impede the propagation of the terrace. Right next to the cluster of atoms, the terrace has significantly retreated. It can be related

to the thermal fluctuations and/or thermal gradients during annealing. The thermal gradients can be caused by the non- uniform distribution of dopant; Nb or oxygen vacancies in this case. It has been shown that reconstruction of these kind of terraces is (2 × 1) [10].

4.2.1.2 (2 × 2)-(√5 × √5)R26.6° reconstructions

When sample was annealed at 1200 °C for 15 min, the surface observed as a result is shown in Figure 4-4.

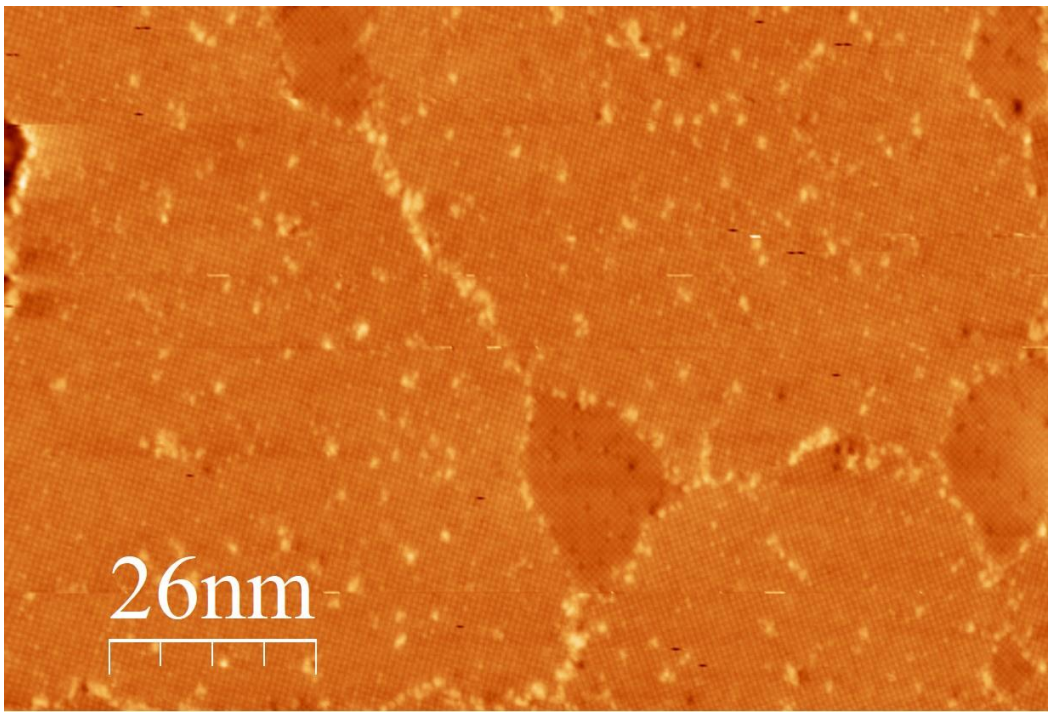


Figure 4-4: $SrTiO_3$ (001) annealed at 1200 °C for 15 min; V_s = 0.91 V, I_t = 0.2 nA.

Two different domains can be observed with two different reconstructions as shown in Figure 4-5. At the bottom left the periodicity is (0.783 ± 0.018) nm that corresponds to (2 × 2). The periodicity of top right domain is (0.868 ± 0.015) nm that corresponds to (√5 × √5)R26.6°. A magnified image is shown in Figure 4-6. The bright atom can possibly be of dopant. Vacancies were present on the surface as can be observed in Figure 4-7. Two vacancies at some distance can be observed. The vacancies were also positioned right next to each other as can be observed in Figure 4-8. The vacancies also positioned themselves

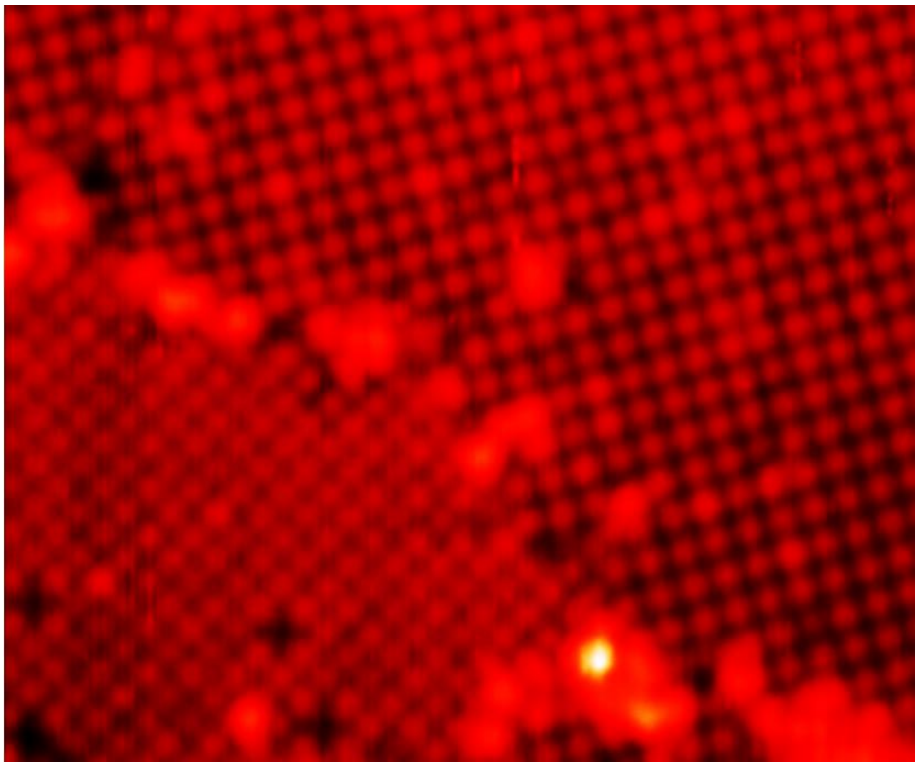


Figure 4-5: $SrTiO_3$ (001) annealed at 1200 °C for 15 min; V_s = 0.91 V, I_t = 0.2 nA. The periodicity of top right reconstruction is 0.868 ± 0.015 that corresponds to (√5 × √5)R26.6° reconstruction and that of bottom left is 0.783 ± 0.018. that corresponds to (2 × 2).

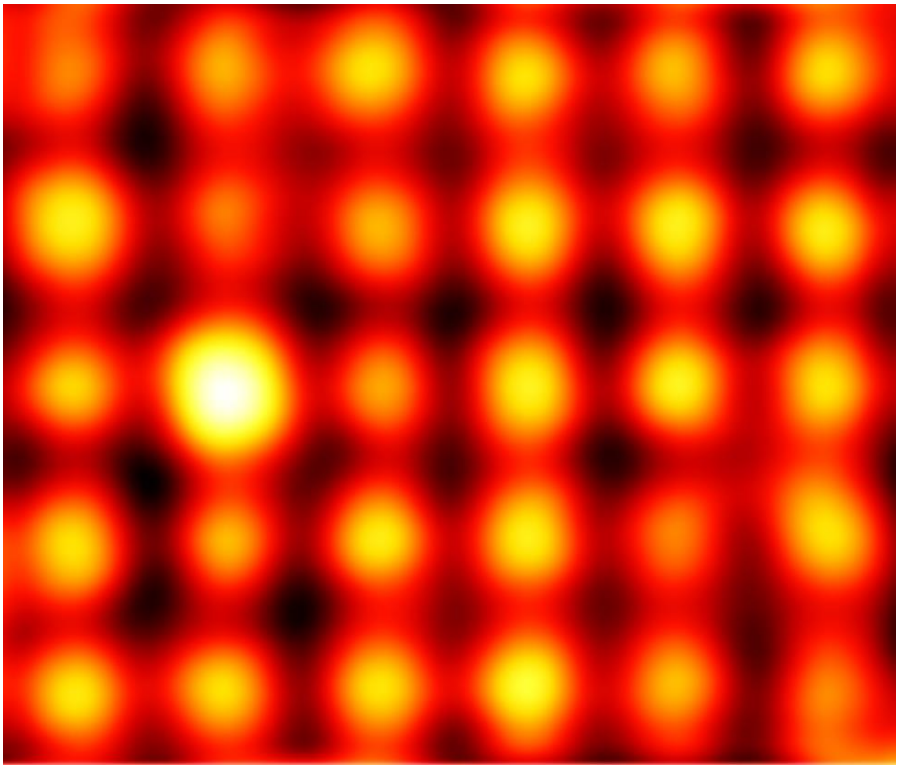


Figure 4-6: $SrTiO_3$ (001) annealed at 1200 °C for 15 min; V_s = 0.91 V, I_t = 0.2 nA. The periodicity is 0.868 ± 0.015 that corresponds to (√5 × √5)R26.6° reconstruction.

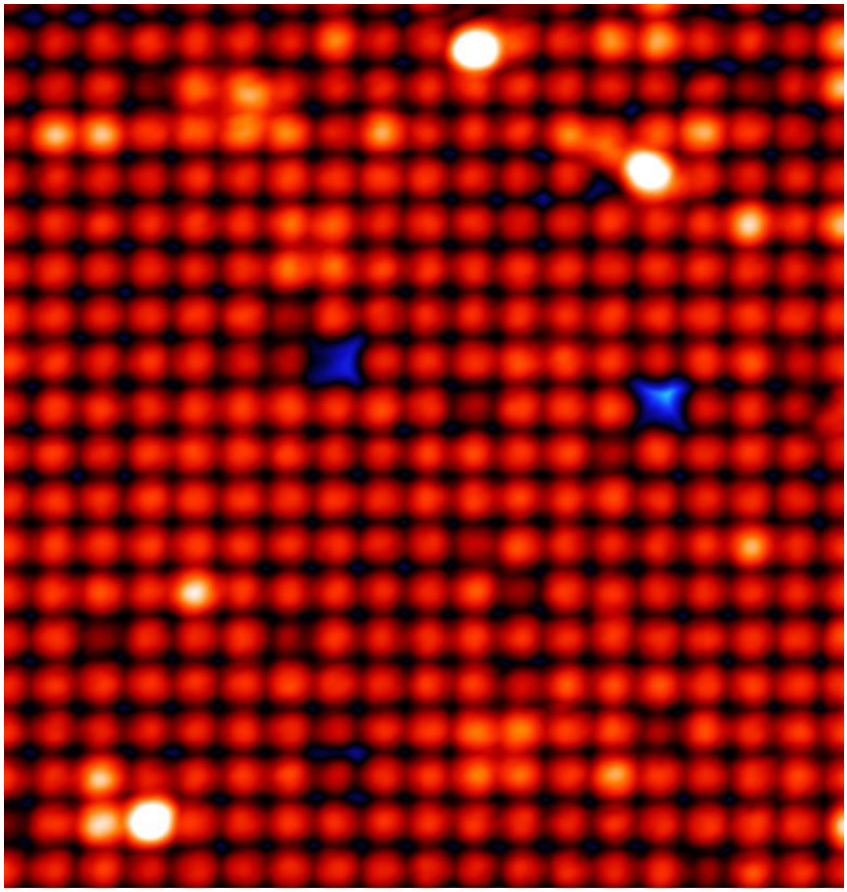


Figure 4-7: $SrTiO_3$ (001) annealed at 1200 °C for 15 min; V_s = 0.91 V, I_t = 0.2 nA. The periodicity is 0.868 ± 0.015 that corresponds to (√5 × √5)R26.6°.

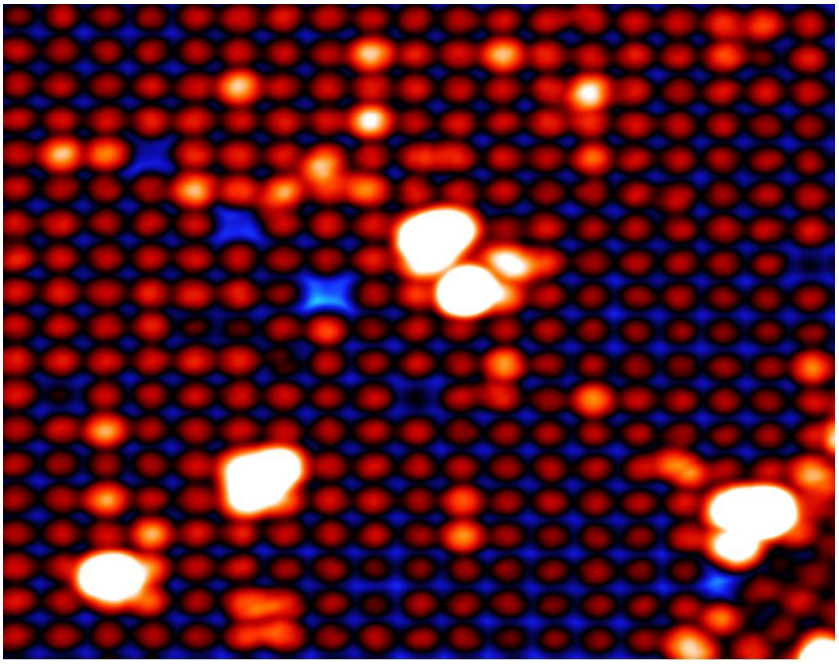


Figure 4-8: $SrTiO_3$ (001) annealed at 1200 °C for 15 min; V_s = 0.91 V, I_t = 0.2 nA. The periodicity is 0.868 ± 0.015 that corresponds to (√5 × √5)R26.6°.

along a straight line as shown in Figure 4-9.

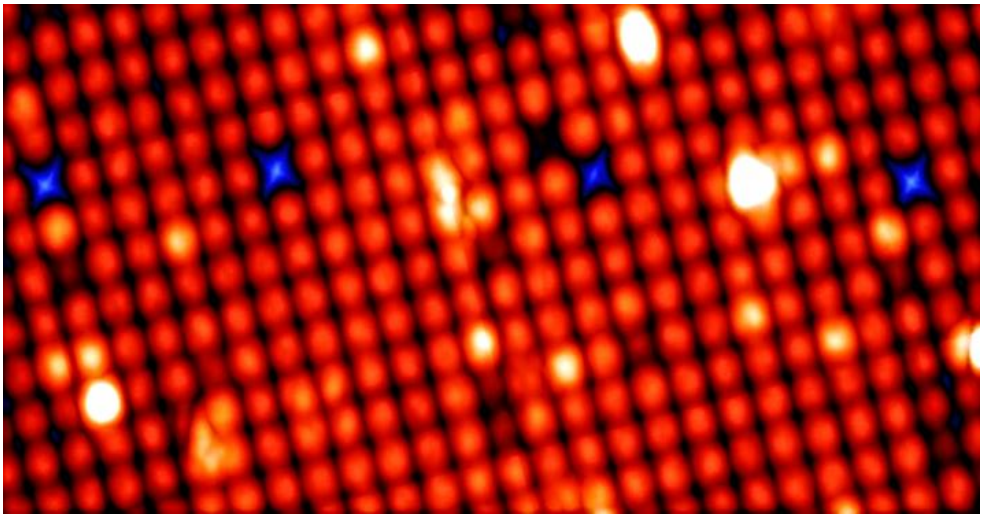


Figure 4-9: $SrTiO_3$ (001) annealed at 1200 °C for 15 min; V_s = 0.91 V, I_t = 0.2 nA. The periodicity is 0.868 ± 0.015 that corresponds to (√5 × √5)R26.6°.

The reconstruction was not only observed on one terrace but on adjacent terraces as well as shown in Figure 4-10.

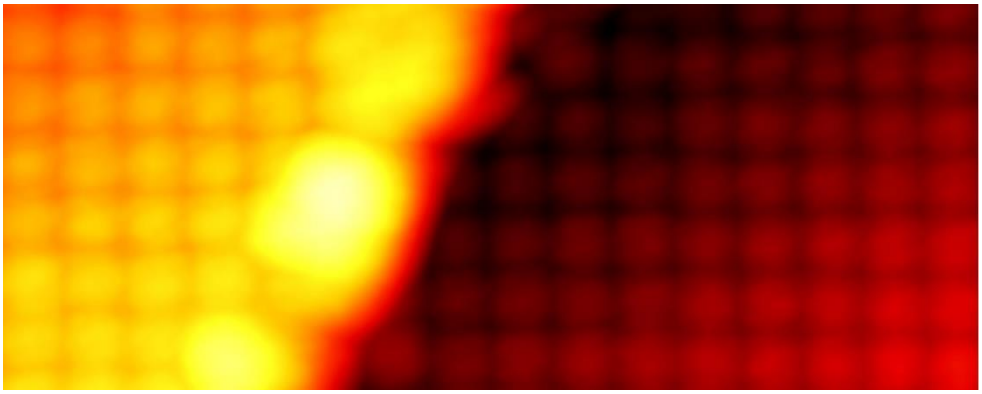


Figure 4-10: $SrTiO_3$ (001) annealed at 1200 °C for 15 min; V_s = 0.91 V, I_t = 0.2 nA. The periodicity is 0.868 ± 0.015 that corresponds to (√5 × √5)R26.6°.

The same reconstruction of (√5 × √5)R26.6° was observed on one terrace but with a domain boundary in between them as shown in Figure 4-11. The one domain was rotated by around 40° with respect to the other domain.

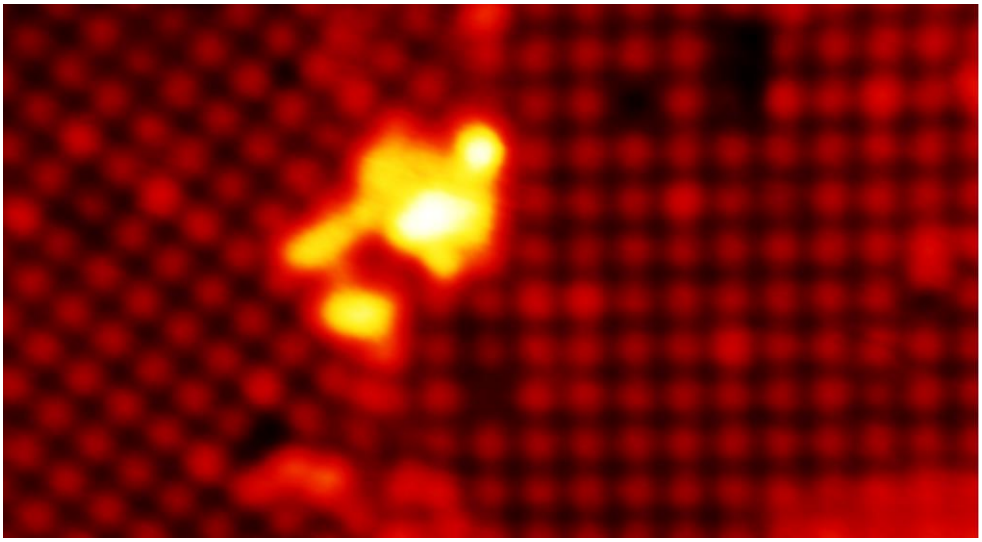


Figure 4-11: $SrTiO_3$ (001) annealed at 1200 °C for 15 min; V_s = 0.91 V, I_t = 0.2 nA. The periodicity is 0.868 ± 0.015 that corresponds to (√5 × √5)R26.6°.

4.2.1.3 Nanolines

When surface of $SrTiO_3$ (001) was sputtered with Ar ions and then annealed nanolines started to appear as shown in Figure 4-12 and Figure 4-13.

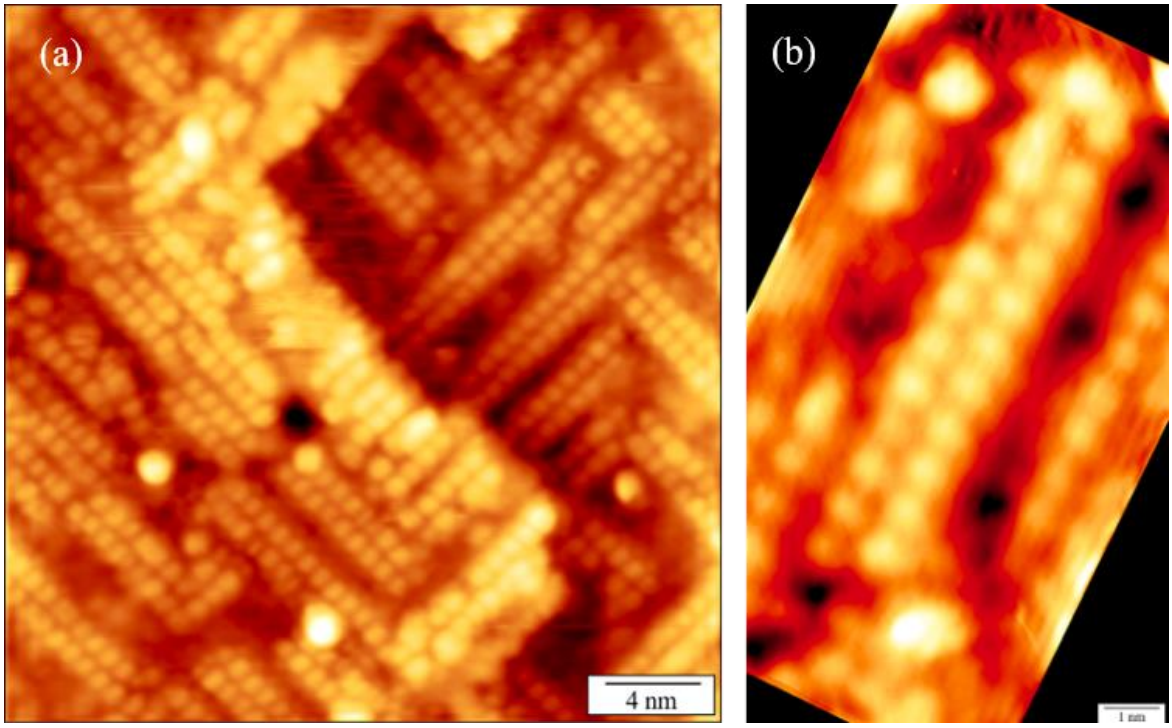


Figure 4-12: (a-b) $SrTiO_3$ (001); V_s = 2 V, I_t = 0.2 nA. The sample was sputtered (0.5 keV, 2.5 µA, 10 min) and annealed at 900 °C for 30 min leading to generation of dilines.

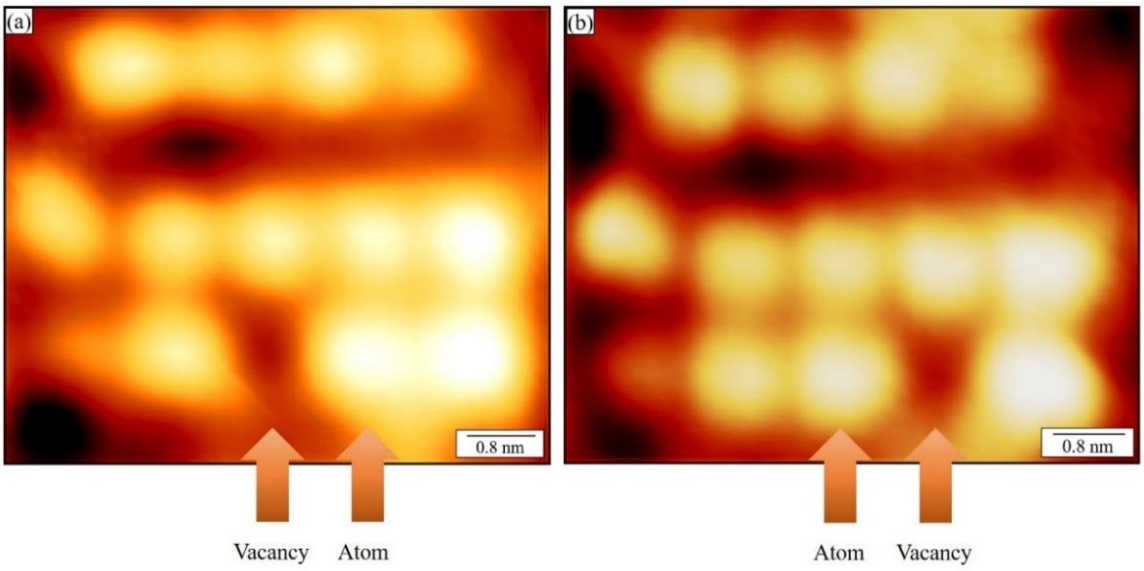


Figure 4-13: $SrTiO_3$ (001)-c(4×2) sputtered (500 eV energy, 7 µA current, 10 min) and then annealed at 900 °C for 30 min with heat/cooling rates at 0.1 V/min; V_s = 2 V, I_t = 0.2 nA.

The sample was sputtered (0.5 keV, 2.4 µA, 10 min) and then annealed at 900 °C for 30 min. The surface got covered with dilines. Two images of the surface with image (a) being 10 min older than image (b) as shown in Figure 4-14.

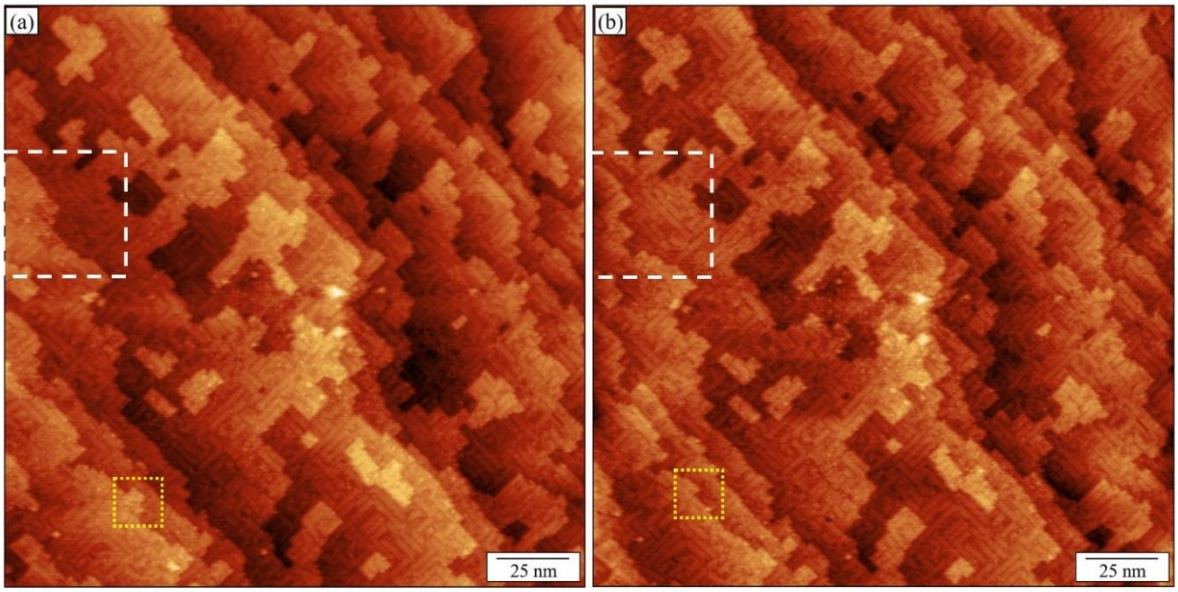


Figure 4-14: $SrTiO_3$ (001)-c(4×2) sputtered (500 eV energy, 2.4 µA current, 10 min) and then annealed at 900 °C for 30 min with heat/cooling rates at 0.1 V/min; V_s = 2 V, I_t = 0.2 nA. Image (b) was taken 10 min after image (a).

The difference in images is prominent as highlighted in white and yellow squares. The regions in white squares show that the terrace is trying to convert its end into sharp edges. The phenomenon occurring in yellow squares is more prominent. A chunk of material existing in the form of a protrusion in terrace has been vanished after 10 min. There is possibility that some material from the surface was plucked away by the scanning tip. During imaging an interesting phenomenon was observed. An atom was found hopping between two position as shown in Figure 4-13. The video can be downloaded using link below;

https://www.dropbox.com/s/32s5t2atz2gq489/1.%20SrTiO3%20atom%20hopping.avi?dl=0

When sputtered sample was further annealed, the whole surface was covered in nanolines as shown in Figure 4-15. The main feature in the image are the two parallel rows of bright spots that run along the length of the diline. Because the separations are equal, and the spots are opposite each other, this type of diline will be referred to as a square diline [10]. The diline height is around 0.2 nm (half a bulk unit cell) above the background level of the

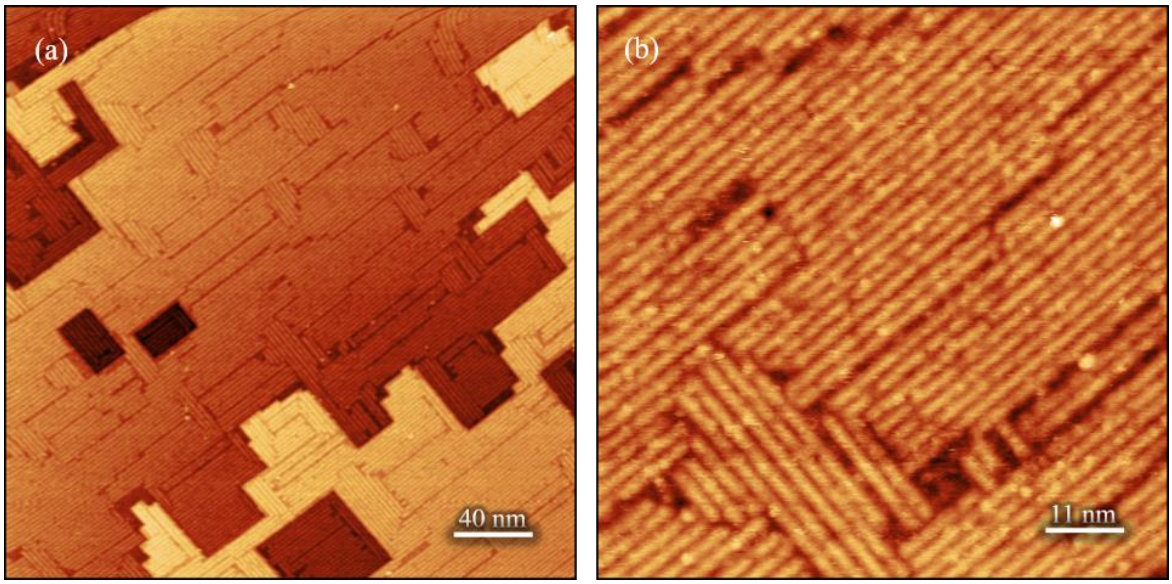


Figure 4-15: (a, b) $SrTiO_3$ (001) sputtered (0.5 keV, 2.5 µA, 10 min) and annealed (980 °C, 30 min); V_s = 0.5 V, I_t = 0.2 nA.

surrounding c(4 × 2) reconstructed surface. 0.2 nm height corresponds to half a bulk unit cell. In another sputtering cycle, sputtering energy was kept 1 keV and current 4.4 µA and sputtering was carried out for 10 min. The sample was then annealed at 900 °C for 30 min. The STM image of resulting surface is shown in Figure 4-16. The surface is covered in nanolines. When sample was further annealed, nanolines were observed comprising of nanolines as shown in Figure 4-17. Because these structures were almost invariably

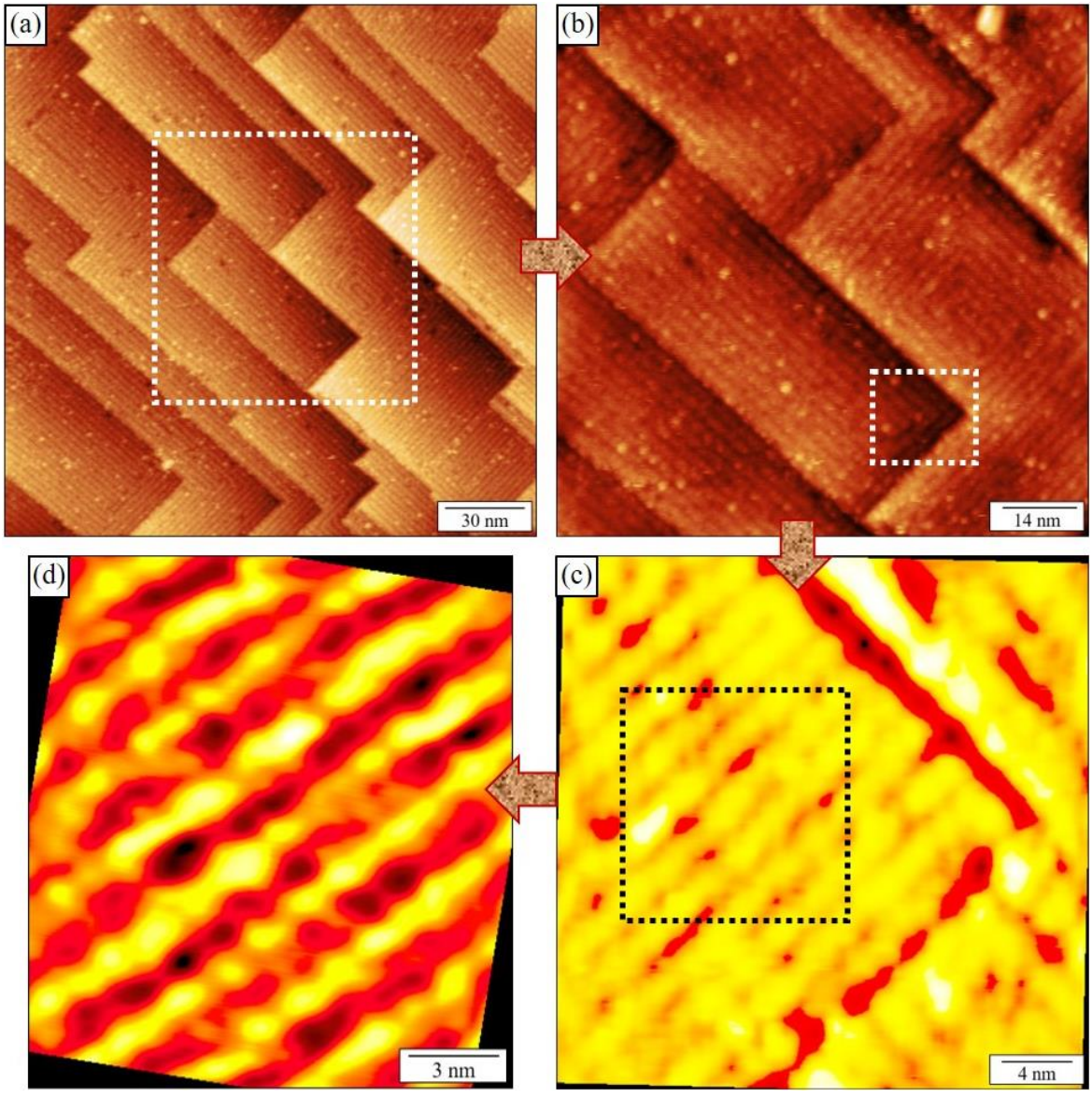


Figure 4-16: $SrTiO_3$ (001) sputtered (1 keV, 4.4 µA, 10 min) and annealed at 900 °C for 30 min; V_s = 2 V, I_t = 0.2 nA.

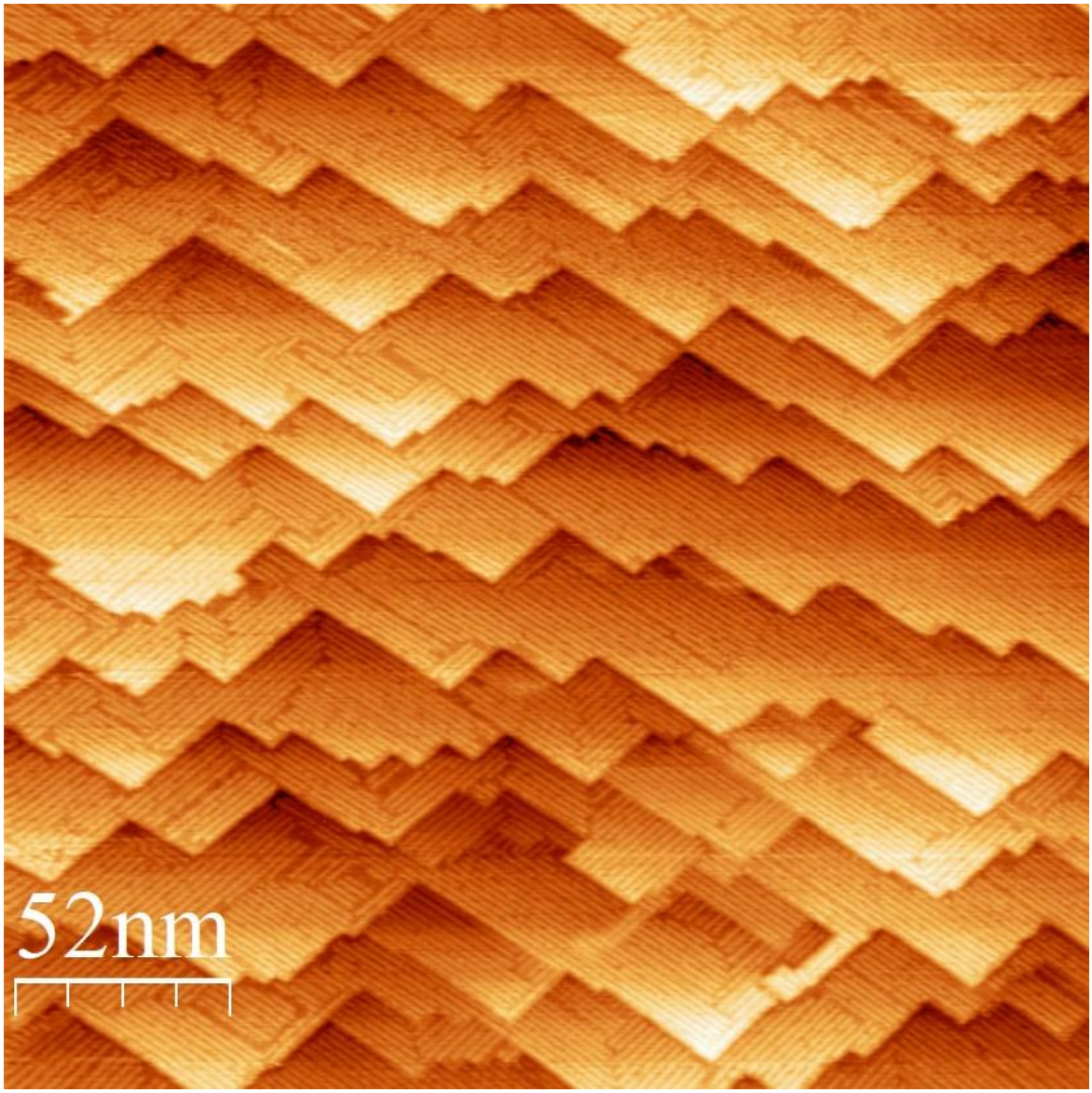


Figure 4-17: $SrTiO_3$ (001); V_s = 0.5 V, I_t = 0.1 nA. The sample was sputtered (0.5 keV, 2.5 µA, 20 min) and annealed at 900 °C for 1 h. The periodicity of nanolines is 2.046 ± 0.220.

atomically straight, Castell named them nanolines [200]. Two most commonly observed nanolines are dilines and trilines. The structure of the surface around the nanolines is still c(4 × 2) as determined by atomically resolved STM and LEED [200]. More prolonged or hotter annealing caused more nanolines to appear on the surface. When the surface is fully covered in nanolines, they adopt a packing arrangement where the minimum periodicity is about 2.4 nm which is equivalent to a separation of six bulk unit cells. The nanolines themselves have a periodicity of 0.8 nm along their length equivalent to two bulk unit

cells. Hence when the nanolines dominate the surface coverage a (6 × 2) reconstruction is formed [200].

4.2.1.4 Nanodots

When sputtered sample was further annealed, the nanolines started to fade away as shown in Figure 4-18 and Figure 4-19. Some of the nanolines were replaced by ordered arrays of dot-like nanostructures; Castell named them nanodots [200]. On all samples tested

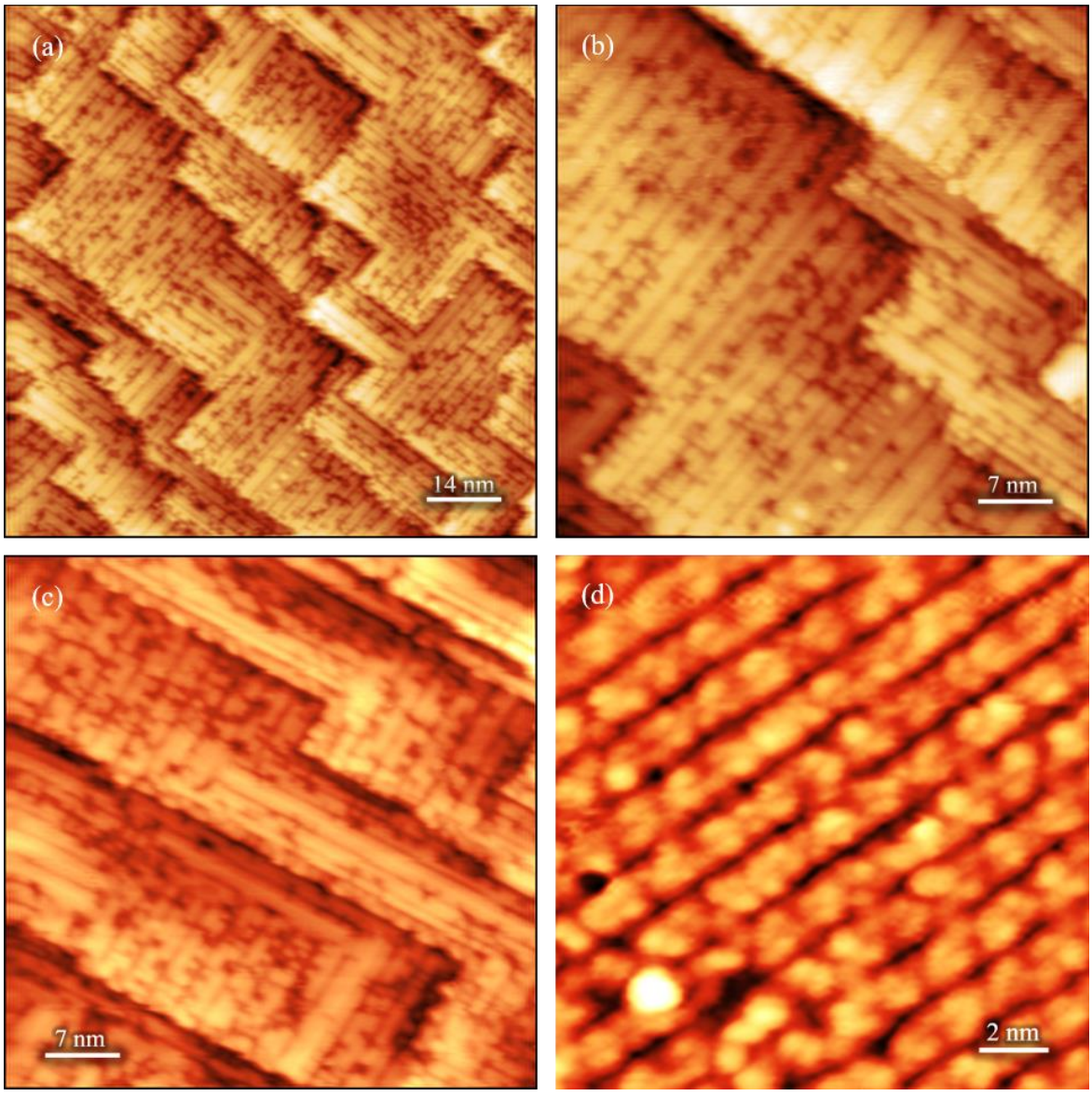


Figure 4-18: $SrTiO_3$ (001) sputtered (0.5 keV, 2.5 µA, 10 min) and annealed at different temperatures. (a,b) 920 °C for 30 min; V_s = 3.2 V, I_t = 0.2 nA. (c) 940 °C for 30 min; V_s = 3.2 V, I_t = 0.2 nA. (d) 960 °C for 30 min; V_s = 2.5 V, I_t = 0.2 nA.

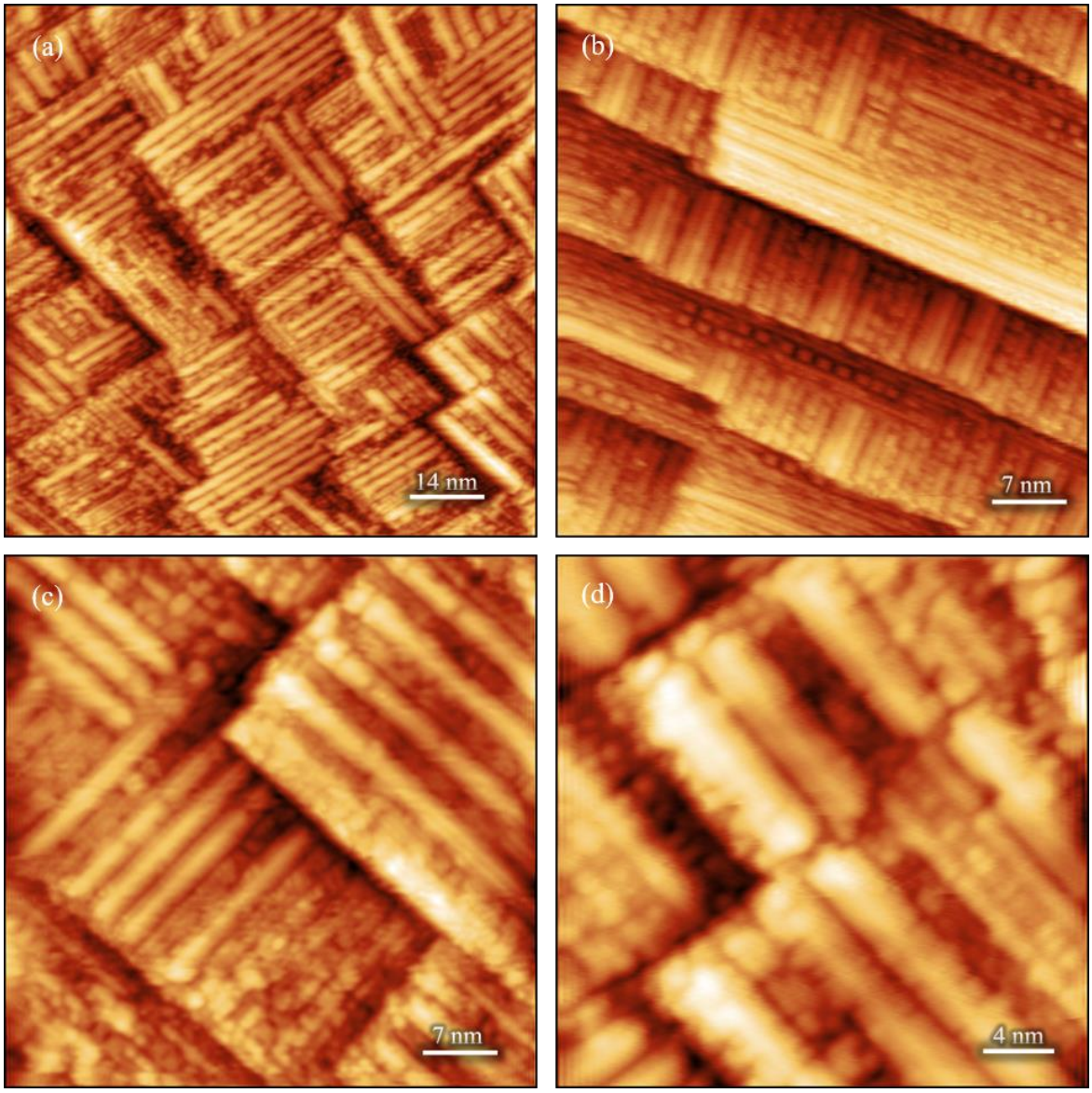


Figure 4-19: $SrTiO_3$ (001) sputtered (0.5 keV, 2.5 µA, 10 min) and annealed at different temperatures. (a,b) 920 °C for 30 min; V_s = 3.2 V, I_t = 0.2 nA. (c) 940 °C for 30 min; V_s = 3.2 V, I_t = 0.2 nA. (d) 960 °C for 30 min; V_s = 2.5 V, I_t = 0.2 nA.

annealing gave rise to nanolines before nanodots, so it is reasonable to assume that the nanodot arrays evolve out of the nanolines. This supposition is further supported by the observation that nanolines can be detected in isolation but that in all images where nanodots were observed there were also some nanolines present. When sample was annealed further, the nanostructures that had formed started to disappear. Atomic resolution STM and LEED of this surface showed that it had still maintained the c(4 × 2)

reconstruction [10]. The dilines have also observed in the form of zig-zag configuration [200]. The zig-zag diline differs from the square diline in that the bright spots are no longer opposite to each other but one row is shifted along by 0.4 nm (one unit cell) with respect to the other.

4.2.1.5 Waffle structure

When sample was further annealed, nanolines further faded away and a specific pattern was observed as shown in Figure 4-20. Waffle structure was observed that possibly

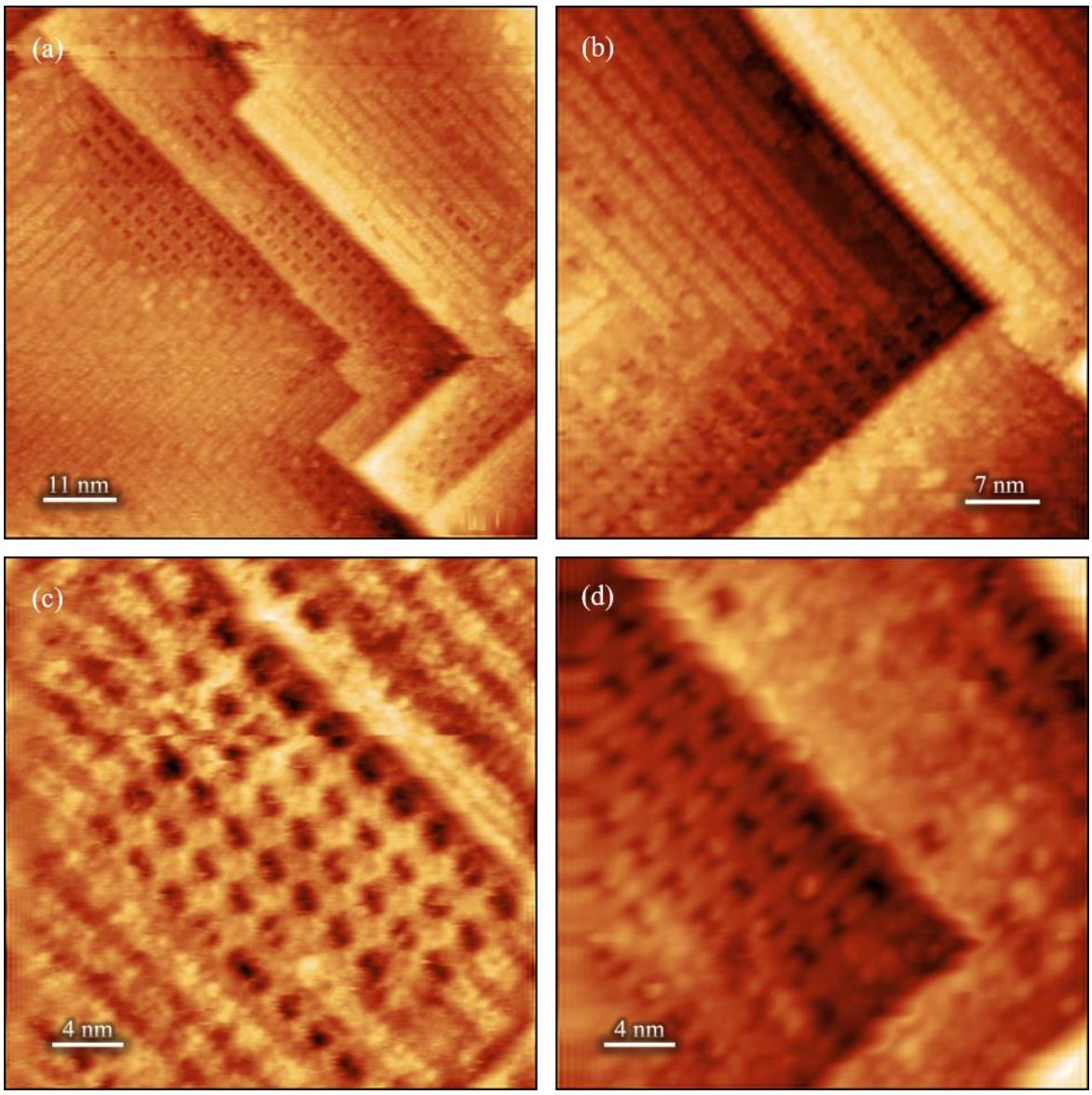


Figure 4-20: (a-d) $SrTiO_3$ (001) sputtered (0.5 keV, 2.5 µA, 10 min) and annealed (960 °C, 30 min); V_s = 2.37 V, I_t = 0.5 nA.

evolved from the rearrangement of dilines. The waffle structure is similar to the cross-linked (2 × 1) surface that forms on the TiO_2 surface [203–205].

4.2.1.6 Disappearance of nanostructures

When sample was annealed at 980 °C for 15 min, nanolines almost disappeared and wide terraces were observed as shown in Figure 4-21. As thermal cycle is varied, the nanolines completely disappeared and terraces were formed with sharp edges as shown in Figure 4-22. It was reported that reconstruction of these kind of terraces is c(4 × 2) [10].

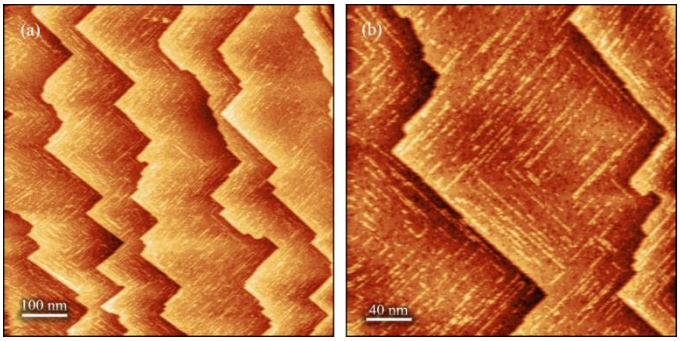


Figure 4-21: (a, b) $SrTiO_3$ (001) sputtered (0.5 keV, 2.5 µA, 10 min) and annealed (980 °C, 15 min); V_s = 2.0 V, I_t = 0.2 nA.

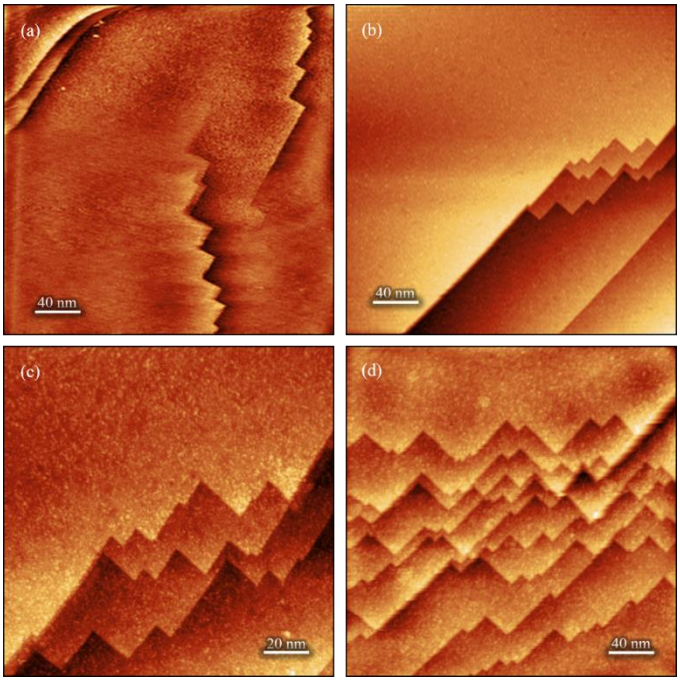


Figure 4-22: Sputtered and annealed $SrTiO_3$ (001) (0.5 keV, 2.5 µA, 10 min). (a) Annealed at 1100 °C for 30 min; V_s = 1.5 V, I_t = 0.2 nA. (b, c) Annealed at 1100 °C for 10 min; V_s = 2 V, I_t = 0.1 nA. (d) Annealed at 1100 °C for 30 min; V_s = 2 V, I_t = 0.2 nA.

4.2.2 $SrTiO_3$ (110)

$SrTiO_3$ (110) sample was sputtered (0.5 keV, 2.5 µA, 10 min) and then annealed at 900 °C for 1 h. The resultant surface is shown in Figure 4-23. The periodicity normal to the nanolines is (2.25 ± 0.05) nm which corresponds to (4 × 1) reconstructions [206,207].

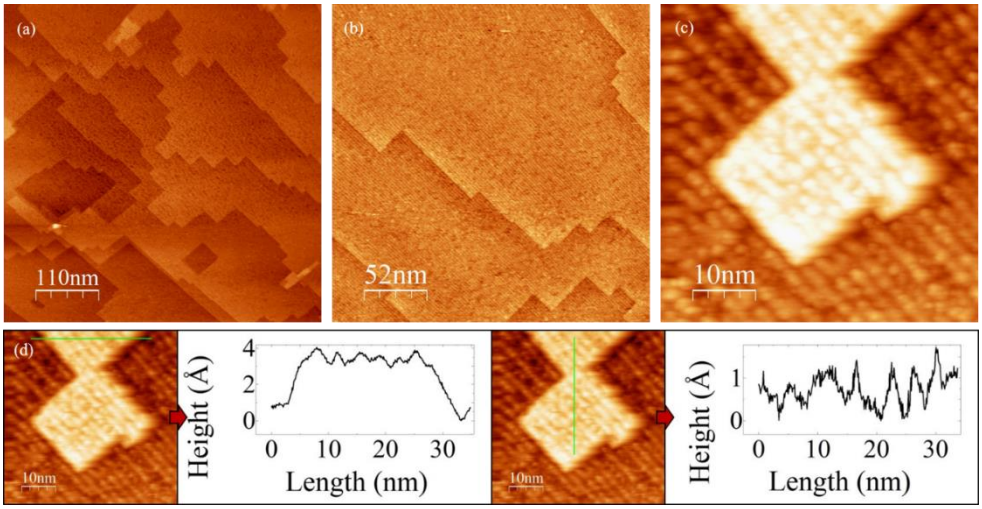


Figure 4-23: (a-c) $SrTiO_3$ (110) sputtered (0.5 keV, 2.5 µA, 10 min) and annealed (900 °C, 1 h); V_s = 1.5 V, I_t = 50 pA. (d) Horizontal and vertical lines and their respective profiles. The periodicity along the nanolines is 2.25 ± 0.05 nm which corresponds to (4 × 1) reconstruction.

4.2.3 $SrTiO_3$ (111)

$SrTiO_3$ (111) sample was sputtered (0.5 keV, 2.6 µA, 10 min) and then annealed at 900 °C for 1 h. The resulting STM image is shown in Figure 4-24. Two distinct reconstructions

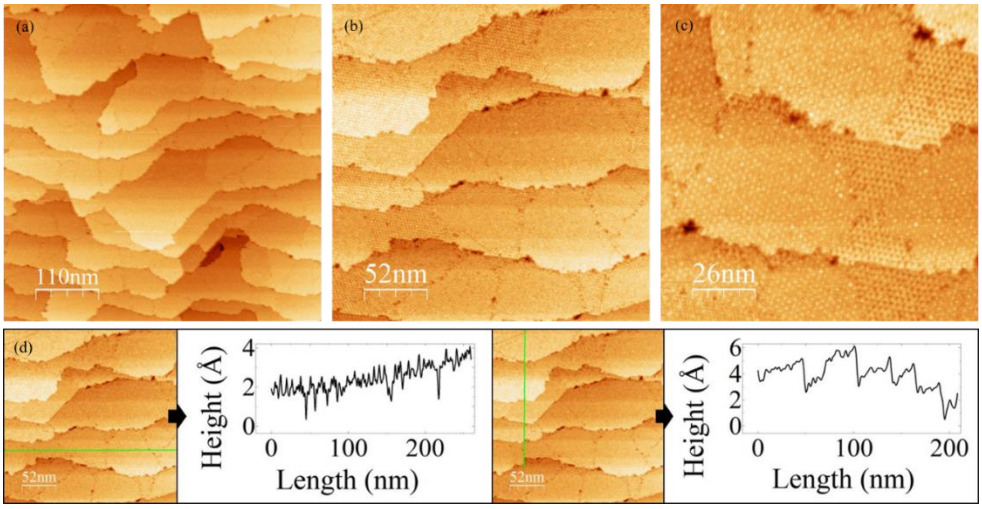


Figure 4-24: (a-c) $SrTiO_3$ (111)-(4 × 4)-(6 × 6) sputtered (0.5 keV, 2.6 µA, 10 min) and annealed (900 °C, 1 h); V_s = 0.92 V, I_t = 0.1 nA. (d) Horizontal and vertical lines and their respective profiles.

were observed. The periodicity of one region was (2.21 ± 0.01) nm which corresponds to (4 × 4) reconstruction. The periodicity of second region was (3.31 ± 0.02) nm which corresponds to (6 × 6) reconstruction. In between there is a region rotated at 30º with respect to (4 × 4) reconstruction with periodicity (2.85 ± 0.05) nm. This region could possibly be (3√3 × 3√3)R30° reconstruction.

4.3 Conclusions

$SrTiO_3$ is capable of producing a multitude of surface reconstructions such as (2 × 1), (2 × 2), (√5 × √5) R26.6°, and c(4 × 2) on (001) termination; (4 × 1) on (110) termination; and (4 × 4) and (6 × 6) on (111) termination. When surface of $SrTiO_3$ (001) is subjected to Ar ion sputtering followed by UHV annealing at different temperatures, nanostructures, straight terraces and terraces with sawtooth like step edges are generated [200]. The thermal cycles and sputtering parameters have significant effect on the structure of $SrTiO_3$ (001) surface. When $SrTiO_3$ surface is sputtered, the surface composition changes that can be because of preferential etching of Sr by Ar^+ ions sputtering in Ti rich surface. During annealing, diffusion rate increases resulting in various reconstructions and nanostructures. The non-stoichiometry of the surface caused by Ar ion sputtering leads to the nanocrystalline growth of either SrO or TiO_x rich non-perovskite nanostructures on the surface of $SrTiO_3$ (001) [200]. Self-assembled nanostructures also appeared on $SrTiO_3$ surface such as nanolines, nanodots and waffle structure. These nanostructures can be investigated for novel electronic devices such as single electron transistors and quantum dot lasers.

Chapter 5:

Ni Nanocrystals

5.1 Background

5.1.1 Overview

Ni is one of the fcc metals and unlike its family members, the difference in surface energy values between the second most dense plane {001} and the third most dense plane {110} is very low. In some cases, it is even predicted that {110} plane has lower surface energy value than that of {001} [208]. The available literature on Ni also shows contrasting results. For example, Mykura [209] reported that {001} planes have the lowest surface energy followed by {111} planes while Barsotti et al. [210] reported the reverse. Similarly, Hong et al. [211] reported that {210} planes had the lowest surface energy which are relatively high surface energy planes in fcc metals [212]. Other high index planes such as {012}, {013}, {135} and {138} were also observed in Equilibrium Crystal Shape (ECS) of Ni [213]. One of the reasons that various ECS of Ni were observed is that ECS can be significantly altered by impurities, adsorption, and surface segregation [212,214]. These phenomena are expedited by high surface energy. As Ni has relatively high surface energy, it is hard to get a standard ECS for Ni nanocrystals. It gets even more complex when Ni nanocrystals are grown on oxide substrates as epitaxial relationships can significantly alter the ECS of nanocrystals.

Perovskite oxides, such as $SrTiO_3$, have been commonly used as substrates to investigate the ECS of various metals. It has been shown that Ni forms truncated octahedron on $SrTiO_3$ (001) substrate with {111} and {001} planes [74]. As epitaxial relationships are very crucial to define the ECS of nanocrystals, it would be interesting to investigate the ECS of Ni nanocrystals on all three low-index terminations of $SrTiO_3$, i.e., {001}, {110} and {111}. It would help us answer whether ECS of Ni nanocrystals varies or remains constant with the change in the substrate termination. It would also help us answer whether

epitaxial relationships $Ni_{(001)}$ || $SrTiO_{3(001)}$, $Ni_{(110)}$ || $SrTiO_{3(110)}$ and $Ni_{(111)}$ || $SrTiO_{3(111)}$ are possible. A reading of this chapter will help further understanding of epitaxial relationships of Ni on $SrTiO_3$ and resulting ECS of Ni nanocrystals.

5.1.2 Experimental details

$SrTiO_3$ substrates were supplied by PI-KEM Ltd, UK. Ni rods were supplied by Alfa and are 99.997% pure. The substrates were sonicate-cleaned in methanol and acetone. The substrates were then transferred into JEOL JSTM-4500xt system operating at 10^{-8} Pa. The substrates were degassed through resistive heating. The substrates were then sputtered/annealed to generate terraces and Ni was deposited using e-beam evaporator on substrates preheated at 320 °C. The substrates were cooled to room temperature after deposition and samples were imaged to observe morphology of as-deposited nanocrystals. Then multiple post-annealings were carried out by applying various thermal cycles to observe variation in morphology of Ni nanocrystals with temperature and time. When the nanocrystals achieved nearly equilibrium morphology, their dimensions were measured and the equilibrium shape was plotted using 'Wulffman' software. The surface energy ratios obtained were compared with the literature. Any peculiar results obtained in this study were attempted to be explained based on established theory and experimental observations.

5.2 Results

5.2.1 Ni on $SrTiO_3$ (001)-(2 × 1)

STM images of $SrTiO_3$ (001) sample annealed at 900 ºC for 1 h are shown in Figure 5-1. The literature suggests that reconstruction of these kind of terraces is (2 × 1) [200]. Ni (1 ML) was then deposited onto sample using e-beam evaporator. The system was post-annealed for four times: (200 ºC, 1 h), (320 ºC, 10 min), (320 ºC, 6 h) and (420 ºC, 6 h).

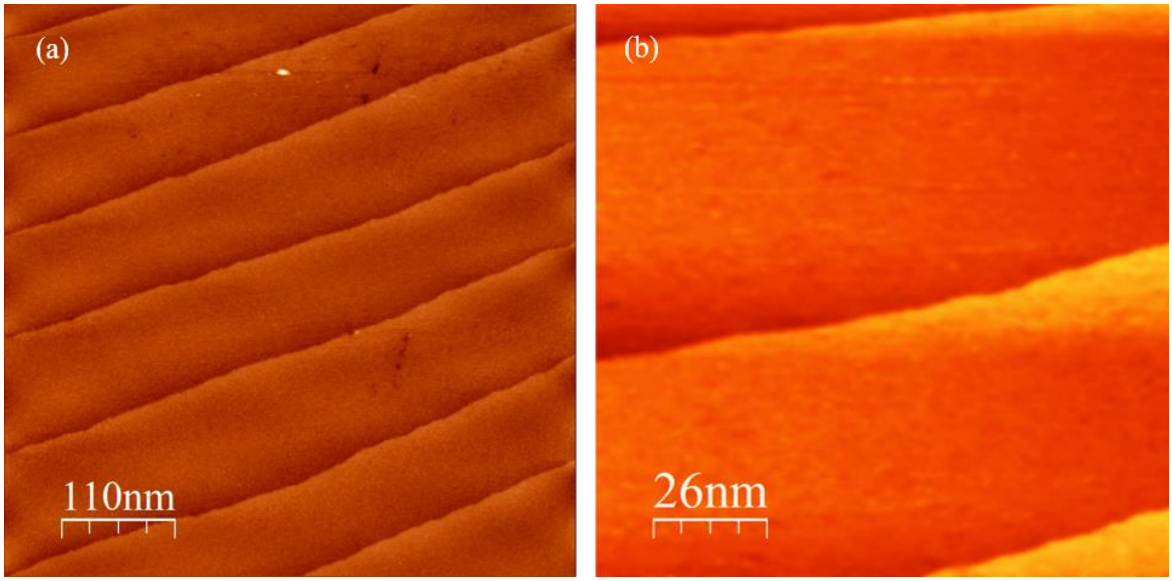


Figure 5-1: (a,b) $SrTiO_3$ (001)-(2 × 1) substrate that was used for Ni deposition. The sample was annealed at 900 °C for 1 h; V_s = 2.0 V, I_t = 0.1 nA.

The resultant structure is shown in Figure 5-2.

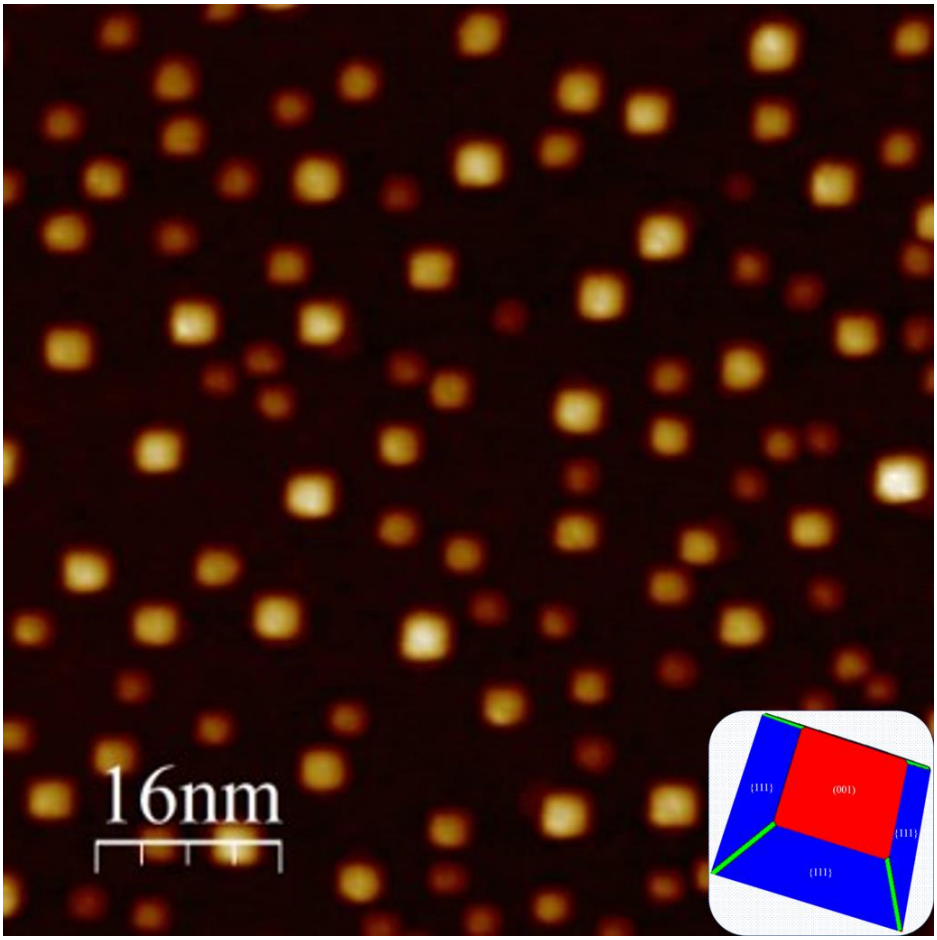


Figure 5-2: (a) Ni on $SrTiO_3$ (001); V_s = 2 V, I_t = 50 pA. The inset shows the geometry of truncated pyramid with one {001} top facet and four {111} side facets.

Ni formed truncated pyramid shaped nanocrystals with a square base. Ni formed truncated pyramid shaped nanocrystals with a square base. The measured angle in the current study is also ~ 54° (and none of the angles is 90°) indicating that nickel formed fcc structure. The 3D view of nanocrystals is shown in Figure 5-3 (a).

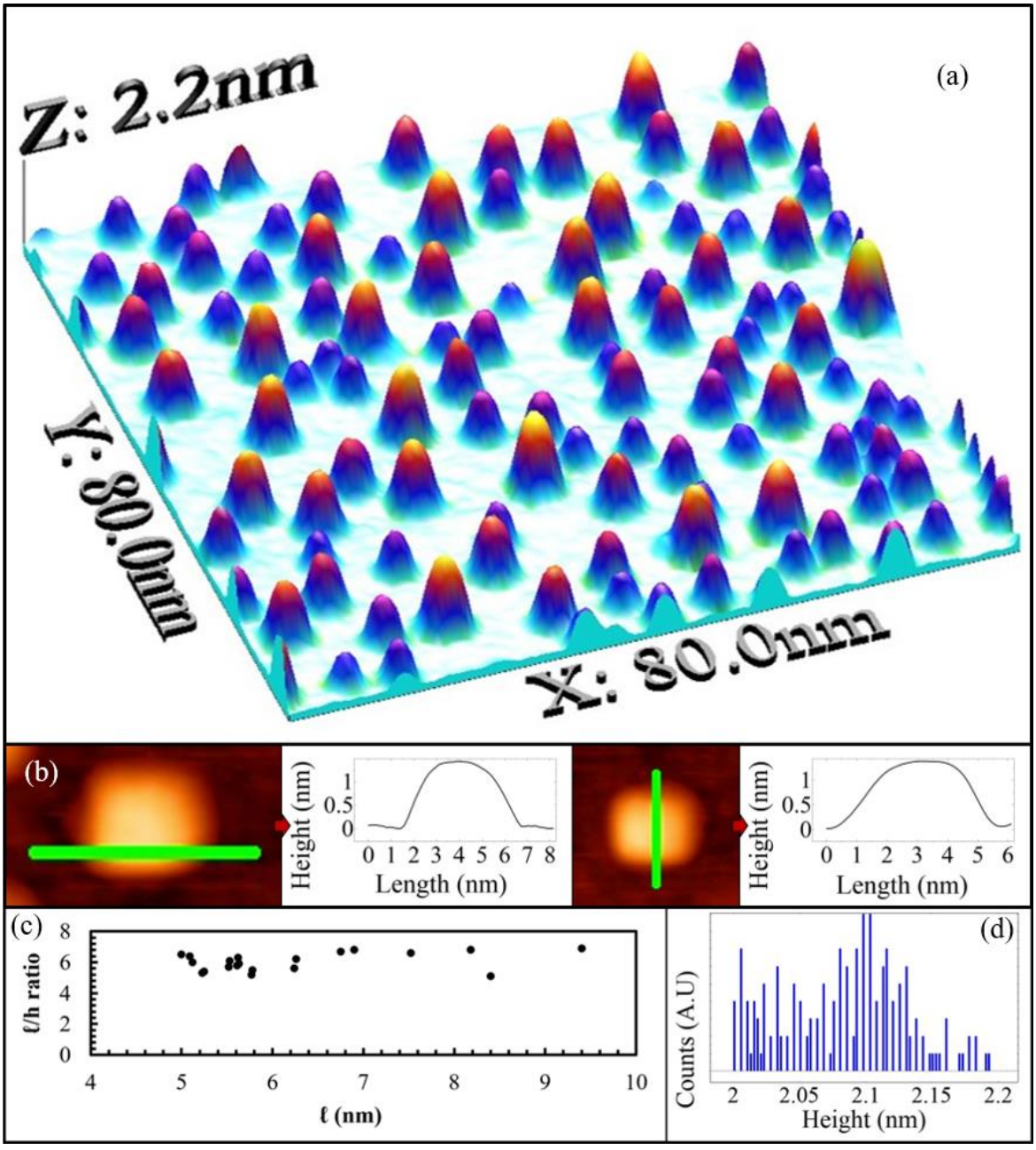


Figure 5-3: (a) 3D view of Ni on $SrTiO_3$ (001). (b) Horizontal and vertical surface profiles of a nanocrystal. (c) ℓ/h ratio of 20 nanocrystals. (d) Height distribution.

The surface profiles (Figure 5-3 (b)) of a nanocrystal show that base length is around 6 nm while height is around 1.2 nm. The average height of studied nanocrystals was 0.78 ± 0.04

nm. The ℓ/h ratios (Figure 5-3(c)) of about 20 nanocrystals were calculated. The ℓ/h ratio is nearly constant that suggests that most of the nanocrystals have achieved their equilibrium shape.

To calculate the adhesion energy of produced nanocrystals, length ℓ was defined as the distance from the center of {111} plane to the center of {111} plane opposite to selected {111} plane. In the observed nanocrystals, there are total 6 facets; a {001} top facet, three {111} side facets, and a {001} interface with the $SrTiO_3$ (001) substrate. The total energy of the system (E_1) as shown in Figure 5-4 (a) is given by,

$$E_1 = \gamma_{Ni(001)}A_{(001)} + \gamma_{Ni(111)}A_{(111)} + \gamma_i A_i + \gamma_{S(001)}A_{S1} \quad \textbf{(8)}$$

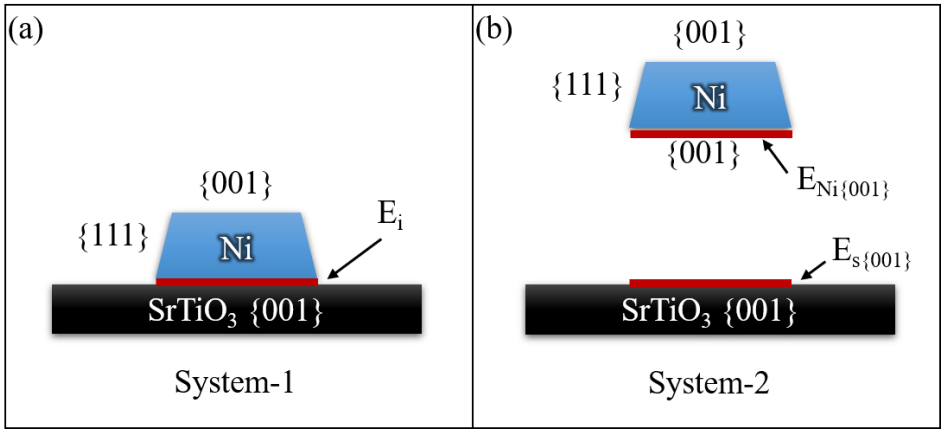


Figure 5-4: Model of the free energy of adhesion shown by the process of separating Ni truncated octahedron from substrate (side view). (a) Before separation, the interface area between Ni and substrate is marked in red. (b) After separation, the areas of the same size are created on the Ni (001) base facet and substrate, marked in red.

Where $\gamma_{Ni(111)}$ and $\gamma_{Ni(001)}$ are surface energies of Ni (111) and (001) planes, $A_{(001)}$ is the total area of Ni (001) top facet, $A_{(111)}$ is the total area of three Ni (111) side facets, γ_i is surface energy of interface, A_i is interfacial area, $\gamma_{S(001)}$ is surface energy of substrate $SrTiO_3$ (001), and A_{S1} is the surface area of the substrate excluding the area of Ni-substrate

interface. When separating Ni from substrate, it was assumed that the shape of Ni truncated octahedron does not change. The base (001) surface with an area of A_b is created on the Ni truncated octahedron. As shown in Figure 5-4 (b), the total energy (E_2) in system 2 when Ni and substrate are apart is,

$$E_2 = \gamma_{Ni(001)}A_{(001)} + \gamma_{Ni(001)}A_b + \gamma_{Ni(111)}A_{(111)} + \gamma_{S(001)}A_{S2} \quad \textbf{(9)}$$

The energy change between systems 1 and 2 is,

$$\Delta E = E_2 - E_1$$

$$\Delta E = \gamma_{Ni(001)}A_b - \gamma_i A_i + \gamma_{S(001)}(A_{S2} - A_{S1}) \quad \textbf{(10)}$$

Where,

$$A_{S2} - A_{S1} = A_b = A_i \quad \textbf{(11)}$$

From eq. (11), eq. (10) becomes,

$$\Delta E = \gamma_{\mathrm{Ni}(111)}A_b - \gamma_i A_i + \gamma_{S(001)}A_i \quad \textbf{(12)}$$

The energy change per unit area, i.e., adhesion energy (W_{adh}) can be obtained by dividing eq. (12) by Ai on both sides:

$$W_{adh} = \gamma_{\mathrm{Ni}(001)} - \{\gamma_i - \gamma_{S(001)}\} \quad \textbf{(13)}$$

The general surface energy r^* defined by Winterbottom [33] is given by,

$$\gamma^* = \gamma_i - \gamma_{S(001)} \quad \textbf{(14)}$$

From eq. (14), eq. (13) becomes,

$$W_{adh} = \gamma_{\mathrm{Ni}(001)} - \gamma^* \quad \textbf{(15)}$$

From the modified Wulff construction [33], r^* is given by,

$$\gamma^* = \sqrt{2}\frac{h}{\ell}\{\sqrt{3}\gamma_{(111)} - \gamma_{(001)}\} - \gamma_{(001)} \quad \textbf{(16)}$$

From experiment, h/ℓ = 0.848 ± 0.085, and $\gamma_{(001)} = 2.426\,J/m^2$, $\gamma_{(111)} = 2.011\,J/m^2$ from theoretical values calculated by Vitos et al. [208]. By putting values,

$$\gamma^* = -1.158 \pm 0.128\,J/m^2 \quad \textbf{(17)}$$

From eq. (17), eq. (16) becomes,

$$W_{adh} = 3.584 \pm 0.149\,J/m^2 \quad \textbf{(18)}$$

Sun et al. grew Ni nanocrystals on $SrTiO_3$ (001) and reported the adhesion energy of the grown nanocrystals to be (3.28 ± 0.17) J/m^2 [74].

5.2.2 Ni on $SrTiO_3$ (001)-Nanolines

STM images of $SrTiO_3$ (001) sample sputtered (0.5 keV, 3.1 µA, 10 min) and annealed at 920 ºC for 1 h are shown in Figure 5-5. The surface got covered in nanolines. Ni was then deposited onto sample using e-beam evaporator. At low coverage, Ni formed irregular-shaped clusters as shown in Figure 5-6 - Figure 5-8. After third post-anneal, nanocrystals started to grew as shown in Figure 5-9. Image of the same sample on the next day is shown in Figure 5-10. Ni formed truncated pyramid shaped nanocrystals with a square base. The 3D view of nanocrystals is shown in Figure 5-11 (a). The surface profiles (Figure 5-11 (b)) of a nanocrystal show that base length is around 6 nm while height is around 1.4 nm. The average height of studied nanocrystals was 0.81 ± 0.05 nm.

From experiment, h/ℓ = 0.816 ± 0.081, and $\gamma_{(001)} = 2.426\,J/m^2$, $\gamma_{(111)} = 2.011\,J/m^2$ from theoretical values calculated by Vitos et al. [208]. By putting values,

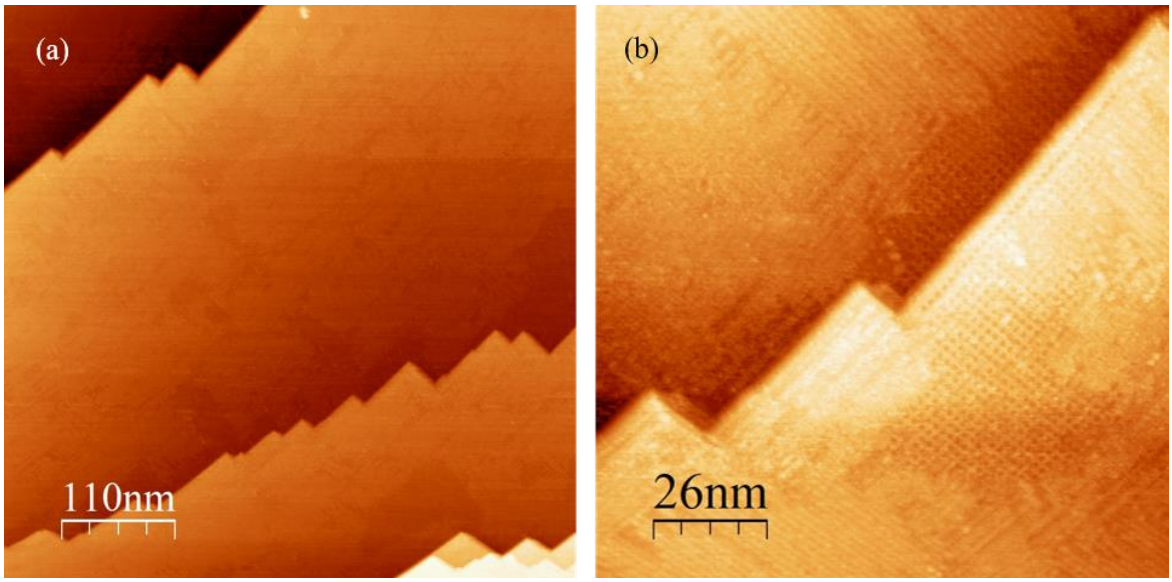


Figure 5-5: (a,b) $SrTiO_3$ (001)-Nanolines. The sample was annealed at 920 °C for 1 h; V_s = 1.5 V, I_t = 0.1 nA. The sample was used as substrate for Ni deposition.

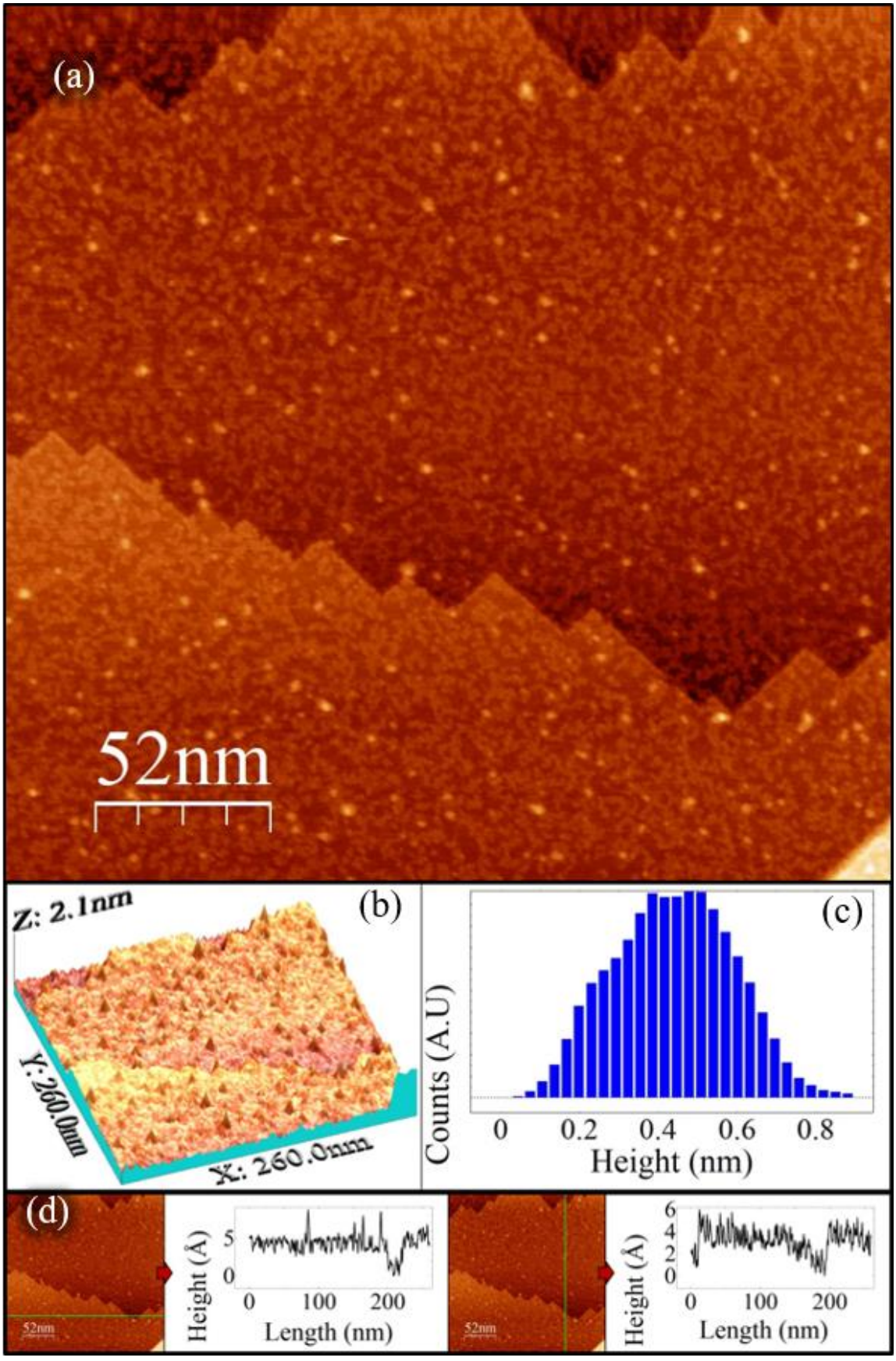


Figure 5-6: (a) Ni on $SrTiO_3$ (001); V_s = 1.72 V, I_t = 50 pA. The system was post-annealed twice after the deposition: (320 °C, 1 h), (320 °C, 12 h).

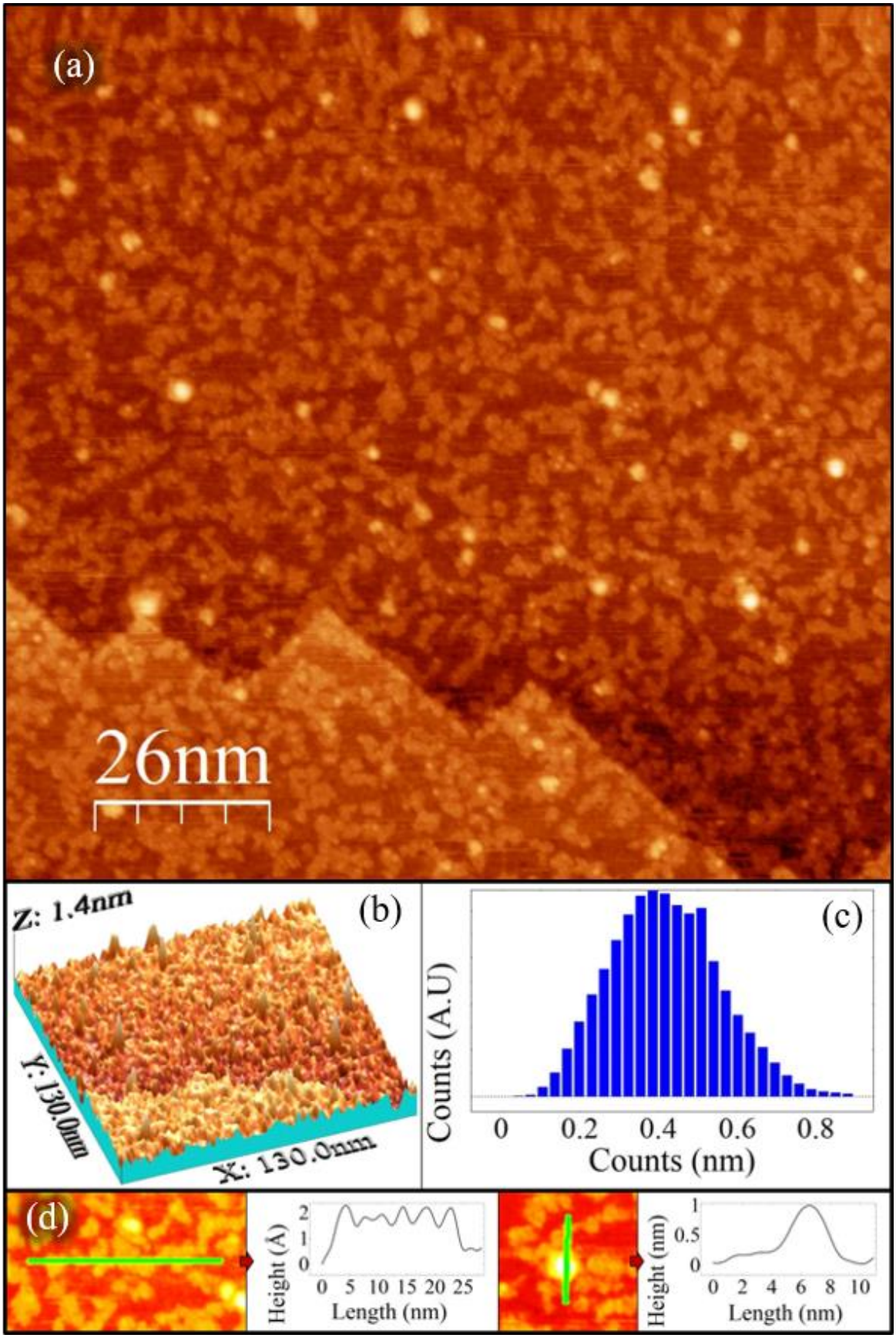


Figure 5-7: (a) Ni on $SrTiO_3$ (001); V_s = 1.72 V, I_t = 50 pA. The system was post-annealed twice after deposition: (320 °C, 1 h), (320 °C, 12 h).

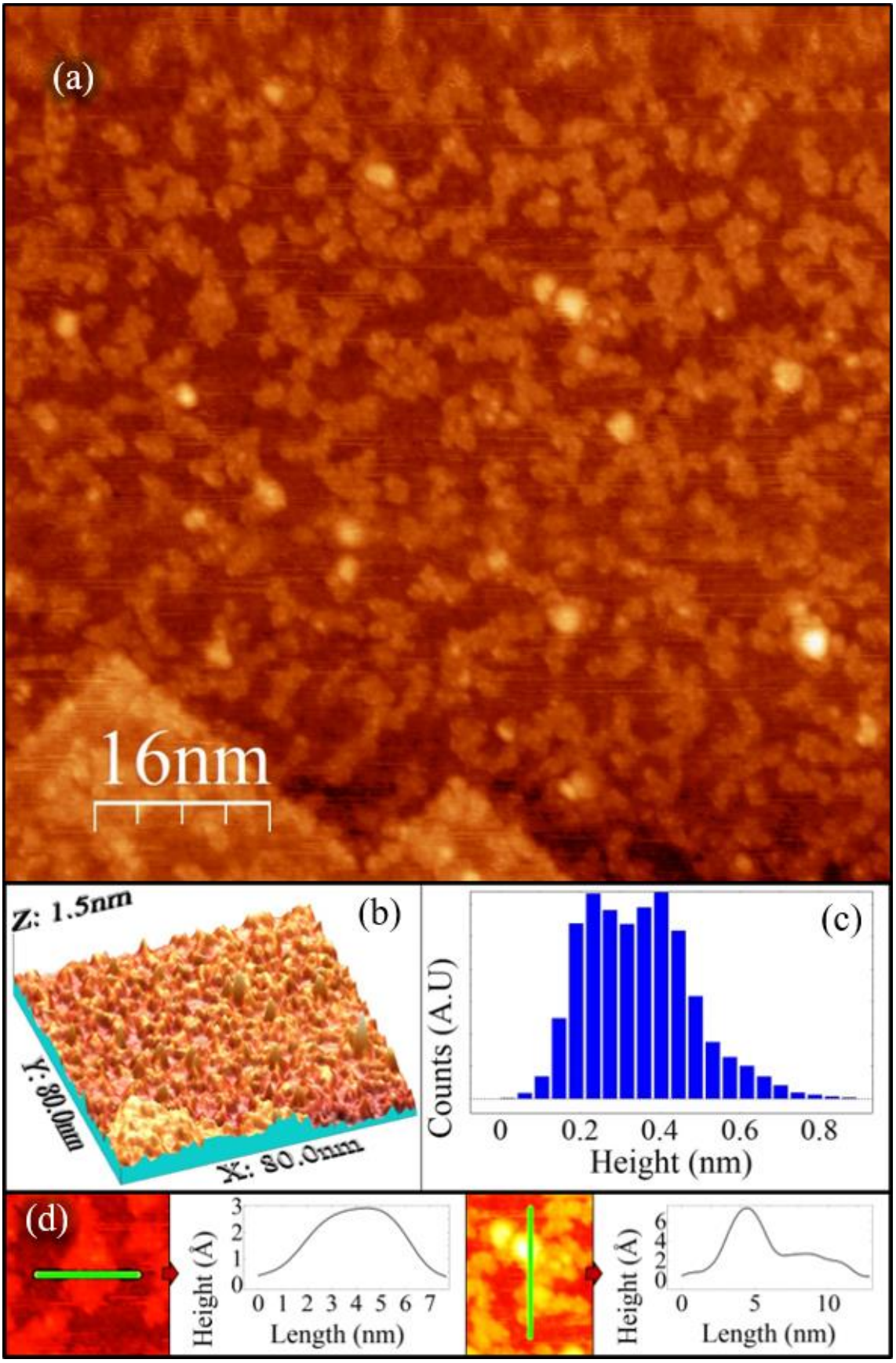


Figure 5-8: (a) Ni on $SrTiO_3$ (001); V_s = 1.72 V, I_t = 50 pA. The system was post-annealed twice after deposition: (320 °C, 1 h), (320 °C, 12 h).

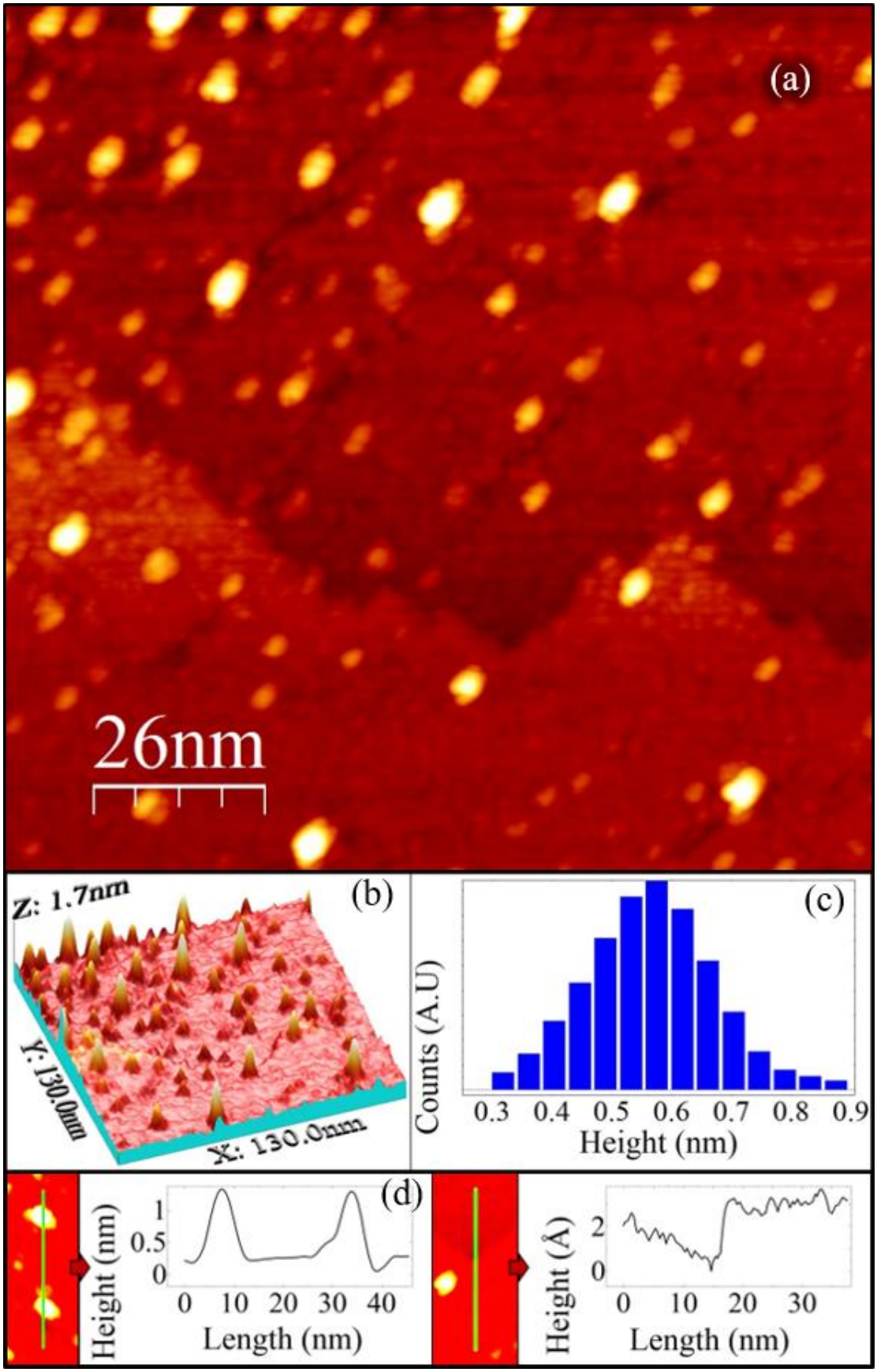


Figure 5-9: (a) Ni on $SrTiO_3$ (001); V_s = 1.72 V, I_t = 50 pA. The system was post-annealed thrice: (320 °C, 1 h), (320 °C, 12 h), (520 °C, 10 min).

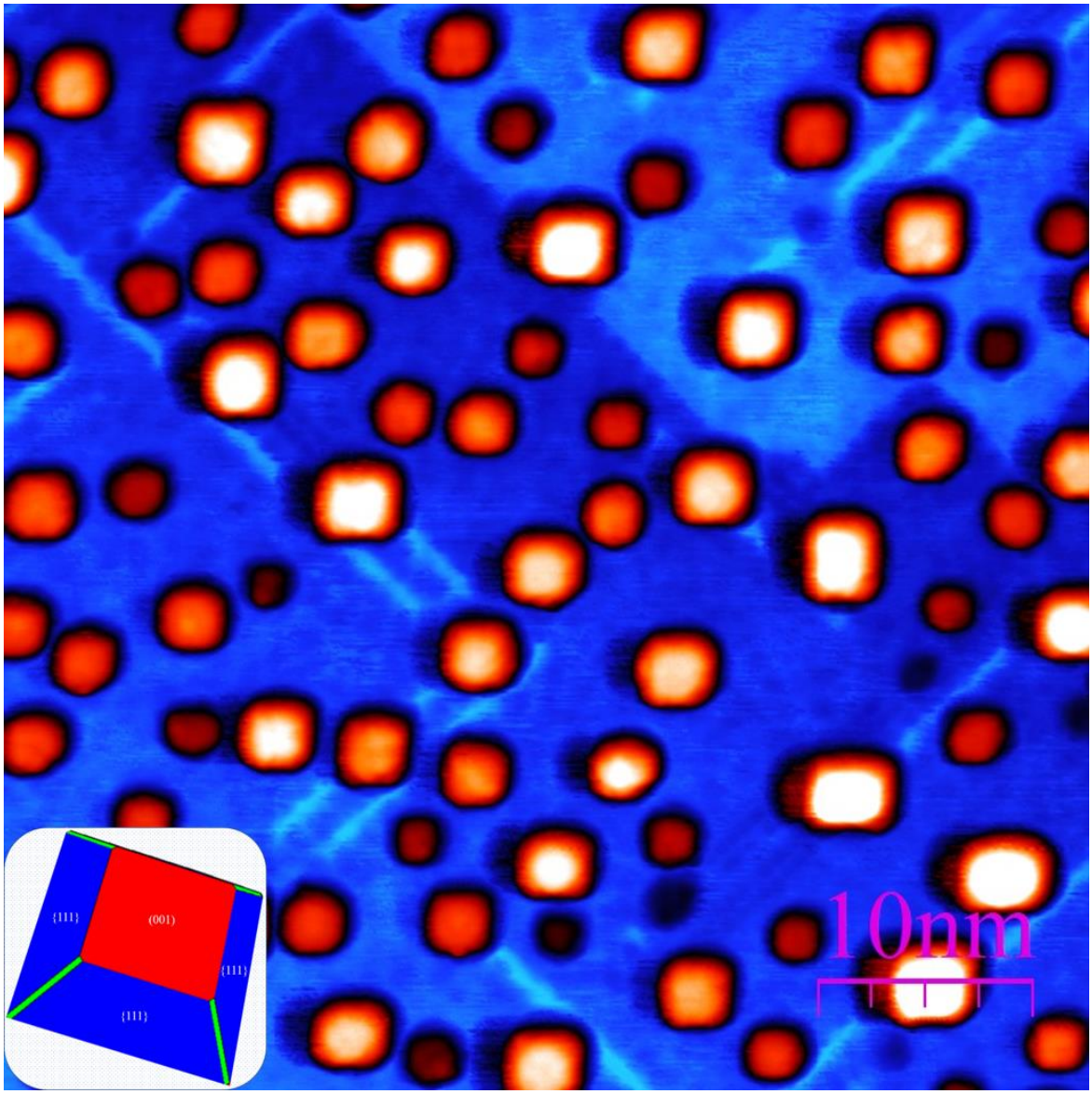


Figure 5-10: Ni on $SrTiO_3$ (001); V_s = 1.50 V, I_t = 50 pA. The system was post-annealed thrice: (320 °C, 1 h), (320 °C, 12 h), (520 °C, 10 min). The inset shows the schematic of truncated pyramid.

$$\gamma^* = -1.158 \pm 0.104 \ J/m^2 \quad \textbf{(19)}$$

$$W_{adh} = 3.601 \pm 0.126 \, J/m^2 \quad \textbf{(20)}$$

5.2.3 Ni on $SrTiO_3$ (110)

$SrTiO_3$ (110) sample was sputtered (0.5 keV, 2.5 µA, 10 min) and then annealed at 900 °C

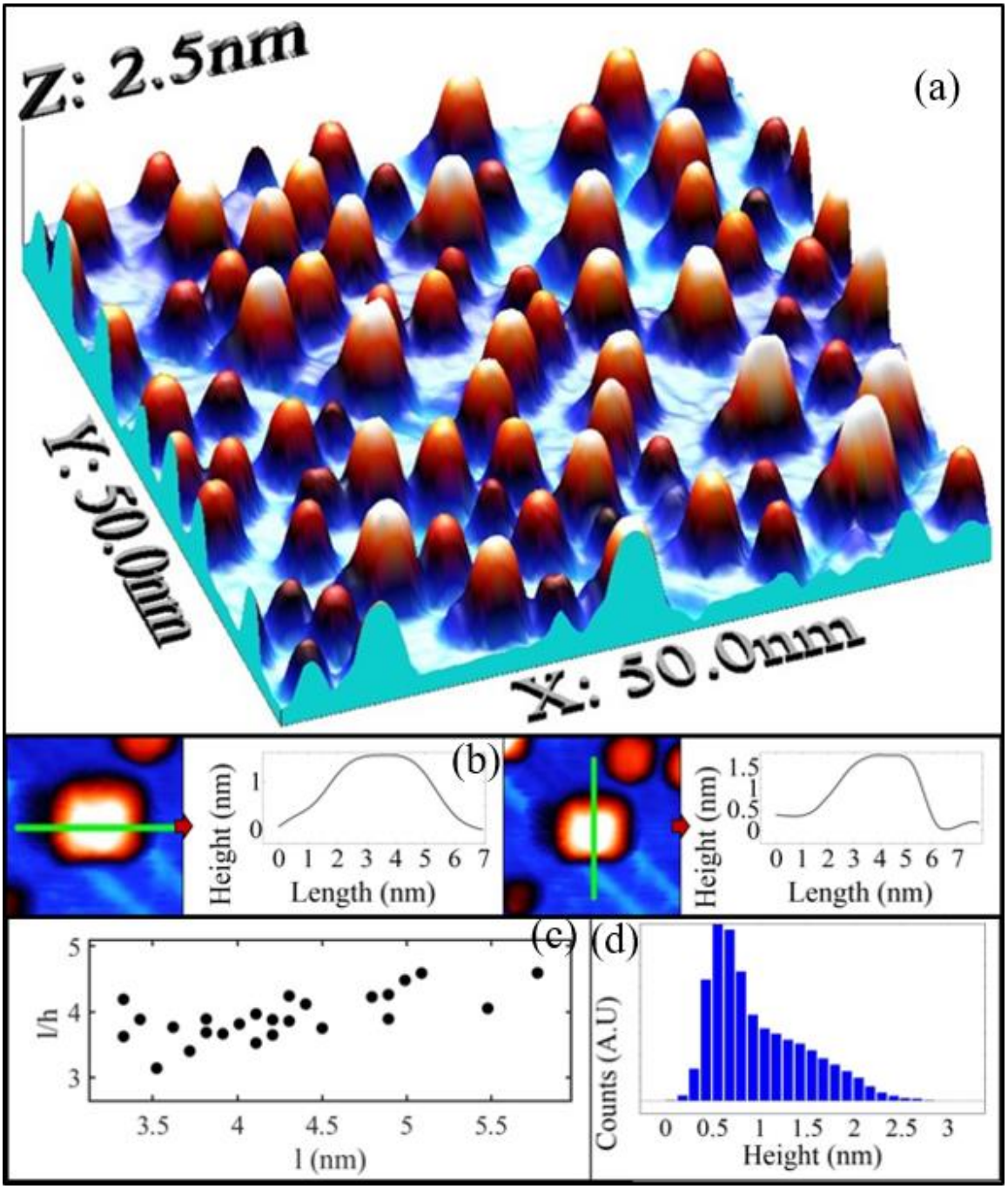


Figure 5-11: (a) 3d view of 1 ML Ni on $SrTiO_3$ (001); V_s = 1.72 V, I_t = 50 pA. (b) Horizontal and vertical lines and their respective profiles. (c) The length-to-height (ℓ/h) ratio of 25 nanocrystals (3.896 ± 0.352). (d) Height distribution.

for 1 h. The resultant surface is shown in Figure 5-12. Wide terraces with periodicity (2.25 ± 0.05) nm which corresponds to (4 × 1) reconstructions. Ni was deposited onto the sample using e-beam evaporator. The system was post-annealed twice: (320 ºC, 1 h), (320 ºC, 6 h). The resultant structure is shown in Figure 5-13. Ni formed rectangular

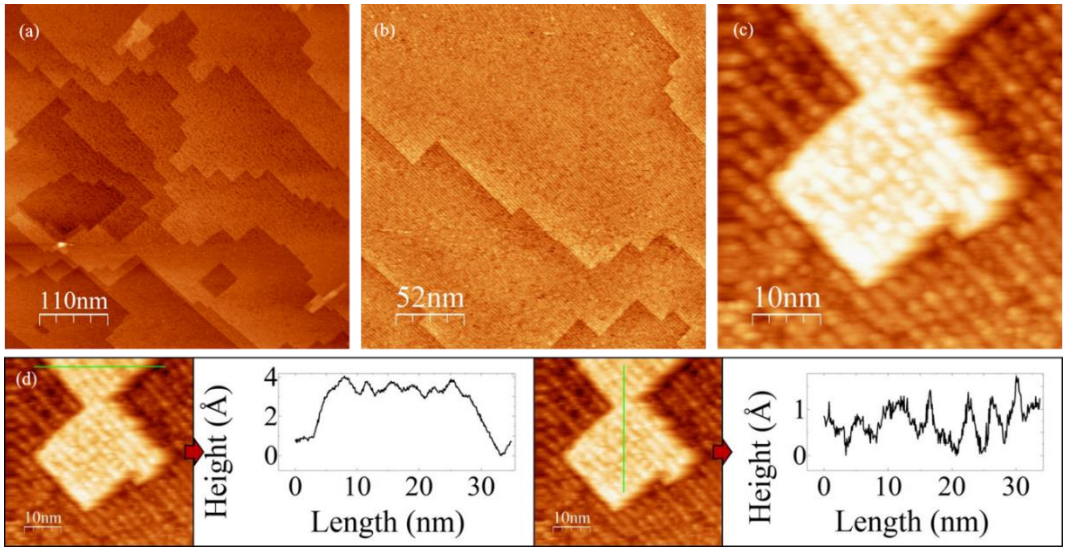


Figure 5-12: (a-c) $SrTiO_3$ (110) sputtered (0.5 keV, 2.5 µA, 10 min) and annealed (900 °C, 1 h); V_s = 1.5 V, I_t = 50 pA. (d) Horizontal and vertical lines and their respective profiles.

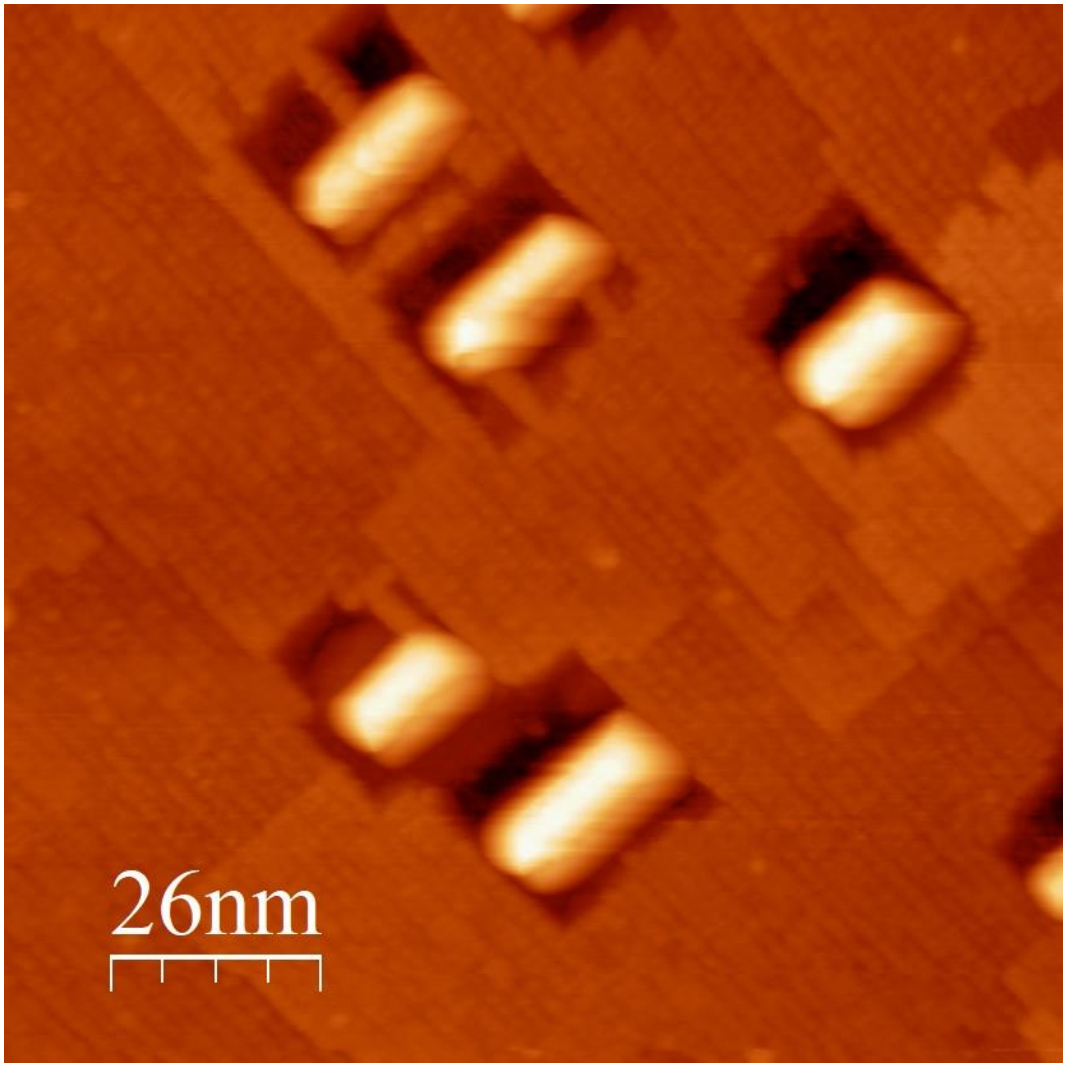


Figure 5-13: Ni (0.2 ML) on $SrTiO_3$ (110); V_s = 0.50 V, I_t = 50 pA.

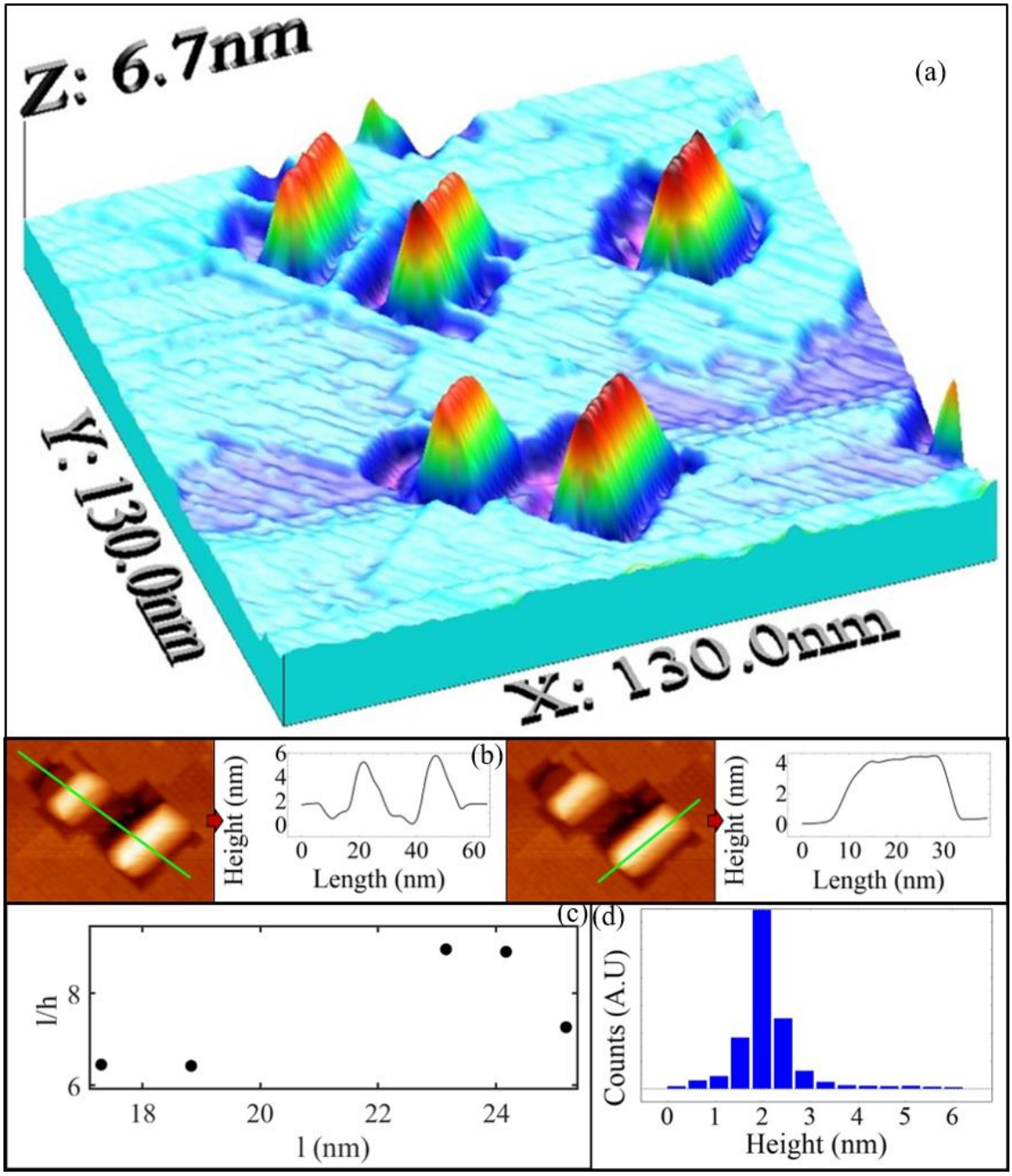


Figure 5-14: (a) 3d view of Ni (0.2 ML) on $SrTiO_3$ (110). (b) Lateral and longitudinal lines and their respective profiles. (c) The length-to-height (ℓ/h) ratio of 5 nanocrystals (7.6 ± 1.13). (d) Height distribution.

nanocrystals aligned at right angle to underlying nanolines. The 3D view of nanocrystals is shown in Figure 5-14 (a). It can be observed that the region around the nanocrystals is trenched. It can be caused by the nanocrystals who would have to restructure the localized region to achieve epitaxy. The surface profiles (Figure 5-14 (b)) of a nanocrystal show that

the base length is around 25 nm while height is around 4 nm. The average height of nanocrystals was around 2.15 ± 0.06 nm while maximum height recorded was 6.72 ± 0.13 nm. To investigate the Wulff construction, Wulffman software was used. The parameters used for Wulffman simulation are listed in Table 5-1 and resulted Wulff constructions are

Table 5-1: Parameters used to generate Wulff construction of Ni on $SrTiO_3$ (110) after second post-annealing.

Parameter	**Values**
Crystal system	Cubic
Point group	$m\bar{3}m$
Plane-1	Miller indices = {111}
	Surface energy: $\gamma_{111} = 0.77\ J/m^2$
	Plane color: Red
Plane-2	Miller indices = {001}
	Surface energy: $\gamma_{001} = 0.86\ J/m^2$
	Plane color: Blue
Plane-3	Miller indices = {110}
	Surface energy: $\gamma_{110} = 0.87\ J/m^2$
	Plane color: Green
Crystal shape	Truncated octahedron
Area	9.932 nm^2
Volume	2.679 nm^3
Facets	26
Edges	72
Vertices	48

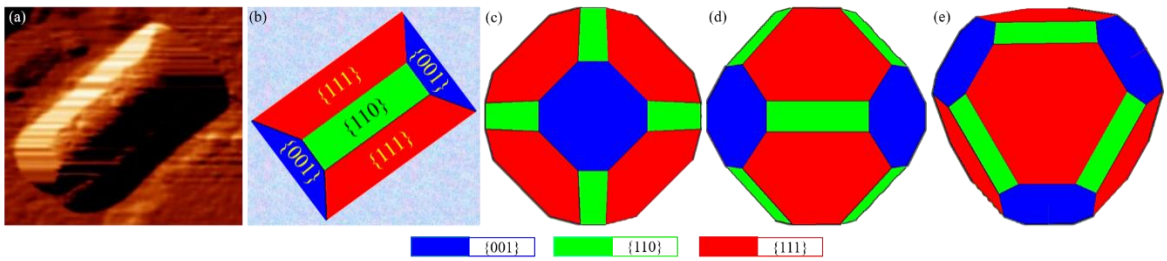


Figure 5-15: Wulffman simulations of equilibrium crystal shapes (ECS) of Ni nanocrystals on $SrTiO_3$ (110): (a) STM image of nanocrystal. The region of the ECS similar to that obtained in the experiment is extracted and shown in (b). The complete equilibrium crystal shape is also shown with (c) {001} as top facet, (d) {110} as top facet and (e) {111} as top facet.

shown in Figure 5-15. The surface energy values were changed until the edge ratios of nanocrystals produced were achieved. The surface energy ratios obtained from the experiment are: $\gamma_{001}/\gamma_{111} = 1.117$, $\gamma_{110}/\gamma_{111} = 1.130$, $\gamma_{001}/\gamma_{110} = 0.989$. The surface energy ratios by Vitos et al. are: $\gamma_{001}/\gamma_{111} = 1.206$, $\gamma_{110}/\gamma_{111} = 1.178$, $\gamma_{001}/\gamma_{110} = 1.024$. The $\gamma_{001}/\gamma_{111}$, $\gamma_{110}/\gamma_{111}$, and $\gamma_{001}/\gamma_{110}$ ratios are -7.4%, -4.1%, and -3.5% different from the energy ratios predicted by Vitos et al. [208].

To calculate the adhesion energy of produced nanocrystals, the length ℓ is defined as the distance from the centers of opposite {001} planes. The ℓ/h ratio is not constant that shows that all the nanocrystals are not in the equilibrium shape. From the modified Wulff construction [33], r^* is given by,

$$\gamma_{Hut}^{*} = \frac{\sqrt{3}\frac{\ell}{h}\gamma_{111} - 4\gamma_{001}}{2\sqrt{2} - \sqrt{2}\frac{\ell}{h}} \qquad \textbf{(21)}$$

From experiment, $h/\ell = 0.150 \pm 0.008$, and $\gamma_{(001)} = 2.426\,J/m^2$, $\gamma_{(111)} = 2.011\,J/m^2$ from theoretical values calculated by Vitos et al. [208]. By putting values,

$$\gamma^* = -2.049 \pm 0.080\, J/m^2 \quad \textbf{(22)}$$

$$W_{adh} = 4.475 \pm 0.097\, J/m^2 \quad \textbf{(23)}$$

Ni was deposited for one more minute on the same substrate and system was post-annealed twice: (320 ºC, 1 h), (320 ºC, 6 h). The resultant structure is shown in Figure 5-16. The

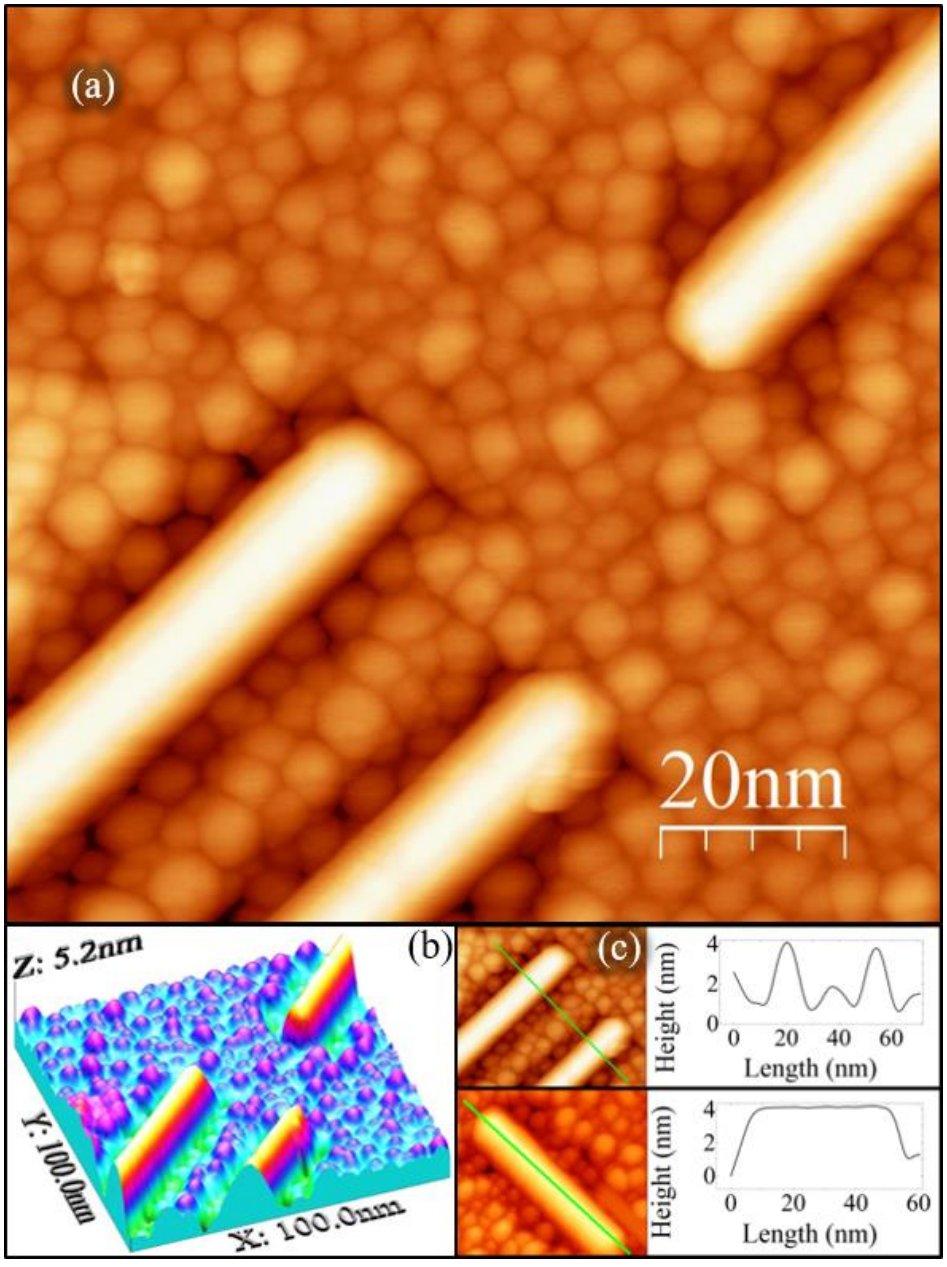


Figure 5-16: (a) Ni on $SrTiO_3$ (110); V_s = 1.0 V, I_t = 50 pA. (b) 3D view. (c) Lateral and longitudinal lines and their respective profiles.

nanocrystals started to nucleate around round Ni clusters. The length of a nanocrystal (Figure 5-16 (c)) is approaching 60 nm. The system was post-annealed for the third time and resultant structure is shown in Figure 5-17. The nanocrystals grew themselves at the

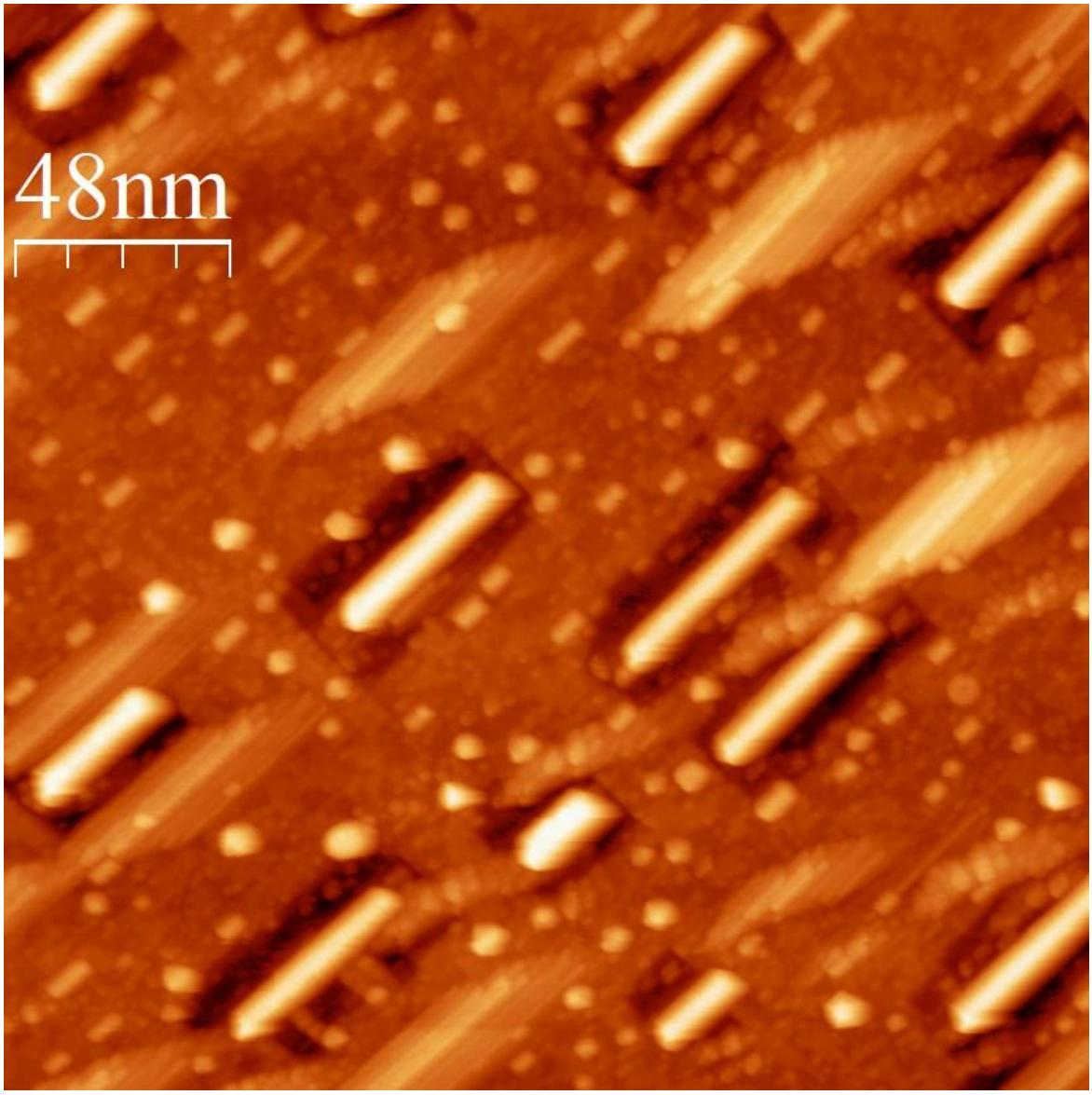


Figure 5-17: Ni (0.3 ML) on $SrTiO_3$ (110); V_s = 1.0 V, I_t = 50 pA.

expense of round Ni deposition. Some round particles are still present at the surface. A closer look at the round particles revealed that these particles have taken the shape of icosahedron as shown in Figure 5-18.

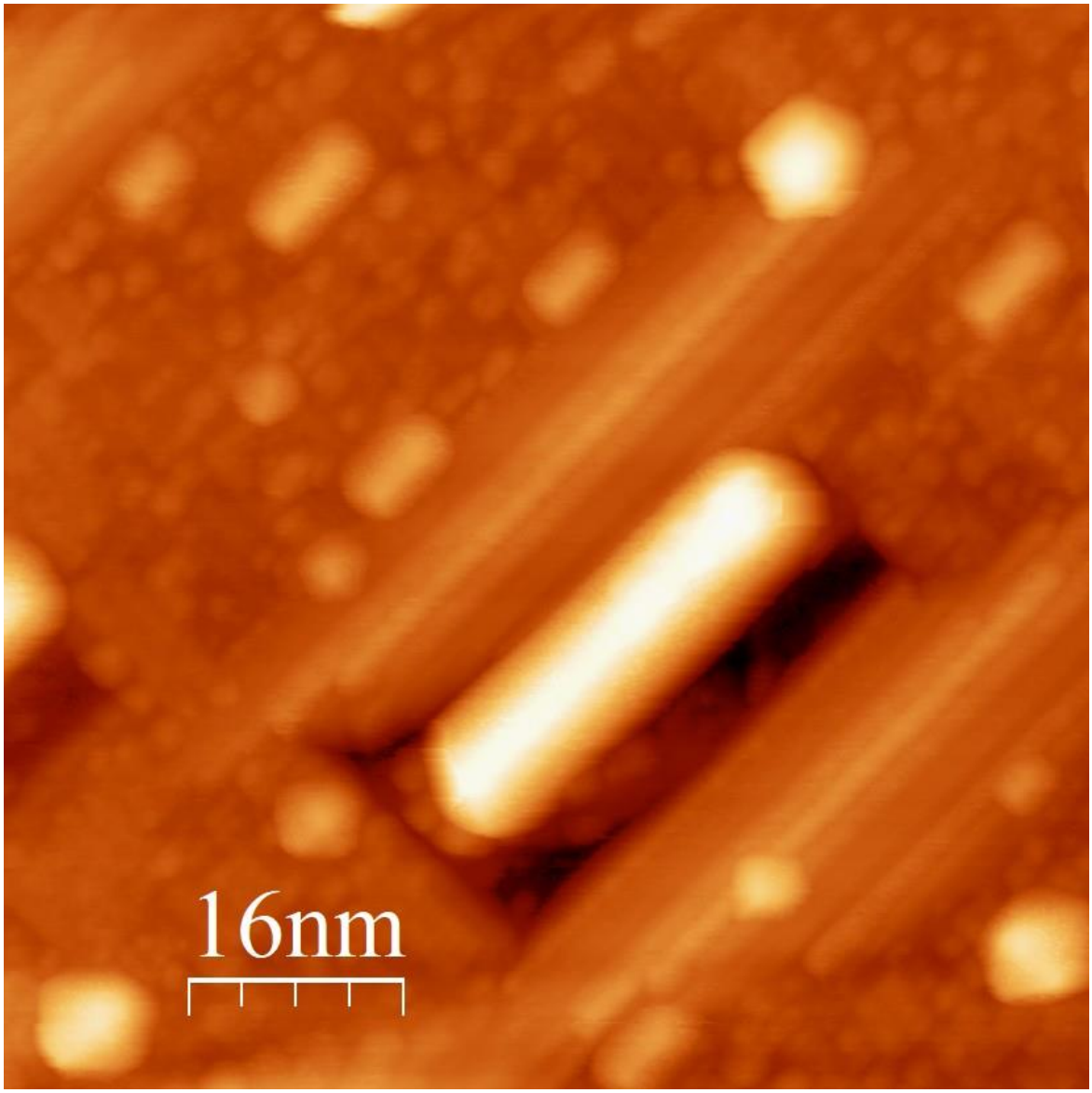


Figure 5-18: (a) Ni on $SrTiO_3$ (110); V_s = 1.0 V, I_t = 50 pA.

The point and edge orientations of icosahedron were observed. However, face orientation was not observed in the obtained images. The 3D view of nanocrystals is shown in Figure 5-19 (a).

The surface profile of nanocrystal (Figure 5-19 (b,c)) show that the height is around 4 nm. The length of nanocrystal in Figure 5-19 (c) is around 40 nm while that in Figure 5-16 (c) is around 60 nm. The height of both nanocrystals is about 4 nm. It shows that nanocrystals have more tendency to grow longer than taller. The dimensions of icosahedrons are

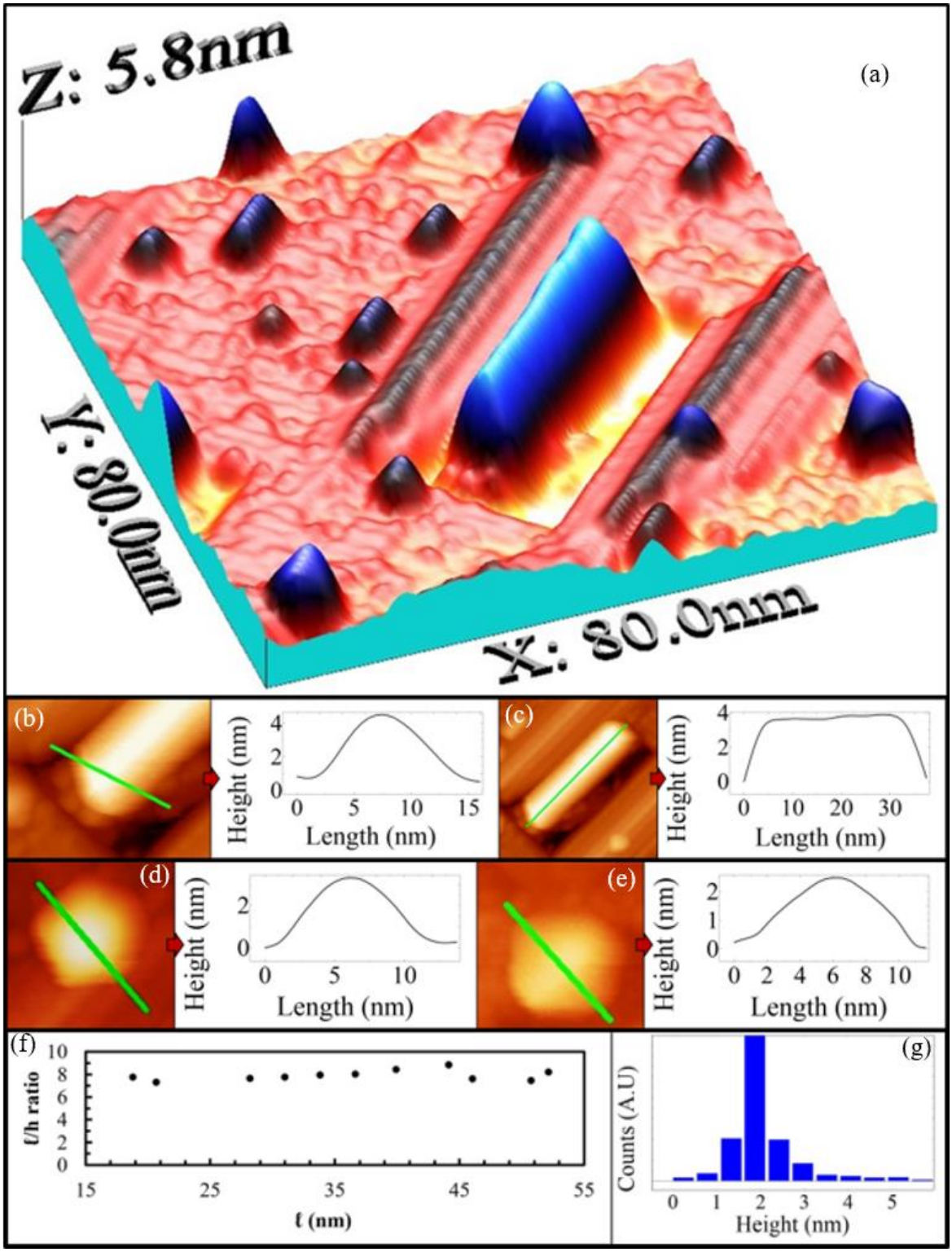


Figure 5-19: (a) 3D view of Ni (0.3 ML) on $SrTiO_3$ (110); V_s = 1.0 V, I_t = 50 pA. (b) Lateral line and profile of nanocrystal. (c) Vertical line and profile of nanocrystal. (d) Line and profile of point-oriented icosahedron. (d) Line and profile of edge-oriented icosahedron. (f) Length-to-height (ℓ/h) ratio of 11 nanocrystals (11.64 ± 4.21).

relatively smaller than the nanocrystals. The height of icosahedron (Figure 5-19 (d,e)) is around 2.2 nm while length is around 10 nm.

To investigate the Wulff construction of the produced nanocrystals, Wulffman software was used. The parameters used for Wulffman simulation are listed in Table 5-2 and

Table 5-2: Parameters used for Wulffman simulation.

Parameter	**Values**
Crystal system	Cubic
Point group	$m\bar{3}m$
Plane-1	Miller indices = {111}
	Surface energy: $\gamma_{111} = 0.76\ J/m^2$
	Plane color: Red
Plane-2	Miller indices = {001}
	Surface energy: $\gamma_{100} = 1.11\ J/m^2$
	Plane color: Blue
Plane-3	Miller indices = {110}
	Surface energy: $\gamma_{110} = 0.9\ J/m^2$
	Plane color: Green
Crystal shape	Truncated octahedron
Area	11.31 nm^2
Volume	2.985 nm^3
Facets	26
Edges	72
Vertices	48

resulted Wulff constructions are shown in Figure 5-15. The surface energy values of planes were changed until the edge ratios of nanocrystals produced were achieved. The surface energy ratios obtained from the experiment are: $\gamma_{001}/\gamma_{111} = 1.461$, $\gamma_{110}/\gamma_{111} = 1.184$, $\gamma_{001}/\gamma_{110} = 1.233$. The surface energy ratios by Vitos et al. are: $\gamma_{001}/\gamma_{111} = 1.206$, $\gamma_{110}/\gamma_{111} = 1.178$, $\gamma_{001}/\gamma_{110} = 1.024$. The $\gamma_{001}/\gamma_{111}$, $\gamma_{110}/\gamma_{111}$, and $\gamma_{001}/\gamma_{110}$ ratios are 21.068%, 0.568%, and 20.385% lower than the energy ratio predicted by Vitos et al. [208].

5.2.4 Ni on $SrTiO_3$ (111)

$SrTiO_3$ (111) sample was sputtered (0.5 keV, 2.6 μA, 10 min) and then annealed at 900 °C for 1 h. The resulting STM image is shown in Figure 4-24. Two distinct reconstructions were observed. The periodicity of one region was (2.21 ± 0.01) nm which corresponds to (4 × 4) reconstruction. The periodicity of second region was (3.31 ± 0.02) nm which corresponds to (6 × 6) reconstruction. In between there is a region rotated at 30º with respect to (4 × 4) reconstruction with periodicity (2.85 ± 0.05) nm. This region could possibly be (3√3 × 3√3)R30° reconstruction. Ni was then deposited onto the sample using e-beam evaporator. The system was post-annealed at 320 ºC for 6 h. The resultant structure is shown in Figure 5-20.

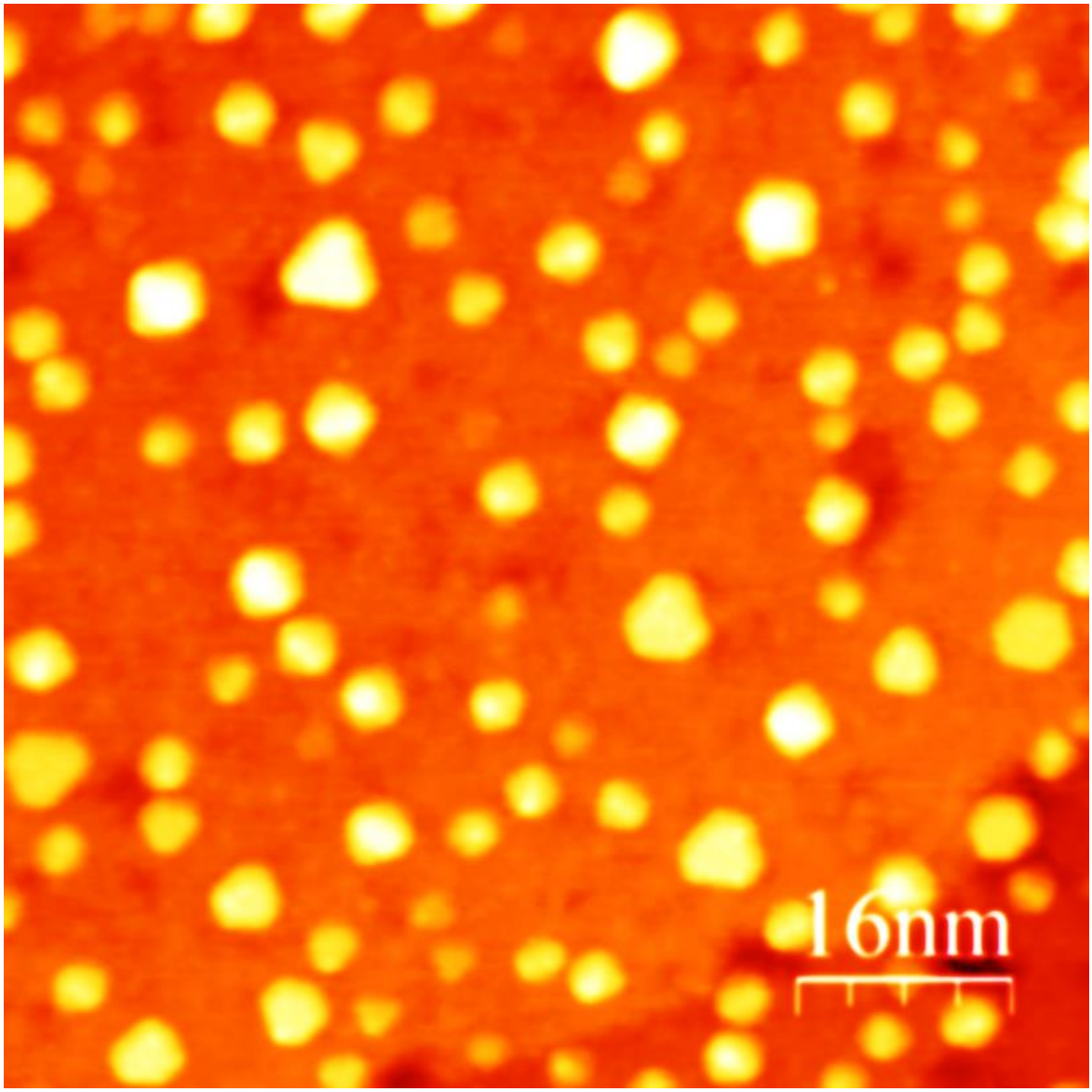


Figure 5-20: (a) Ni on $SrTiO_3$ (111); V_s = 1.47 V, I_t = 0.05 nA.

Ni grew in the shape of icosahedrons and truncated octahedrons. The 3D view of the nanocrystals is shown in Figure 5-21 (a). The surface profiles (Figure 5-21 (b-e)) show that icosahedrons have height about 1.5 nm and the base length is about 7-8 nm while truncated octahedrons are about 0.8-1 nm high with base length about 8 nm. Wulff constructions of three truncated octahedrons and an icosahedron were generated using Wulffman software. The parameters used for Wulffman simulation are listed in Table 5-3 and resulted Wulff constructions are shown in Figure 5-22 and Figure 5-23. The surface energy ratio of truncated octahedron-1 (TO-1) obtained from the experiment is $\gamma_{001}/\gamma_{111}$ = 1.270. The

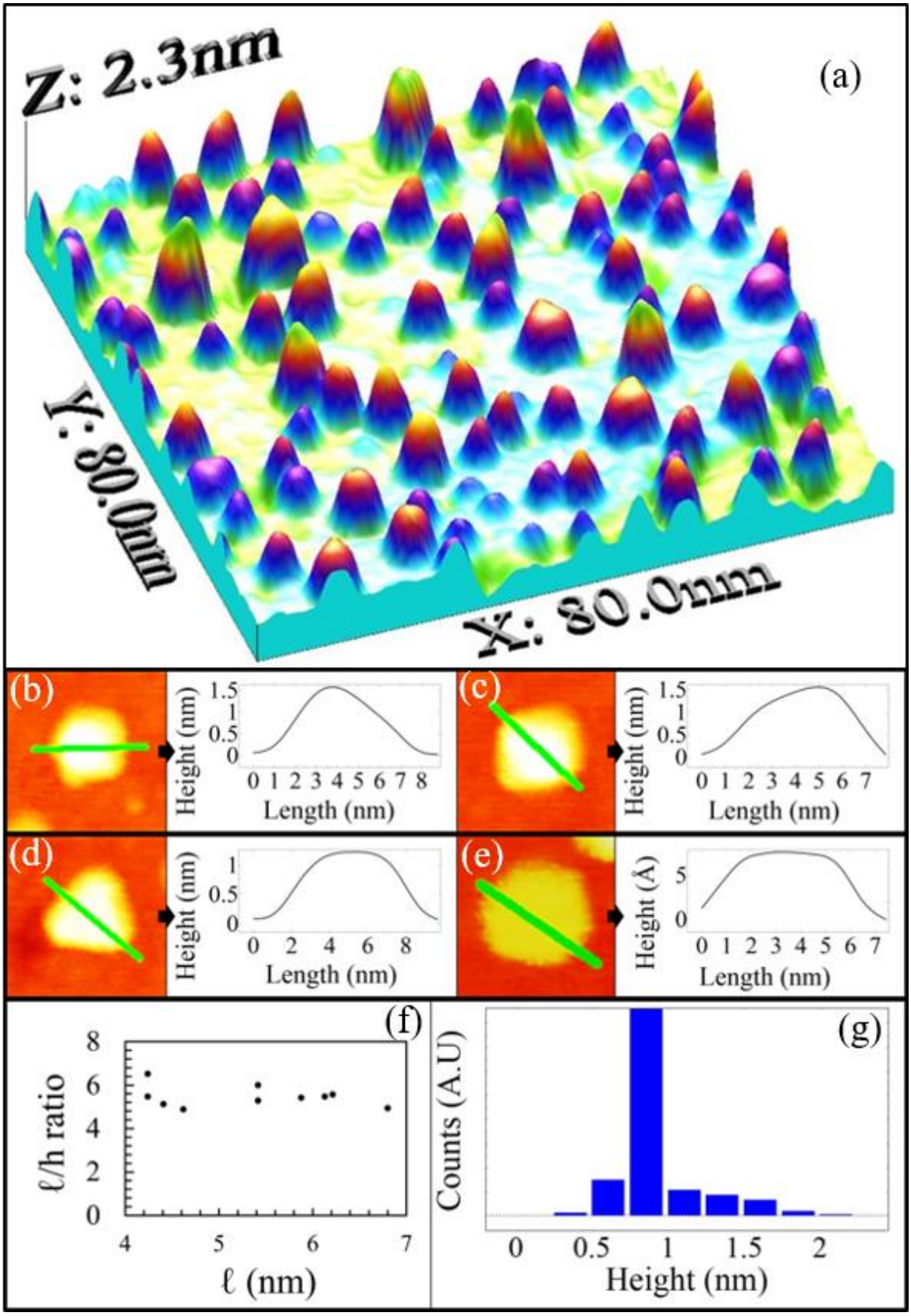


Figure 5-21: (a) 3D view of Ni on $SrTiO_3$ (111). Surface profiles of two (b,c) icosahedrons and (d,e) truncated octahedrons. (f) ℓ/h ratio of ten truncated octahedrons. (g) Height distribution.

Table 5-3: Parameters used for Wulffman simulation.

Parameter	**TO-1**	**TO-2**	**TO-3**	**Ico-1**
Crystal system	Cubic	Cubic	Cubic	Icosahedron
Point group	$m\bar{3}m$	$m\bar{3}m$	$m\bar{3}m$	$m\bar{3}\bar{5}$
γ_{111} (J/m^2)	2.011	2.011	2.011	2.011
γ_{001} (J/m^2)	2.554	2.514	2.353	2.132
Area (nm^2)	18.909	18.827	18.001	15.162
Volume (nm^3)	6.533	6.5075	6.218	5.054
Facets	14	14	14	20
Edges	36	36	36	30
Vertices	24	24	24	12
Comparison with Vitos et al.				
$\gamma_{001}/\gamma_{111}$ (%)	+5.3	+3.65	-2.985	

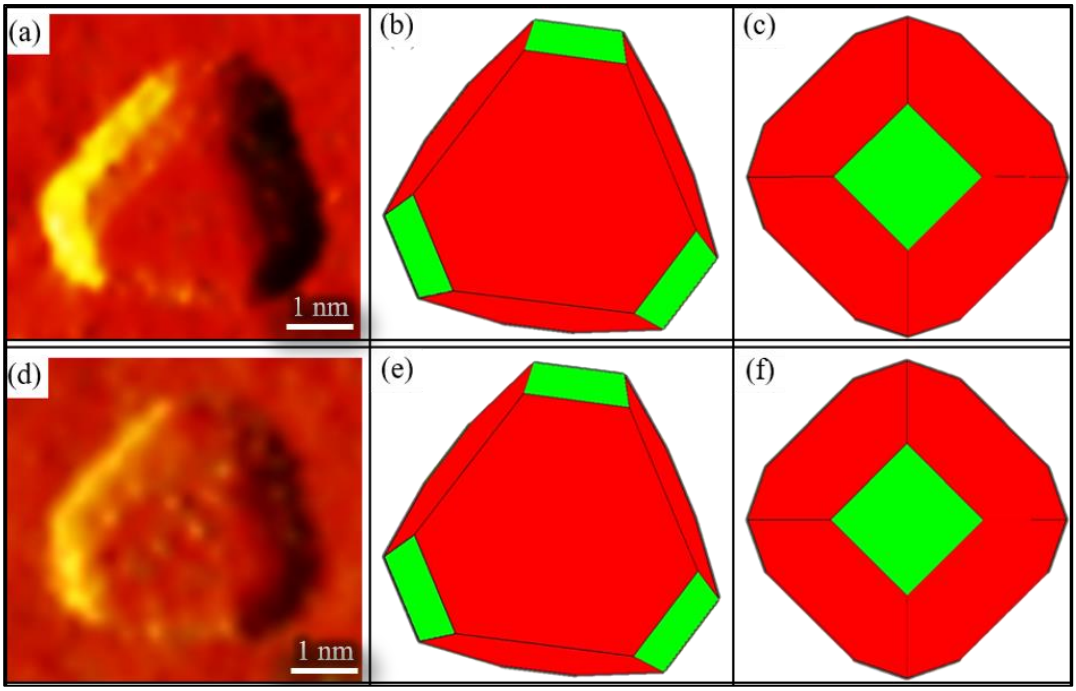


Figure 5-22: (a,d) Horizontal derivatives of STM images of truncated octahedrons. Wulff constructions with (b,e) {111} as top facet and (c,f) {001} as top facet.

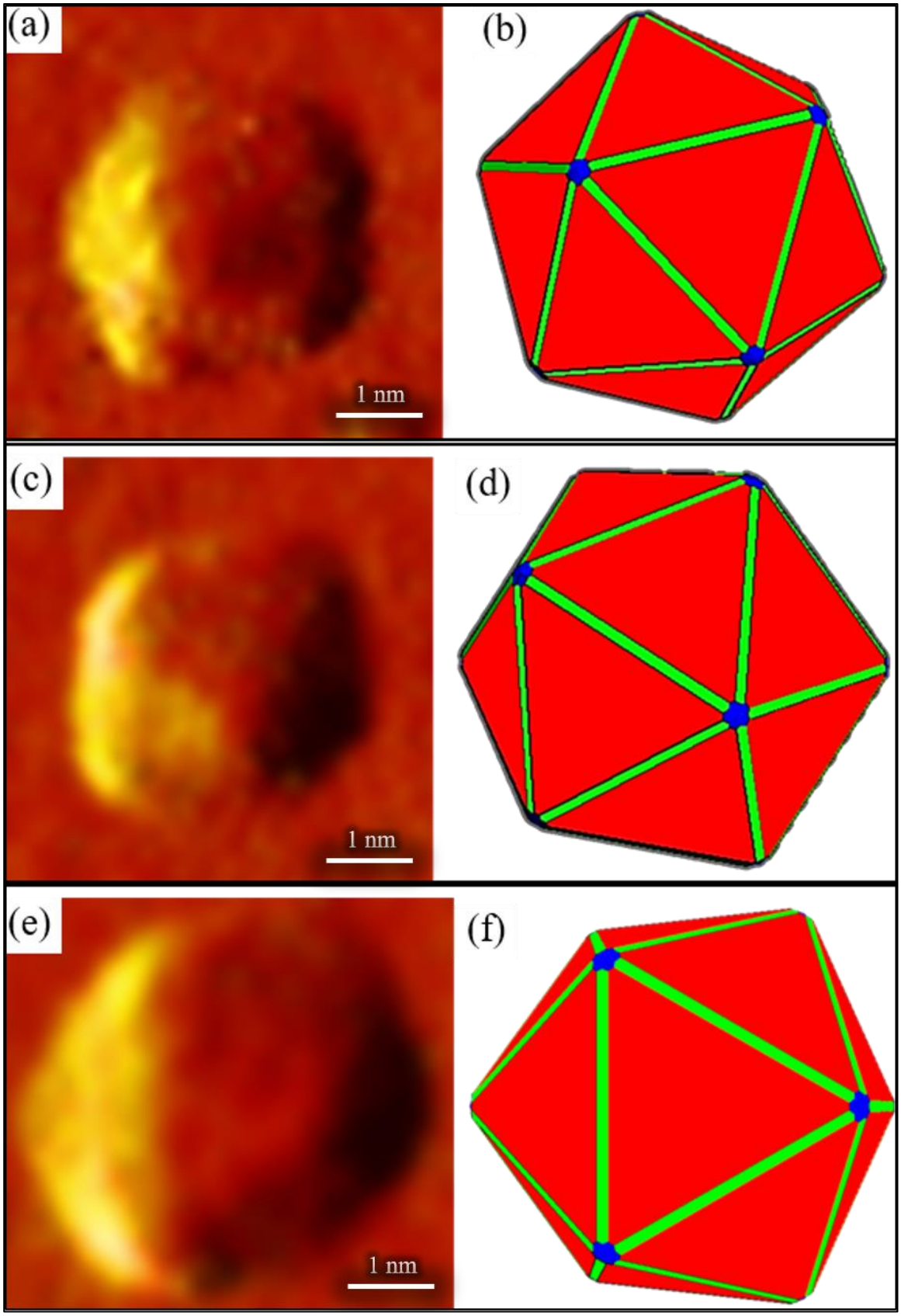


Figure 5-23: (a,c,e) Derivatives of STM images of nickel icosahedrons. (b,d,f) Wulff constructions with orientations matching those of experimental results.

surface energy ratio by Vitos et al. is $\gamma_{001}/\gamma_{111}$ = 1.206. The $\gamma_{001}/\gamma_{111}$ ratio is 5.3% higher than the energy ratio predicted by Vitos et al. [208].

The surface energy ratio of TO-2 obtained from the experiment is $\gamma_{001}/\gamma_{111}$ = 1.250. The surface energy ratio by Vitos et al. is $\gamma_{001}/\gamma_{111}$ = 1.206. The $\gamma_{001}/\gamma_{111}$ ratio is 3.65% higher than the energy ratio predicted by Vitos et al. [208]. The surface energy ratio of TO-3 obtained from the experiment is $\gamma_{001}/\gamma_{111}$ = 1.170. The surface energy ratio by Vitos et al. is $\gamma_{001}/\gamma_{111}$ = 1.206. The $\gamma_{001}/\gamma_{111}$ ratio is 2.985% lower than the energy ratio predicted by Vitos et al. [208].

To calculate the adhesion energy of truncated octahedrons, the length ℓ was defined as the distance from the center of {111} plane to the center to {111} plane opposite to selected {111} plane. The ℓ/h ratio is not constant that shows that all the nanocrystals are not in the equilibrium shape. In the observed nanocrystals, there are total 8 facets; a {111} top facet, three {111} side facets, three {001} side facets, and a {111} interface with the $SrTiO_3$ (111) substrate. The total energy of the system (E_1) is given by,

$$\gamma^* = -1.463 \pm 0.138\, J/m^2 \quad \textbf{(24)}$$

$$W_{adh} = 3.889 \pm 0.167\, J/m^2 \quad \textbf{(25)}$$

5.3 Conclusions

On $SrTiO_3$ (001) substrate, Ni formed truncated pyramidal shaped nanocrystals. Each nanocrystal comprised of six facets: a (001) top facet, four (110) side facets, and a (001) base facet. On $SrTiO_3$ (110) substrate, Ni formed truncated hut shaped nanocrystals. Each nanocrystal comprised of six facets; a (110) top facet, two (111) side facets, two (001) side facets, and a (110) base facet. On $SrTiO_3$ (111) substrate, Ni formed two shapes:

icosahedron and truncated octahedron. The icosahedrons had (111) facets and point, edge and face orientations were observed. The truncated octahedron had eight facets: a (111) top facet, three (111) side facets, three (001) side facets, and a (111) base facet. The unit cell of STO is 3.905 Å and that of Ni is 3.52 Å which results in a tensile lattice mismatch of 9.86%. However, nine $SrTiO_3$ match 10 Ni perfectly and therefore there is a coherent lattice match.

Chapter 6:

Fe Nanocrystals

6.1 Background

6.2 Experimental details

$SrTiO_3$ substrates were supplied by PI-KEM Ltd, UK. Fe rods were supplied by Goodfellow and are 99.99% pure. The substrates were sonicate-cleaned in methanol and acetone. The substrates were then transferred into JEOL JSTM-4500xt system operating at 10^{-8} Pa. The substrates were degassed through resistive heating. The substrates were then sputtered/annealed to generate terraces and Fe was deposited using e-beam evaporator on substrates preheated at 320 °C. The substrates were cooled to room temperature after deposition and samples were imaged to observe morphology of as-deposited nanocrystals. Then multiple post-annealings were carried out by applying various thermal cycles to observe variation in morphology of Fe nanocrystals with temperature and time. When the nanocrystals achieved nearly equilibrium morphology, their dimensions were measured and the equilibrium shape was plotted using 'Wulffman' software. The surface energy ratios obtained were compared with the literature. The adhesion energy of nanocrystals was also calculated. Any peculiar results obtained in this study were attempted to be explained based on established theory and experimental observations.

6.3 Results and discussion

6.3.1 Fe on $SrTiO_3$ (001)

STM images of $SrTiO_3$ (001) substrate annealed at 900 ºC for 1 h are shown in Figure 6-1. The literature suggests that reconstruction of these kind of terraces is (2 × 1) [200]. Fe was then deposited onto the substrate using e-beam evaporator. The system was post-annealed at 320 ºC for 1 h. The resultant structure is shown in Figure 6-2. Fe formed truncated pyramid shaped nanocrystals with a square base. The 3D view of nanocrystals is shown in Figure 6-3 (a). The surface profiles (Figure 6-3(b)) of a nanocrystal show that base length

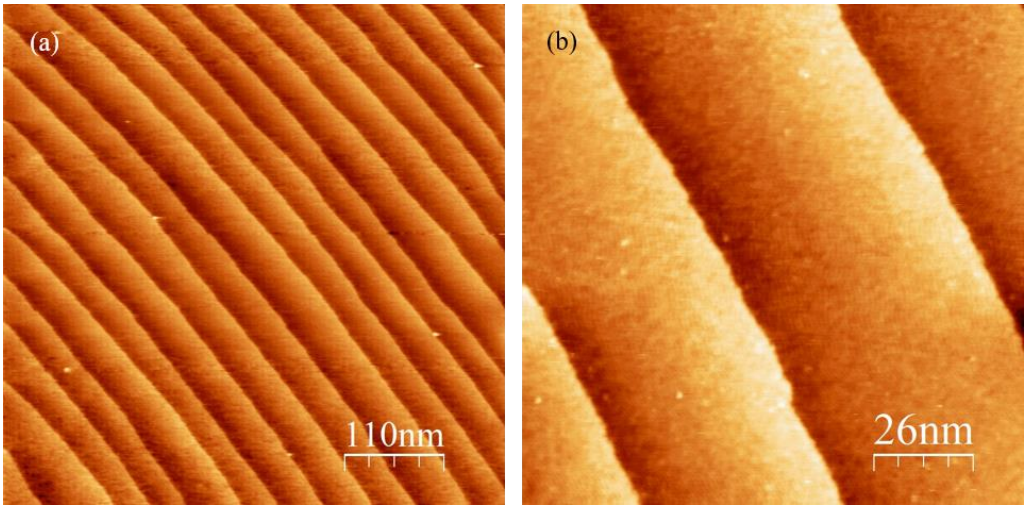


Figure 6-1: (a-b) $SrTiO_3$ (001) substrate used to deposit Fe nanocrystals. (a) V_s = 1.8 V, I_t = 0.1 nA. (b) V_s = 1.46 V, I_t = 0.1 nA. The sample was annealed at 900 °C for 1 h.

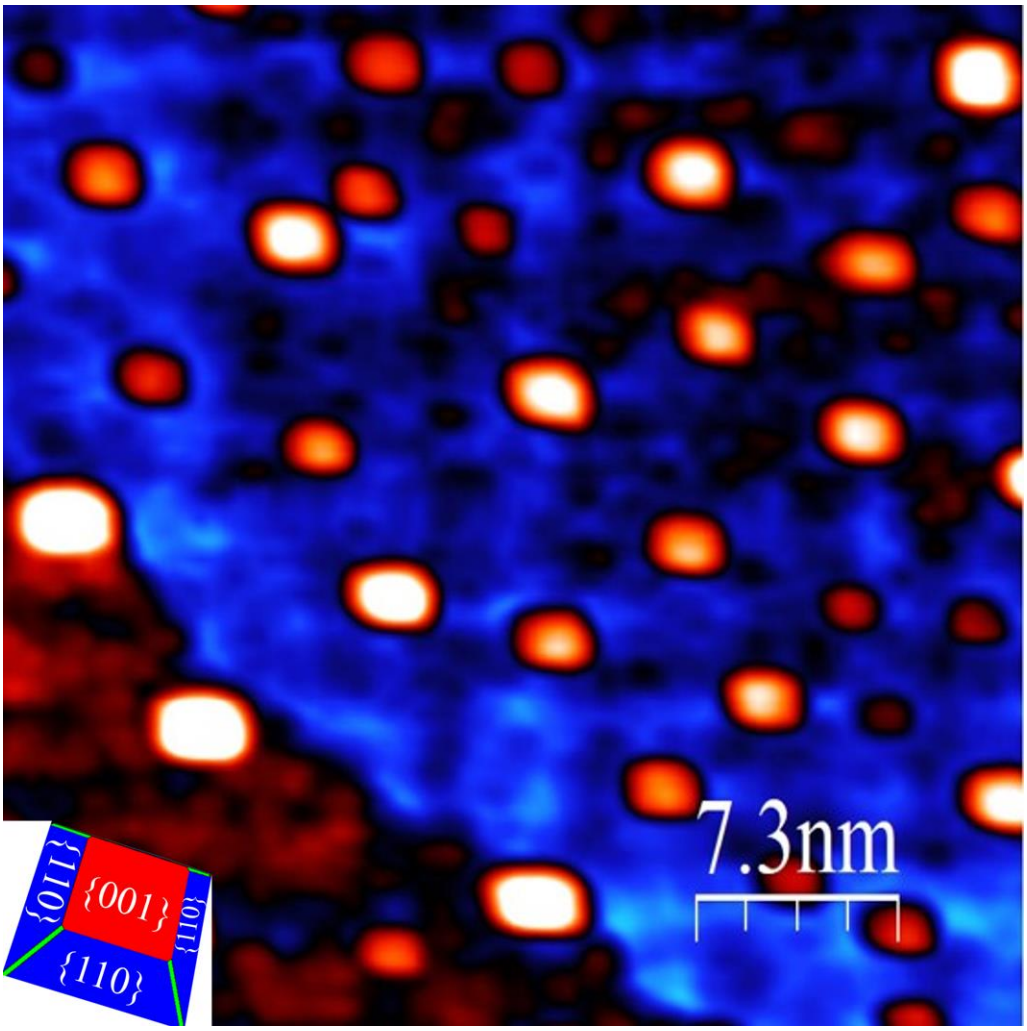


Figure 6-2: Fe on $SrTiO_3$ (001); V_s = 1.8 V, I_t = 50 pA. The substrate was annealed at 900 °C for 1 h. Fe (0.2 ML) was then deposited for 1 min with substrate pre-heated to 320 °C. The system was then post-annealed at 320 °C for 1 h.

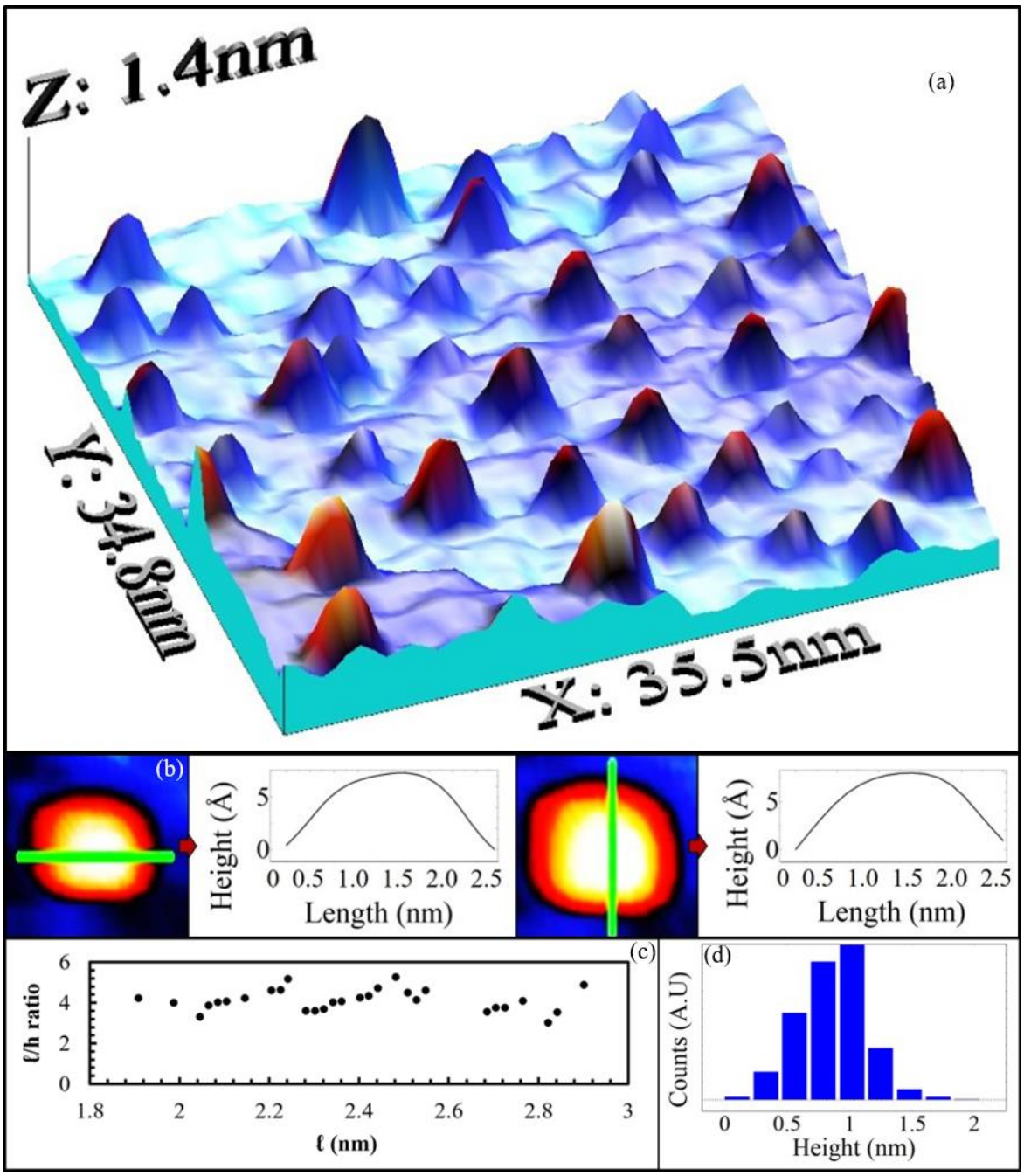


Figure 6-3: (a) 3D view of Fe (0.2 ML) on $SrTiO_3$ (001); V_s = 1.8 V, I_t = 50 pA. (b) Horizontal and vertical lines and their respective profiles. (c) Length-to-height (ℓ/h) ratio of nanocrystals (4.156 ± 0.590). (d) Height distribution.

is around 2.5 nm while height is around 0.7 nm. The average height of studied nanocrystals was 0.88 ± 0.04 nm. The ℓ/h ratios (Figure 6-3 (c)) of about 30 nanocrystals were calculated. The ℓ/h ratio is nearly constant that suggests that most of the nanocrystals have achieved their equilibrium shape.

In the observed nanocrystals, there are total 6 facets; a {001} top facet, three {110} side facets, and a {001} interface with the $SrTiO_3$ (001) substrate. To calculate the adhesion energy of produced nanocrystals, length ℓ was defined as the distance from the center of the edge of {110} plane to the center to {110} plane opposite to selected {110} plane. The ℓ/h ratio is nearly constant that shows that most of the nanocrystals have achieved their equilibrium shape. The total energy of the system (E_1) is given by,

$$E_1 = \gamma_{\mathrm{Fe}(001)}A_{(001)} + \gamma_{Fe(110)}A_{(110)} + \gamma_i A_i + \gamma_{S(001)}A_{S1} \quad \textbf{(26)}$$

Where $\gamma_{Fe(110)}$ and $\gamma_{Fe(001)}$ are surface energies of Fe (110) and (001) planes, $A_{(001)}$ is the total area of Fe (001) top facet, $A_{(110)}$ is the total area of four Fe (110) side facets, γ_i is surface energy of interface, A_i is interfacial area, $\gamma_{S(001)}$ is surface energy of substrate $SrTiO_3$ (001), and A_{S1} is the surface area of the substrate excluding the area of Fe-substrate interface. When separating Fe from substrate, it was assumed that the shape of Fe truncated pyramid does not change. The base (001) surface with an area of A_b is created on the Fe truncated pyramid. The total energy (E_2) in system 2 when the Fe and substrate are apart is,

$$E_2 = \gamma_{Fe(001)}A_{(001)} + \gamma_{Fe(001)}A_b + \gamma_{Fe(110)}A_{(110)} + \gamma_{S(001)}A_{S2} \quad \textbf{(27)}$$

The energy change between systems 1 and 2 is,

$$\Delta E = E_2 - E_1$$

$$\Delta E = \gamma_{Fe(001)} A_b - \gamma_i A_i + \gamma_{S(001)} (A_{S2} - A_{S1}) \quad \textbf{(28)}$$

Where,

$$A_{S2} - A_{S1} = A_b = A_i \quad \textbf{(29)}$$

From eq. (29), eq. (28) becomes,

$$\Delta E = \gamma_{\mathrm{Fe}(001)} A_b - \gamma_i A_i + \gamma_{S(001)} A_i \quad \textbf{(30)}$$

The energy change per unit area, i.e., adhesion energy (W_{adh}) can be obtained by dividing eq. (30) by Ai on both sides:

$$W_{adh} = \gamma_{\mathrm{Fe}(001)} - \{\gamma_i - \gamma_{S(001)}\} \quad \textbf{(31)}$$

The general surface energy r^* defined by Winterbottom [33] is given by,

$$\gamma^* = \gamma_i - \gamma_{S(001)} \quad \textbf{(32)}$$

From eq. (32), eq. (31) becomes,

$$W_{adh} = \gamma_{\mathrm{Fe}(001)} - \gamma^* \quad \textbf{(33)}$$

From the modified Wulff construction [33], r^* is given by,

$$\gamma^* = \sqrt{2}\frac{h}{\ell}\{\sqrt{3}\gamma_{(110)} - \gamma_{(001)}\} - \gamma_{(001)} \quad \textbf{(34)}$$

Where $\gamma_{(001)} = 2.222\, J/m^2$ and $\gamma_{(110)} = 2.430\, J/m^2$ are theoretical values as calculated by Vitos et al. [208]. The h/ℓ ratio is 0.246 ± 0.036. By putting values, the values of γ^* and W_{adh} are;

$$\gamma^* = -1.350 \pm 0.181\, J/m^2 \quad \textbf{(35)}$$

$$W_{adh} = 3.572 \pm 0.223\, J/m^2 \quad \textbf{(36)}$$

Silly and Castell. grew Fe nanocrystals on $SrTiO_3$ (001)-c(4 × 2) and reported the adhesion energy of the grown nanocrystals to be (3.05 ± 0.15) J/m^2 [6].

Another $SrTiO_3$ (001) substrate was prepared by annealing at 850 ºC for 6 h. The idea was to get a more regular shape of Fe nanocrystals than shown in Figure 6-2. Fe was deposited for 1 min on substrate preheated to 320 ºC. The system was then post-annealed twice: (320 ºC, 1 h), (320 ºC, 6 h). The resultant structure is shown in Figure 6-4 (a). Fe clusters can be observed at the step edges. As atoms at the step edges have dangling bonds, they are high energy sites. Therefore, they become preferred heterogeneous nucleation site where Fe could form clusters. Hence, we see clusters along the step edges. On the same sample, Fe was again deposited for ten times for 30 sec each and system was post-annealed at 320 ºC for 6 h after each deposition. The resultant structures are shown in Figure 6-4 (b-k). As shown in Figure 6-4 (b), there are Fe clusters at step edges while surface is covered with irregular shaped top layer with height around 0.25 nm. This top layer was not there before

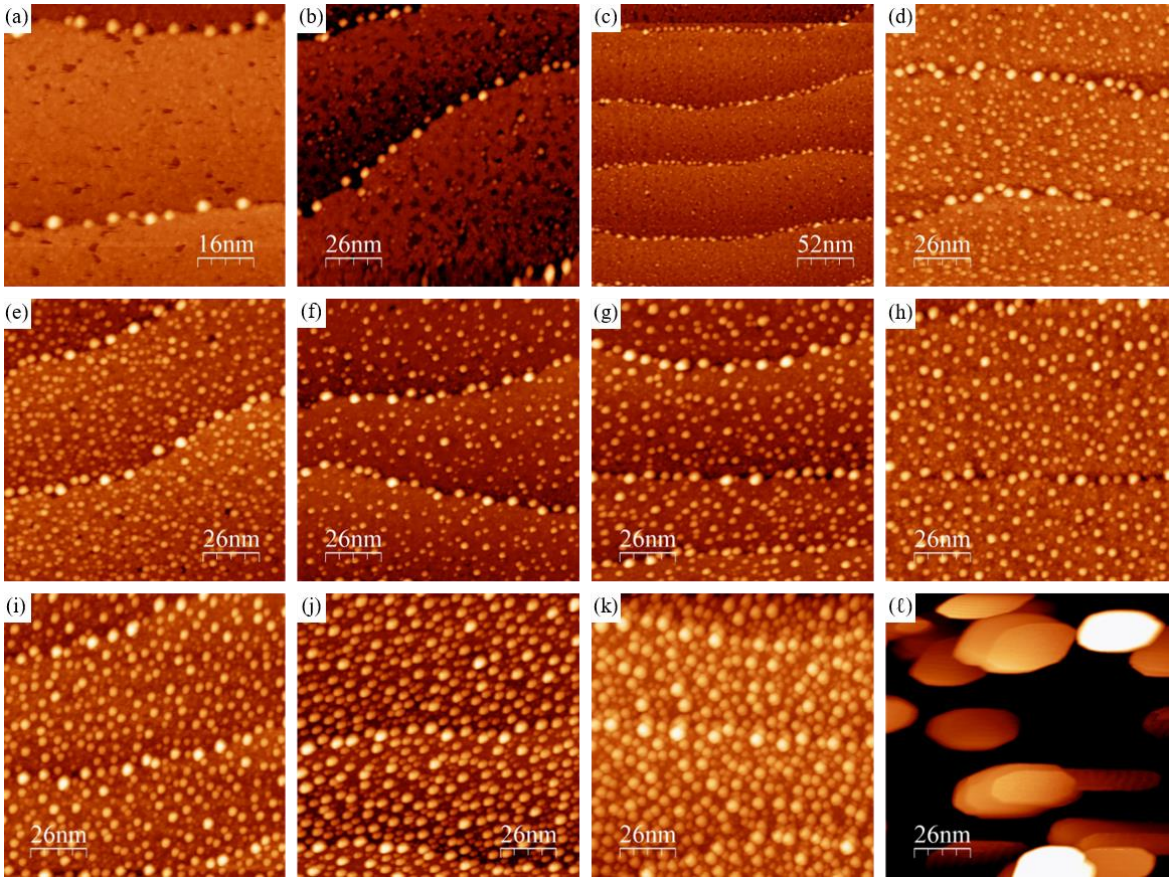


Figure 6-4: Gradual increase of Fe coverage on $SrTiO_3$ (001). The substrate was annealed at 850 °C for 6 h. (a) Fe was then deposited for 1 min with substrate pre-heated to 320 °C. The system was then post-annealed twice (320 °C, 1 h), (320 °C, 6 h). (b-k) Then Fe was deposited for another ten times for 30 sec each with substrate pre-heated to 320 °C. The system was post-annealed at 320 °C for 6 h after each deposition. (ℓ) Then Fe was deposited for another five minutes with sub pre-heated to 520 °C. The system was then post-annealed thrice: (520 °C, 6 h), (620 °C, 6 h), (720 °C, 6 h). The values of voltage and tunneling current are; (a-g) V_s = 1.67 V, I_t = 50 pA, (h-k) V_s = 2.85 V, I_t = 0.1 nA, (ℓ) V_s = 1.8 V, I_t = 0.1 nA.

Fe deposition. Hence, it could be Fe monolayer. As deposition and time increased, Fe clusters started to appear on the surface. However, no definite geometric shape was observed. In desperation, Fe was deposited for five more minutes in one go and the system was post-annealed multiple times. This is where interesting shapes and phenomena were observed. A representative image is shown in Figure 6-4 (ℓ). Chamfered square-shaped and rectangular-shaped nanocrystals can be observed as shown in Figure 6-5-Figure 6-7.

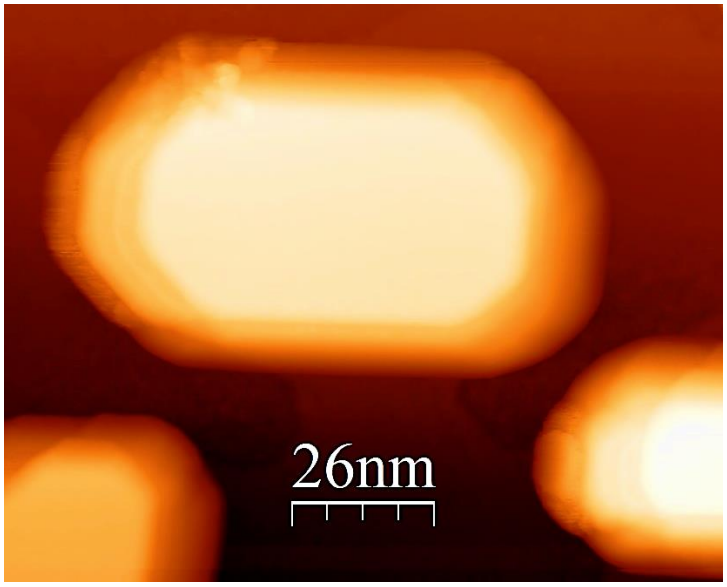


Figure 6-5: Fe on $SrTiO_3$ (001); V_s = 1.8 V, I_t = 0.1 nA. The system was then post-annealed twice (320 °C, 1 h), (320 °C, 6 h).

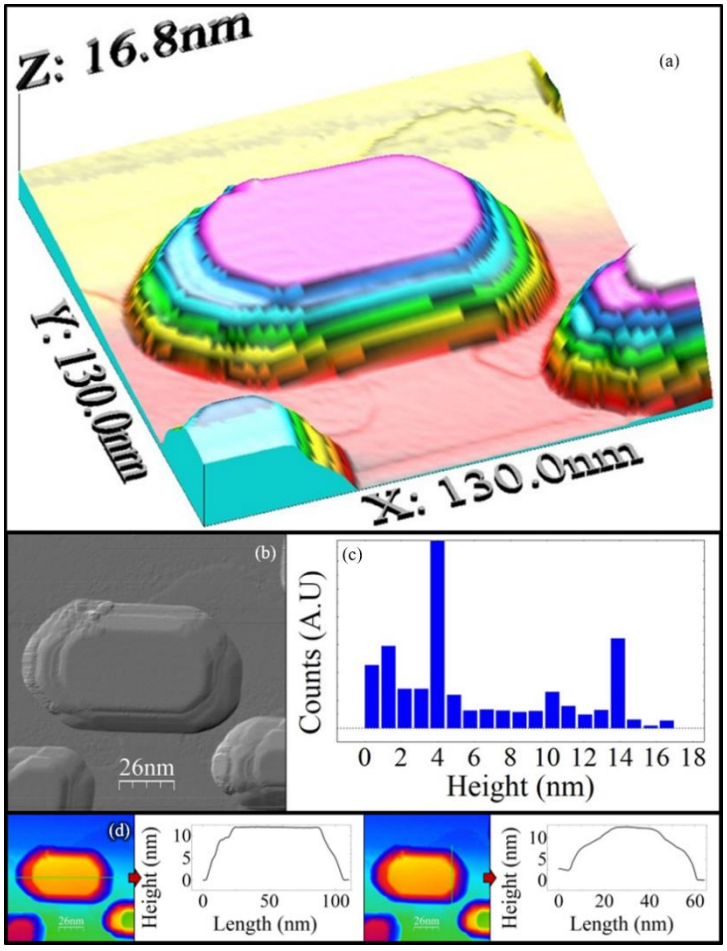


Figure 6-6: Fe on $SrTiO_3$ (001); V_s = 1.8 V, I_t = 0.1 nA. The system was then post-annealed twice (320 °C, 1 h), (320 °C, 6 h).

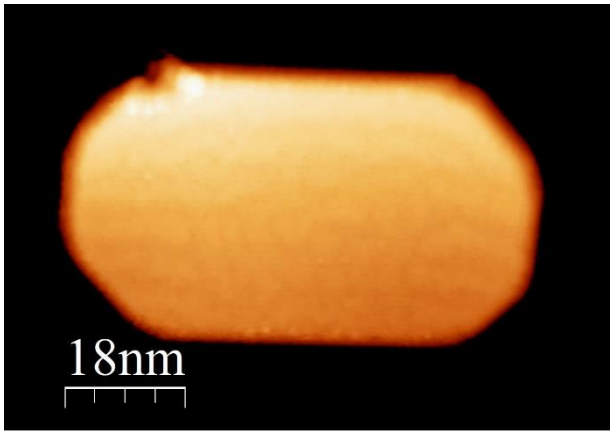


Figure 6-7: Fe on $SrTiO_3$ (001); V_s = 1.8 V, I_t = 0.1 nA. The system was post-annealed twice (320 °C, 1 h), (320 °C, 6 h).

6.4 Wulffman simulations for iron oxide

As longer periods of anneals were carried out, there was a possibility that the whole crystal is not elemental form and has totally converted into an oxide or iron. To determine equilibrium crystal shape of iron oxide, Wulffman software was used with theoretical surface energies values, as listed in Table 6-1, taken from Guo and Barnard [215] and

Table 6-1: Parameters used for Wulffman simulation.

Parameter	Values
Crystal system	Cubic
Point group	$m\bar{3}m$
Plane-1	Miller indices = {110}
	Surface energy: $\gamma_{110} = 2.28\ J/m^2$
	Plane color: Red
Plane-2	Miller indices = {001}
	Surface energy: $\gamma_{001} = 2.252\ J/m^2$
	Plane color: Green
Plane-3	Miller indices = {211}

	Surface energy: $\gamma_{211} = 2.689\ J/m^2$
	Plane color: Yellow
Plane-4	Miller indices = {310}
	Surface energy: $\gamma_{310} = 2.443\ J/m^2$
	Plane color: Blue
Plane-5	Miller indices = {111}
	Surface energy: $\gamma_{111} = 2.553\ J/m^2$
	Plane color: Pink
Crystal shape	Truncated pyramid
Area	77.72 nm^2
Volume	59.277 nm^3
Facets	26
Edges	72
Vertices	48

resulted Wulff constructions are shown in Figure 6-8 and Figure 6-9. The Wulff

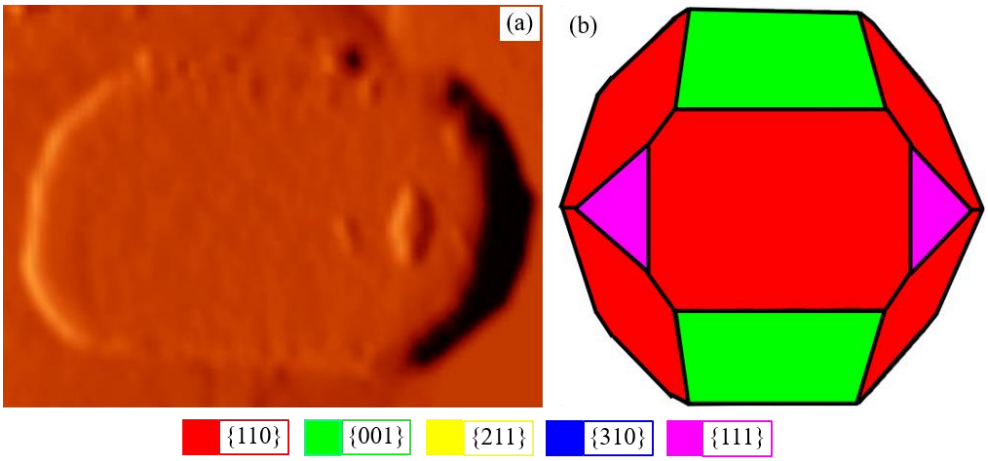


Figure 6-8: Wulffman simulations of equilibrium crystal shapes (ECS) of Fe nanocrystals: (a) STM image of Fe nanocrystal. (b) Wulffman simulation of equilibrium crystal shape (ECS) of Fe nanocrystal.

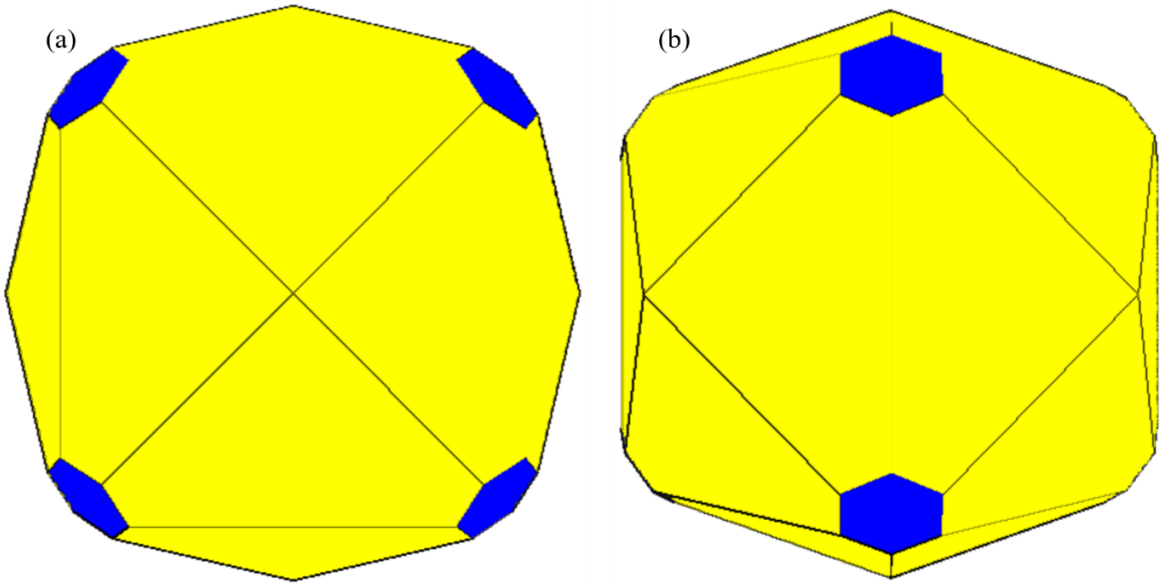


Figure 6-9: Wulff construction of α-Fe_2O_3.

construction is predominantly composed of {210} facets and {111} facets appearing at the corners. The observed nanocrystals were significantly different from the Wulff constructions. Such difference hinted that nanocrystals will be comprising both of elemental iron and its oxide at the surface. Therefore, comparisons were made both based on bcc and fcc crystal structures and discussed below.

6.5 Chamfered rectangular nanocrystals

The deposited iron grew in the form of rectangular nanocrystals with chamfered corners. A magnified image of chamfered rectangular nanocrystal is previously shown in Figure 6-5. The height of nanocrystal is around 10 nm while length is around 100 nm. The values of roughness average (R_a), root mean square roughness (R_{rms}), average height (H_a), and maximum height (H_{max}) are 4.02 ± 0.12 nm, 4.63 ± 0.14 nm, 6.19 ± 0.43 nm, and 16.82 ± 1.35 nm, respectively. These were the biggest nanocrystals observed in this work and significantly larger than the reported literature on iron nanocrystals [6]. To generate Wulff construction, surface energy values were taken from Vitos et al. [208] for bcc iron and then the energy values of the planes were changed until the faceting edge ratios of the

experimentally produced nanocrystals were achieved. The surface energy values used to obtain Wulff constructions are shown in Table 6.2 and a comparison of the experimental and theoretical shapes is shown in Figure 6-10. The surface energy values based on fcc

Table 6-2:Comparison of predicted surface energy values with current experimental results based on bcc iron for chamfered rectangular iron nanocrystals.

Sr.	Facet	Vitos et al. [208]	Current experimental values	% difference
1	{110}	2.43	2.43	0
2	{001}	2.222	2.222	0
3	{211}	2.589	2.589	0
4	{310}	2.393	2.393	0
5	{111}	2.733	2.533	7.32

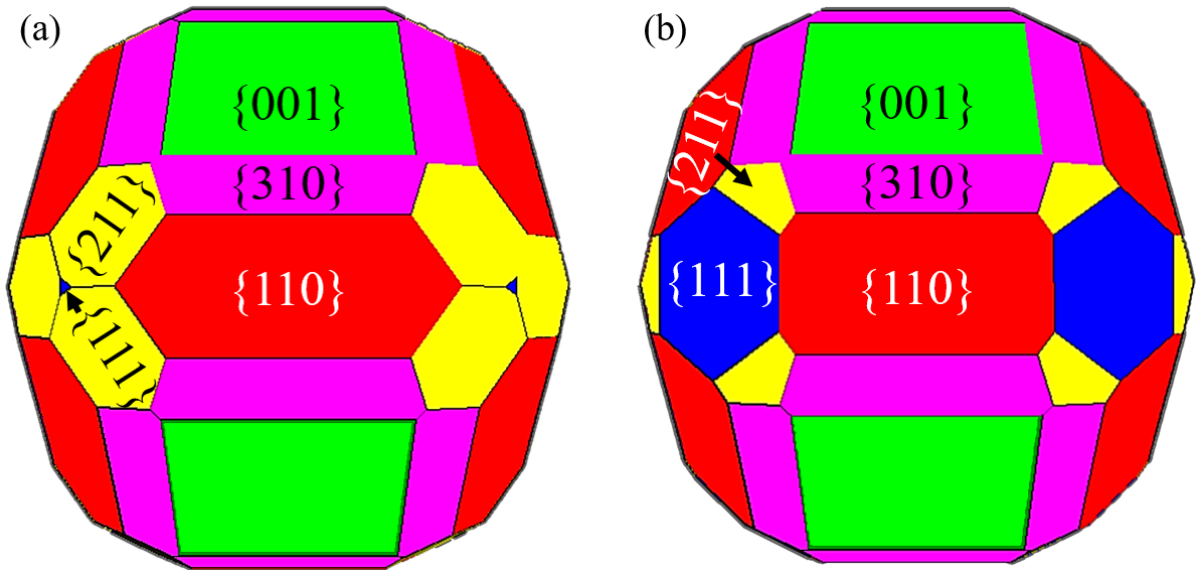


Figure 6-10: Wulff constructions with {110} as top facets based on (a) Vitos et al. [208] **and (b) current experimental results.**

iron have also been predicted as listed in Table 6.3. Wulff constructions were generated using those values and are shown in Figure 6-11 with {110} as top facet. All the shapes

Table 6-3: Comparison of predicted surface energy values with current experimental results based on fcc iron for chamfered rectangular iron nanocrystals.

Method	**γ(001)**	**γ(110)**	**γ(111)**	**Ref.**
GGA-PW91 (unrelaxed)*	2.956	3.082	2.762	[216]
GGA-PW91 (relaxed)	2.133	2.255	2.077	[216]
GGA-PBE (unrelaxed)	2.973	3.095	2.782	[216]
GGA-PBE (relaxed)	2.152	2.268	2.096	[216]
DFT (relaxed)	2.265	2.38	2.169	[217]
Current experimental results**	2.265	2.34	2.169	
* GGA-PW91 and -PBE are based on the Perdew–Wang [218], and Perdew–Burke–Ernzerhof approximations [219]. ** γ(211) for the current experimental results is 2.39 J/m^2.				

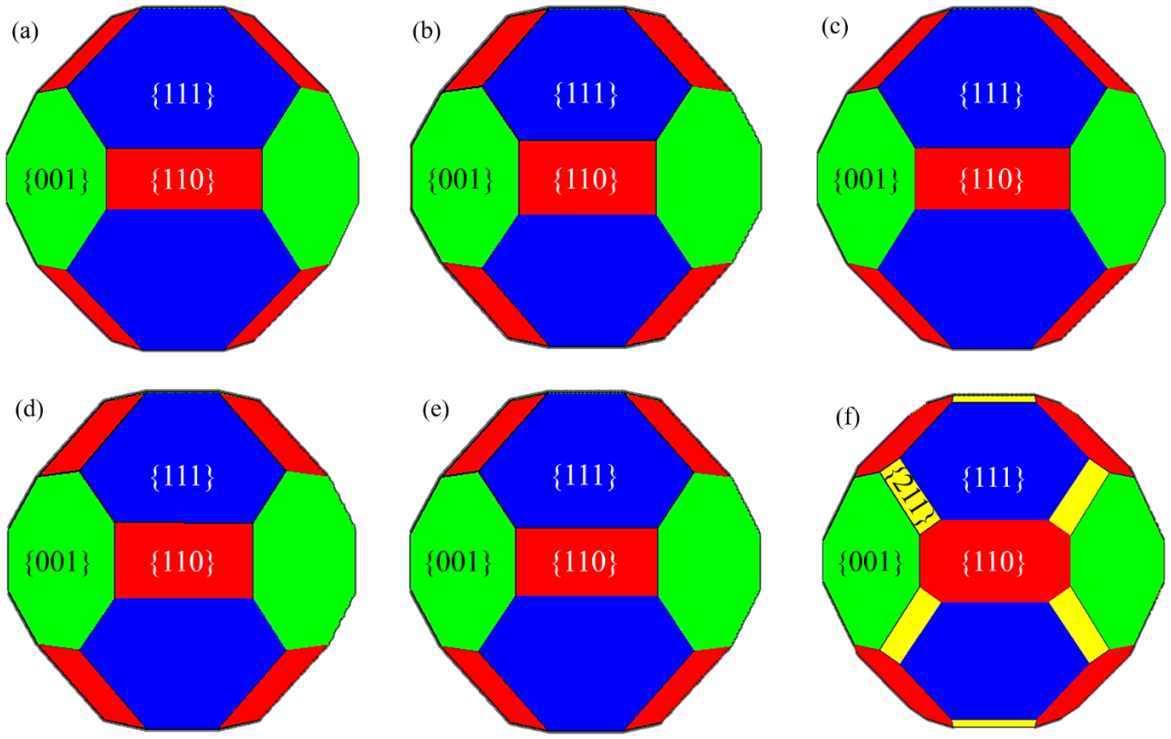


Figure 6-11: Wulff constructions with {110} as top facet for fcc iron based on different theoretical values and experimental results: (a) GGA-PW91 (unrelaxed), (b) GGA-PW91 (relaxed), (c) GGA-PBE (unrelaxed), (d) GGA-PBE (relaxed), (e) DFT (relaxed), (f) current experimental results.

have rectangular top {110} facet, however, they are not chamfered. To get the chambered edges, we have introduced {211} planes which are relatively low energy planes in fcc. The $\gamma_{(211)}$ was set at 2.39 J/m^2 and the resultant construction is shown in Figure 6-11 (f). Apart from introducing $\gamma_{(211)}$, we only had to change the $\gamma_{(110)}$ values from 2.38 J/m^2 (as predicted by DFT [217]) to 2.34 J/m^2 to match the faceting edge ratios with our experimental results. The facets obtained based on bcc (Figure 6-12 (b)) and fcc (Figure 6-12 (c)) iron are

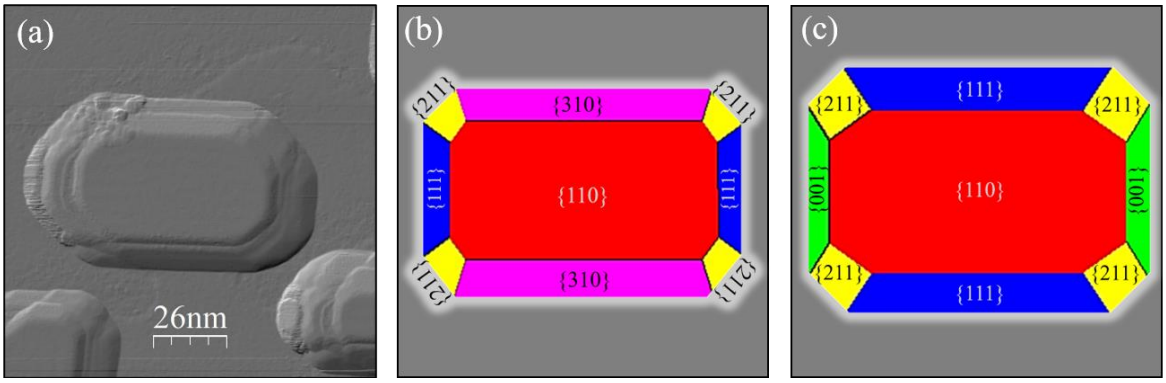


Figure 6-12: (a) Horizontal derivative of STM image of chamfered rectangular iron nanocrystal. (b,c) Wulff constructions based on (b) bcc and (c) fcc iron.

compared with the horizontal derivative of the STM image of the chamfered rectangular iron nanocrystal (Figure 6-12 (a)). Both bcc and fcc based Wulff constructions predict that there are ten total facets. Based on bcc iron, the top facet is {110}, two side facets each for {111}, {211}, and {310}, and a base facet of {110} making epitaxy with {001} facet of the substrate. There is a major anomaly in this predicted construction. Firstly, {001} facets which are low-index and low energy facets are completely missing while high-index and high energy facets are present, i.e., {211} and {310}. This anomaly makes the predicted structure energetically unfavorable. In contrary, based on fcc iron, there is a {110} top facet, two side facets each for {001}, {111}, {211}, and a base facet {110}. This structure seems energetically more favorable as it mainly consists of low-index planes in good proportion. This similarity in values hints that the produced nanocrystals have fcc structure. It will be further discussed later that it is energetically unfavorable for

nanocrystals to undergo transformation from rectangle to square if we assume they have bcc structure. In contrary, if we assume fcc crystal structure, the observed shape transition can be achieved simply by turning them over.

6.6 Chamfered square nanocrystals

When the sample was further post-annealed at 820 °C for 1 h, the resultant structure is shown in Figure 6-13 and Figure 6-14. Square nanocrystals as high as 12 nm and as long

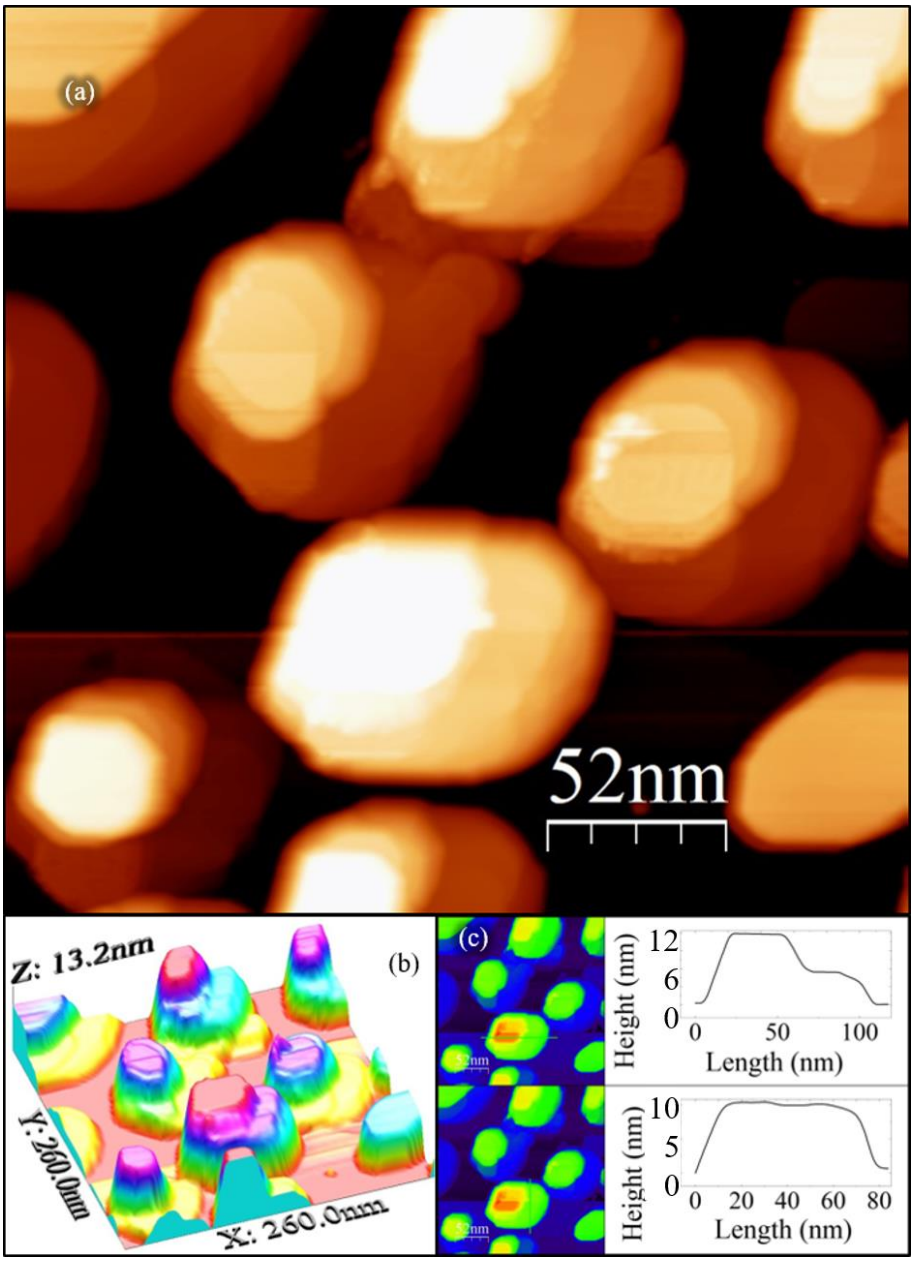


Figure 6-13: (a) Chamfered square iron nanocrystals on $SrTiO_3$ (001); V_s = 1.8 V, I_t = 0.1 nA. (b) 3D view. (c) Horizontal and vertical lines and their respective surface profiles.

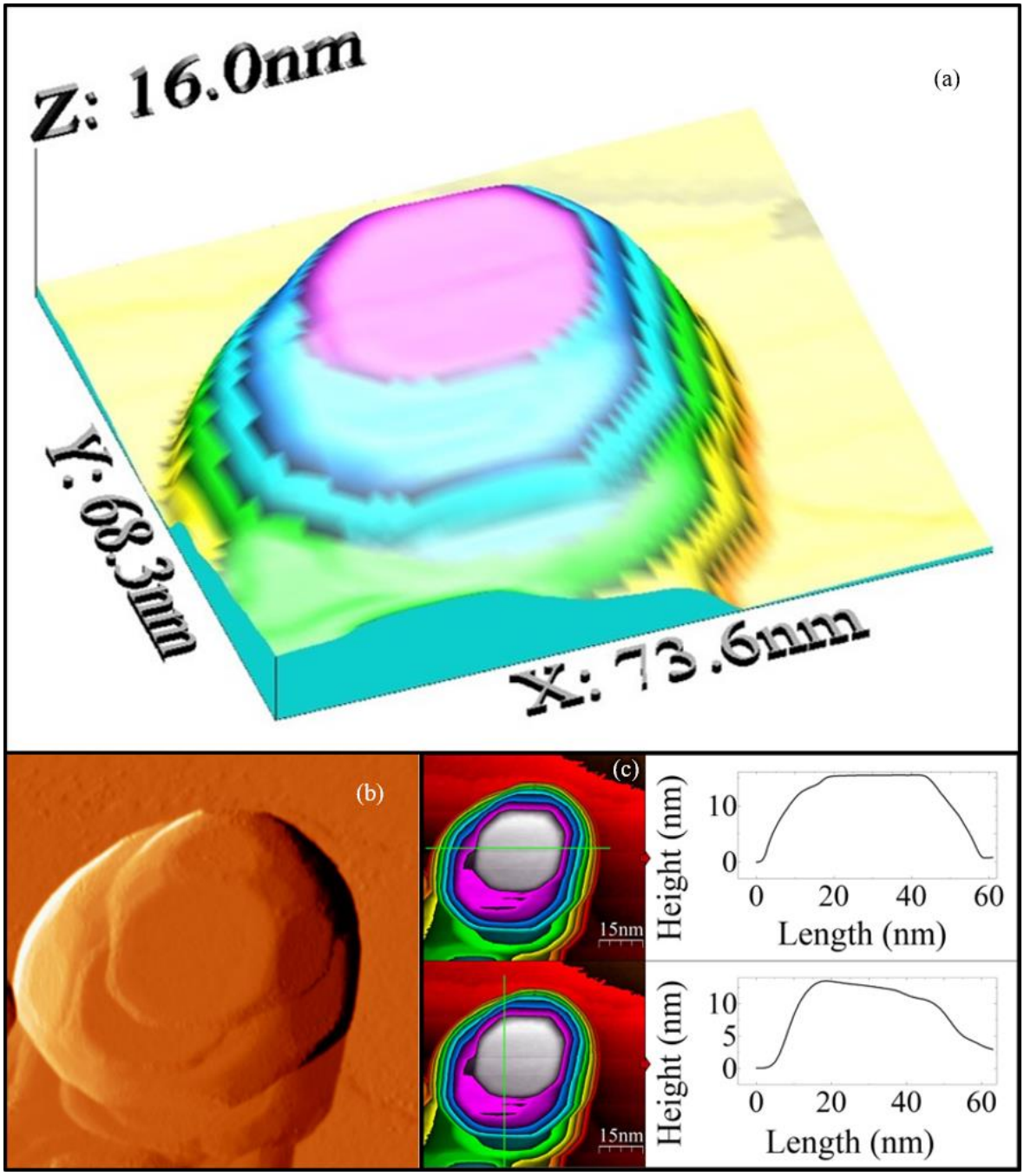


Figure 6-14: (a) 3D view of a chamfered square iron nanocrystal on $SrTiO_3$ (001). (b) Horizontal derivative of the STM image. (c) Horizontal and vertical lines and their respective surface profiles.

as 80 nm can be observed. The values of R_a, R_{rms}, H_a, and H_{max} are 1.99 ± 0.12 nm, 2.37 ± 0.14 nm, 6.46 ± 0.43 nm, and 13.19 ± 0.35 nm, respectively. To measure the faceting edge ratios of the top surface of the nanocrystals, background of the STM image was darkened using WSxM software until only top surface was visible as shown in Figure 6-15. The Wulff constructions based on theoretical surface energy values for bcc iron are listed in

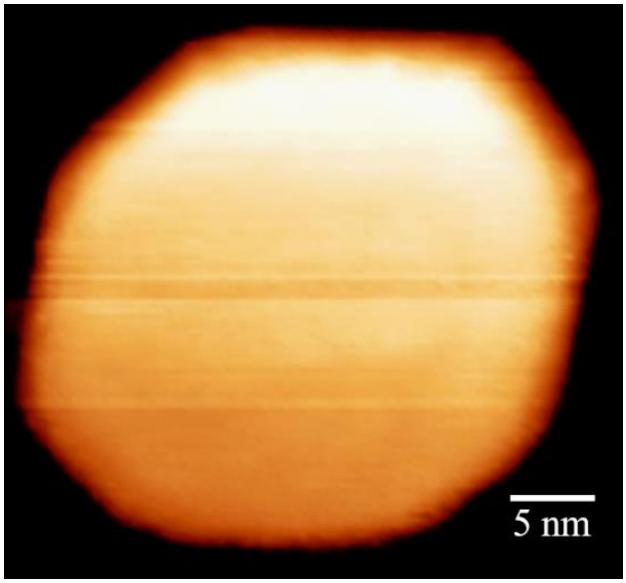


Figure 6-15: STM image of chamfered square iron nanocrystal with background darkened by WSxM software.

Table 6.4 and shown in Figure 6-16. The surface energy values were taken from Vitos et al. [208] to generate Wulff shape and then the energy values of the planes were changed until the faceting edge ratios of experimentally produced nanocrystals were achieved. The Wulff constructions based as theoretical surface energy values for fcc iron (previously listed in Table 6.2) are shown in Figure 6-17 (a-e). To get experimental faceting edge ratios, $\gamma_{\{110\}}$ was decreased and the resultant Wulff construction is shown in Figure 6-17

Table 6-4: Comparison of predicted surface energy values with current experimental results based on bcc iron for chamfered square iron nanocrystals.

Sr.	Facet	Vitos et al.	Current experimental values	% difference
1	{110}	2.43	2.43	0.0
2	{011}	2.222	2.222	0.0
3	{211}	2.589	2.589	0.0
4	{310}	2.393	2.543	-6.3
5	{111}	2.733	2.7333	0.0

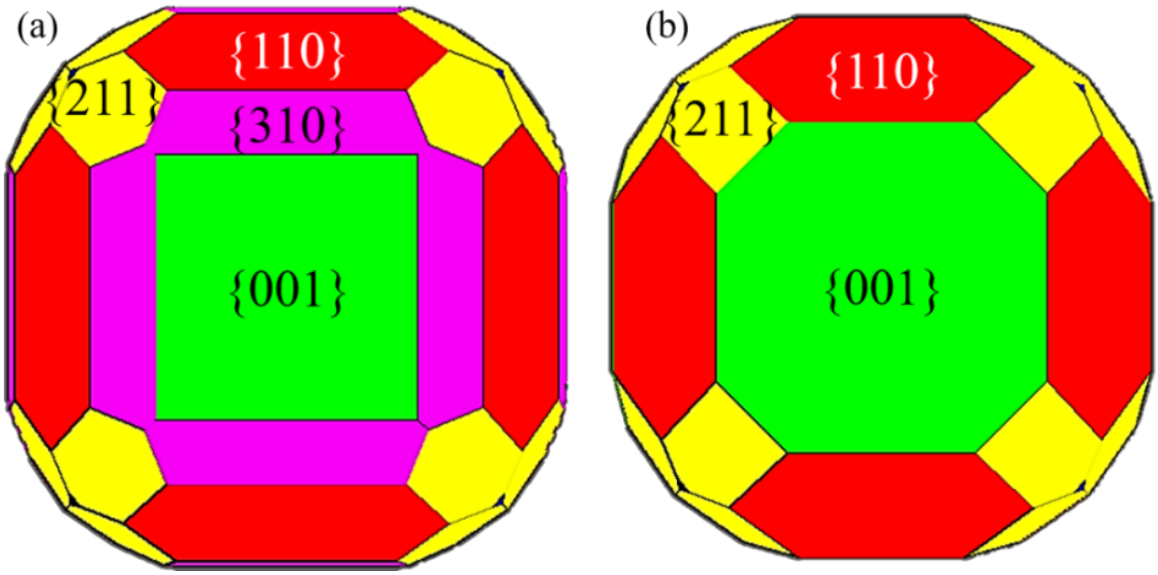


Figure 6-16: Wulff constructions with {001} as top facets based on (a) Vitos et al. [208] **and (b) current experimental results.**

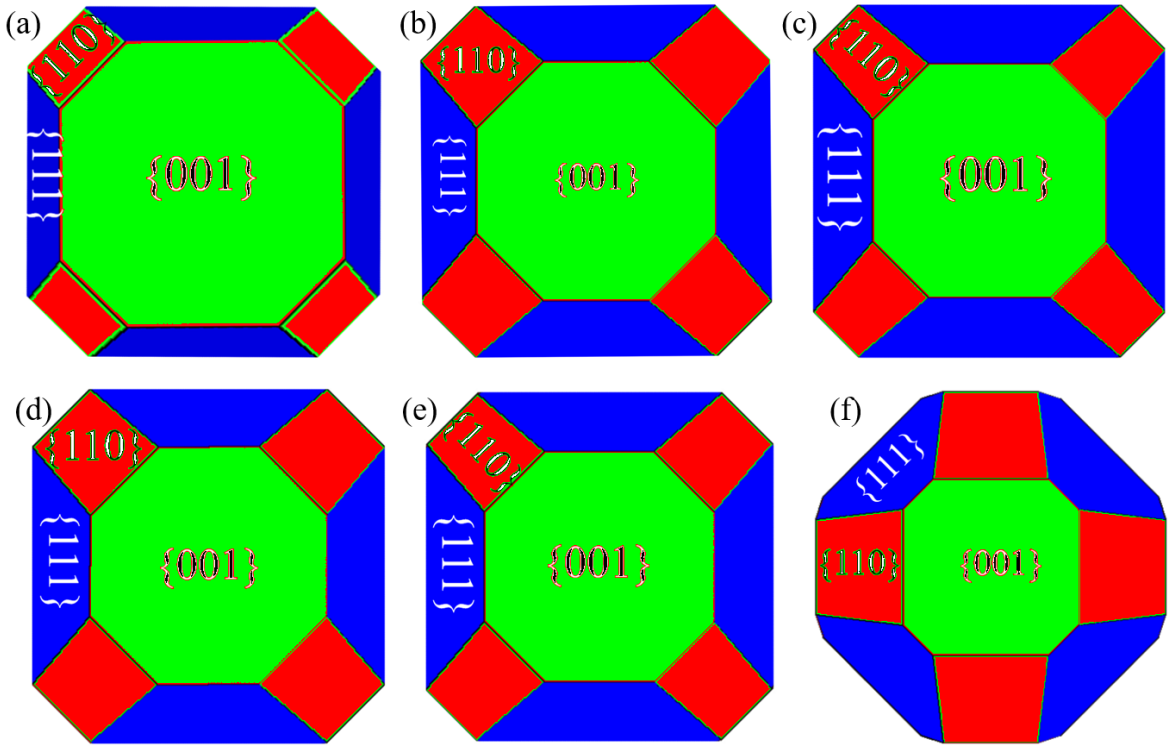


Figure 6-17: Wulff constructions with {001} as top facet for fcc iron based on different theoretical values and experimental results: (a) GGA-PW91 (unrelaxed), (b) GGA-PW91 (relaxed), (c) GGA-PBE (unrelaxed), (d) GGA-PBE (relaxed), (e) DFT (relaxed), (f) current experimental results.

(f). A comparison of Wulff constructions based as bcc and fcc iron with experimental results is shown in Figure 6-18. The predicted nanocrystal based on fcc iron is only

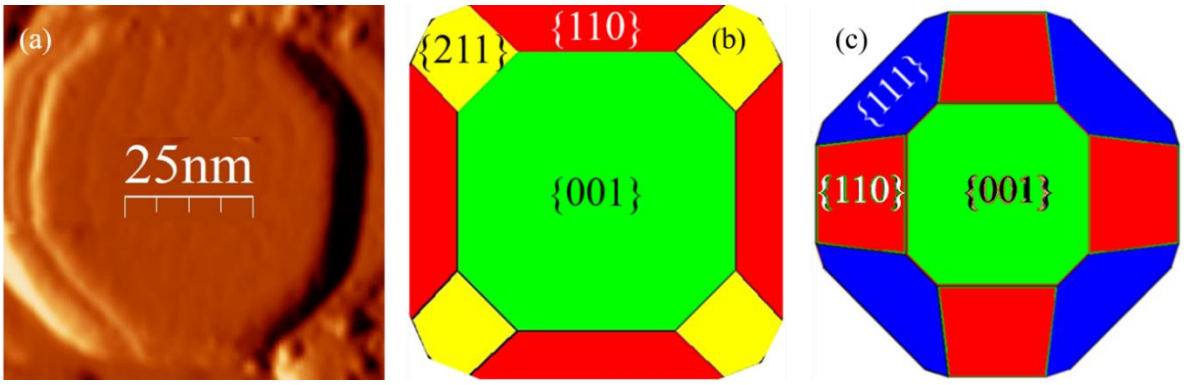


Figure 6-18: (a) Derivative of STM image of chamfered square iron nanocrystal. (b,c) Wulff constructions based on (b) bcc and (c) fcc iron.

comprised of low-index planes in contrast to the shape for bcc iron where {211} and {310} facets were also present. In addition {111} planes are missing from the Wulff construction based on bcc iron. Probability for the existence of {211} planes and {310} planes when {111} planes are missing is almost zero as they are high-index planes with high surface energy. In contrary, the probability that the nanocrystals comprise of low-index planes of {001}, {110}, {111} is very high. Therefore, it further hints that the square nanocrystals have fcc structure.

6.7 Co-existence of the two shapes

The results show that chamfered rectangular and chamfered square nanocrystals can coexist as shown in Figure 6-19 and Figure 6-20. The Wulff constructions for rectangular and square shapes based on bcc structure are shown in Figure 6-21. As previously mentioned, an hour post-anneal at 820 °C does not explain such a major transformation in which {111} planes completely disappear and {211} and {310} planes suddenly appear. On the other hand, if we consider fcc structure and analyze the Wulff constructions shown in Figure 6-22, we notice that nothing has changed but the orientation. If we turn

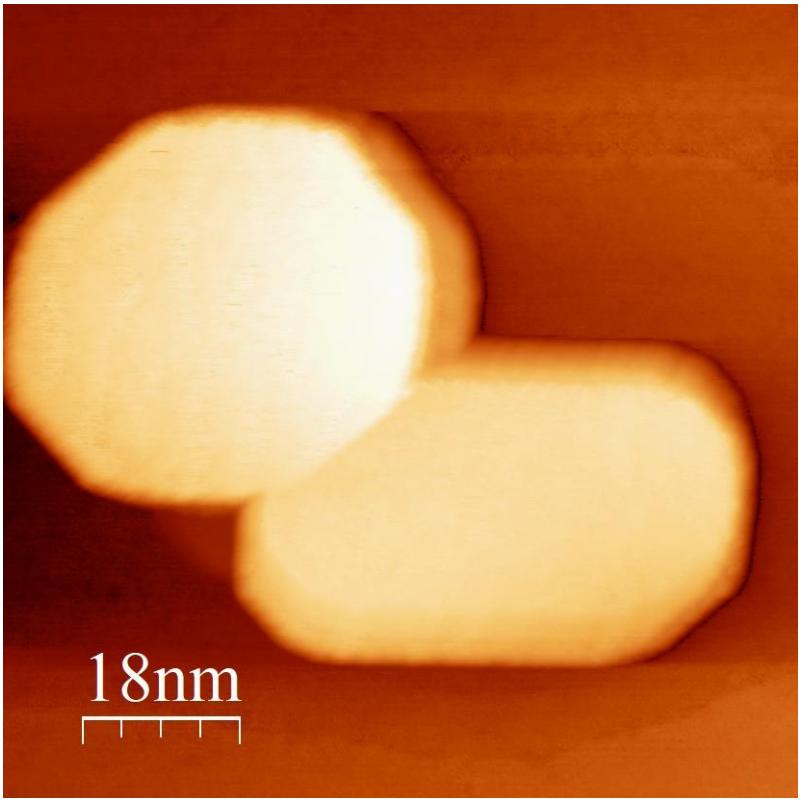


Figure 6-19: Connected chamfered rectangular and square iron nanocrystals on $SrTiO_3$ (001); V_s = 1.8 V, I_t = 0.1 nA.

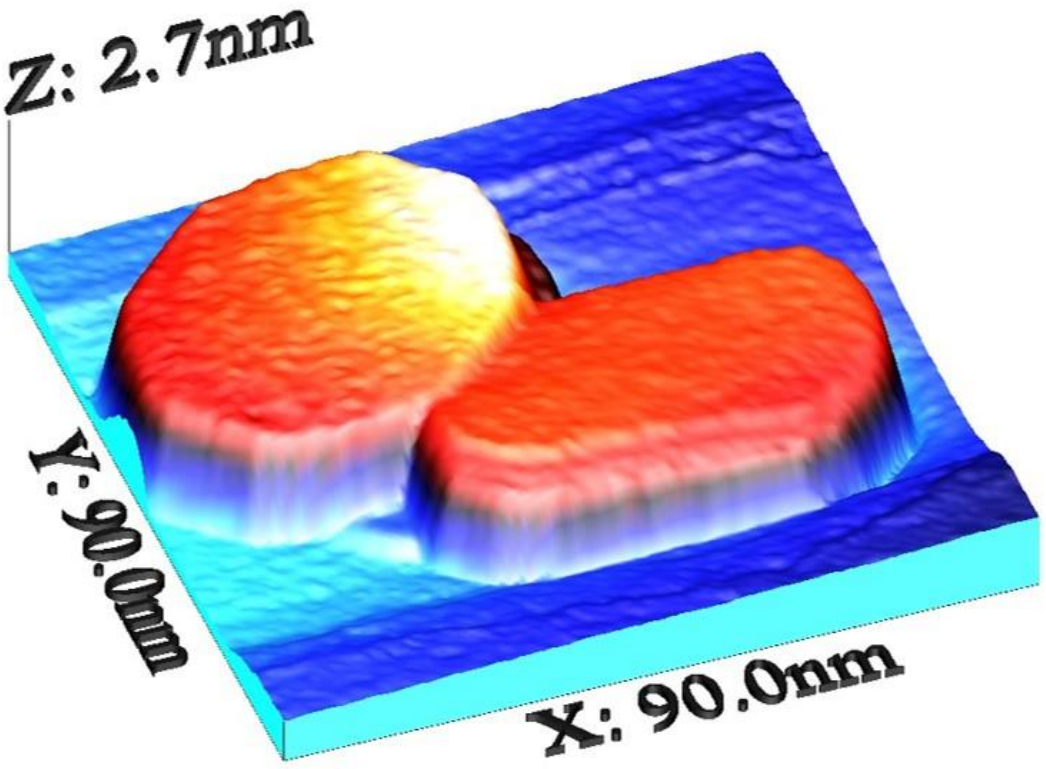


Figure 6-20: 3D view of the STM image.

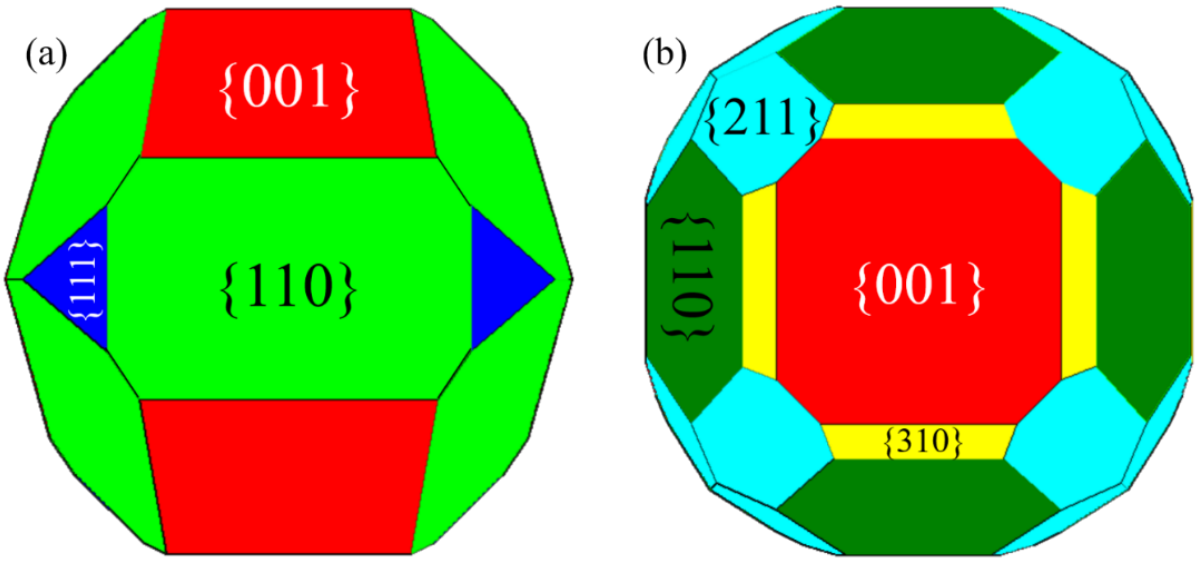


Figure 6-21: Proposed Wulff constructions for iron nanocrystals based on surface energy values for bcc iron: (a) {110} as top facet and (b) {001} as top facet.

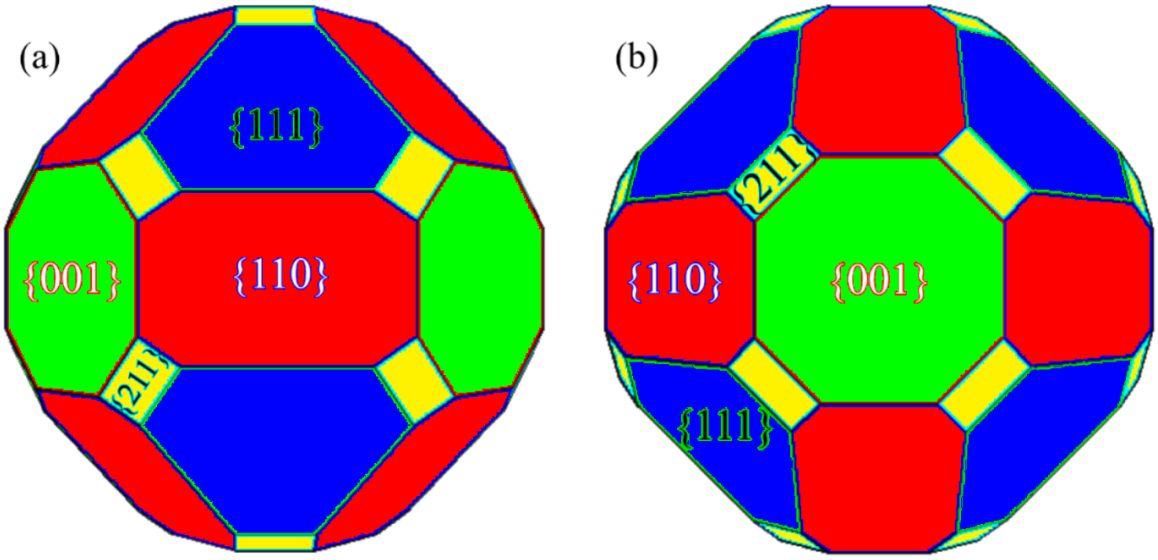


Figure 6-22: Proposed Wulff constructions for iron nanocrystals based on fcc iron: (a) {110} as top facet and (b) {001} as top facet.

Figure 6-22 (a) by 45°, we will get Figure 6-22 (b). This rotation can be easily justified based on multiple reasons. Firstly, as we provided thermal energy during post-annealing, the nanocrystals became more mobile than before. Secondly, the size increased after post-anneal at 820 °C which could cause this orientation change. Thirdly, as size increased, the lattice strain increases and to keep the system in lower energy state, system would have changed the nanocrystal orientation. Fourthly, there can be change in the composition. Iron

gets oxidized quickly, and there is plenty of oxygen in $SrTiO_3$ substrate. The possibility that a small amount of gas phase oxygen still comes into the lattice at a few structural defect sites and then diffuses through the bulk of the crystal, analogous to the Mars- Van Krevelen reaction mechanism in heterogeneous catalysis, can also be not completely ruled out [220]. The bulk, being the oxidant, is slightly reduced in the process of oxidizing the surface [221]. It has been reported that under equilibrium conditions, when sample is annealed up to ~950 °C under atmospheric pressure of 10^{-8} Pa, Fe_3O_4 is more stable phase than α-Fe_2O_3 [222]. The surface energy of the oxide formed would be such that it would have favored the formation of square-shaped nanocrystals. In addition, as the size increases, the contribution of the volume-dependent strain energy starts to dominate which can be an additional driving force for the variation in the morphology [223]. As the size further increases, it is more likely to find crystal lattice defects, such as dislocations and stacking faults, which result in the relaxation of the bulk strain energy (due to the disclination defect) [223]. In rectangular nanocrystals, the base facet is {110} on top of {001} of the substrate while in square nanocrystals, the base is {001}.

To continue study of the system and whether square shape evolves from rectangular shape or vice-versa, and whether this transformation is reversible, we further annealed the system at 820 °C for 1 h. To make a comparison with the earlier structure, an STM image before post-annealing at 820 °C is shown in Figure 6-23 where chamfered rectangular nanocrystals are predominant. After post-annealing at 820 °C, mainly chamfered square nanocrystals surrounded by irregular clusters were observed as shown in Figure 6-24. There were no clusters in this region before. It is likely that clusters are formed by Oswald ripening. If this is the case, then it suggests that chamfered square nanocrystals are the most stable geometric nanocrystals under the given set of conditions.

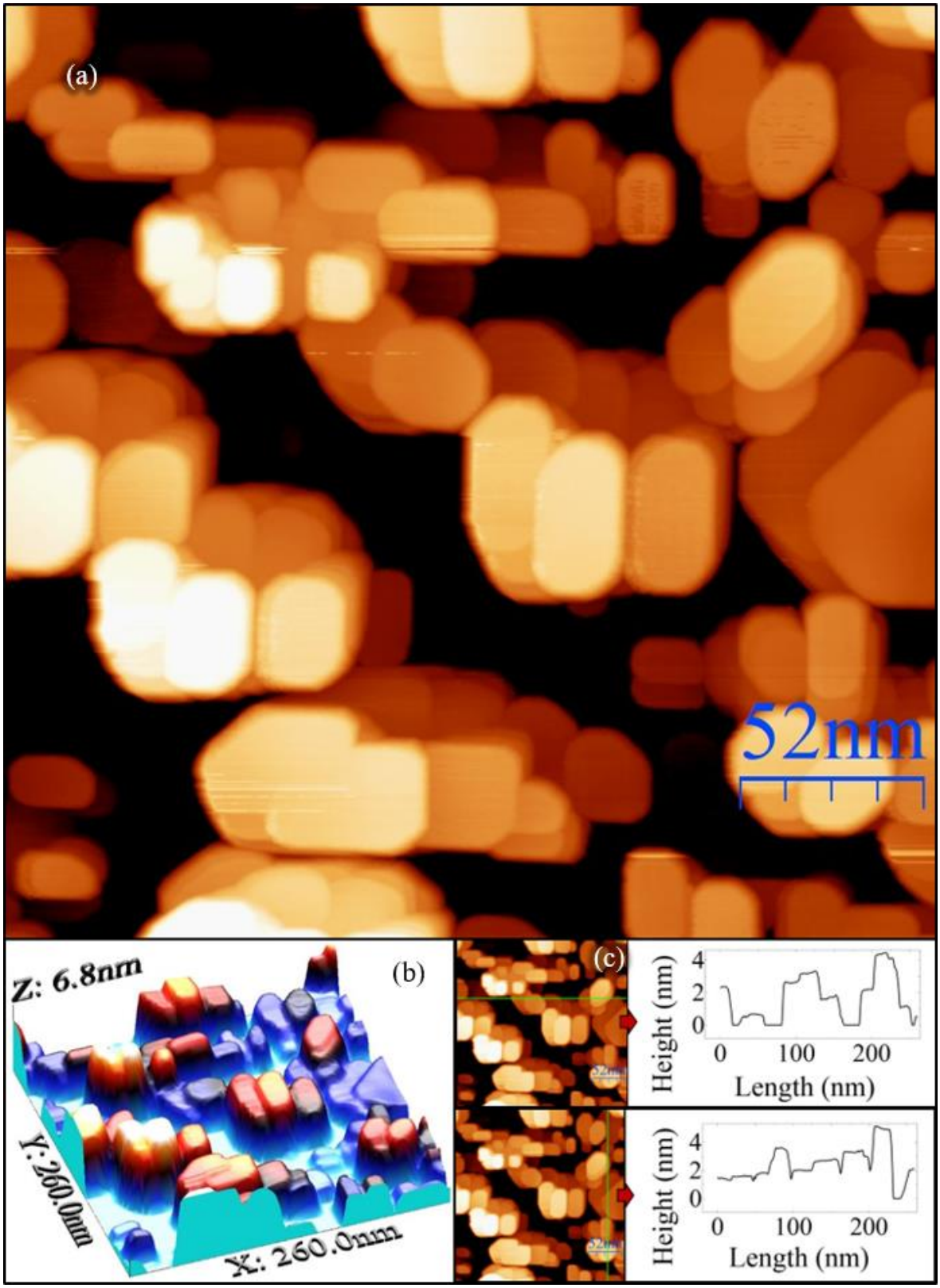


Figure 6-23: (a) Iron nanocrystals on $SrTiO_3$ (001) before post-annealing at 820 °C; V_s = 1.80 V, I_t = 0.2 nA. (b) 3D view. (c) Horizontal and vertical lines and their respective surface profiles.

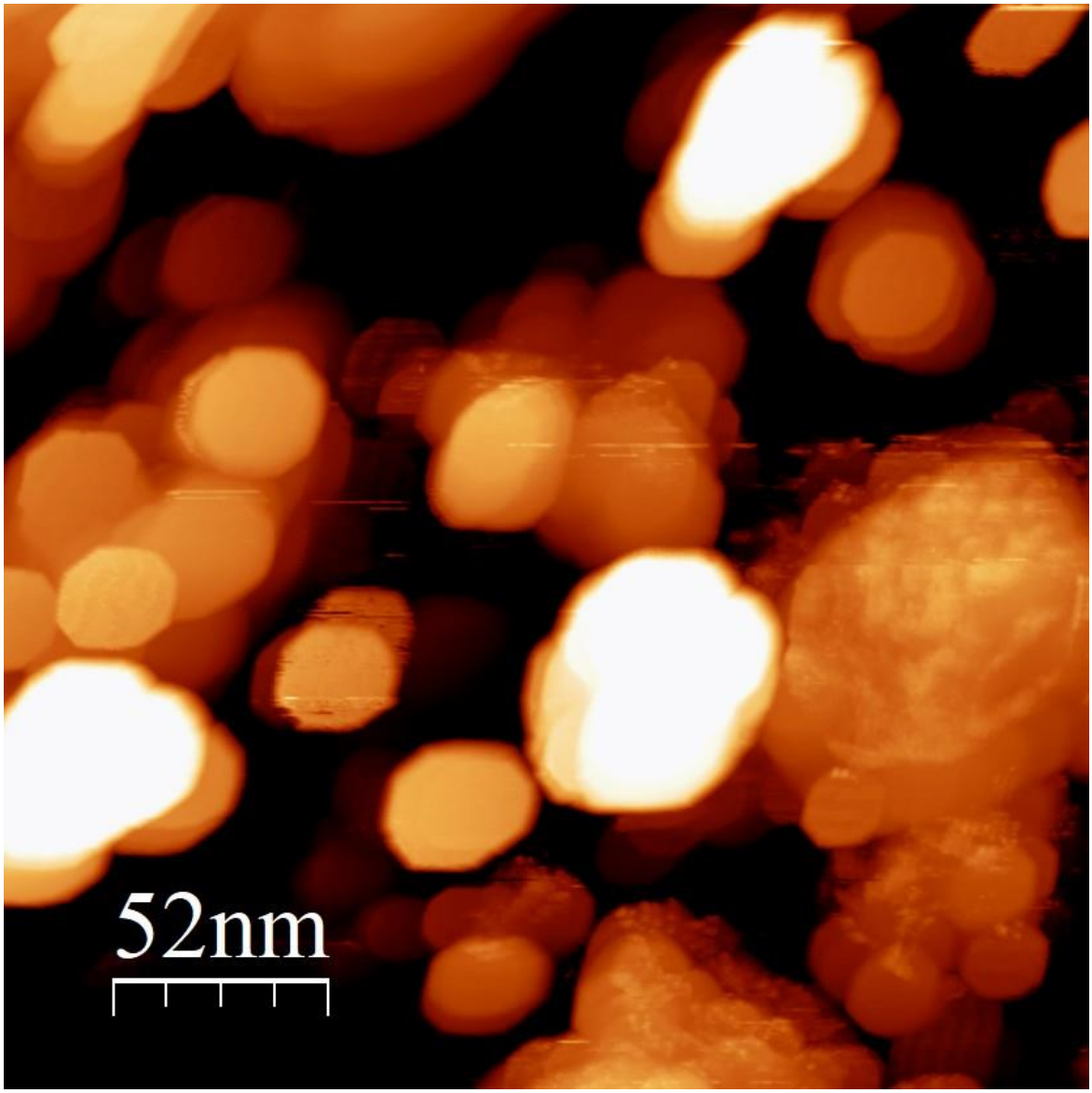


Figure 6-24: Iron nanocrystals on $SrTiO_3$ (001) after post-annealing at 820 °C for 1 h; V_s = 1.8 V, I_t = 0.1 nA.

6.8 Bias-dependence

The achieved nanocrystals had textured surface as shown in Figure 6-25 whose morphological details are shown in Figure 6-26. The nanocrystal is about 50 nm × 40 nm × 4 nm, surface of the nanocrystal has specific pattern whose magnified image is shown in Figure 6-27 [2,81]. The values of R_a, R_{rms}, H_a, and H_{max} are 0.23 ± 0.03 Å, 0.28 ± 0.04 Å, 1.06 ± 0.03 Å, and 1.77 ± 0.05 Å, respectively. Horizontal and vertical domains can be observed whose surface

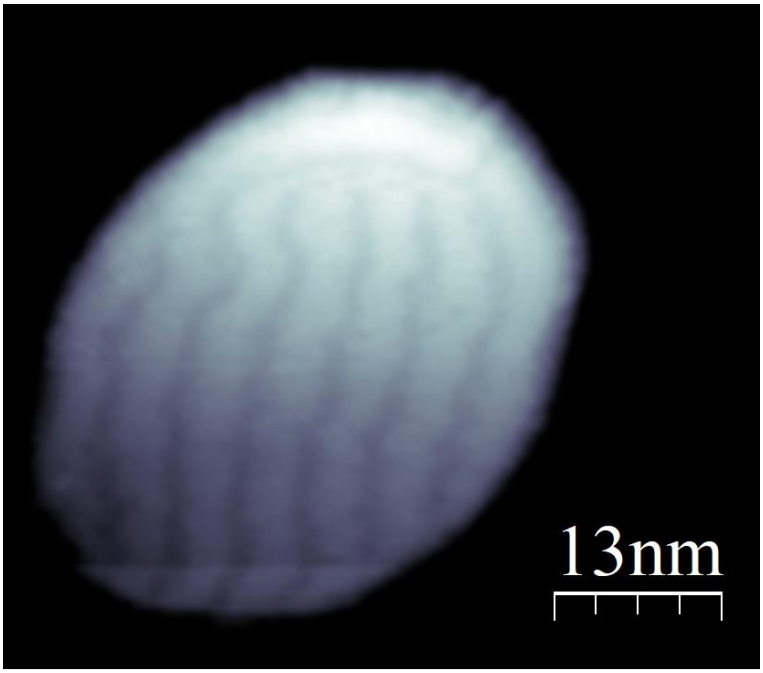


Figure 6-25: Iron nanocrystal with textured surface on $SrTiO_3$ (001); V_s = 1.8 V, I_t = 0.1 nA.

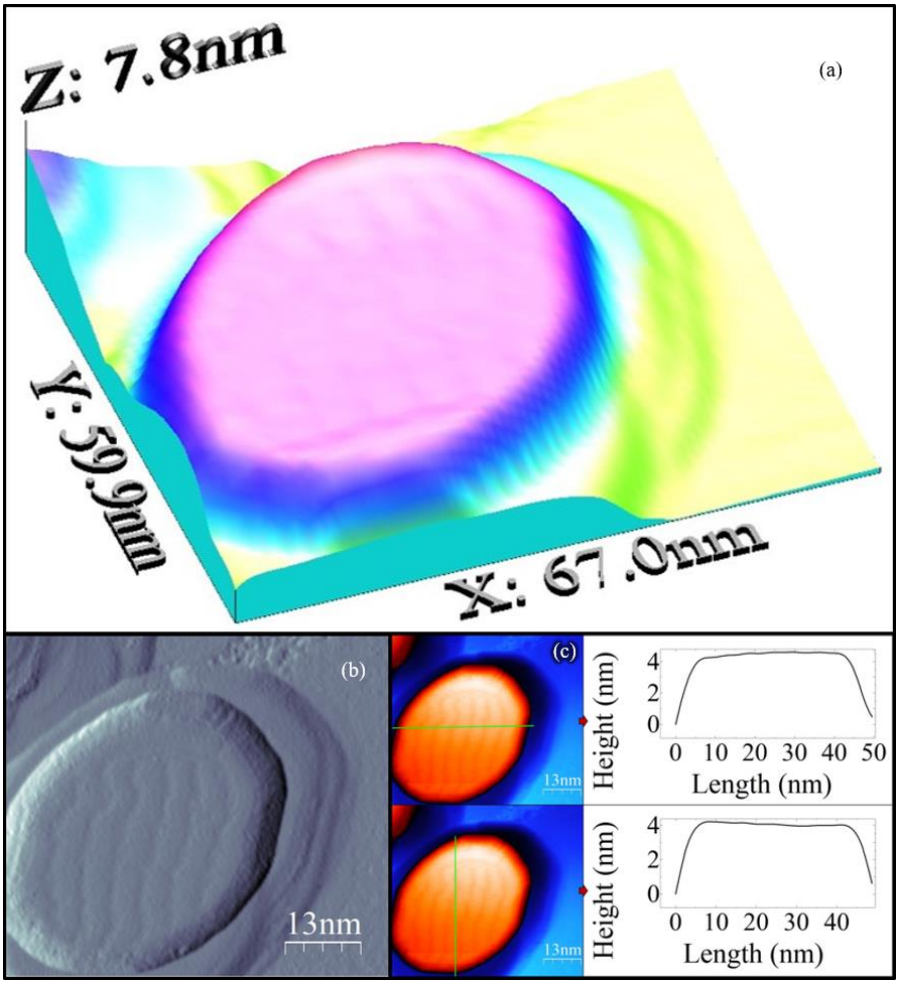


Figure 6-26: (a) 3D view and (b) horizontal derivative of the STM image. (c) Horizontal and vertical lines and their respective surface profiles.

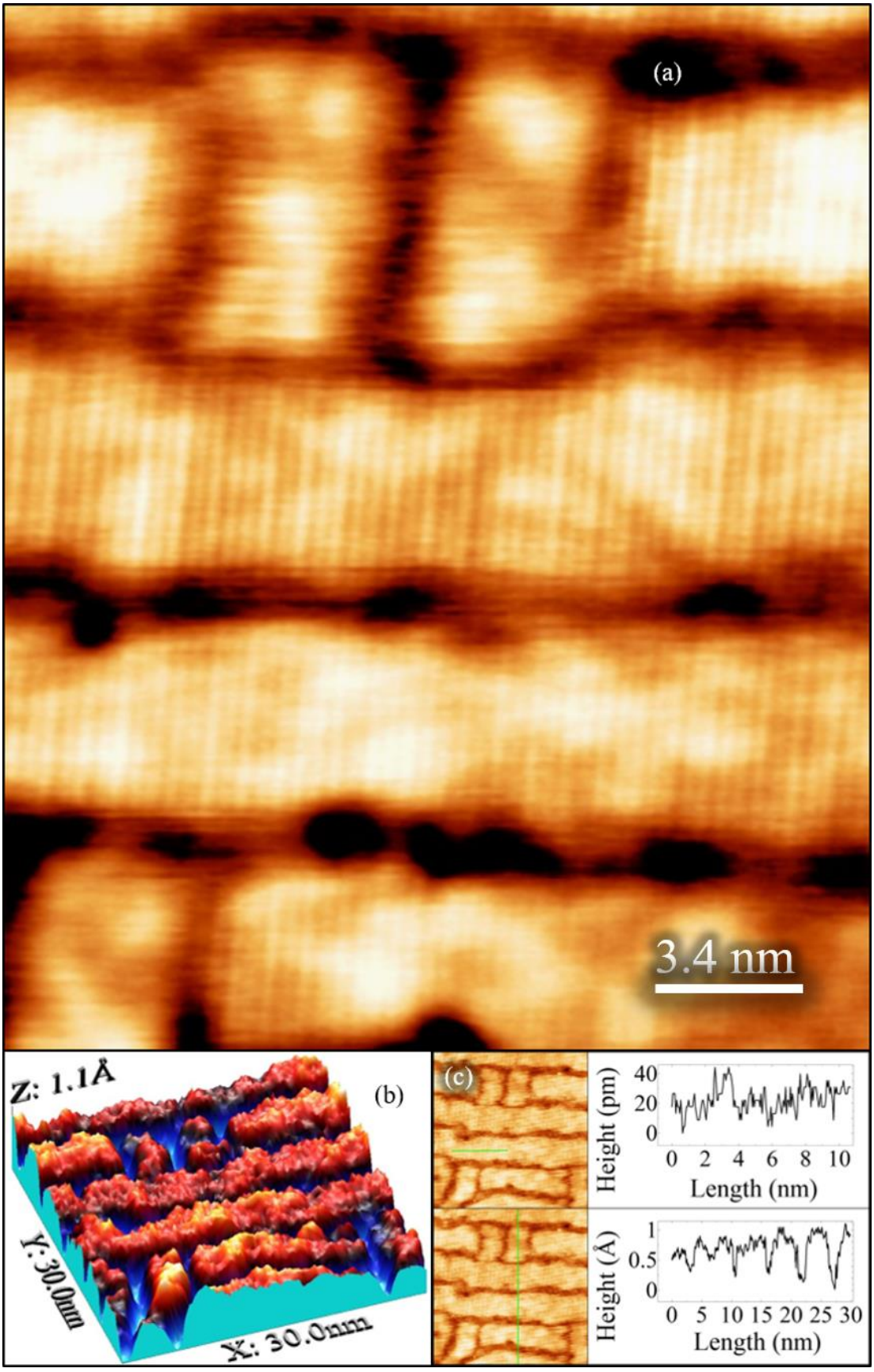


Figure 6-27: (a) Close shot of the surface texture; V_s = 2.0 V, I_t = 0.1 nA. (b) 3D view. (c) Horizontal and vertical lines and their respective surface profiles.

profile (Figure 6-27 (c)) shows that the height of the rows is around 20 pm. A further magnified image is shown in Figure 6-28. The horizontal distance between two bright

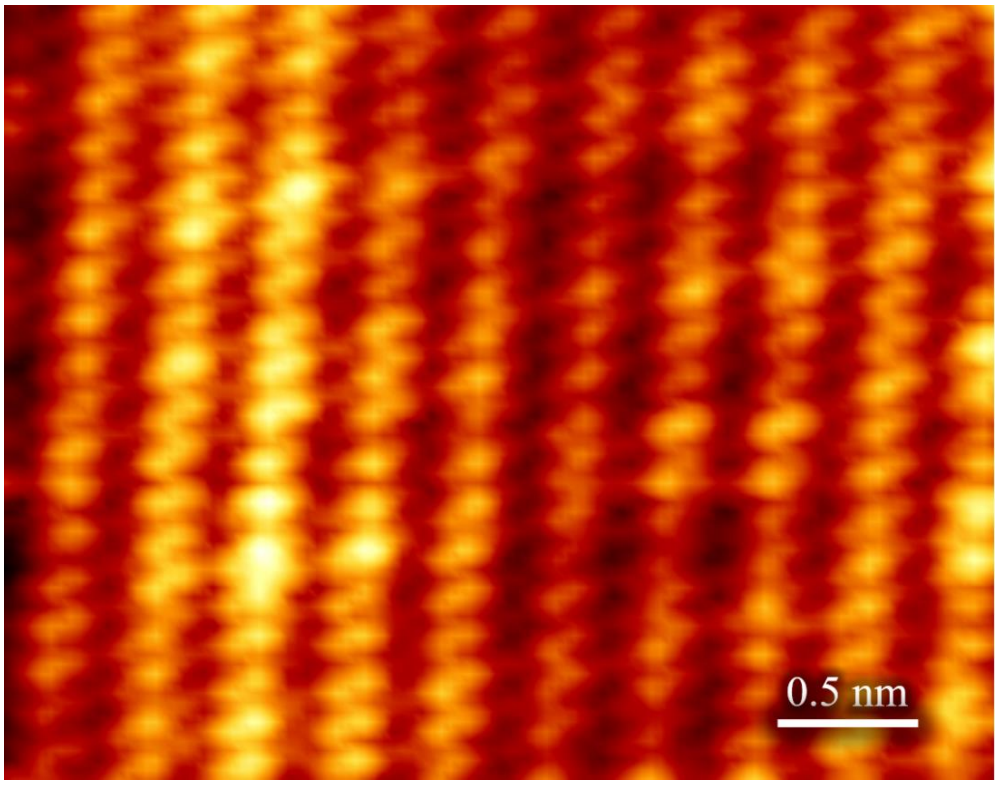


Figure 6-28: Atomic scale resolution of the surface texture.

spots is around 0.4 nm (which is close to the unit cell of $SrTiO_3$ (0.3905 nm)) while the vertical distance is around 0.28 nm (which is close to the unit cell of Fe (0.2866 nm)).

It was observed that these textures are bias-sensitive. When bias was changed, the texture changed as shown in Figure 6-29. There are two vertical domains in the second row (Figure 6-29 (b)). This image was taken at 1.8 V tip bias. The bias was then increased to 2 V. The left- hand vertical domain was eaten up by horizontal domain (Figure 6-29 (c-e)). Then bias was reversed to -0.61 V. The vertical domain became dark. The horizontal domains detached themselves and then reattached but with horizontal domains which were initially one step above/below them (Figure 6-29 (f-h)). This process was completed successfully and horizontally domains became slightly slanted (Figure 6-29 (i)). Then tip bias was reversed and fixed at 2.20 V. The resultant structure is shown in Figure 6-29 (ℓ). The two vertical domains in the second row have disappeared and the slightly slanted

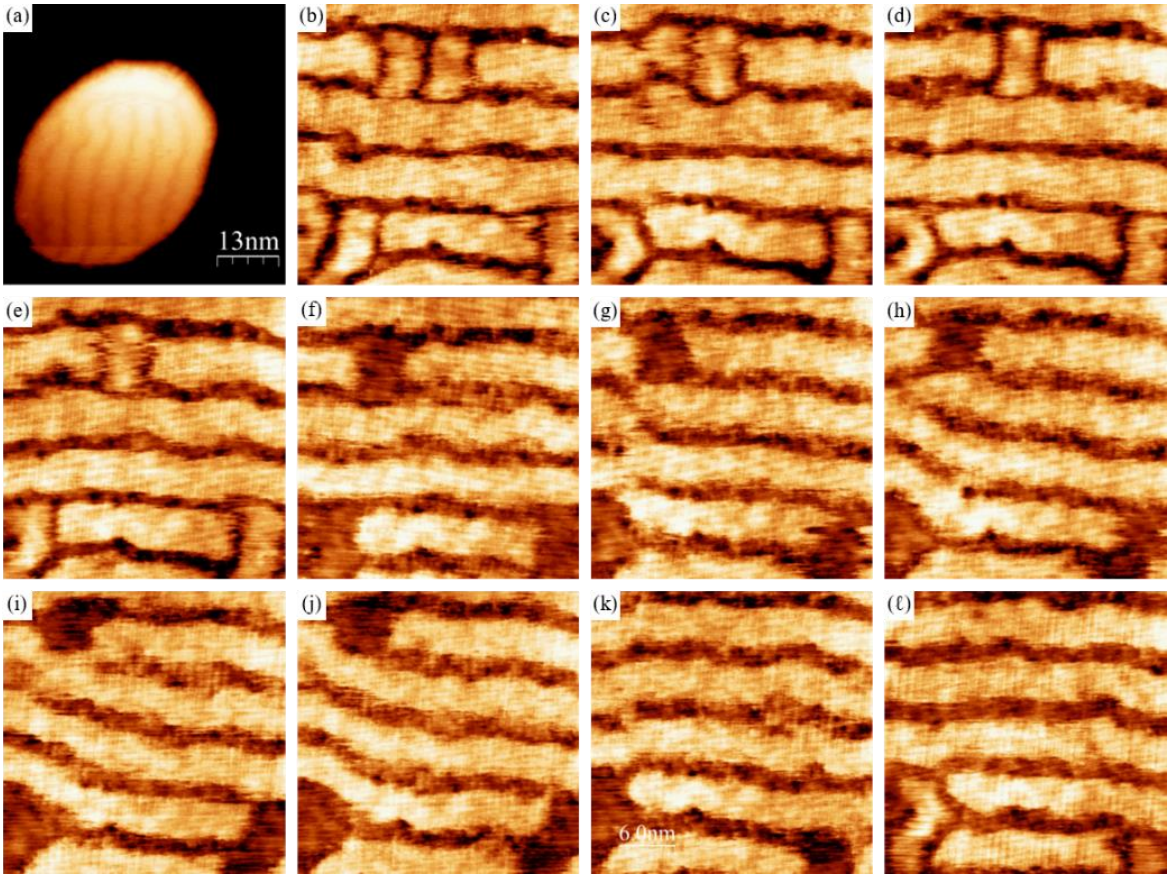


Figure 6-29: Bias-dependence of the surface texture: (a) V_s = 1.8 V, I_t = 0.1 nA, (b-e) V_s = 2.0 V, I_t = 0.1 nA, (f-h) V_s = -0.61 V, I_t = 0.2 nA, (i-k) V_s = -0.50 V, I_t = 0.2 nA, (ℓ) V_s = 2.20 V, I_t = 0.2 nA.

domains have again become horizontal. The real-time video showing the change in the surface texture with time and bias can be viewed using the link below.

https://www.dropbox.com/s/gb31x3nrk50mz0c/5.%20Fe%20on%20SrTiO3%20%28001%29.avi?dl=0

The exact composition of the surface cannot be predicted based on the STM images, however, this unique bias-dependence and mobility of the surface can have many potential applications in modern electronics and therefore should be a interesting topic for future research.

6.9 Fe on $SrTiO_3$ (110)

$SrTiO_3$ (110) substrate was sputtered (0.5 keV, 0.1 µA, 10 min) and then annealed at 900 ºC for 1 h. The resultant surface is shown in Figure 6-30. Two different periodicities were

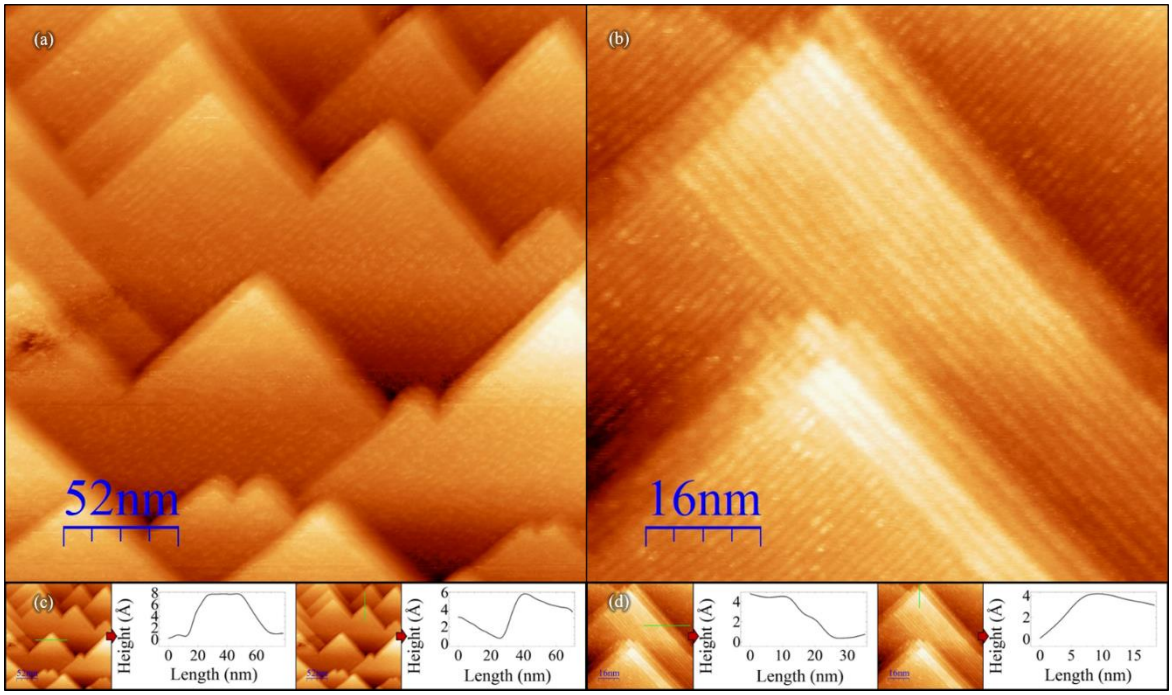


Figure 6-30: (a, b) $SrTiO_3$ (110) substrate used for Fe deposition; (a) V_s = 0.8 V, I_t = 0.1 nA; (a) V_s = 0.58 V, I_t = 50 pA. (c, d) Horizontal and vertical lines and their respective profiles. The periodicities are 1.612 ± 0.10 nm and 2.322 ± 0.11 nm that correspond to (4 × 1) and (6 × 1).

observed: 1.612 ± 0.10 nm that corresponds to (4 × 1) reconstruction and 2.322 ± 0.11 nm that corresponds to (6 × 1) reconstruction. Fe was deposited for 1 min and system was post-annealed twice: (520 ºC, 6 h) and (620 ºC, 6 h). The sample was imaged but its coverage was very low. Then Fe was deposited for 15 sec and the system was post-annealed for five times: (320 ºC, 6 h), (360 ºC, 6 h), (620 ºC, 6 h), (720 ºC, 1 h) and (820 ºC, 1 h). The coverage was still low. Fe was then deposited for the third time for 15 sec and system was post-annealed at 360 ºC for 6 h. Fe coverage was still very low. Then Fe was deposited for the fourth time for 15 sec and the system was post-annealed twice: (360 ºC, 6 h) and (520 ºC, 1 h). The resultant structure is shown in Figure 6-31. Fe formed small islands with no definite geometric shape. Fe was then deposited for the fifth time for 15 sec and the system was post-annealed thrice: (360 ºC, 6 h), (520 ºC, 1 h) and (720 ºC, 1 h) and (320 ºC, 1 h). The resultant structure is shown in Figure 6-32. The surface got covered in rectangular layers. They can be one or two atom thick layers of Fe. As there is oxygen

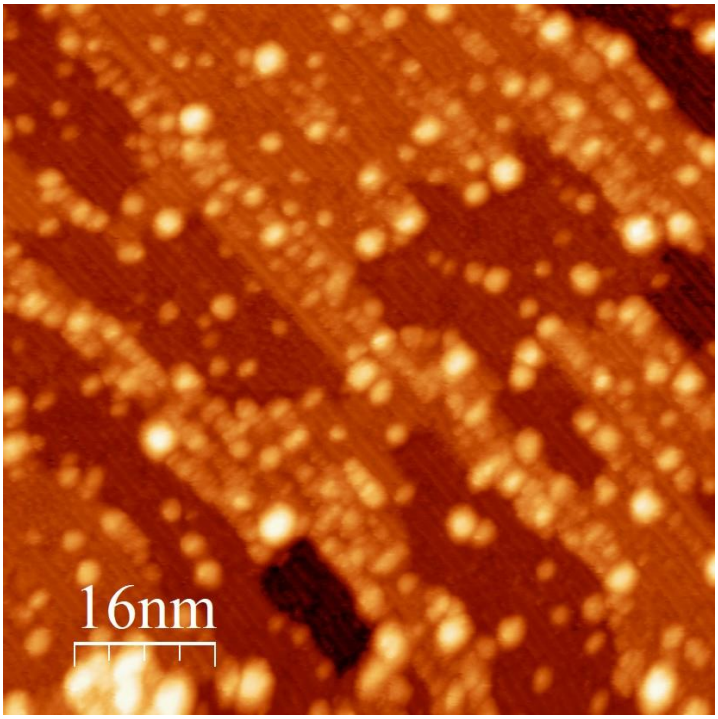


Figure 6-31: Fe on $SrTiO_3$ (110); V_s = 0.92 V, I_t = 50 pA.

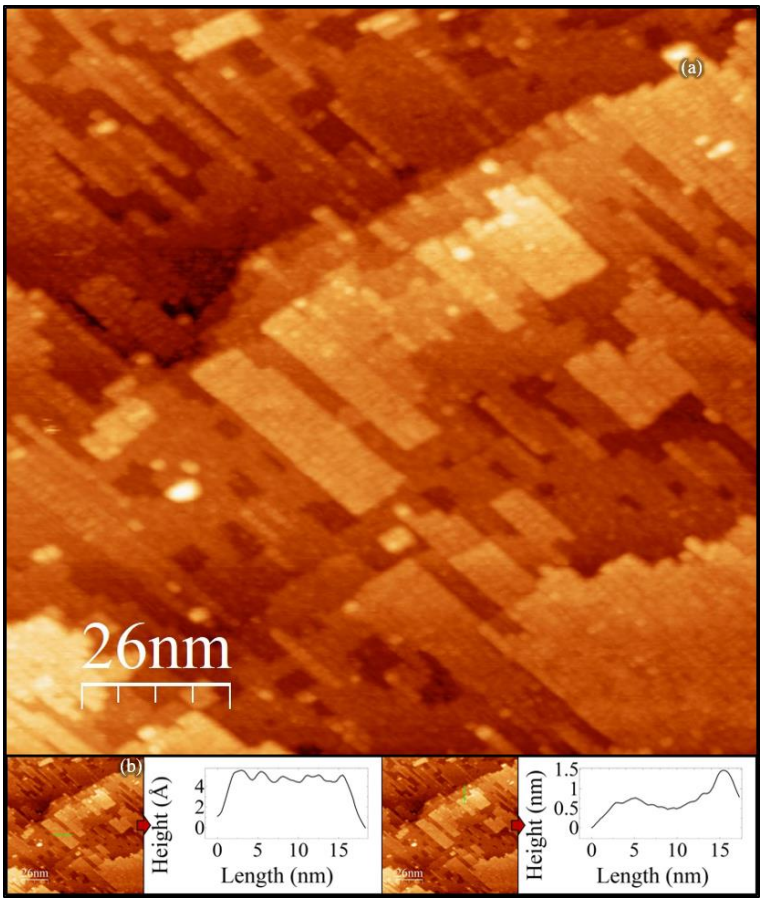


Figure 6-32: Fe on $SrTiO_3$ (110); V_s = 0.8 V, I_t = 50 pA. The system was post-annealed twice; (720 °C, 1 h), (320 °C, 1 h).

in the structure and possibly in the chamber, there is a possibility that some Fe has been oxidized. On the sample, Fe was deposited for the seventh time and the system was post-annealed at 320 ºC for 6 h. Then Fe was deposited for the ninth time and the system was post-annealed for five times: (320 ºC, 6 h), (520 ºC, 6 h), (620 ºC, 6 h), (720 ºC, 1 h) and (720 ºC, 1 h). Then Fe was deposited for the tenth time and the system was post-annealed twice: (720 ºC, 1 h) and (820 ºC, 1 h). The resultant structure is shown in Figure 6-33. The

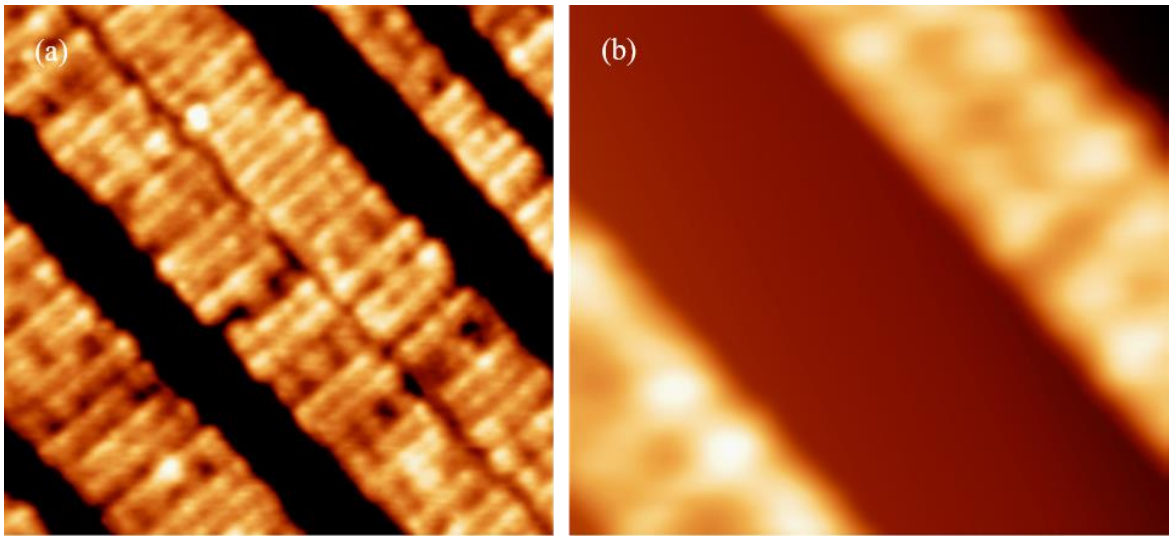


Figure 6-33: Fe on $SrTiO_3$ (110); V_s = 0.53 V, I_t = 0.1 nA. The periodicity of atoms within one row is (2 × 1) while two rows are separated by a distance of six atomic spacing.

periodicity of atoms within one row is (2 × 1) while two atoms are separated by a distance of six atomic spacing. When the same system was observed the next day, rod-like clusters were observed as shown in Figure 6-34. Ordered structure can still be observed around the rod-like clusters. The height of rod-like clusters is about 2 nm and length is around 40-50 nm. This system was post-annealed one more time at 820 ºC for 1 h. The resultant structure is shown in Figure 6-35. The rod-like clusters are still present while it appears as if the whole system is trying to change into rod-like structure. This system was post-annealed one more time at 820 ºC for 1 h. The resultant structure is shown in Figure 6-36. The rod-like clusters still persist while the background has become flat. The rod-like

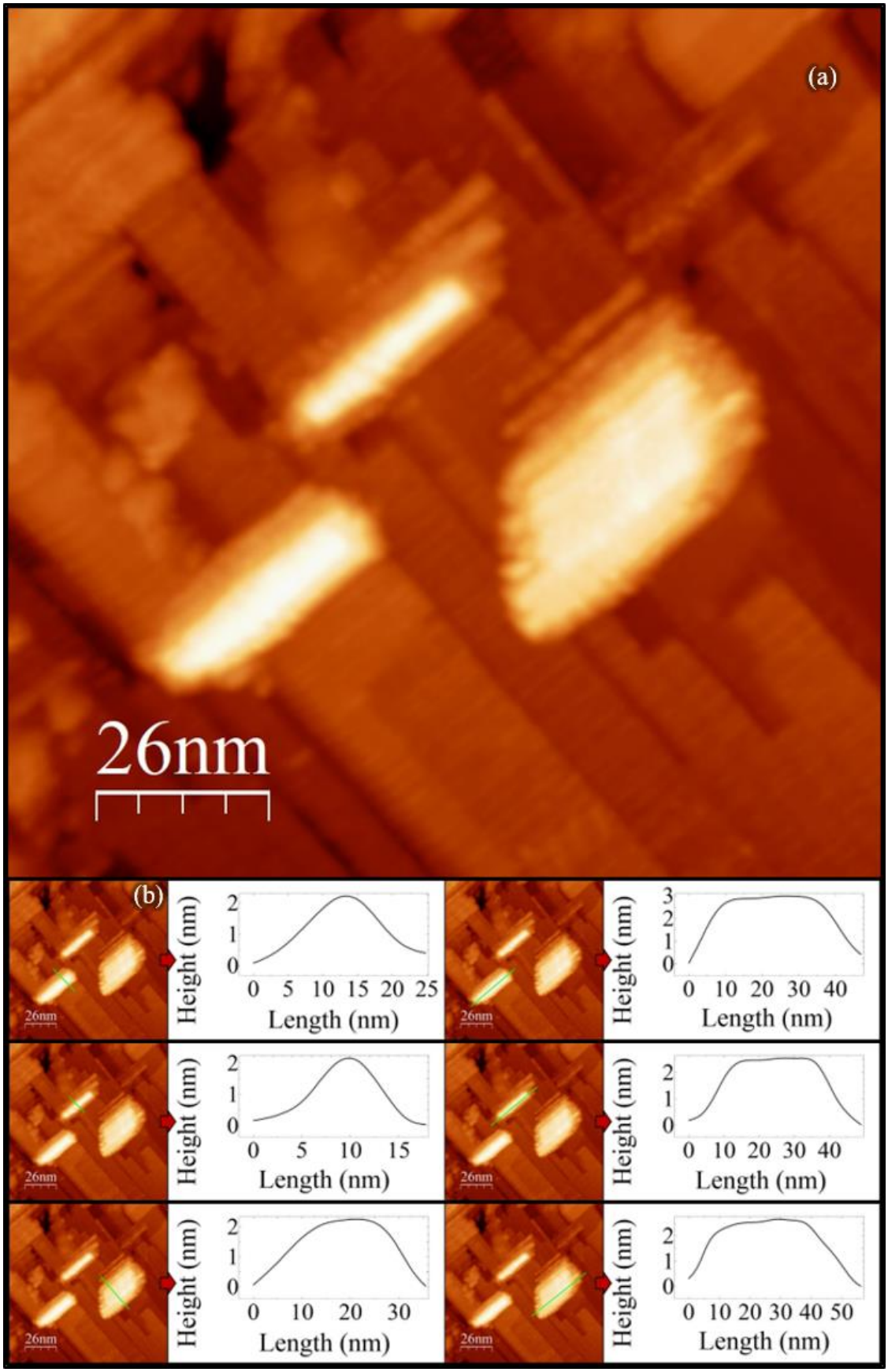


Figure 6-34: Fe on $SrTiO_3$ (110); V_s = 0.53 V, I_t = 0.1 nA. The system was post-annealed twice; (720 °C, 1 h), (820 °C, 1 h).

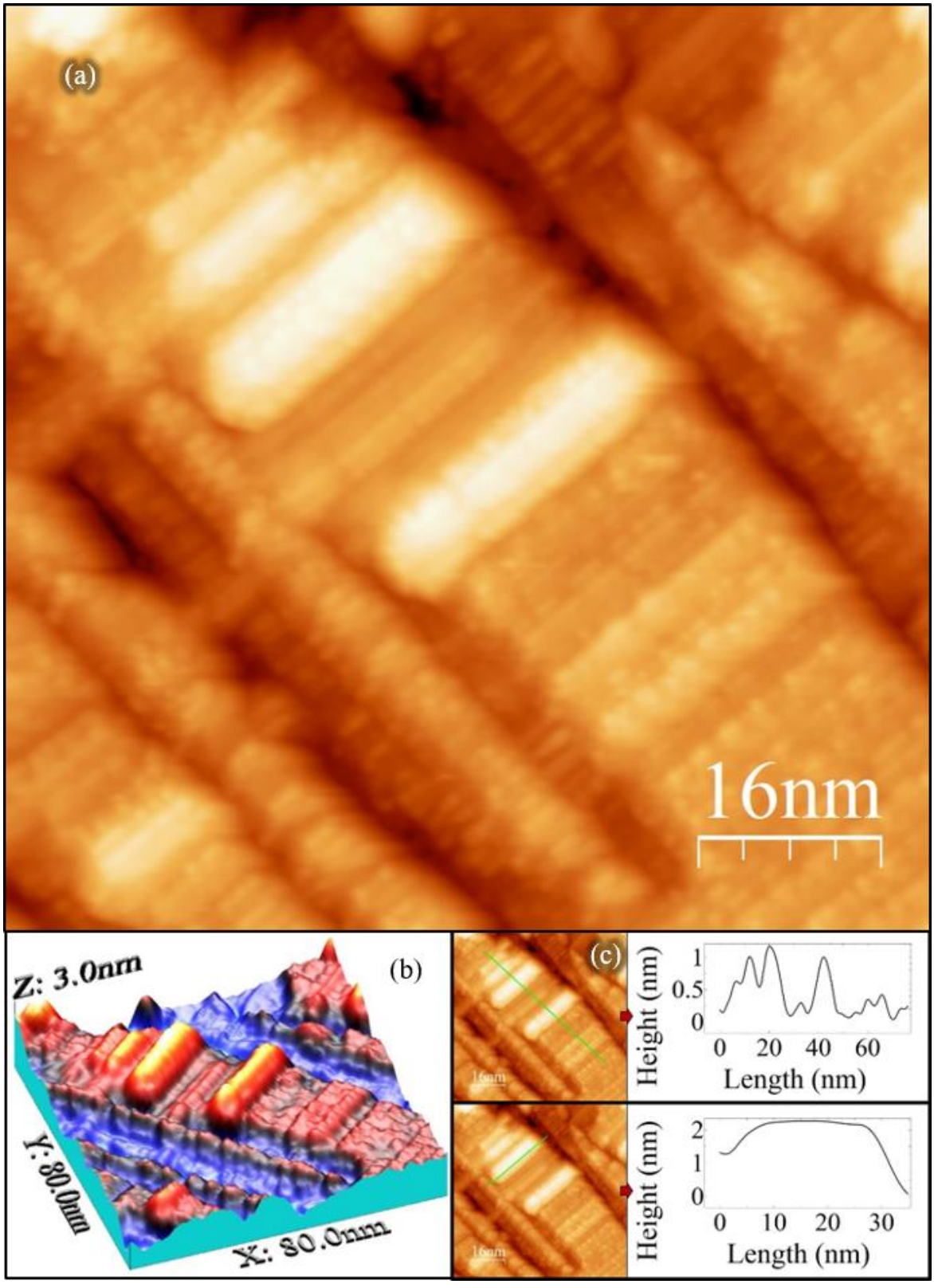


Figure 6-35: Fe on $SrTiO_3$ (110); V_s = 0.8 V, I_t = 0.1 nA. The system was post-annealed thrice; (720 °C, 1 h), (820 °C, 1 h), (820 °C, 1 h).

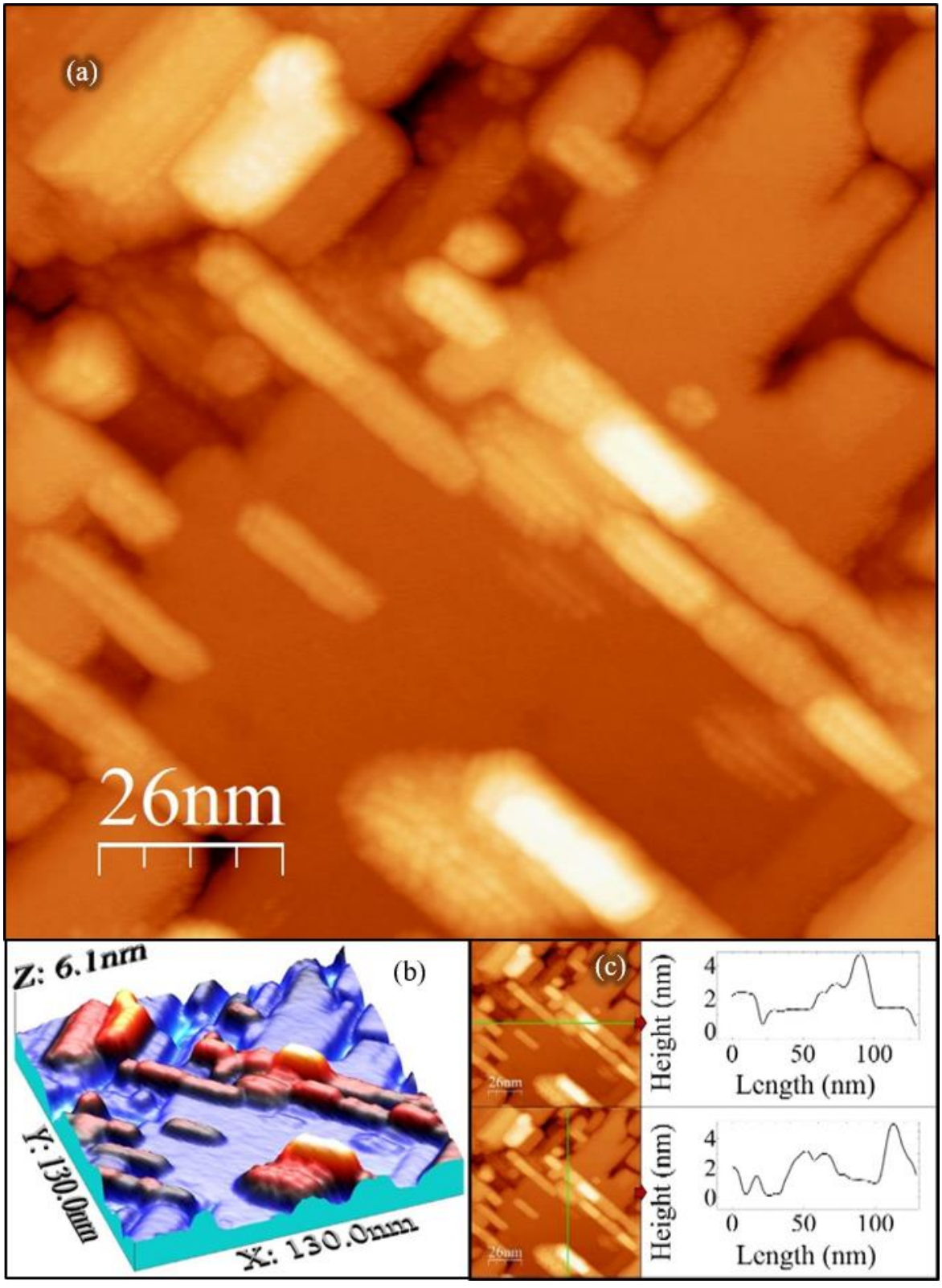


Figure 6-36: Fe on $SrTiO_3$ (110); V_s = 1.14 V, I_t = 20 pA. The system was post-annealed four times; (720 °C, 1 h), (820 °C, 1 h), (820 °C, 1 h), (820 °C, 1 h).

nanocrystals of Ni showed clear facets on $SrTiO_3$ (110). However, although Fe formed rod-like clusters, facets were not observed in this work.

6.9.1 Fe on $SrTiO_3$(111)

$SrTiO_3$ (111) substrate was sputtered (0.5 keV, 2.3 µA, 10 min) and annealed at 900 ºC for 1 h. The resultant structure is shown in Figure 6-37. The periodicity is 2.34 ± 0.026 nm that

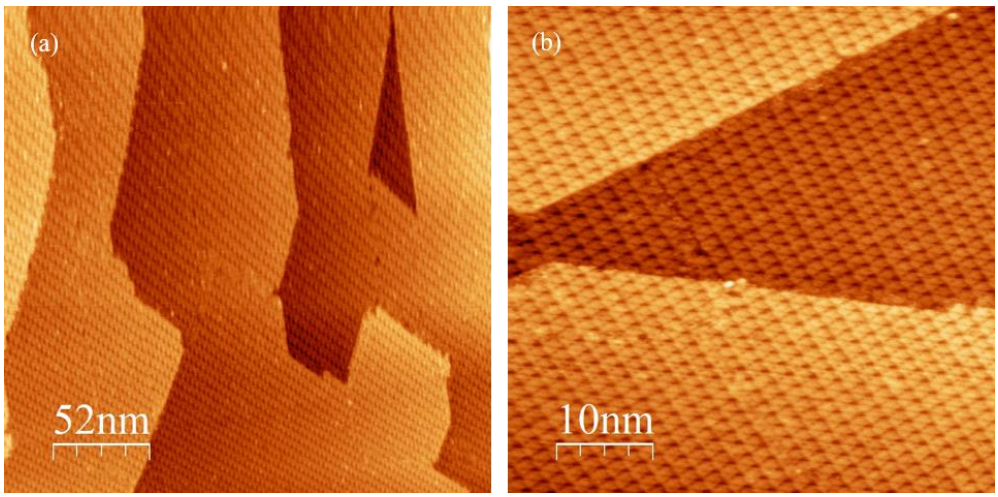


Figure 6-37: (a,b) $SrTiO_3$ (111) substrate used for Fe deposition; (a) V_s = 1.50 V, I_t = 0.1 nA, (b) V_s = 1.04 V, I_t = 0.1 nA. The periodicity is 2.34 ± 0.026 nm that corresponds to (6 × 6) reconstruction.

corresponds to (6 × 6) reconstruction. The substrate was heated to 320 ºC and Fe was deposited for 1 min. The system was post-annealed twice: (520 ºC, 6 h) and (850 ºC, 1 h). The resultant structure is shown in Figure 6-38-Figure 6-39. Fe grew in the form of

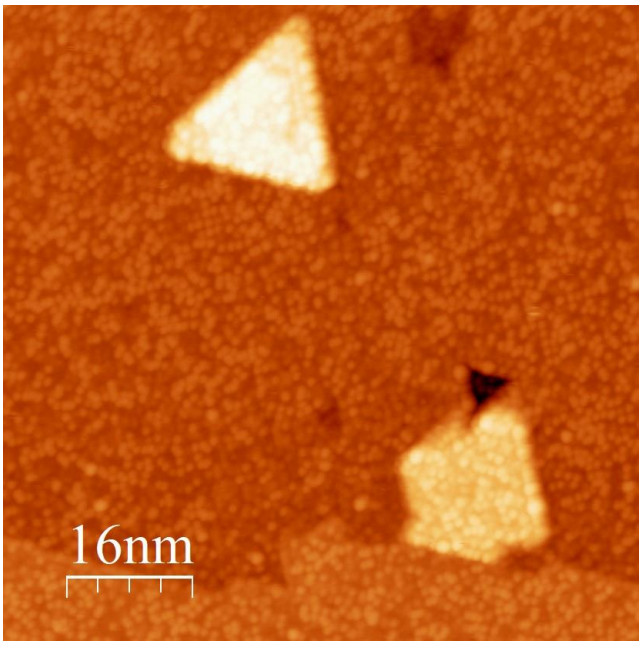


Figure 6-38: Fe on $SrTiO_3$ (111); V_s = 1.20 V, I_t = 50 pA.

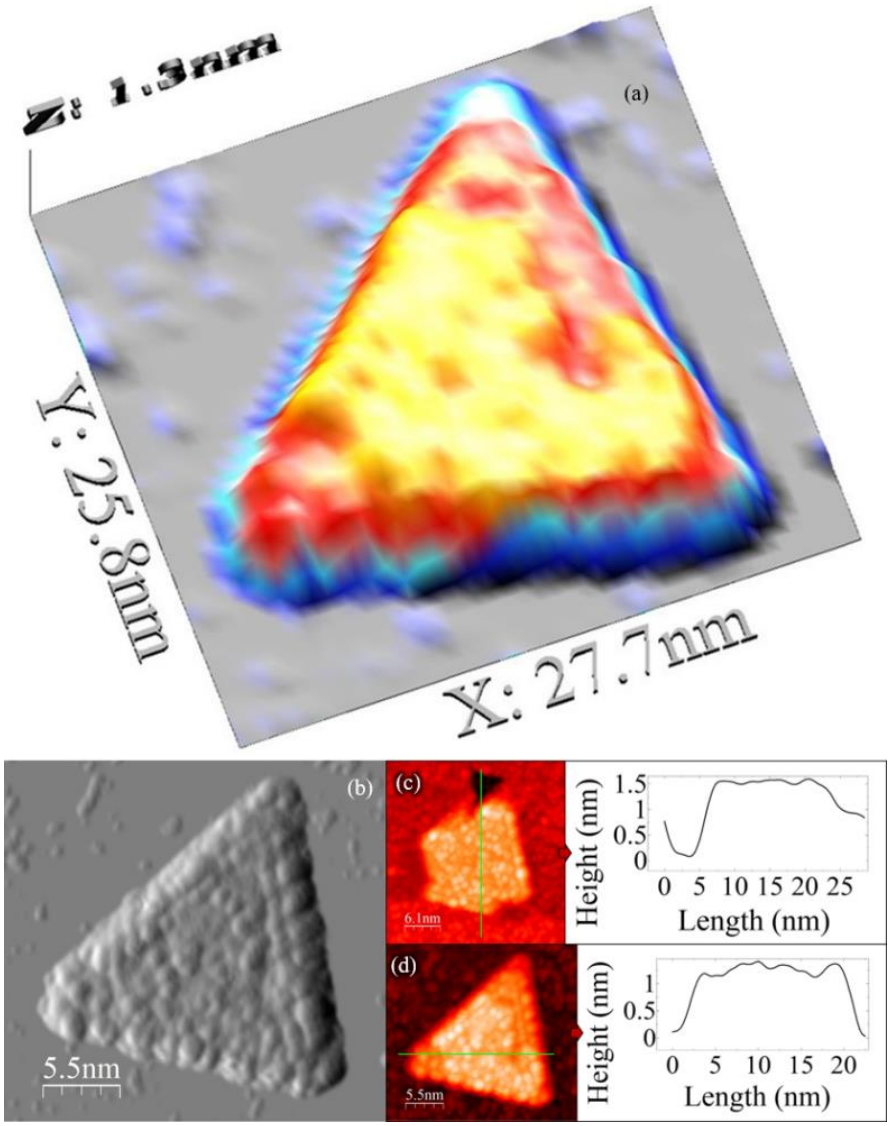


Figure 6-39: (a) 3D view of Fe on $SrTiO_3$ (111); V_s = 1.20 V, I_t = 50 pA. (b) Derivative of STM image. (c,d) two nanocrystals and their respective profiles.

triangular nanocrystals. The height of nanocrystal is about 1.3 nm while length is about 20 nm.

To investigate the Wulff shape, Wulffman software was used. The parameters used for Wulffman simulation are listed in Table 6-5 and resulted Wulff constructions are shown in Figure 6-40. The surface energy values were taken from Vitos et al. to generate Wulff shape and then the energy values of planes were changed until the edge ratios of nanocrystals produced were achieved. The surface energy ratios obtained from the experiment are: $\gamma_{001}/\gamma_{111} = 0.841$, $\gamma_{110}/\gamma_{111} = 0.919$, $\gamma_{001}/\gamma_{110} = 0.914$, $\gamma_{211}/\gamma_{310} = 1.082$. The

Table 6-5: Parameters used for Wulffman simulation.

Parameter	Values
Crystal system	Cubic
Point group	$m\bar{3}m$
Plane-1	Miller indices = {110}
	Surface energy: $\gamma_{110} = 2.430\ J/m^2$
	Plane color: Red
Plane-2	Miller indices = {001}
	Surface energy: $\gamma_{001} = 2.222\ J/m^2$
	Plane color: Green
Plane-3	Miller indices = {211}
	Surface energy: $\gamma_{211} = 2.589\ J/m^2$
	Plane color: Yellow
Plane-4	Miller indices = {310}
	Surface energy: $\gamma_{310} = 2.393\ J/m^2$
	Plane color: Blue
Plane-5	Miller indices = {111}
	Surface energy: $\gamma_{111} = 2.643\ J/m^2$
	Plane color: Pink
Crystal shape	Truncated pyramid
Area	79.81 nm^2
Volume	63.87 nm^3
Facets	74
Edges	216
Vertices	144

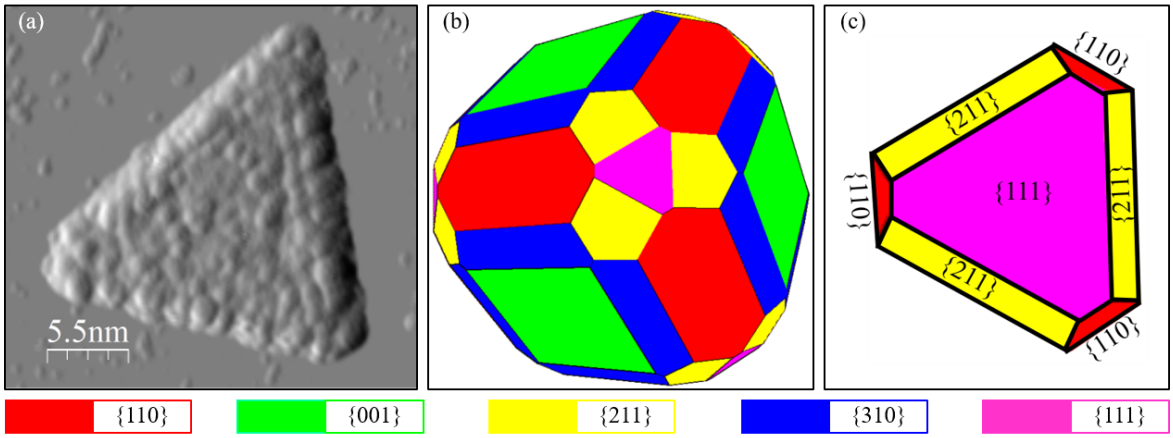


Figure 6-40: Wulffman simulations of equilibrium crystal shapes (ECS) of Fe nanocrystals: (a) STM image of Fe nanocrystal. (b) Wulffman simulation of equilibrium crystal shape (ECS) of Fe nanocrystal.

surface energy ratios by Vitos et al. are: $\gamma_{001}/\gamma_{111}$ = 0.813, $\gamma_{110}/\gamma_{111}$ = 0.889, $\gamma_{001}/\gamma_{110}$ = 0.914, $\gamma_{210}/\gamma_{310}$ = 1.082. The $\gamma_{001}/\gamma_{111}$, $\gamma_{110}/\gamma_{111}$, $\gamma_{001}/\gamma_{110}$, and $\gamma_{211}/\gamma_{310}$ ratios are 3.405%, 3.405%, 0% and 0% different from the energy ratio predicted by Vitos et al. [208].

6.10 Conclusions

On $SrTiO_3$ (001), Fe formed truncated pyramid shaped nanocrystals. Each nanocrystal had six facets: a (001) top facet, four (110) side facets and a (001) base facet. On $SrTiO_3$ (110), Fe formed truncated hut shaped nanocrystals. Each nanocrystal had six facets: a (110) top facet, two (111) side facets, two (001) side facets, and a (110) base facet. On $SrTiO_3$ (111), Fe formed truncated octahedron shaped nanocrystals. Each nanocrystal had eight facets: a (111) top facet, three (211) side facets, three (110) side facets, and a (111) base facet. The exact composition of this nanocrystal is not known. If it is pure Fe, it should be fcc (austenite). However, as substrate has oxygen and Fe is prone to oxidation, there is probability that Fe has formed oxide. On all three terminations of $SrTiO_3$, Fe showed epitaxy. The unit cell of STO is 3.905 Å and that of Fe is 2.866 Å which results in a tensile lattice mismatch of 26.61%. The epitaxial arrangement is therefore not possible without

the introduction of misfit dislocations at the metal-oxide interface, formation of FeO_x, and rotation of FeO_x with respect to substrate to reduce lattice mismatch.

Chapter 9:

Conclusions and Future work

7.1 Conclusions

7.1.1 $SrTiO_3$

$SrTiO_3$ is capable of producing a multitude of surface reconstructions such as (2 × 1), (2 × 2), (√5 × √5) R26.6°, and c(4 × 2) on (001) termination; (4 × 1) on (110) termination; and (4 × 4) and (6 × 6) on (111) termination. Self-assembled nanostructures also appeared on $SrTiO_3$ surface such as nanolines, nanodots and waffle structure. These nanostructures can be investigated for novel electronic devices such as single electron transistors and quantum dot lasers.

7.1.2 Ni on $SrTiO_3$

On $SrTiO_3$ (001) substrate, Ni formed truncated pyramidal shaped nanocrystals. Each nanocrystal comprised of six facets: a (001) top facet, four (110) side facets, and a (001) base facet. On $SrTiO_3$ (110) substrate, Ni formed truncated hut shaped nanocrystals. Each nanocrystal comprised of six facets; a (110) top facet, two (111) side facets, two (001) side facets, and a (110) base facet. On $SrTiO_3$ (111) substrate, Ni formed two shapes: icosahedron and truncated octahedron. The icosahedrons had (111) facets and point, edge and face orientations were observed. The truncated octahedron had eight facets: a (111) top facet, three (111) side facets, three (001) side facets, and a (111) base facet. The unit cell of $SrTiO_3$ is 3.905 Å and that of Ni is 3.52 Å which results in a tensile lattice mismatch of 9.86%. However, ten units of Ni can sit perfectly on nine units of $SrTiO_3$ without the creation of misfit dislocations and therefore guarantee epitaxial arrangement.

7.1.3 Fe on $SrTiO_3$

On $SrTiO_3$ (001), Fe formed truncated pyramid shaped nanocrystals. Each nanocrystal had six facets: a (001) top facet, four (110) side facets and a (001) base facet. On $SrTiO_3$ (110), Fe formed truncated hut shaped nanocrystals. Each nanocrystal had six facets: a (110) top facet, two (111) side facets, two (001) side facets, and a (110) base facet. On $SrTiO_3$ (111),

Fe formed truncated octahedron shaped nanocrystals. Each nanocrystal had eight facets: a (111) top facet, three (211) side facets, three (110) side facets, and a (111) base facet. The exact composition of this nanocrystal is not known. If it is pure Fe, it should be fcc (austenite). However, as substrate has oxygen and Fe is prone to oxidation, there is probability that Fe has formed oxide. On all three terminations of $SrTiO_3$, Fe showed epitaxy. The unit cell of STO is 3.905 Å and that of Fe is 2.866 Å which results in a tensile lattice mismatch of 26.61%. The epitaxial arrangement is therefore not possible without the introduction of misfit dislocations at the metal-oxide interface, formation of FeO_x, and rotation of FeO_x with respect to substrate to achieve lattice match. As Fe gets oxidized quickly, to investigate whether crystals were either fully or partially oxidized, Wulffman simulations were carried out. The crystal shapes observed in the current experiments did not match with those predicted theoretically. Therefore, it was concluded that iron nanocrystals were partially oxidized as surfaces of the crystals were comprised of specific stripes indicating oxide formation.

7.2 Future work

The key objective of the current work was to try to produce austenite stabilized iron nanocrystals. In the current work, it was not confirmed that triangular nanocrystals of Fe on $SrTiO_3$ (111) were actually pure iron or iron oxide. Therefore, first objective of future work should be to investigate whether nanocrystals are of iron or iron oxide. Such analysis is possible with Auger electron spectroscopy (AES) and X-ray photoelectron spectroscopy (XPS). Secondly, Fe and Ni can be deposited simultaneously to investigate whether they form alloy or grow as separate crystals. Room temperature Fe is bcc while Ni is fcc and although they are miscible at the bulk scale, it is unsure if they will form an alloy at nanoscale. If they are not miscible at nanoscale, they will form separate islands. If they can work a mechanism together to lower the system energy, then they can also form core-shell

structures with either core of Fe and shell of Ni or vice-versa. Whatever the outcome, it will be interesting to investigate their electronic and magnetic properties.

References:

1. Feng, Z.; Kazimirov, A.; Bedzyk, M.J. Atomic Imaging of Oxide-Supported Metallic Nanocrystals. *ACS Nano* **2011**, *5*, 9755–9760, doi:10.1021/nn203273e.
2. Silly, F.; Castell, M.R. Bimodal Growth of Au on SrTiO3(001). *Phys. Rev. Lett.* **2006**, *96*, 086104, doi:10.1103/PhysRevLett.96.086104.
3. Zhou, D.; Shi, Y.; Zhao, W.; Dennis, A.R.; Beck, M.; Ainslie, M.D.; Palmer, K.G.B.; Cardwell, D.A.; Durrell, J.H. Magnets With Various Rare-Earth Elements Using Pulsed Fields at 77 K. *IEEE Trans. Appl. Supercond.* **2017**, *27*, 18–21, doi:10.1109/TASC.2016.2638200.
4. Cao, X.; Chen, L.; Guo, S.; Chen, R.; Yan, G.; Yan, A. Impact of TbF3 Diffusion on Coercivity and Microstructure in Sintered Nd-Fe-B Magnets by Electrophoretic Deposition. *Scr. Mater.* **2016**, *116*, 40–43, doi:10.1016/j.scriptamat.2016.01.034.
5. Peschke, S.; Weippert, V.; Senyshyn, A.; Mühlbauer, M.J.; Janka, O.; Pöttgen, R.; Holenstein, S.; Luetkens, H.; Johrendt, D. Flux Synthesis, Crystal Structures, and Magnetic Ordering of the Rare-Earth Chromium(II) Oxyselenides $RE_2CrSe_2O_2$ (RE = La–Nd). *Inorg. Chem.* **2017**, *56*, 2241–2247, doi:10.1021/acs.inorgchem.6b02895.
6. Silly, F.; Castell, M.R. Fe Nanocrystal Growth on SrTiO3(001). *Appl. Phys. Lett.* **2005**, *87*, 063106, doi:10.1063/1.2008375.
7. Marti, X.; Fina, I.; Frontera, C.; Liu, J.; Wadley, P.; He, Q.; Paull, R.J.; Clarkson, J.D.; Kudrnovský, J.; Turek, I.; et al. Room-Temperature Antiferromagnetic Memory Resistor. *Nat. Mater.* **2014**, *13*, 367–374, doi:10.1038/nmat3861.
8. Daughton, J.M.; Pohm, A. V; Fayfield, R.T.; Smith, C.H. Applications of Spin Dependent Transport Materials. *J. Phys. D. Appl. Phys.* **1999**, *32*, R169, doi:10.1088/0022-3727/32/22/201.
9. *ASM Handbook, Vol. 1: Properties and Selection Irons, Steels, and High-Performance Alloys*; Zwilsky, K.M., Ed.; 2001; Vol. 1; ISBN 0871700077.
10. Castell, M.R. Scanning Tunneling Microscopy of Reconstructions on the SrTiO3(001) Surface. *Surf. Sci.* **2002**, *505*, 1–13, doi:10.1016/S0039-6028(02)01393-6.
11. Roy Moulik, S.; Samanta, S.; Ghosh, B. Photoresponse in Thin Films of WO3 Grown by Pulsed Laser Deposition. *Appl. Phys. Lett.* **2014**, *104*, 232107, doi:10.1063/1.4882658.
12. Zhang, M.; Ma, X.L.; Li, D.X.; Lu, H.B.; Chen, Z.H.; Yang, G.Z. Patterned Nanoclusters in the Indium-Doped SrTiO3 Films. *Appl. Phys. Lett.* **2004**, *85*, 5899–5901, doi:10.1063/1.1836879.
13. Binnig, G.; Rohrer, H. Scanning Tunneling Microscopy. *Phys. B* **1984**, *127*, 37–45.
14. Binnig, G.; Rohrer, H. Scanning Tunneling Microscopy. *Surf. Sci.* **1985**, *152–153*, 17–26, doi:10.1016/0039-6028(85)90120-7.
15. Schweizer, D.K.; Eigler, E.K. Positioning Single Atoms with a Scanning Tunneling Microscope. *Nature* 1990, *344*, 524–525.
16. Giaever, I. Electron Tunneling between Two Superconductors. *Phys. Rev. Lett.* **1960**, *5*, 464–466, doi:10.1103/PhysRevLett.5.464.
17. Young, R.; Ward, J.; Scire, F. Observation of Metal-Vacuum-Metal Tunneling, Field Emission, and the Transistion Region. *Phys. Rev. Lett.* **1971**, *27*, 922–924.
18. Young, R.; Ward, J.; Scire, F. The Topografiner: An Instrument for Measuring Surface Microtopography. *Rev. Sci. Instrum.* **1972**, *43*, 999–1011, doi:10.1063/1.1685846.
19. Binnig, G.; Rohrer, H. Scanning Tunneling Microscopy—from Birth to Adolescence. *Angew. Chemie Int. Ed. English* **1987**, *26*, 606–614, doi:10.1002/anie.198706061.
20. Instructions: JSPM-4500S Ultrahigh Vacuum Scanning Tunneling Microscope. (JEOL Ltd., 2000).
21. EX03 Ion Gun System: Operating Manual. (VG Microtech, 2000).
22. Gao, Y. Scanning Tunnelling Microscopy of Epitaxial Nanomaterials on SrTiO3, DPhil Thesis, Department of Materials, University of Oxford, 2017.
23. Chen, C.J. *Introduction to Scanning Tunneling Microscopy*; 2nd ed.; Oxford university press, 2008;
24. Mini E-Beam Evaporator Model EGCO4: Serial No. S1944/GB5766 Operating and Service Manual. (Oxford Applied Research, 2000).
25. Leite, E.R.; Ribeiro, C. *Crystallization and Growth of Colloidal Nanocrystals*; Springer, 2012; ISBN 9781461413073.
26. Zangwill, A. *Physics at Surfaces*; Cambridge University Press, 1988; ISBN 978-0-521-34752-5.
27. Frank, F.C.; van der Merwe, J.H. One-Dimensional Dislocations: I. Static Theory. In Proceedings of the Proceedings of the Royal Society A; 1949; pp. 205–216.
28. Frank, F.C.; van der Merwe, J.H. One-Dimensional Dislocations: II. Misfitting Monolayers and Oriented Overgrowth. In Proceedings of the Proceedings of the Royal Rociety A; 1949; pp. 216–225.
29. Volmer, M.; Weber, A. Nucleus Formation in Supersaturated Systems. *Z. phys. Chem.* **1926**, *119*, 277.

30. Stranski, I.N.; Krastanow, L. V. Abhandlungen Der Mathematisch-Naturwissenschaftlichen Klasse IIb. *Naturwiss. Kl., Abt. B* **1938**, *146*, 797.
31. Kowarik, S.; Broch, K.; Hinderhofer, A.; Schwartzberg, A.; Osso, J.O.; Kilcoyne, D.; Schreiber, F.; Leone, S.R. Crystal Grain Orientation in Organic Homo- and Heteroepitaxy of Pentacene and Perfluoropentacene Studied with X-Ray Spectromicroscopy. *J. Phys. Chem. C* **2010**, *114*, 13061–13067, doi:10.1021/jp103713z.
32. *Handbook of Crystal Growth: Fundamentals: Transport and Stability*; Nishinaga, T., Ed.; Elsevier, 2015; Vol. I; ISBN 9780444563699.
33. Winterbottom, W.. Equilibrium Shape of a Small Particle in Contact with a Foreign Substrate. *Acta Metall.* **1967**, *15*, 303–310, doi:10.1016/0001-6160(67)90206-4.
34. Geuens, P.; Lebedev, O.I.; Van Tendeloo, G. Reconstruction of the La0.9Sr0.1MnO3-SrTiO3 Interface by Quantitative High-Resolution Electron Microscopy. *Solid State Commun.* **2000**, *116*, 643–648, doi:10.1016/S0038-1098(00)00411-7.
35. Lee, J.; Choi, J.K.J.H.; Moon, S.Y.; Park, J.; Kim, J.S.; Hwang, C.S.; Baek, S.H.; Choi, J.K.J.H.; Chang, H.J. Symmetry-Dependent Interfacial Reconstruction to Compensate Polar Discontinuity at Perovskite Oxide Interfaces (LaAlO3/SrTiO3 and LaAlO3/CaTiO3). *Appl. Phys. Lett.* **2015**, *106*, 071601, doi:10.1063/1.4913242.
36. Aruta, C.; Schlueter, C.; Lee, T.-L.; Di Castro, D.; Innocenti, D.; Tebano, A.; Zegenhagen, J.; Balestrino, G. Interface Reconstruction in Superconducting CaCuO2/SrTiO3 Superlattices: A Hard x-Ray Photoelectron Spectroscopy Study. *Phys. Rev. B* **2013**, *87*, 155145, doi:10.1103/PhysRevB.87.155145.
37. Brinkman, A.; Huijben, M.; Van Zalk, M.; Huijben, J.; Zeitler, U.; Maan, J.C.; van der Wiel, W.G.; Rijnders, G.; Blank, D.H.A.A.; Hilgenkamp, H. Magnetic Effects at the Interface between Non-Magnetic Oxides. *Nat. Mater.* **2007**, *6*, 493–496, doi:10.1038/nmat1931.
38. Millis, A.J. Oxide Interfaces: Moment of Magnetism. *Nat. Phys.* **2011**, *7*, 749–750, doi:10.1038/nphys2087.
39. Kalisky, B.; Bert, J.A.; Klopfer, B.B.; Bell, C.; Sato, H.K.; Hosoda, M.; Hikita, Y.; Hwang, H.Y.; Moler, K.A. Critical Thickness for Ferromagnetism in LaAlO3/SrTiO3 Heterostructures. *Nat. Commun.* **2012**, *922*, ncomms1931, doi:10.1038/ncomms1931.
40. Banerjee, S.; Erten, O.; Randeria, M. Ferromagnetic Exchange, Spin–Orbit Coupling and Spiral Magnetism at the LaAlO3/SrTiO3 Interface. *Nat. Phys.* **2013**, *9*, 626–630, doi:10.1038/nphys2702.
41. Gabay, M.; Triscone, J.-M. Oxide Heterostructures: Hund Rules with a Twist. *Nat. Phys.* **2013**, *9*, 610–611, doi:10.1038/nphys2737.
42. Ohtomo, A.; Hwang, H.Y. A High-Mobility Electron Gas at the LaAlO3/SrTiO3 Heterointerface. *Nature* **2004**, *427*, 423–426, doi:10.1038/nature02308.
43. Biscaras, J.; Bergeal, N.; Hurand, S.; Feuillet-Palma, C.; Rastogi, A.; Budhani, R.C.; Grilli, M.; Caprara, S.; Lesueur, J. Multiple Quantum Criticality in a Two-Dimensional Superconductor. *Nat. Mater.* **2013**, *12*, 542–548, doi:10.1038/nmat3624.
44. Richter, C.; Boschker, H.; Dietsche, W.; Fillis-Tsirakis, E.; Jany, R.; Loder, F.; Kourkoutis, L.F.; Muller, D.; Kirtley, J.R.; Schneider, C.W.; et al. Interface Superconductor with Gap Behaviour like a High-Temperature Superconductor. *Nature* **2013**, *502*, 528–531, doi:10.1038/nature12494.
45. Dikin, D.A.; Mehta, M.; Bark, C.W.; Folkman, C.M.; Eom, C.B.; Chandrasekhar, V. Coexistence of Superconductivity and Ferromagnetism in Two Dimensions. *Phys. Rev. Lett.* **2011**, *107*, 056802, doi:10.1103/PhysRevLett.107.056802.
46. Li, L.; Richter, C.; Mannhart, J.; Ashoori, R.C. Coexistence of Magnetic Order and Two-Dimensional Superconductivity at LaAlO3/SrTiO3 Interfaces. *Nat. Phys.* **2011**, *7*, 762–766, doi:10.1038/NPHYS2080.
47. Bert, J.A.; Kalisky, B.; Bell, C.; Kim, M.; Hikita, Y.; Hwang, H.Y.; Moler, K.A. Direct Imaging of the Coexistence of Ferromagnetism and Superconductivity at the LaAlO3/SrTiO3 Interface. *Nat. Phys.* **2011**, *7*, 767–771, doi:10.1038/nphys2079.
48. Han, Y.L.; Shen, S.C.; You, J.; Li, H.O.; Luo, Z.Z.; Li, C.J.; Qu, G.L.; Xiong, C.M.; Dou, R.F.; He, L.; et al. Two-Dimensional Superconductivity at (110) LaAlO3/SrTiO3 Interfaces. *Appl. Phys. Lett.* **2014**, *105*, 115304, doi:10.1063/1.4901940.
49. Jia, C.L.; Mi, S.B.; Faley, M.; Poppe, U.; Schubert, J.; Urban, K. Oxygen Octahedron Reconstruction in the SrTiO3/LaAlO3 Heterointerfaces Investigated Using Aberration-Corrected Ultrahigh-Resolution Transmission Electron Microscopy. *Phys. Rev. B* **2009**, *79*, 081405, doi:10.1103/PhysRevB.79.081405.
50. Salluzzo, M.; Gariglio, S.; Torrelles, X.; Ristic, Z.; Di Capua, R.; Drnec, J.; Sala, M.M.; Ghiringhelli, G.; Felici, R.; Brookes, N.B. Structural and Electronic Reconstructions at the LaAlO3/SrTiO3 Interface. *Adv. Mater.* **2013**, *25*, 2333–2338, doi:10.1002/adma.201204555.

51. Doennig, D.; Pentcheva, R. Control of Orbital Reconstruction in (LaAlO3)M/(SrTiO3)N(001) Quantum Wells by Strain and Confinement. *Sci. Rep.* **2015**, *5*, 7909, doi:10.1038/srep07909.
52. Ardhuin, H.; Snoeck, E.; Casanove, M.-J. Epitaxial Growth of Magnetic Au/Co/Au Sandwiches Studied by TEM. *J. Cryst. Growth* **1997**, *182*, 394–402, doi:10.1016/S0022-0248(97)00372-2.
53. Borisevich, A.Y.; Chang, H.J.; Huijben, M.; Oxley, M.P.; Okamoto, S.; Niranjan, M.K.; Burton, J.D.; Tsymbal, E.Y.; Chu, Y.H.; Yu, P.; et al. Suppression of Octahedral Tilts and Associated Changes in Electronic Properties at Epitaxial Oxide Heterostructure Interfaces. *Phys. Rev. Lett.* **2010**, *105*, 087204, doi:10.1103/PhysRevLett.105.087204.
54. Chang, H.J.; Kalinin, S. V.; Morozovska, A.N.; Huijben, M.; Chu, Y.H.; Yu, P.; Ramesh, R.; Eliseev, E.A.; Svechnikov, G.S.; Pennycook, S.J.; et al. Atomically Resolved Mapping of Polarization and Electric Fields across Ferroelectric/Oxide Interfaces by z-Contrast Imaging. *Adv. Mater.* **2011**, *23*, 2474–2479, doi:10.1002/adma.201004641.
55. Chisholm, M.F.; Luo, W.; Oxley, M.P.; Pantelides, S.T.; Lee, H.N. Atomic-Scale Compensation Phenomena at Polar Interfaces. *Phys. Rev. Lett.* **2010**, *105*, 197602, doi:10.1103/PhysRevLett.105.197602.
56. Pentcheva, R.; Pickett, W.E. Avoiding the Polarization Catastrophe in LaAlO3 Overlayers on SrTiO3(001) through Polar Distortion. *Phys. Rev. Lett.* **2009**, *102*, 107602, doi:10.1103/PhysRevLett.102.107602.
57. Liu, J.Y.; Cheng, X.; Nagarajan, V.; Xin, H.L. Understanding Growth Mechanisms of Epitaxial Manganese Oxide (Mn3O4) Nanostructures on Strontium Titanate (STO) Oxide Substrates. *MRS Commun.* **2015**, *5*, 277–284, doi:10.1557/mrc.2015.12.
58. Oropeza, F.E.; Zhang, K.H.L.; Regoutz, A.; Lazarov, V.K.; Wermeille, D.; Poll, C.G.; Egdell, R.G. Growth of Epitaxial Anatase Nano Islands on SrTiO3(001) by Dip Coating. *Cryst. Growth Des.* **2013**, *13*, 1438–1444, doi:10.1021/cg301455q.
59. Yoo, Y.; Yoon, I.; Lee, H.; Ahn, J.; Ahn, J.P.; Kim, B. Pattern-Selective Epitaxial Growth of Twin-Free Pd Nanowires from Supported Nanocrystal Seeds. *ACS Nano* **2010**, *4*, 2919–2927, doi:10.1021/nn100151c.
60. Silly, F.; Castell, M.R. Temperature-Dependent Stability of Supported Five-Fold Twinned Copper Nanocrystals. *ACS Nano* **2009**, *3*, 901–906, doi:10.1021/nn900059v.
61. Francis, A.J.; Salvador, P.A. Crystal Orientation and Surface Morphology of Face-Centered-Cubic Metal Thin Films Deposited upon Single-Crystal Ceramic Substrates Using Pulsed Laser Deposition. *J. Mater. Res.* **2007**, *22*, 89–102, doi:10.1557/jmr.2007.0014.
62. Silly, F.; Castell, M.R. Selecting the Shape of Supported Metal Nanocrystals: Pd Huts, Hexagons, or Pyramids on SrTiO3(001). *Phys. Rev. Lett.* **2005**, *94*, 046103, doi:10.1103/PhysRevLett.94.046103.
63. Silly, F.; Castell, M.R. Self-Assembled Supported Co Nanocrystals: The Adhesion Energy of Face-Centered-Cubic Co on SrTiO3(001)-(2×2). *Appl. Phys. Lett.* **2005**, *87*, 053106, doi:10.1063/1.2005390.
64. Chambers, S.A.; Wang, C.M.; Thevuthasan, S.; Droubay, T.; McCready, D.E.; Lea, A.S.; Shutthanandan, V.; Windisch, J.F. Epitaxial Growth and Properties of MBE-Grown Ferromagnetic Co-Doped TiO2 Anatase Films on SrTiO3(001) and LaAlO3(001). *Thin Solid Films* **2002**, *418*, 197–210, doi:10.1016/S0040-6090(02)00709-5.
65. Qiao, L.; Droubay, T.C.; Shutthanandan, V.; Zhu, Z.; Sushko, P. V; Chambers, S.A. Thermodynamic Instability at the Stoichiometric LaAlO3/SrTiO3 (001) Interface. *J. Phys. Condens. Matter* **2010**, *22*, 312201–312206, doi:10.1088/0953-8984/22/31/312201.
66. Nakagawa, N.; Hwang, H.Y.; Muller, D.A. Why Some Interfaces Cannot Be Sharp. *Nat. Mater.* **2006**, *5*, 204–209, doi:10.1038/nmat1569.
67. Boschker, H.; Verbeeck, J.; Egoavil, R.; Bals, S.; Van Tendeloo, G.; Huijben, M.; Houwman, E.P.; Koster, G.; Blank, D.H.A.; Rijnders, G. Preventing the Reconstruction of the Polar Discontinuity at Oxide Heterointerfaces. *Adv. Funct. Mater.* **2012**, *22*, 2235–2240, doi:10.1002/adfm.201102763.
68. Sum, R.; Lang, H.P.; Güntherodt, H.J. Scanning Force Microscopy Study of Single-Crystal Substrates Used for Thin-Film Growth of High-Temperature Superconductors. *Phys. C Supercond. its Appl.* **1995**, *242*, 174–182, doi:10.1016/0921-4534(94)02414-6.
69. Endo, K.; Badica, P.; Itoh, J. AFM Observation of As-Grown (119) Bi-2223 and (103) Y-123 Thin Films by MOCVD. *Phys. C Supercond.* **2003**, *386*, 292–295, doi:10.1016/S0921-4534(02)02136-6.
70. Hadamek, T.; Posadas, A.B.; Dhamdhere, A.; Smith, D.J.; Demkov, A.A. Spectral Identification Scheme for Epitaxially Grown Single-Phase Niobium Dioxide. *J. Appl. Phys.* **2016**, *119*, 095308, doi:10.1063/1.4942834.
71. Posadas, A.B.; O'Hara, A.; Rangan, S.; Bartynski, R.A.; Demkov, A.A. Band Gap of Epitaxial In-Plane-Dimerized Single-Phase NbO2 Films. *Appl. Phys. Lett.* **2014**, *104*, 86–91, doi:10.1063/1.4867085.

72. Cheng, X.; Sullaphen, J.; Weyland, M.; Liu, H.; Valanoor, N. Role of Interface Structure and Chemistry in Resistive Switching of NiO Nanocrystals on SrTiO3. *APL Mater.* **2014**, *2*, 032109, doi:10.1063/1.4869457.
73. Takahashi, R.; Misumi, H.; Yamamoto, T.; Lippmaa, M. Spontaneous Growth of Strain-Free Magnetite Nanocrystals via Temperature-Driven Dewetting. *Cryst. Growth Des.* **2014**, *14*, 1264–1271, doi:10.1021/cg5000414.
74. Sun, J.; Wu, C.; Silly, F.; Koós, A.A.; Dillon, F.; Grobert, N.; Castell, M.R. Controlled Growth of Ni Nanocrystals on SrTiO3 and Their Application in the Catalytic Synthesis of Carbon Nanotubes. *Chem. Commun.* **2013**, *49*, 3748–3750, doi:10.1039/c3cc39114k.
75. Konstantinović, Z.; Sandiumenge, F.; Santiso, J.; Balcells, L.; Martínez, B. Self-Assembled Pit Arrays as Templates for the Integration of Au Nanocrystals in Oxide Surfaces. *Nanoscale* **2013**, *5*, 1001–1008, doi:10.1039/c2nr33181k.
76. Zhang, Z.; Feng, J.; Wang, Z.; Yang, F.; Guo, Q.; Guo, J. Guided Growth of Ag Nanoparticles on SrTiO3 (110) Surface. *J. Chem. Phys.* **2011**, *135*, 144702, doi:10.1063/1.3648052.
77. Enterkin, J.A.; Poeppelmeier, K.R.; Marks, L.D. Oriented Catalytic Platinum Nanoparticles on High Surface Area Strontium Titanate Nanocuboids. *Nano Lett.* **2011**, *11*, 993–997, doi:10.1021/nl104263j.
78. Komanicky, V.; Iddir, H.; Chang, K.C.; Menzel, A.; Karapetrov, G.; Hennessy, D.C.; Zapol, P.; You, H. Fabrication and Characterization of Platinum Nanoparticle Arrays of Controlled Size, Shape and Orientation. *Electrochim. Acta* **2010**, *55*, 7934–7938, doi:10.1016/j.electacta.2010.03.024.
79. Son, J.; Cagnon, J.; Stemmer, S. Strain Relaxation in Epitaxial Pt Films on (001) SrTiO3. *J. Appl. Phys.* **2009**, *106*, 13–16, doi:10.1063/1.3207795.
80. Christensen, S.T.; Elam, J.W.; Rabuffetti, F.A.; Ma, Q.; Weigand, S.J.; Lee, B.; Seifert, S.; Stair, P.C.; Poeppelmeier, K.R.; Hersam, M.C.; et al. Controlled Growth of Platinum Nanoparticles on Strontium Titanate Nanocubes by Atomic Layer Deposition. *Small* **2009**, *5*, 750–757, doi:10.1002/smll.200801920.
81. Silly, F.; Castell, M.R. Growth of Ag Icosahedral Nanocrystals on a SrTiO3(001) Support. *Appl. Phys. Lett.* **2005**, *87*, 213107, doi:10.1063/1.2133909.
82. Wang, C.M.; Shutthanandan, V.; Zhang, Y.; Thomas, L.E.; Baer, D.R.; Thevuthasan, S.; Duscher, G. Precipitation of Au Nanoclusters in SrTiO3 by Ion Implantation. *J. Appl. Phys.* **2004**, *95*, 5060–5068, doi:10.1063/1.1691187.
83. Zhong, Z.; Kelly, P.J. Electronic Structure Induced Reconstruction and Magnetic Ordering at the LaAlO3|SrTiO3 Interface. *Europhys. Lett.* **2008**, *84*, 27001, doi:10.1209/0295-5075/84/27001.
84. Bubendorff, J.L.; Beaurepaire, E.; Meny, C.; Panissod, P.; Bucher, J.P. Perpendicular Magnetization in Ultrathin Electrodeposited Cobalt Films. *Phys. Rev. B* **1997**, *56*, R7120–R7123, doi:10.1103/PhysRevB.56.R7120.
85. Bubendorff, J.L.; Beaurepaire, E.; Meny, C.; Bucher, J.P. Overpotential Driven Perpendicular Magnetization of Electrodeposited Ultrathin Cobalt Films. *J. Appl. Phys.* **1998**, *83*, 7043–7045, doi:10.1063/1.367820.
86. Wright, J.G. The F.C.C.-H.C.P. Phase Transition in Electrolytically Deposited Epitaxial Cobalt Films. *Thin Solid Films* **1974**, *22*, 197–201, doi:10.1016/0040-6090(74)90006-6.
87. Wadati, H.; Hawthorn, D.G.; Geck, J.; Higuchi, T.; Hikita, Y.; Hwang, H.Y.; Kourkoutis, L.F.; Muller, D.A.; Huang, S.W.; Huang, D.J.; et al. Resonant Soft X-Ray Scattering Studies of Interface Reconstructions in SrTiO3/LaAlO3 Superlattices. *J. Appl. Phys.* **2009**, *106*, 083705, doi:10.1063/1.3246788.
88. Chang, Y.J.; Kim, C.H.; Phark, S.H.; Kim, Y.S.; Yu, J.; Noh, T.W. Fundamental Thickness Limit of Itinerant Ferromagnetic SrRuO3 Thin Films. *Phys. Rev. Lett.* **2009**, *103*, 057201, doi:10.1103/PhysRevLett.103.057201.
89. Vasco, E.; Karthäuser, S.; Dittmann, R.; He, J.Q.; Jia, C.L.; Szot, K.; Waser, R. SrZrO3 Nanopatterning Using Self-Organized SrRuO3 as a Template. *Adv. Mater.* **2005**, *17*, 281–284, doi:10.1002/adma.200400718.
90. Phark, S.H.; Chang, Y.J.; Noh, T.W. Selective Growth of Perovskite Oxides on SrTiO3(001) by Control of Surface Reconstructions. *Appl. Phys. Lett.* **2011**, *98*, 98–101, doi:10.1063/1.3583443.
91. Mundschau, M.; Bauer, E.; Telieps, W.; Święch, W. Initial Epitaxial Growth of Copper Silicide on Si{111} Studied by Low-Energy Electron Microscopy and Photoemission Electron Microscopy. *J. Appl. Phys.* **1989**, *65*, 4747–4752, doi:10.1063/1.343227.
92. *The Chemical Physics of Solid Surfaces and Heterogeneous Catalysis: Growth and Properties of Ultrathin Epitaxial Layers*; King, D.A., Woodruff, D.P., Eds.; Elsevier: Amsterdam, Netherland, 2012; Vol. 8; ISBN 0444601309.
93. Oura, K.; Lifshits, V.G.; Saranin, A.A.; Zotov, A. V; Katayama, M. *Surface Science: An*

Introduction; Springer Berlin Heidelberg, 2003;
94. Somorjai, G.A.; Li, Y. *Introduction to Surface Chemistry and Catalysis*; John Wiley & Sons, Inc., USA, 2010;
95. Park, R.L.; Madden, H.H. Annealing Changes on the (100) Surface of Palladium and Their Effect on CO Adsorption. *Surf. Sci.* **1968**, *11*, 188–202.
96. Wood, E.A. Vocabulary of Surface Crystallography. *J. Appl. Phys.* **1964**, *35*, 1306–1312, doi:10.1063/1.1713610.
97. Michailowski, A.; Almawlawi, D.; Cheng, G.; Moskovits, M. Highly Regular Anatase Nanotubule Arrays Fabricated in Porous Anodic Templates. *Chem. Phys. Lett.* **2001**, *349*, 1–5, doi:10.1016/S0009-2614(01)01159-9.
98. Shelimov, K.B.; Moskovits, M. Composite Nanostructures Based on Template-Grown Boron Nitride Nanotubules. *Chem. Mater.* **2000**, *12*, 250–254, doi:10.1021/cm9905996.
99. Shin, T.-Y.; Yoo, S.-H.; Park, S. Gold Nanotubes with a Nanoporous Wall: Their Ultrathin Platinum Coating and Superior Electrocatalytic Activity toward Methanol Oxidation. *Chem. Mater.* **2008**, *20*, 5682–5686, doi:10.1021/cm800859k.
100. Xiao, R.; Seung, I.C.; Liu, R.; Sang, B.L. Controlled Electrochemical Synthesis of Conductive Polymer Nanotube Structures. *J. Am. Chem. Soc.* **2007**, *129*, 4483–4489, doi:10.1021/ja068924v.
101. Bok, H.M.; Kim, S.; Yoo, S.H.; Kim, S.K.; Park, S. Synthesis of Perpendicular Nanorod Arrays with Hierarchical Architecture and Water Slipping Superhydrophobic Properties. *Langmuir* **2008**, *24*, 4168–4173, doi:10.1021/la7026972.
102. Bok, H.M.; Shuford, K.L.; Kim, S.; Kim, S.K.; Park, S. Multiple Surface Plasmon Modes for a Colloidal Solution of Nanoporous Gold Nanorods and Their Comparison to Smooth Gold Nanorods. *Nano Lett.* **2008**, *8*, 2265–2270, doi:10.1021/nl800924r.
103. Nicewarner-Pena, S.R. Submicrometer Metallic Barcodes. *Science.* **2001**, *294*, 137–141, doi:10.1126/science.294.5540.137.
104. Park, S.; Chung, S.W.; Mirkin, C.A. Hybrid Organic-Inorganic, Rod-Shaped Nanoresistors and Diodes. *J. Am. Chem. Soc.* **2004**, *126*, 11772–11773, doi:10.1021/ja046077v.
105. Park, S.; Lim, J.-H.; Chung, S.-W.; Mirkin, C.A. Self-Assembly of Mesoscopic Metal-Polymer Amphiphiles. *Science.* **2004**, *303*, 348–351, doi:10.1126/science.1093276.
106. Paxton, W.F.; Kistler, K.C.; Olmeda, C.C.; Sen, A.; St. Angelo, S.K.; Cao, Y.; Mallouk, T.E.; Lammert, P.E.; Crespi, V.H. Catalytic Nanomotors: Autonomous Movement of Striped Nanorods. *J. Am. Chem. Soc.* **2004**, *126*, 13424–13431, doi:10.1021/ja047697z.
107. Peng, X.; Manna, L.; Yang, W.; Wickham, J.; Scher, E.; Kadavanich, A.; Alivisatos, A.P. Shape Control of CdSe Nanocrystals. *Nature* **2000**, *404*, 59–61, doi:10.1038/35003535.
108. Yoo, S.-H.; Park, S. Platinum-Coated, Nanoporous Gold Nanorod Arrays: Synthesis and Characterization. *Adv. Mater.* **2007**, *19*, 1612–1615, doi:10.1002/adma.200602551.
109. Cao, G.; Liu, D. Template-Based Synthesis of Nanorod, Nanowire, and Nanotube Arrays. *Adv. Colloid Interface Sci.* **2008**, *136*, 45–64, doi:10.1016/j.cis.2007.07.003.
110. Kline, T.R.; Tian, M.; Wang, J.; Sen, A.; Chan, M.W.H.; Mallouk, T.E. Template-Grown Metal Nanowires. *Inorg. Chem.* **2006**, *45*, 7555–7565, doi:10.1021/ic0601384.
111. Li, M.; Mayer, T.S.; Sioss, J.A.; Keating, C.D.; Bhiladvala, R.B. Template-Grown Metal Nanowires as Resonators: Performance and Characterization of Dissipative and Elastic Properties. *Nano Lett.* **2007**, *7*, 3281–3284, doi:10.1021/nl071416e.
112. Liu, Z.; Elbert, D.; Chien, C.; Searson, P.C. FIB/TEM Characterization of the Composition and Structure of Core/Shell Cu-Ni Nanowires. *Nano Lett.* **2008**, *8*, 2166–2170, doi:10.1021/nl080492u.
113. Peña, D.J.; Mbindyo, J.K.N.; Carado, A.J.; Mallouk, T.E.; Keating, C.D.; Razavi, B.; Mayer, T.S. Template Growth of Photoconductive Metal-CdSe-Metal Nanowires. *J. Phys. Chem. B* **2002**, *106*, 7458–7462, doi:10.1021/jp0256591.
114. Routkevitch, D.; Bigioni, T.; Moskovits, M.; Xu, J.M. Electrochemical Fabrication of CdS Nanowire Arrays in Porous Anodic Aluminum Oxide Templates. *J. Phys. Chem.* **1996**, *100*, 14037–14047, doi:10.1021/jp952910m.
115. Sioss, J.A.; Keating, C.D. Batch Preparation of Linear Au and Ag Nanoparticle Chains via Wet Chemistry. *Nano Lett.* **2005**, *5*, 1779–1783, doi:10.1021/nl051370u.
116. Wu, Y.; Livneh, T.; Zhang, Y.X.; Cheng, G.; Wang, J.; Tang, J.; Moskovits, M.; Stucky, G.D. Templated Synthesis of Highly Ordered Mesostructured Nanowires and Nanowire Arrays. *Nano Lett.* **2004**, *4*, 2337–2342, doi:10.1021/nl048653r.
117. Qu, X.; Omar, L.; Le, T.B.H.; Tetley, L.; Bolton, K.; Chooi, K.W.; Wang, W.; Uchegbu, I.F. Polymeric Amphiphile Branching Leads to Rare Nanodisc Shaped Planar Self-Assemblies. *Langmuir* **2008**, *24*, 9997–10004, doi:10.1021/la8007848.
118. Schmidt, E.; Vargas, A.; Mallat, T.; Baiker, A. Shape-Selective Enantioselective Hydrogenation on

Pt Nanoparticles. *J. Am. Chem. Soc* **2009**, *131*, 12358–12367, doi:10.1021/ja9043328.
119. Wang, Z.L.; Ahmad, T.S.; E1-Sayed, M.A. Steps, Ledges and Kinks on the Surfaces of Platinum Nanoparticles of Different Shapes. *Surf. Sci.* **1997**, *380*, 302–310, doi:10.1016/S0039-6028(97)05180-7.
120. Ren, T.Z.; Yuan, Z.Y.; Hu, W.; Zou, X. Single Crystal Manganese Oxide Hexagonal Plates with Regulated Mesoporous Structures. *Microporous Mesoporous Mater.* **2008**, *112*, 467–473, doi:10.1016/j.micromeso.2007.10.025.
121. Ren, X.; Han, D.; Chen, D.; Tang, F. Large-Scale Synthesis of Hexagonal Cone-Shaped ZnO Nanoparticles with a Simple Route and Their Application to Photocatalytic Degradation. *Mater. Res. Bull.* **2007**, *42*, 807–813, doi:10.1016/j.materresbull.2006.08.030.
122. Suematsu, N.J.; Ogawa, Y.; Yamamoto, Y.; Yamaguchi, T. Dewetting Self-Assembly of Nanoparticles into Hexagonal Array of Nanorings. *J. Colloid Interface Sci.* **2007**, *310*, 648–652, doi:10.1016/j.jcis.2007.02.037.
123. Wu, L.; Yu, J.C.; Zhang, L.; Wang, X.; Li, S. Selective Self-Propagating Combustion Synthesis of Hexagonal and Orthorhombic Nanocrystalline Yttrium Iron Oxide. *J. Solid State Chem.* **2004**, *177*, 3666–3674, doi:10.1016/j.jssc.2004.06.020.
124. Hu, J.S.; Guo, Y.G.; Liang, H.P.; Wan, L.J.; Jiang, L. Three-Dimensional Self-Organization of Supramolecular Self-Assembled Porphyrin Hollow Hexagonal Nanoprisms. *J. Am. Chem. Soc.* **2005**, *127*, 17090–17095, doi:10.1021/ja0553912.
125. Jitianu, M.; Goia, D. V. Zinc Oxide Colloids with Controlled Size, Shape, and Structure. *J. Colloid Interface Sci.* **2007**, *309*, 78–85, doi:10.1016/j.jcis.2006.12.020.
126. Ahmed, J.; Sharma, S.; Ramanujachary, K. V.; Lofland, S.E.; Ganguli, A.K. Microemulsion-Mediated Synthesis of Cobalt (Pure Fcc and Hexagonal Phases) and Cobalt-Nickel Alloy Nanoparticles. *J. Colloid Interface Sci.* **2009**, *336*, 814–819, doi:10.1016/j.jcis.2009.04.062.
127. El-Safty, S.A. Synthesis, Characterization and Catalytic Activity of Highly Ordered Hexagonal and Cubic Composite Monoliths. *J. Colloid Interface Sci.* **2008**, *319*, 477–488, doi:10.1016/j.jcis.2007.12.010.
128. Song, Q.; Zhang, Z.J. Shape Control and Associated Magnetic Properties of Spinel Cobalt Ferrite Nanocrystals. *J. Am. Chem. Soc.* **2004**, *126*, 6164–6168, doi:10.1021/ja049931r.
129. Salazar-Alvarez, G.; Qin, J.; Sepelak, V.; Bergmann, I.; Vasilakaki, M.; Trohidou, K.N.; Ardisson, J.D.; Macedo, W.A.A.; Mikhaylova, M.; Muhammed, M.; et al. Cubic versus Spherical Magnetic Nanoparticles : The Role of Surface Anisotropy. *J. Am. Chem. Soc.* **2008**, *130*, 13234–13239, doi:10.1021/ja0768744.
130. Wei, X.W.; Zhu, G.X.; Liu, Y.J.; Ni, Y.H.; Song, Y.; Xu, Z. Large-Scale Controlled Synthesis of FeCo Nanocubes and Microcages by Wet Chemistry. *Chem. Mater.* **2008**, *20*, 6248–6253, doi:10.1021/cm800518x.
131. Yamada, M.; Kon, S.; Miyake, M. Synthesis and Size Control of Pt Nanocubes with High Selectivity Using the Additive Effect of NaI. *Chem. Lett.* **2005**, *34*, 1050–1051, doi:10.1246/cl.2005.1050.
132. Shimizu, T.; Teranishi, T.; Hasegawa, S.; Miyake, M. Size Evolution of Alkanethiol-Protected Gold Nanoparticles by Heat Treatment in the Solid State. *J. Phys. Chem. B* **2003**, *107*, 2719–2724, doi:10.1021/jp026920g.
133. Pong, B.K.; Elim, H.I.; Chong, J.X.; Ji, W.; Trout, B.L.; Lee, J.Y. New Insights on the Nanoparticle Growth Mechanism in the Citrate Reduction of Gold(III) Salt: Formation of the Au Nanowire Intermediate and Its Nonlinear Optical Properties. *J. Phys. Chem. C* **2007**, *111*, 6281–6287, doi:10.1021/jp068666o.
134. Sau, T.K.; Murphy, C.J. Seeded High Yield Synthesis of Short Au Nanorods in Aqueous Solution. *Langmuir* **2004**, *20*, 6414–6420, doi:10.1021/la049463z.
135. Wang, Z.L.; Mohamed, M.B.; Link, S.; El-Sayed, M.A. Crystallographic Facets and Shapes of Gold Nanorods of Different Aspect Ratios. *Surf. Sci.* **1999**, *440*, L809–L814, doi:10.1016/S0039-6028(99)00865-1.
136. Carbó-Argibay, E.; Rodríguez-González, B.; Pacifico, J.; Pastoriza-Santos, I.; Pérez-Juste, J.; Liz-Marzán, L.M. Chemical Sharpening of Gold Nanorods: The Rod-to-Octahedron Transition. *Angew. Chemie - Int. Ed.* **2007**, *46*, 8983–8987, doi:10.1002/anie.200703259.
137. Oldenburg, S.J.; Averitt, R.D.; Westcott, S.L.; Halas, N.J. Nanoengineering of Optical Resonances. *Chem. Phys. Lett.* **1998**, *288*, 243–247, doi:10.1016/S0009-2614(98)00277-2.
138. Lu, X.; Au, L.; McLellan, J.; Li, Z.Y.; Marquez, M.; Xia, Y. Fabrication of Cubic Nanocages and Nanoframes by Dealloying Au/Ag Alloy Nanoboxes with an Aqueous Etchant Based on Fe(NO 3) 3 or NH 4OH. *Nano Lett.* **2007**, *7*, 1764–1769, doi:10.1021/nl070838l.
139. Liang, H.P.; Wan, L.J.; Bai, C.L.; Jiang, L. Gold Hollow Nanospheres: Tunable Surface Plasmon Resonance Controlled by Interior-Cavity Sizes. *J. Phys. Chem. B* **2005**, *109*, 7795–7800,

doi:10.1021/jp045006f.
140. Kim, F.; Connor, S.; Song, H.; Kuykendall, T.; Yang, P. Platonic Gold Nanocrystals. *Angew. Chemie - Int. Ed.* **2004**, *43*, 3673–3677, doi:10.1002/anie.200454216.
141. Niu, W.; Zheng, S.; Wang, D.; Liu, X.; Li, H.; Han, S.; Chen, J.; Tang, Z.; Xu, G. Selective Synthesis of Single-Crystalline Rhombic Dodecahedral, Octahedral, and Cubic Gold Nanocrystals. *J. Am. Chem. Soc.* **2009**, *131*, 697–703, doi:10.1021/ja804115r.
142. Zhang, J.; Langille, M.R.; Personick, M.L.; Zhang, K.; Li, S.; Mirkin, C.A. Concave Cubic Gold Nanocrystals with High- Index Facets. *J. Am. Chem. Soc. Commun.* **2010**, *132*, 14012–14014, doi:10.1021/ja106394k.
143. Ming, T.; Feng, W.; Tang, Q.; Wang, F.; Sun, L.; Wang, J.; Yan, C. Growth of Tetrahexahedral Gold Nanocrystals with High-Index Facets. *J. Am. Chem. Soc.* **2009**, *131*, 16350–16351, doi:10.1021/ja907549n.
144. Personick, M.L.; Langille, M.R.; Zhang, J.; Harris, N.; Schatz, G.C.; Mirkin, C.A. Synthesis and Isolation of {110}-Faceted Gold Bipyramids and Rhombic Dodecahedra. *J. Am. Chem. Soc.* **2011**, *133*, 6170–6173, doi:10.1021/ja201826r.
145. Ma, Y.; Kuang, Q.; Jiang, Z.; Xie, Z.; Huang, R.; Zheng, L. Synthesis of Trisoctahedral Gold Nanocrystals with Exposed High-Index Facets by a Facile Chemical Method. *Angew. Chemie - Int. Ed.* **2008**, *47*, 8901–8904, doi:10.1002/anie.200802750.
146. Millstone, J.E.; Park, S.; Shuford, K.L.; Qin, L.; Schatz, G.C.; Mirkin, C.A. Observation of a Quadrupole Plasmon Mode for a Colloidal Solution of Gold Nanoprisms. *J. Am. Chem. Soc.* **2005**, *127*, 5312–5313, doi:10.1021/ja043245a.
147. Lu, J.L.; Gao, H.J.; Shaikhutdinov, S.; Freund, H.J. Gold Supported on Well-Ordered Ceria Films: Nucleation, Growth and Morphology in CO Oxidation Reaction. *Catal. Letters* **2007**, *114*, 8–16, doi:10.1007/s10562-007-9039-3.
148. Valden, M. Onset of Catalytic Activity of Gold Clusters on Titania with the Appearance of Nonmetallic Properties. *Science.* **1998**, *281*, 1647–1650, doi:10.1126/science.281.5383.1647.
149. Szafraniak, I.; Chu, M.W.; Harnagea, C.; Scholz, R.; Hesse, D.; Alexe, M. Epitaxial Lead Zirconate Titanate Nanocrystals Obtained by a Self-Patterning Method. *Integr. Ferroelectr.* **2004**, *61*, 231–238, doi:10.1080/10584580490460123.
150. Chen, J.; Herricks, T.; Xia, Y. Polyol Synthesis of Platinum Nanostructures: Control of Morphology through the Manipulation of Reduction Kinetics. *Angew. Chemie - Int. Ed.* **2005**, *44*, 2589–2592, doi:10.1002/anie.200462668.
151. Talati, M.; Jha, P.K.; Gupta, S.K. Shape and Size Dependent Melting Point Temperature of Nanoparticles. *Mater. Sci. Forum* **2008**, *570*, 132–137, doi:10.4028/www.scientific.net/MSF.570.132.
152. Millstone, J.E.; Hurst, S.J.; Métraux, G.S.; Cutler, J.I.; Mirkin, C.A. Colloidal Gold and Silver Triangular Nanoprisms. *Small* **2009**, *5*, 646–664, doi:10.1002/smll.200801480.
153. Lieber, C.M. One-Dimensional Nanostructures: Chemistry, Physics & Applications. *Solid State Commun.* **1998**, *107*, 607–616, doi:10.1016/S0038-1098(98)00209-9.
154. Smalley, R.E.; Yakobson, B.I. The Future of the Fullerenes. *Solid State Commun.* **1998**, *107*, 597–606, doi:10.1016/S0038-1098(98)00210-5.
155. Zheng, Y.; Cheng, Y.; Wang, Y.; Bao, F.; Zhou, L.; Wei, X.; Zhang, Y.; Zheng, Q. Quasicubic α-Fe2O3 Nanoparticles with Excellent Catalytic Performance. *J. Phys. Chem. B* **2006**, *110*, 3093–3097, doi:10.1021/jp056617q.
156. Narayanan, R.; El-Sayed, M.A. Changing Catalytic Activity during Colloidal Platinum Nanocatalysis Due to Shape Changes: Electron-Transfer Reaction. *J. Am. Chem. Soc.* **2004**, *126*, 7194–7195, doi:10.1021/ja0486061.
157. Lee, H.; Habas, S.E.; Kweskin, S.; Butcher, D.; Somorjai, G.A.; Yang, P. Morphological Control of Catalytically Active Platinum Nanocrystals. *Angew. Chemie - Int. Ed.* **2006**, *45*, 7824–7828, doi:10.1002/anie.200603068.
158. Sun, Y.; Xia, Y. Triangular Nanoplates of Silver: Synthesis, Characterization, and Use as Sacrificial Templates for Generating Triangular Nanorings of Gold. *Adv. Mater.* **2003**, *15*, 695–699, doi:10.1002/adma.200304652.
159. Iddir, H.; Komanicky, V.; Ogut, S.; You, H.; Zapol, P. Shape of Platinum Nanoparticles Supported on SrTiO3: Experiment and Theory. *J. Phys. Chem. C* **2007**, *111*, 14782–14789, doi:10.1021/jp073041r.
160. Koslowski, B.; Notz, R.; Ziemann, P. Epitaxial Growth of Iridium on Strontium-Titanated Studied by in Situ Scanning Tunneling Microscopy. *Surf. Sci.* **2002**, *496*, 153–159.
161. Yang, G.Z.; Lu, H.B.; Chen, F.; Zhao, T.; Chen, Z.H. Laser Molecular Beam Epitaxy and Characterization of Perovskite Oxide Thin Films. *J. Cryst. Growth* **2001**, *227–228*, 929–935,

doi:10.1016/S0022-0248(01)00930-7.
162. Ahn, K.S.; Lee, S.H.; Dillon, A.C.; Tracy, C.E.; Pitts, R. The Effect of Thermal Annealing on Photoelectrochemical Responses of WO3 Thin Films. *J. Appl. Phys.* **2007**, *101*, 093524, doi:10.1063/1.2729472.
163. Fang, G.; Liu, Z.; Yao, K.L. Fabrication and Characterization of Electrochromic Nanocrystalline WO3/Si (111) Thin Films for Infrared Emittance Modulation Applications. *J. Phys. D. Appl. Phys.* **2001**, *34*, 2260, doi:10.1088/0022-3727/34/15/304.
164. Hao, J.; Studenikin, S.A.; Cocivera, M. Transient Photoconductivity Properties of Tungsten Oxide Thin Films Prepared by Spray Pyrolysis. *J. Appl. Phys.* **2001**, *90*, 5064–5069, doi:10.1063/1.1412567.
165. Cheung, J.; Okatan, M.B.; Sullaphen, J.; Cheng, X.; Nagarajan, V.; Chen, Y.-L.; Chu, Y.-H. Epitaxial NiO Nanocrystals: A Dimensional Analysis. *MRS Commun.* **2013**, *3*, 107–111, doi:10.1557/mrc.2013.16.
166. Cheng, J.; Regreny, P.; Largeau, L.; Patriarche, G.; Mauguin, O.; Naji, K.; Hollinger, G.; Saint-Girons, G. Influence of the Surface Reconstruction on the Growth of InP on SrTiO3(001). *J. Cryst. Growth* **2009**, *311*, 1042–1045, doi:http://dx.doi.org/10.1016/j.jcrysgro.2008.12.014.
167. Lyubinetsky, I.; Thevuthasan, S.; Mccready, D.E.; Lea, A.S.; Baer, D.R. Formation of Self-Assembled Cuprous Oxide Nano-Dots on SrTi03(001) Surfaces. *Nanotechnology* **2003**, *03*, 667–670, doi:10.1109/NANO.2003.1231000.
168. Yang, B.; Barnes, P.R.F.; Bertram, W.; Luca, V. Strong Photoresponse of Nanostructured Tungsten Trioxide Films Prepared via a Sol-Gel Route. *J. Mater. Chem.* **2007**, *17*, 2722, doi:10.1039/b702097j.
169. Garg, A.; Leake, J.A.; Barber, Z.H. Epitaxial Growth of WO3 Films on SrTiO3 and Sapphire. *J. Phys. D. Appl. Phys.* **2000**, *33*, 1048–1053, doi:10.1088/0022-3727/33/9/303.
170. Kobayashi, Y.; Terada, S.; Kubota, K. Epitaxial Growth of WO3 Thin Films on MgO and Al2O3. *Thin Solid Films* **1989**, *168*, 133–139.
171. Schmid, G.; Corain, B. Nanoparticulated Gold: Syntheses, Structures, Electronics, and Reactivities. *Eur. J. Inorg. Chem.* **2003**, *2003*, 3081–3098, doi:10.1002/ejic.200300187.
172. Chaudhuri, R.G.; Paria, S. Core/Shell Nanoparticles: Classes, Properties, Synthesis Mechanisms, Characterization, and Applications. *Chem. Rev.* **2012**, *112*, 2373–2433, doi:10.1021/cr100449n.
173. Dreaden, E.C.; Alkilany, A.M.; Huang, X.; Murphy, C.J.; El-Sayed, M.A. The Golden Age: Gold Nanoparticles for Biomedicine. *Chem. Soc. Rev.* **2012**, *41*, 2740, doi:10.1039/c1cs15237h.
174. West, J.L.; Halas, N.J. Engineered Nanomaterials for Biophotonics Applications: Improving Sensing, Imaging, and Therapeutics. *Annu. Rev. Biomed. Eng.* **2003**, *5*, 285–292, doi:10.1146/annurev.bioeng.5.011303.120723.
175. Skrabalak, S.E.; Au, L.; Li, X.; Xia, Y. Facile Synthesis of Ag Nanocubes and Au Nanocages. *Nat. Protoc.* **2007**, *2*, 2182–2190, doi:10.1038/nprot.2007.326.
176. Chen, M.S.; Goodman, D.W. The Structure of Catalytically Active Au on Titania. *Science.* **2004**, *306*, 252–255.
177. Valden, M.; Lai, X.; Goodman, D.W.W. Onset of Catalytic Activity of Gold Clusters on Titania with the Appearance of Nonmetallic Properties. *Science.* **1998**, *281*, 1647–1650, doi:10.1126/science.281.5383.1647.
178. Valden, M.; Pak, S.; Lai, X.; Goodman, D.W. Structure Sensitivity of CO Oxidation over Model Au/TiO2 Catalysts. *Catal. Letters* **1998**, *56*, 7–10, doi:10.1023/A:1019028205985.
179. Lopez, N.; Janssens, T.V.W.; Clausen, B.S.; Xu, Y.; Mavrikakis, M.; Bligaard, T.; Nørskov, J.K. On the Origin of the Catalytic Activity of Gold Nanoparticles for Low-Temperature CO Oxidation. *J. Catal.* **2004**, *223*, 232–235, doi:10.1016/j.jcat.2004.01.001.
180. Bell, A.T. The Impact of Nanoscience on Heterogeneous Catalysis. *Science (80-.).* **2003**, *299*, 1688–1691, doi:10.1126/science.1083671.
181. Henglein, A. Small-Particle Research: Physicochemical Properties of Extremely Small Colloidal Metal and Semiconductor Particles. *Chem. Rev.* **1989**, *89*, 1861–1873, doi:10.1021/cr00098a010.
182. Spanhel, L.; Weller, H.; Henglein, A. Photochemistry of Semiconductor Colloids. 22. Electron Ejection from Illuminated Cadmium Sulfide into Attached Titanium and Zinc Oxide Particles. *J. Am. Chem. Soc.* **1987**, *109*, 6632–6635, doi:10.1021/ja00256a012.
183. Youn, H.C.; Baral, S.; Fendler, J.H. Dihexadecyl Phosphate, Vesicle-Stabilized and in Situ Generated Mixed Cadmium Sulfide and Zinc Sulfide Semiconductor Particles: Preparation and Utilization for Photosensitized Charge Separation and Hydrogen Generation. *J. Phys. Chem.* **1988**, *92*, 6320–6327, doi:10.1021/j100333a029.
184. Hoener, C.F.; Allan, K.A.; Bard, A.J.; Campion, A.; Fox, M.A.; Mallouk, T.E.; Webber, S.E.; White, J.M. Demonstration of a Shell-Core Structure in Layered CdSe-ZnSe Small Particles by X-Ray

Photoelectron and Auger Spectroscopies. *J. Phys. Chem.* **1992**, *96*, 3812–3817, doi:10.1021/j100188a045.
185. Honma, I.; Sano, T.; Komiyama, H. Surface-Enhanced Raman Scattering (SERS) for Semiconductor Microcrystallites Observed in Silver-Cadmium Sulfide Hybrid Particles. *J. Phys. Chem.* **1993**, *97*, 6692–6695, doi:10.1021/j100127a020.
186. Zhou, H.S.; Sasahara, H.; Honma, I.; Komiyama, H.; Haus, J.W. Coated Semiconductor Nanoparticles: The CdS/PbS System's Photoluminescence Properties. *Chem. Mater.* **1994**, *6*, 1534–1541, doi:10.1021/cm00045a010.
187. Gawande, M.B.; Goswami, A.; Asefa, T.; Guo, H.; Biradar, A. V; Peng, D.; Zboril, R.; Varma, R.S. Core-Shell Nanoparticles: Synthesis and Applications in Catalysis and Electrocatalysis. *Chem. Soc. Rev.* **2015**, *44*, 7540–7590, doi:10.1039/C5CS00343A.
188. Henrich, V.E.; Dresselhaus, G.; Zeiger, H.J. Surface Defects and the Electronic Structure of SrTiO3 Surfaces. *Phys. Rev. B* **1978**, *17*, 4908–4921, doi:10.1103/PhysRevB.17.4908.
189. Reihl, B.; Bednorz, J.G.; Müller, K.A.; Jugnet, Y.; Landgren, G.; Morar, J.F. Electronic Structure of Strontium Titanate. *Phys. Rev. B* **1984**, *30*, 803–806, doi:10.1103/PhysRevB.30.803.
190. Møller, P.J.; Komolov, S.A.; Lazneva, E.F. Total Current Spectroscopy Study of Metal Oxide Surfaces: II. Unoccupied Electronic States on TiO2(110) and SrTiO3(100) Surfaces. *J. Phys. Condens. Matter* **2000**, *12*, 7705–7711, doi:10.1088/0953-8984/12/35/305.
191. Van Benthem, K.; French, R.H.; Sigle, W.; Elsasser, C.; Ruhle, M. Valence Electron Energy Loss Study of Fe-Doped SrTiO3 and a Σ13 Boundary: Electronic Structure and Dispersion Forces. *Ultramicroscopy* **2001**, *86*, 303–318, doi:10.1016/S0304-3991(00)00121-2.
192. Higuchi, T.; Tsukamoto, T.; Sata, N.; Ishigame, M.; Tezuka, Y.; Shin, S. Electronic Structure of P-Type SrTiO3 by Photoemission Spectroscopy. *Phys. Rev. B* **1998**, *57*, 6978–6983, doi:10.1103/PhysRevB.57.6978.
193. Marsh, H.L.; Deak, D.S.; Silly, F.; Kirkland, a I.; Castell, M.R. Hot STM of Nanostructure Dynamics on SrTiO(3)(001). *Nanotechnology* **2006**, *17*, 3543–3548, doi:10.1088/0957-4484/17/14/031.
194. Webb, C.; Weng, S.L.; Eckstein, J.N.; Missert, N.; Char, K.; Schlom, D.G.; Hellman, E.S.; Beasley, M.R.; Kapitulnik, A.; Harris, J.S. Growth of High Tcsuperconducting Thin Films Using Molecular Beam Epitaxy Techniques. *Appl. Phys. Lett.* **1987**, *51*, 1191–1193, doi:10.1063/1.98729.
195. McKee, R.A.; Walker, F.J.; Chisholm, M.F. Crystalline Oxides on Silicon: The First Five Monolayers. *Phys. Rev. Lett.* **1998**, *81*, 3014–3017, doi:10.1103/PhysRevLett.81.3014.
196. McKee, R.A. Physical Structure and Inversion Charge at a Semiconductor Interface with a Crystalline Oxide. *Science (80-.).* **2001**, *293*, 468–471, doi:10.1126/science.293.5529.468.
197. Minami, T.; Yamanishi, M.; Structures, B.; Choi, N.; Kimura, M.; Kataura, H.; Yong-nian, X.; Kai-ming, Z.; Xi-, X. Semiconductors: GaAs Meets Its Match. **2001**, *14*.
198. Gudiksen, M.S.; Lauhon, L.J.; Wang, J.; Smith, D.C.; Lieber, C.M. Growth of Nanowire Superlattice Structures for Nanoscale Photonics and Electronics. *Nature* **2002**, *415*, 617–620, doi:10.1038/415617a.
199. Ledentsov, N.N.; Ustinov, V.M.; Shchukin, V.A.; Kop'ev, P.S.; Alferov, Z.I.; Bimberg, D. Quantum Dot Heterostructures: Fabrication, Properties, Lasers (Review). *Semiconductors* **1998**, *32*, 343–365, doi:10.1134/1.1187396.
200. Castell, M.R. Nanostructures on the SrTiO3(001) Surface Studied by STM. *Surf. Sci.* **2002**, *516*, 33–42, doi:10.1016/S0039-6028(02)02053-8.
201. Silly, F.; Castell, M.R. Encapsulated Pd Nanocrystals Supported by Nanoline-Structured SrTiO 3(001). *J. Phys. Chem. B* **2005**, *109*, 12316–12319, doi:10.1021/jp051358q.
202. Deak, D.S.; Silly, F.; Newell, D.T.; Castell, M.R. Ordering of TiO2-Based Nanostructures on SrTiO3(001) Surfaces. *J. Phys. Chem. B* **2006**, *110*, 9246–9251, doi:10.1021/jp060954x.
203. Bennett, R.A.; Stone, P.; Price, N.J.; Bowker, M. Two (1×2) Reconstructions of TiO2(110): Surface Rearrangement and Reactivity Studied Using Elevated Temperature Scanning Tunneling Microscopy. *Phys. Rev. Lett.* **1999**, *82*, 3831–3834, doi:10.1103/PhysRevLett.82.3831.
204. Smith, R.D.; Bennett, R.A.; Bowker, M. Measurement of the Surface-Growth Kinetics of Reduced (Formula Presented) during Reoxidation Using Time-Resolved Scanning Tunneling Microscopy. *Phys. Rev. B - Condens. Matter Mater. Phys.* **2002**, *66*, 1–7, doi:10.1103/PhysRevB.66.035409.
205. Diebold, U. The Surface Science of Titanium Dioxide. *Surf. Sci. Rep.* 2003, *48*, 53–229.
206. Russell, B.C.; Castell, M.R. Reconstructions on the Polar SrTiO3 (110) Surface: Analysis Using STM, LEED, and AES. *Phys. Rev. B* **2008**, *77*, 245414, doi:10.1103/PhysRevB.77.245414.
207. Enterkin, J.A.; Subramanian, A.K.; Russell, B.C.; Castell, M.R.; Poeppelmeier, K.R.; Marks, L.D. A Homologous Series of Structures on the Surface of SrTiO3 (110). *Nat. Mater.* **2010**, *9*, 245–248, doi:10.1038/nmat2636.

208. Vitos, L.; Ruban, A.V.; Skriver, H.L.; Kollár, J. The Surface Energy of Metals. *Surf. Sci.* **1998**, *411*, 186–202, doi:10.1016/S0039-6028(98)00363-X.
209. Mykura, H. The Variation of the Surface Tension of Nickel with Crystallographic Orientation. *Acta Mater.* **1961**, *9*, 570–576.
210. Barsotti, T.; Bermond, J.M.; Drechsler, M. The Anisotropy of the Surface Energy of Nickel Measured by TEM of Field Emitters. *J. Phys. Colloq.* **1984**, *45*, 43–46.
211. Hong, J.S.; Jo, W.; Ko, K.J.; Hwang, N.M.; Kim, D.Y. Equilibrium Shape of Nickel Crystal. *Philos. Mag.* **2009**, *89*, 2989–2999, doi:10.1080/14786430903164598.
212. Wynblatt, P.; Chatain, D. Surface Segregation Anisotropy and the Equilibrium Shape of Alloy Crystals. *Rev. Adv. Mater. Sci.* **2009**, *21*, 44–56.
213. Meltzman, H.; Chatain, D.; Avizemer, D.; Besmann, T.M.; Kaplan, W.D. The Equilibrium Crystal Shape of Nickel. *Acta Mater.* **2011**, *59*, 3473–3483, doi:10.1016/j.actamat.2011.02.021.
214. Brillo, J.; Egry, I. Surface Tension of Nickel, Copper, Iron and Their Binary Alloys. *J. Mater. Sci.* **2005**, *40*, 2213–2216, doi:10.1007/s10853-005-1935-6.
215. Guo, H.; Barnard, A.S. Thermodynamic Modelling of Nanomorphologies of Hematite and Goethite. *J. Mater. Chem.* **2011**, *21*, 11566–11577, doi:10.1039/c1jm10381d.
216. Yu, J.; Lin, X.; Wang, J.; Chen, J.; Huang, W. First-Principles Study of the Relaxation and Energy of Bcc-Fe, Fcc-Fe and AISI-304 Stainless Steel Surfaces. *Appl. Surf. Sci.* **2009**, *255*, 9032–9039, doi:10.1016/j.apsusc.2009.06.087.
217. Chamati, H.; Papanicolaou, N.I.; Mishin, Y.; Papaconstantopoulos, D.A. Embedded-Atom Potential for Fe and Its Application to Self-Diffusion on Fe(100). *Surf. Sci.* **2006**, *600*, 1793–1803, doi:10.1016/j.susc.2006.02.010.
218. Perdew, J.P.; Wang, Y. Accurate and Simple Analytic Representation of the Electron-Gas Correlation Energy. *Phys. Rev. B* **1992**, *45*, 244–249, doi:10.1103/PhysRevB.98.079904.
219. Perdew, J.P.; Burke, K.; Ernzerhof, M. Generalized Gradient Approximation Made Simple. *Phys. Rev. Lett.* **1996**, *77*, 3865–3868, doi:10.1103/PhysRevLett.77.3865.
220. Chiaramonti, A.N.; Lanier, C.H.; Marks, L.D.; Stair, P.C. Time, Temperature, and Oxygen Partial Pressure-Dependent Surface Reconstructions on SrTiO3(111): A Systematic Study of Oxygen-Rich Conditions. *Surf. Sci.* **2008**, *602*, 3018–3025, doi:10.1016/j.susc.2008.07.033.
221. Henderson, M.A. A Surface Perspective on Self-Diffusion in Rutile TiO2. *Surf. Sci.* **1999**, *419*, 174–187, doi:10.1016/S0039-6028(98)00778-X.
222. Lanier, C.H.; Chiaramonti, A.N.; Marks, L.D.; Poeppelmeier, K.R. The Fe3O4 Origin of the "Biphase" Reconstruction on α-Fe2O3(0 0 0 1). *Surf. Sci.* **2009**, *603*, 2574–2579, doi:10.1016/j.susc.2009.06.006.
223. Patala, S.; Marks, L.D.; De La Cruz, M.O. Elastic Strain Energy Effects in Faceted Decahedral Nanoparticles. *J. Phys. Chem. C* **2013**, *117*, 1485–1494, doi:10.1021/jp310045g.